Nanoscale metal tips as an electron source for time-resolved microscopy and diffraction.

Bainbridge, Alexander Robert

Nanoscale metal tips as an electron source for time-resolved microscopy and diffraction

Alexander Robert Bainbridge

Swansea University
Prifysgol Abertawe

Department of Physics
College of Science
Swansea University
Singleton Park
Swansea
United Kingdom
SA2 8PP

November 2015

Submitted to Swansea University in fulfilment of the requirements for the Degree of Doctor of Philosophy

In the beginning the Universe was created. This has made a lot of people very angry and has been widely regarded as a bad move. - Douglas Adams

Human beings make life so interesting. Do you know, that in a universe so full of wonders, they have managed to invent boredom? - Terry Pratchett

Abstract

One of the ultimate goals of modern science is to image the evolution of systems on atomic time and length scales, allowing intimate details at the heart of molecular physics and chemistry to be revealed. Until recently this has required the use of short and bright x-ray pulses which are difficult to produce and can cause extensive damage to the sample being imaged. Recent developments in electron microscopy and diffraction have provided a complementary technique which is viable on the scale of a university laboratory and is capable of imaging both static systems and dynamic processes such as charge propagation with atomic spatial resolution, and is rapidly advancing into the imaging in the sub-100 femtosecond temporal regime.

Tungsten nanotips are investigated as a source of ultrashort electron bunches to facilitate electron diffraction and microscopy experiments. A variety of experiments have been performed to measure the energy spectrum and coherence of electron bunches produced by strong-field femtosecond laser driven emission from the apex of a tungsten nanotip, culminating in the first successful use of the velocity map imaging technique to characterise photoelectron emission from a solid.

Following characterisation, femtosecond electron bunches are produced and utilised to perform laser-pump electron-probe point projection microscopy experiments examining the very process that produces them. Charge propagation induced by a laser pulse is recorded in a tungsten nanotip with sub-micron spatial resolution and temporal resolution on the order of 100 femtoseconds, the first time this process has been directly imaged, confirming the viability of using ultrashort electron bunches to track charge propagation with unprecedented precision.

Declarations and statements

This work has not previously been accepted in substance for any degree and is not being concurrently submitted in candidature for any degree.

Signed ..... (candidate)

Date 23/11/2015

This thesis is the result of my own investigations, except where otherwise stated. No correction services have been used. Other sources and reproduced/adapted figures are acknowledged by explicit references. A bibliography is appended.

Signed .... (candidate)

Date 23/11/2015

I hereby give consent for my thesis, if accepted, to be available for photocopying and for inter-library loan, and for the title and summary to be made available to outside organisations.

Signed ... . (candidate)

Date 23/11/2015

Acknowledgements

There are many people to thank who have supported me through my PhD, both personally and professionally. Amongst the most important are my fellow PhD students who have become both colleagues and friends. In particular Ginge, Rhys, Katie and Alex who, amongst other friends, have kept me at a nice healthy level of insanity. Ginge's gift of a coffee machine to the office is particularly appreciated.

For personal support I would like thank my family for putting up with me being awkward throughout this project and always being a phone call away. I would also like to thank my friends from the fencing club for giving me an often welcome distraction and giving me, the geeky kid at school who hated sports, the chance to represent the university. In particular I would like to thank Swifty for moral support, and James Harrington for getting me into the sport and providing many hours of entertainment.

Professional support has come from all manner of people and organisations. Swansea University and the EPSRC have funded and supported me. The whole team at Artemis, in particular Emma, have made entire experiments possible with their expertise and equipment. Julian and Phil have made countless pieces of equipment for me with great skill. There are many undergraduate and summer students who have helped greatly with this project, in particular Chris and Matt for researching tip etching and Connor for taking over simulation work. Special thanks go to the EPSRC Laser Loan Pool and especially Ian Clark for his support.

But above all else I would like to thank my supervisor Will, who has guided me through my PhD with endless patience and somehow resisted the temptation to murder me. This project started in the summer of 2011 as nothing more than a hunch, a good direction in which to take the research at Swansea. In that time we have worked together to achieve something fantastic, and despite often having the help of other students and the Artemis team we have mostly been an army of two, battling to complete projects that larger and richer groups than us took years to perfect. I could not have completed my PhD without Will guiding me.

Publications and presentations

Peer reviewed publications

A. R. Bainbridge and W. A. Bryan. "Velocity map imaging of femtosecond laser induced photoelectron emission from metal nanotips." *New Journal of Physics* **16** 103031 (2014).

A. R. Bainbridge, J. Harrington, A. Kirrander, C. Cacho, E. Springate, W. A. Bryan and R. S. Minns. "VUV Excitation of a Vibrational Wavepacket in D_2 Measured Through Strong-Field Dissociative Ionisation." *New Journal of Physics* **17** 103013 (2015). From work not presented here.

Other publications

A. R. Bainbridge, D. Thorne, W. A. Bryan, P. Lane, S. Young, M. Robinson, D. Wann, R. Chapman, P. Rice and E. Springate. "Coherence studies of pulsed electron beams from point sources." *CLF annual report 2013.*

A. R. Bainbridge, M. B. Nicholson, C. Saul and W. A. Bryan. "Photoemission from nanoscale metal tips for time-resolved electron diffraction." *CLF annual report 2012.*

Conference Presentations

"Femtosecond electron microscopy of charge motion along the surface of a nanoscale object". Presented at ICUSD 2015 (Zurich) by Will Bryan.

"Velocity map imaging of ultrafast electron emission from fs-laser illuminated nanoscale metal tips". Presented both at the Annual conference of the German Physical Society 2015 (Berlin) and at the LSF user meeting 2015 (Abingdon).

"Towards time-resolved molecular imaging by ultrafast electron diffraction". AMIG 2013 (Maynooth, ROI). Awarded prize for best postgraduate presentation at the event.

"Development of a new electron source for time-resolved electron diffraction". Poster presentation at QuAMP 2013 (Swansea).

"Generation of ultrashort electron pulses from nanoscale metal tips". Poster presentation at the LSF-Artemis user meeting 2012 (Abingdon).

Contents

Chapter 1

Introduction and literature review

In this chapter is presented a brief history of time-resolved measurements, a discussion of methods used for observations on ever decreasing time scales, and a detailed introduction to femtosecond electron microscopy and diffraction. The story of how basic microscopy has evolved to include time resolution, through achieving imaging on atomic time and length scales through x-ray diffraction and advancement to the cutting edge technique of ultrafast electron microscopy and diffraction is long and fascinating. In addition to the brief history and context presented here there are some excellent comprehensive reviews in the literature [1–6] which give a complete story of the development of electron microscopy and diffraction from the static to the ultrafast regime.

1.1 Motivation

It has long been known that a huge number of interesting processes that govern everything that we see around us occur on time and length scales too small and fast for the human eye to resolve without assistance from advanced techniques. At the extreme of these processes are those governing the behaviour and structure of individual molecules. Determining the structure of complex molecules, and to observe the evolution of their structure, is one of the great challenges of modern science. There has been much progress made in this field to date, the determination of the double helix structure of DNA by Crick, Watson & Franklin [7, 8] being a prime example. There is still a wealth of knowledge to be gained, however, and the structure of many complex and important biological molecules such as proteins and enzymes is known only theoretically, with millions of potential folding patterns determining the actual physical shape of the molecule. In addition, the structure of these molecules does not remain constant as a function of time, particularly under reaction with

other molecules or interaction with light [9]. Molecules constantly oscillate in both vibrational and rotational modes, determined in turn by patterns in their electronic structure [10, 11]. Changes in these patterns are of great interest as they are key to chemical reactions such as DNA construction (and repair) as well as photosynthesis, two important processes without which life itself could not exist. Gaining time-resolved observations of these processes is therefore of paramount importance.

This objective represents a fine example of the application of physics to its sibling sciences of biology and chemistry. Whilst the techniques of measuring molecular evolution are based in physics, the motivation to achieve this arises from applications across all the sciences in a huge number of fields. An excellent example is highlighted in [2], where it is pointed out that during the process of a chemical reaction the starting molecules and end products may have well defined and static structures, but these alone are not always sufficient to determine the reaction pathway. A direct view of the initial contact between the reagents would reveal the intricate workings of the principles of femtochemistry [3, 10–16]. Similarly biological processes rely on complex molecules following set reaction pathways. To define these pathways a series of correlated processes must occur, including atomic motions and charge propagation, however the static molecular structure alone is often not sufficient information to predict this sequence.

Beyond biological physics, atomic scale time-resolved imaging can provide a wealth of information on even shorter scales via diffraction through small molecules in the gas phase [17], or on larger scales to provide new insights into condensed matter, where many coupled events or processes on a range of scales may be occurring simultaneously to define the behaviour of a material. For example a drastic event such as a phase change which is clearly measurable in the bulk material even on visible scales is fundamentally related to effects such as phonon coupling with electrons on the atomic scale [18], which is often difficult to predict, especially in a complex or non-symmetric lattice. This makes atomic scale imaging vital in mapping changes in parameters such as bond length to achieve fundamental understanding of these processes.

To film such a process (making a so-called "molecular movie") would allow currently undetermined aspects of chemical and biological interactions to be definitively classified and understood. This could potentially apply across a massive range, from small molecules a few nanometres or even angstroms across to millimetre scale bulk transitions in solids, and across timescales from the sub-femtosecond through to, in the case of materials science in particular, changes that happen on timescales up to those perceivable with the naked eye. Furthermore the understanding of activity

of a system acquired from imaging a process or evolution raises the possibility of controlling said activity. It is already possible, at the bleeding edge of our current abilities, to exercise control of molecular targets using short coherent laser pulses to manipulate molecular wavepackets on the femtosecond timescale [15, 19–23], as well as the common and much cruder practise of controlling phase changes through concentrated energy delivery. It can therefore be said that the motivation of this work conducted in various groups around the world, of which this project is a small part of the many which are slowly coming together to form something spectacular, can be summed up as no less than the lofty goal of the ability to exercise control of our surroundings at the molecular level. In the long term the potential applications are endless, from driving chemical reactions to synthesize new molecules for pharmaceuticals to developing new materials tailored for specific purposes.

1.2 History and development of atomic scale time-resolved imaging

1.2.1 Introduction

The history of microscopy is extensive and complex, starting with the first use of glass beads as lenses in the Roman era, through the invention of the first true microscope by Antonie van Leeuwenhoek [24] and to to the modern era of atomic scale electron microscopy. Similarly, the challenge of developing imaging on the shortest possible timescale has a shorter but no less substantial history, beginning with Eadweard Muybridge's ground breaking photographs of the galloping horse at Palo Alto [25], to modern pump-probe experiments using x-ray and XUV pulses so short that information on the scale of a few femtoseconds [11, 12, 23, 26, 27] or in extreme cases even hundreds of attoseconds [28–35] can be obtained.

Whilst this full story of developments is of great interest, the discussion here must be limited. The detailed history of time-resolved microscopy can fill entire volumes. This thesis focuses specifically on advanced techniques covering the femtosecond timescale, namely the development of femtosecond electron microscopy and diffraction as a complementary technique to existing light-based imaging methods. As such, the detailed introduction into the history of the technique presented below shall focus only on the modern developments specifically leading to the current work, starting with how temporal resolution was first obtained, followed by combination with atomic scale imaging achieved through the use of x-rays. The use of electrons as an alternative method in the purely spatial regime is then discussed, before fi-

nally detailing new developments that for the first time allow the use of electrons to achieve atomic scale imaging in the temporal and spatial regimes simultaneously, and discussing how this compares to the use of x-rays, the most common technique at the present time.

1.2.2 Atomic scale spatial and temporal imaging through photonic techniques.

The advent of imaging on the femtosecond timescale required an extensive adaptation of traditional techniques. Whilst strobe illumination is a staple of fast imaging, it is limited by the electronic switching time which has a theoretical best resolution of a few nanoseconds, whilst engineering limitations typically require falling short of this limit by a significant amount. Even at its best, this is still six orders of magnitude too slow to resolve the action of atomic and molecular systems. The breakthrough in imaging on the femtosecond timescale was achieved with the invention of modelocking [36–38], allowing the first femtosecond laser systems to be produced. This allowed snapshots with femtosecond resolution to be obtained for the first time, albeit at a small range of optical wavelengths prohibiting direct imaging on molecular spatial scales.

Although the wavelength range available rendered femtosecond laser systems by themselves unsuitable for direct diffraction and microscopy from molecular scale targets they have been used to provide an enormous amount of information regarding the electronic, vibrational and rotational structure of atoms and molecules, particularly in the gas phase. Experiments of this nature are generally performed using the pump-probe scheme proposed by Norrish and Porter [9], and rely on the high intensities delivered by femtosecond lasers, in particular those that utilise chirped pulse amplification [39]. The classic technique is to split the femtosecond pulse into two arms, one of which has a variable delay controlled by a moveable translation stage, before overlapping the beams spatially with the point of temporal overlap occurring within the range of travel of the stage. The pulse travelling along the fixed arm is generally used as a "pump", which excites a desired electronic, vibrational or rotational mode in the target before the second "probe" pulse causes dissociation into molecular fragments. Repeated snapshots of the incidence rate and energy of the fragments at a variety of delays yield information about the nature of the excitation.

This idea is refined further by photoelectron spectrometry, where the energy spectra (and in certain techniques such as velocity map imaging and angle-resolved photoelectron spectrometry, also the emission directions or angles) of photoelectrons are recorded with subtle changes in the electron energy yielding information about

the evolution of the target.

More recently techniques have evolved to the point where information can be obtained without the destruction of the target molecule, where instead a photon emitted by the target is detected. Of particular interest are multi-dimensional spectroscopy techniques such as Two Dimensional Photon Echo (2DPE) spectroscopy [40–42]. Another purely photonic technique which avoids damage to the sample is femtosecond Raman spectroscopy [43–46], particularly useful for studying changes in chemical composition over time.

Prior to this, and neglecting the temporal component required for true atomic scale imaging, the discovery of x-rays by Röntgen [47] in 1895 opened up the first possibility of using light with sub-nanometre wavelength, allowing atomic scale objects to be directly imaged (albeit statically) for the first time. Achievement of this was far from immediate, due to a lack of technological ability to reliably produce, control and detect x-rays at the time. It is well known that one of first atomic scale uses of x-rays to achieve imaging was by Bragg in 1912 [48], who observed the scattering of x-rays from a crystalline structure and was able to resolve the planar arrangement of atoms within the crystal. Furthermore, this technique allows the distance between the planes to be measured, highlighting the spatial resolution that can be achieved in a technique still used to this day [49–52].

Whilst Bragg achieved diffractive imaging relatively early, real-space imaging was not achieved until much later. Optical resolutions of a few microns were achieved using x-rays for the first time using point-projection microscopy in 1939 [53]. Interest in the ability of x-ray microscopy to achieve extremely high spatial resolutions dramatically accelerated after the second world war [54], with a number of devices being developed. These devices generated x-rays at the impact point of electrons with a thin metallic plate allowing a reasonably controllable point source [55] but, with the technology of the time, were limited to operating as a continuous beam, allowing only static images to be obtained. Further advances allowed the production of x-ray optics using zone plates to act as x-ray lenses [56], allowing deviations from the technique of steering a continuous beam of electrons to create a point-source of x-rays and opening the possibility of using alternate pulsed sources of light.

The first transmission x-ray microscope device was constructed in 1974 [57] using the zone plate focusing technique, allowing the x-rays to be derived form a source some distance from the sample. This was then adapted to operate using a synchrotron x-ray source [58, 59] and later XFEL sources (although modern systems use glancing reflections from toroidal mirrors as an alternative focusing technique), allowing microscopy using pulsed x-rays for the first time making pump-probe exper-

iments in real space using x-rays possible, with recent examples being x-ray probing of femtosecond laser excited nanoparticles [60]. These devices were capable of operating with sub-micron spatial resolution, and work by transmission of x-rays through the target. This was soon followed by the first devices similar in which the beam is scanned across the target [61–63]. Those devices developed for pulsed operation were still prevented from achieving imaging on atomic spatial and time scales by the quality of the x-rays provided by synchrotron sources, both in terms of pulse length and coherence [64, 65]. The synchrotrons of the time were not capable of producing coherent pulses of x-rays short enough to resolve motion on the atomic scale.

The problem of coherence was partially resolved by the invention of the x-ray laser [66], however initially the repetition rate of these systems was far too low to collect sufficient data for extensive pump-probe experiments. The true breakthrough came when a new generation of synchrotron was developed capable of delivering sub-picosecond x-ray pulses with high repetition rate [67, 68]. This sparked the development of new and highly capable synchrotron light sources, examples of which include the National Synchrotron Light Source (NSLS) in the USA, Diamond Light Source (DLS) in the UK, ELETTRA in Italy and Soleil in France. These facilities and others like them are capable of delivering x-ray pulses with sufficiently short wavelength (sub-angstrom) and at a high enough repetition rate to reliably image by both microscopy and diffraction systems with atomic spatial resolution, although pulse lengths are generally too long for femtosecond temporal resolution (a notable exception being the I06 beamline at DLS [69]). As such they remain the standard "go to" technology whenever an image with with these parameters is required. They are universal throughout a variety of fields, and whilst they are still often used for traditional crystallography they are also routinely used to perform studies in tomographic imaging of a variety of samples including complex biological systems [70–74].

In 1999 a major milestone was reached when diffraction imaging of a complex structure was achieved [75]. Prior to this development x-ray diffraction imaging was only possible through regular, or crystalline, structures. The ability to apply the extreme spatial resolution of x-ray diffractive imaging to non-regular systems with femtosecond temporal resolution, in particular biological systems, allows a phenomenal amount of microscopic information to be obtained [76]. The modern pinnacle of time-resolved x-ray imaging consists of both modern synchrotron light sources and new X-ray Free Electron Lasers (XFELs) [77] such as FLASH, SACLA, LCLS and European XFEL currently under construction, which deliver many more photons per shot than synchrotrons albeit at a significantly lower repetition rate.

Such techniques allow temporal resolution of the order of 10 fs to be readily obtained [78]. XFELs have already seen successes in ultrafast x-ray holography [79], imaging structural changes in proteins [80], gas phase imaging [81], and have even achieved 1.5 Å resolution in room temperature targets [82].

1.3 The alternative to light: Electron microscopy

Whilst photons of various wavelengths from the visible to the x-ray range have been the prime tool for microscopic and time-resolved imaging throughout history, and continue to be a widely used technique, it is readily apparent that the limitations of light at the atomic scale necessitate an alternative. The damage to samples arising from exposure to intense x-ray pulses is a significant inconvenience. Furthermore x-ray diffraction experiments are rarely feasible on the scale of the typical laboratory, instead requiring large and expensive centralised facilities such as synchrotrons or X-FELs to produce x-ray pulses of sufficient intensity and repetition rate to be usable. X-ray pulses are also significantly more troublesome to apply to a target than visible light; conventional optics are insufficient to steer and focus x-rays, which instead require control through glancing-angle reflections from expensive customised optics such as gold coated toroidal mirrors.

In searching for a new technique it is important to note that achieving diffraction of an object is greatlt simplified by having a flat coherent wavefront, but the requirements are much less stringent for simple microscopy. Crucially a wave of any type will suffice as long as the wavelength is relevant to the scale of the target. Louis de Broglie predicted in 1923 [83, 84] that every form of matter could behave with wave-like properties, opening up the new possibility of using particles in place of photons as the imaging wavefront. Building on the work of Einstein, de Broglie predicted that every particle has a wavelength given by equation 1.1

$$\lambda = \frac{h}{p} = \frac{h}{mv}\sqrt{1 - \frac{v^2}{c^2}}. \tag{1.1}$$

where h is the Planck constant, p the particle momentum, m its mass and v and c the velocities of the particle and light respectively. This equation predicts that the wavelength is proportional to the Planck constant divided by the relativistic momentum of the particle, allowing changing of the wavelength at will simply by accelerating or decelerating the particle to the desired momentum. This was experimentally confirmed in 1927 by Davisson and Germer, who observed indications of a diffraction pattern in electrons scattered from crystalline nickel [85], and soon after

by Thomson and Reid who observed diffraction from a thin film of celluloid [86].

Although any particle could in theory be used, electrons are the obvious choice due to their ease of production and, being the lightest particle available, they are the simplest to accelerate and control. An electron with energy 100 eV has a wavelength of 1.23 Å, comparable to the size of an atom (1-1.5 Å). This wavelength allows atomic spatial resolution to be achieved, albeit with a very large diffraction angles and Coulomb explosion in the electron beam. With modern technology where acceleration to tens of keV is feasible in a relatively compact device, these limitations are overcome as the short flight time (often only a few nanoseconds) helps to negate space-charge issues and the short wavelength results in a clear diffraction pattern at narrow angles such that several orders of diffraction may be captured.

Electron microscopy was first achieved by Knoll and Ruska in 1931, with the first Transmission Electron Microscope (TEM) [87]. Their design, which has remained through to modern times with remarkably few changes, is based in the same techniques as optical microscopy. An electron source produces a continuous beam, normally through thermionic emission [88]. A magnetic lens collimates the beam before a second lens focuses it through the sample, the image of which is imprinted onto the electron beam. A second series of lenses then project the image onto position sensitive detector, originally a photographic plate but now more commonly an electronic detector [89–92] such as a phosphor screen imaged with a CCD or even using a CCD to directly detect electrons [93].

Whilst the central design is preserved, modern TEMs are generally larger and capable of achieving significantly higher beam energies, commercial TEMs capable of up to 300 keV are readily available. The first commercial TEMs were capable of achieving a spatial resolution of approximately 100 Å at best, whereas modern TEMs are capable of achieving 0.1 Å resolution. The resolution is primarily dependent on the de Broglie wavelength of the electrons but will realistically be lower than theoretically possible for a given beam energy. This is due to limitations in the equipment itself in two key areas. Firstly the detector itself has an inherent resolution limit, secondly the beam is manipulated by no less than four (often more) lenses. These can be electrostatic or magnetic though are almost always the latter. Both methods of focusing introduce aberrations into the electron beam, which can often introduce minor distortion into the image. Methods have been developed for compensating for these aberrations [94–96], though it is not possible to completely remove their effect without removing the lenses. Generally magnetic lenses are preferred as for high beam energies an einzel lens [1] requires very high applied voltages

[1]From the german "Einzellinse" which translates to english as "single lens". A series of electo-

to achieve focusing, often difficult to achieve within the electrical breakdown limit, whereas a magnetic lens can achieve similar focusing with only a small current.

Transmission electron microscopy remains a common technique, and several minor variations have been implemented to fulfil requirements for specific situations. These include Immuno-EM, where certain parts of a biological sample are labelled with gold nanoparticles which interact strongly with the imaging electrons, allowing any feature which can be labelled (including for example antibodies, which were the first to be tagged with this technique, hence the name) to be tracked in real time. Other examples include cryo-EM, useful for examining targets crystallized onto surfaces and so highly relevant to examining complex molecular systems, and 3d-volume EM which expands the use of TEM from thin transmissive targets to enable tomographic imaging of surfaces of bulk objects.

Electron-based imaging is not limited to microscopy. If electrons are produced with sufficient quantum coherence and are collimated to form a flat wavefront then imaging by diffraction is also possible, in direct analogue to the same technique regularly used with x-ray pulses. As with x-rays the use of diffraction allows extremely high spatial resolution to be achieved, making atomic and molecular scale imaging viable. The idea of using electrons to image by diffraction actually pre-dates the more direct technique of TEM, with Mark and Wierl first reporting electron diffraction through gas phase molecules of CCl_4 as early as 1930 [97]. The method was refined further by Pauling and Brockway, who took several images highlighting chemical bonds [98] and later developed the first reliable technique for reconstructing diffraction pattersns to a real-space image by applying a Fourier transform to the data [99]. Further refinements in the late 1930's incorporated a metal disk on a thin arm to obstruct the center of the pattern, removing the noise generated by zero order electrons and enhancing the signal from the first and higher diffraction orders. This disk was rotatable such that the arm would not constantly obstruct a single area of the pattern [100–102]. The combination of these techniques has been instrumental in understanding the structure of molecules and the nature of chemical bonds in the static approximation [103, 104]. The cutting edge of this technique allows static images to be obtained with up to 10 nm spatial resolution using real space imaging [105] and up to 2 Angstrom resolution by a combination of microscopy and diffraction [106] using low energy electrons.

static apertures which acts as a charged particle lens.

1.4 The advent of electron microscopy and diffraction on the femtosecond timescale

The use of electron microscopy as a static imaging process was achieved rapidly and has remained in use partly due to the ease of producing a continuous beam of electrons, readily achievable simply by heating a pointed cathode [88]. Temporally resolving a changing sample requires that the electron beam be pulsed, which is much more complex to achieve. The traditional DC emission processes such as heating the cathode cannot be used for pulsing due to the extreme hysteresis and long resulting pulse lengths which offer little benefit over continuous beams. Instead the electrons must either be mechanically or electromagnetically chopped to achieve pulsed delivery, or be produced from a photocathode with the emission being gated by a pulsed laser. Furthermore electrons liberated by the photoelectric effect may be suitable for microscopy but are limited for diffraction purposes, generally lacking the coherence required to obtain diffraction images without an enormous background signal.

It is only in the last decade that it has been possible to produce short coherent pulses of electrons that are suitable for both microscopy and diffraction, a revolution brought about by the development of the femtosecond laser system. Modern femtosecond laser systems allow the production of sufficiently intense laser pulses to induce strong-field photoemission over a comparable time scale to the incoming laser pulse, even when the photon energy is below the work function of the cathode, especially when the cathode is shaped to induce an enhancement of the incident laser field. Electrons emitted by this technique can form a highly coherent wavefront, allowing femtosecond time scale imaging by electron diffraction to be realised with a high signal-to-noise ratio.

The first attempt at introducing time resolution to electron diffraction was by Ischenko *et al* [3, 107], who performed a series of experiments of the pump-probe variety pioneered by Norrish and Porter [9]. Ischenko and colleagues were the first to use a short pulse of electrons as a probe to examine changes to a group of molecules after a chemical reaction was induced by a laser pump pulse. These experiments used the first dedicated electron diffraction apparatus which was constructed in 1980 at Moscow State University, with a beam energy of up to 60 keV and an electron pulse length of at best 20 ns at creation and of the order of 100 μs at the sample. The limited time resolution was due to the fact that the electrons were not photoemitted by a coherent laser pulse, instead a continuous beam was produced which was periodically steered onto a target by a solenoid. The temporal

resolution is therefore limited by the switching time of the electronics controlling the solenoid, which is limited to a few nanoseconds at shortest, combined by the long distances travelled by the electrons whilst burdened with a significant initial spread of energies. This technique generated much interest, being refined to produce shorter and shorter electron pulses, from 100 μs resolution dissociation studies of ClO_2 [108] to phase change studies with a temporal resolution of 1 μs [109].

The first use of pulsed laser photoemission to overcome the limitations of electromagnetic chopping was by Ewbank *et al* who observed photo-fragmentation of molecules with nanosecond temporal resolution [110, 111]. Enhancements to electron detection through the use of streak cameras allowed images with temporal resolution on the order of 100 ps to be recorded [112], followed shortly by production of 20 ps pulses [113, 114].

In more recent times the advent of modern digital technologies such as CCD cameras and computers fast enough to collect and process large amounts of data in real time, combined with the ready availability of femtosecond laser systems, has allowed electron diffraction on the femtosecond timescale to be realised. This temporal sensitivity allows the evolution of molecular structure to be observed following pumping or chemical reaction. The first confirmed diffraction image on the femtosecond timescale was taken in 2001, showing the simple ring molecule cyclohexadine [14, 115–118]. The typically low signal-to-noise ratio means the most convenient way to observe effects over this timescale is by the difference method, where diffraction patterns are compared to a pattern taken before the main experiment which acts as a reference where the sample is in the ground state [1, 119]. This technique is currently still under development, but represents the cutting edge of imaging technology [2], with ever shorter pulses being produced. Time-resolved electron diffraction is not limited to the gas phas, and has been achieved through solid targets with fast processes in thin films being of particular interest [120, 121].

Whilst keeping electron pulses short is difficult due to space-charge effects, this is now being overcome, first by Siwick *et al* who observed structural transitions with 600 fs electron pulses [121]. Other technologies such as compression in an RF cavity have allowed the effects of space-charge to be actively countered, as shown in figure 1.1. The pinnacle of this technology has allowed bunches of up to 10^6 electrons to be temporally focused to sub-100 fs duration [122, 123].

It has been demonstrated recently that it is possible to preserve the spatial resolution obtained in static imaging even when generating femtosecond electron pulses from a point source. Barwick and colleagues conducted an experiment (results shown in figure 1.2) to demonstrate that it was possible to transfer between DC

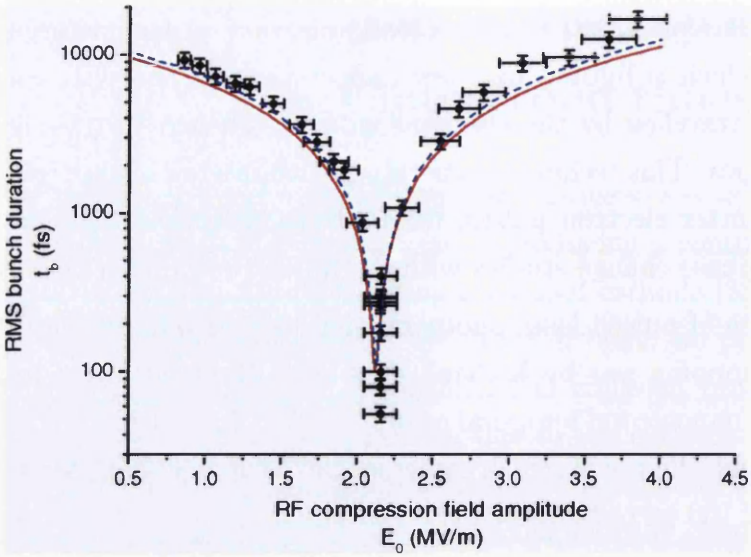

Figure 1.1: Experiment by Luiten *et al*, reproduced from [122], showing RF compression of electron bunches to counter dispersion arising from space-charge effects. Foe the right cavity parameters a clear temporal focus is demonstrated with a sub-100 fs electron bunch length.

emission and femtosecond laser induced emission from a nanotip with relative ease. They imaged nanowires deposited on a TEM grid by point projection microscopy at a variety of magnifications using DC field emission. The experiment was then repeated with the cathode voltage lowered using photoelectrons emitted by a femtosecond laser. By using a high repetition rate, low power oscillator (10 nJ in 80 fs at 80 MHz) they demonstrated that by continuously collecting emission at the order of 1 electron per laser shot it is possible to overcome the resolution and clarity limitations often imposed by space-charge at the point of emission. Methods of producing suitable electrons are discussed further in chapter 2.

Recently pump-probe experiments have begun utilising laser pump and electron probe pulses to image changes in materials, ranging from the drastic changes such as the reordering of the entire crystal structure [125] to more subtle processes such as charge density wave propagation [126]. These two examples are shown in figures 1.3 and 1.4 respectively. Combined with the results of Barwick *et al* [124], this should allow processes on the timescale of hundreds or even tens of femtoseconds and on the atomic spatial scale to be imaged in the very near future.

1.5 Comparison between imaging techniques

There are clearly advantages and disadvantages to the use of both electrons and x-rays for diffractive imaging with femtosecond temporal resolution, especially when

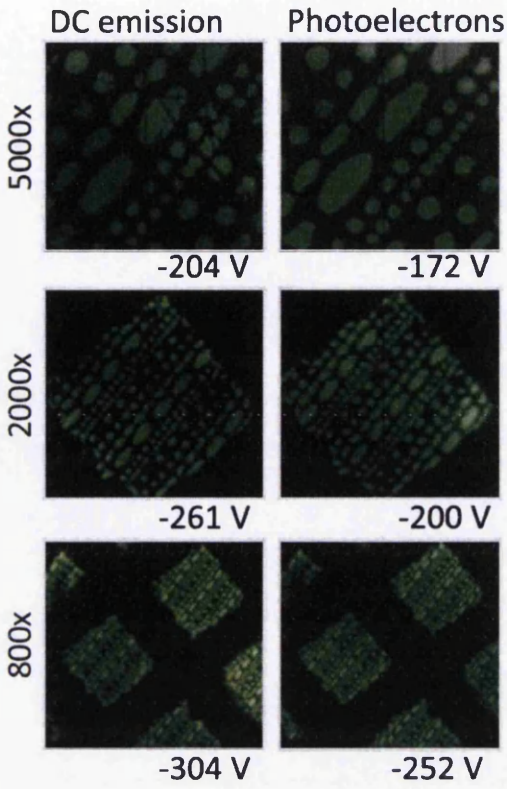

Figure 1.2: Experiment by Barwick *et al*, reproduced from [124], showing that it is possible to retain spatial resolution when moving from a continuous beam of electrons to imaging with femtosecond electron bunches. Left: Point projection electron microscope images of 100 nm diameter silver nanowires supported by a TEM grid with DC emission. Right: Image of the same target obtained with photoelectrons emitted by a femtosecond laser.

considered from the experimental standpoint. In addition to the aforementioned effective control over the de Broglie wavelength, electrons have a further advantage in that a given electron will exhibit an elastic scattering cross section with molecular targets on the order 10^5 to 10^6 higher than that of an x-ray photon [2, 6, 13, 127], meaning that approximately 10^5 electrons in total are required in a region of diameter 100 μm to obtain a complete image with an acceptable SNR [2]. This allows weak pulses of electrons to be used, whereas x-ray diffraction requires the application of intense pulses to achieve sufficient signal. This in turn introduces a problem as x-rays are likely to inelastically scatter and damage samples, as such applying intense pulses results in samples having a relatively short lifespan and needing regular replacement. The high scattering cross-section allows electrons to reliably examine almost any target, from the gas phase to thin films, as even a monolayer has a significant scattering cross section [128–131]. Conversely, this feature makes electrons unsuitable, particularly at low energies, for examining targets with significant depth

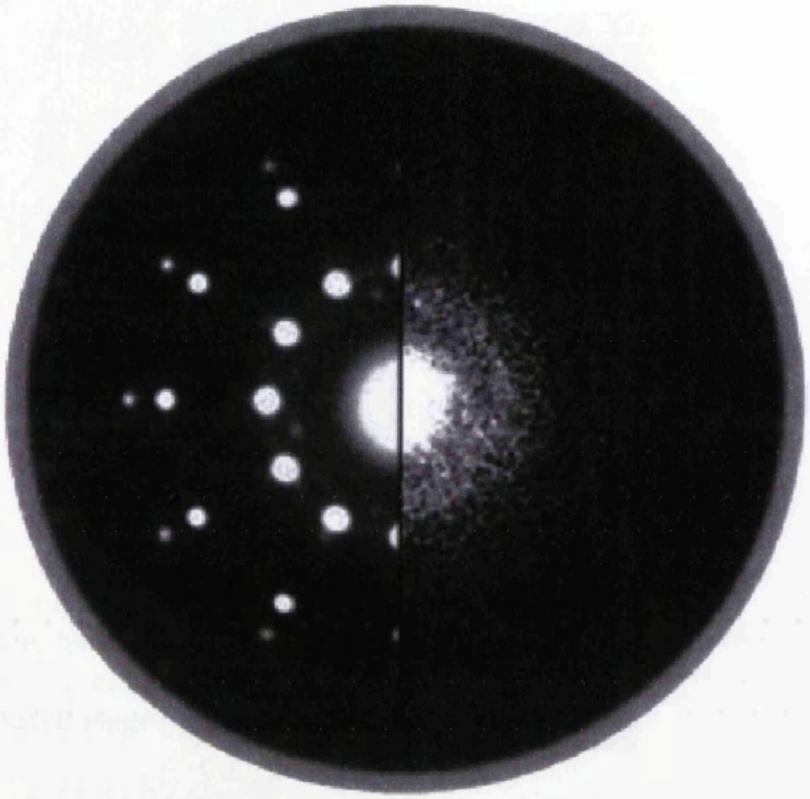

Figure 1.3: Example of the temporal and spatial resolution that can be achieved by femtosecond electron diffraction, in this case showing melting of Bismuth. Reproduced from [2], in turn adapted from [125]. Left: Crystal imaged under static conditions. Right: Average of 60 shots at 1 ps after laser induced melting occurs. The loss of structure indicates a rapid transition to a liquid phase.

(more than 100 nm). In such situations, particularly prevalent in crystallography, x-rays remain the desired tool as electrons require extremely high energies to achieve the necessary penetration into the target.

In addition electron imaging can be rapidly and simply switched between the diffraction and microscopy regimes by adding or removing the beam collimation apparatus [106, 131, 132], as shown in figure 1.5. Switching between the flat wavefront of diffraction and the expanded wavefront of microscopy may be trivial with visible and infra-red laser light but is much less so when the spatial resolution granted by x-rays is required, as x-ray optics are highly specialised for a particular set of conditions and require light to be incident in a narrow range of grazing angles. Switching between regimes therefore requires an extensive remodelling of the optical layout. An excellent example of how electron diffraction and microscopy can be easily combined in a single experiment is found in [106], reproduced and presented in figure 1.6.

A significant benefit of using electrons over x-rays is that electrons are highly

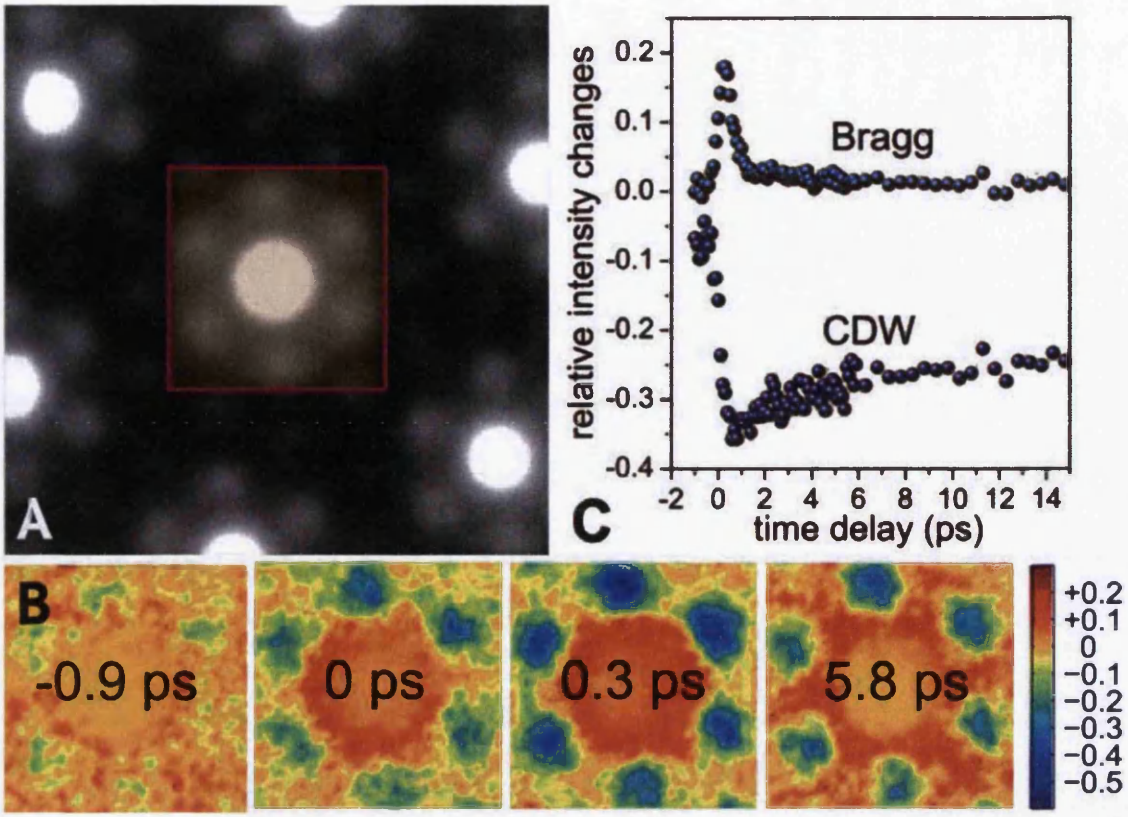

Figure 1.4: Example of the temporal and spatial resolution that can be achieved by femtosecond electron diffraction, in this case used to film suppression of Charge Density Waves (CDW). Reproduced from [2], in turn adapted from [126]. (A) Magnified view of the electron diffraction pattern from a 1T-TaS_2 crystalline lattice. (B) Relative change in the diffraction pattern as a function of time following photoexcitation. (C) Relative intensity change of the central Bragg peak and surrounding CDW peaks.

sensitive to charge in and around the sample, a fact exploited for the experiment detailed in chapter 8. This is significant as it allows areas of localised charge to be detected and tracked, allowing processes such as charge migration through molecules or the propagation of a charge density wave across a surface to be tracked. An excellent example experiment was conducted by Miller *et al*, who utilised a laser pump and electron probe to image suppression of charge density waves in a crystal [126] with temporal resolution on the order of a hundred femtoseconds. The results ofthis experiment are presented in figure 1.4, where it is demonstrated that peaks in the diffraction pattern of a 1T-TaS_2 crystalline lattice arising from the charge density waves are suppressed over within a picosecond by a laser pulse, before recovering over 10's of picoseconds. Conversely the Bragg peak is enhanced and decays over less than 2 picoseconds. A sub-300 fs temporal resolution is achieved, making Miller's experiment a milestone in time-resolved electron diffraction.

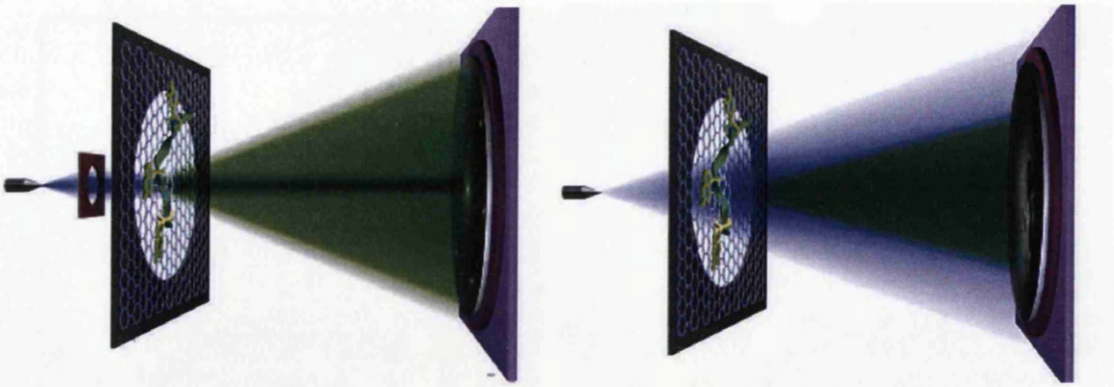

Figure 1.5: Experiment by Fink *et al* showing how the same apparatus can be used for both electron diffraction and microscopy with the alteration of a single component. Adapted from [106], this layout was used to obtain the results presented in figure 1.6.Left: Coherent electron diffraction achieved by collimating the electron beam before the target. Right: Point projection microscopy performed simply by removing the collimation lens and adjusting the distance between source and target.

Furthermore there is a key engineering and logistics aspect to these experiments which leans heavily in the favour of electron microscopy. As stated above the production of suitable x-ray pulses generally requires the use of a synchrotron or XFEL, extremely large and expensive devices generally operated as national facilities, requiring transport of apparatus and forcing experiments to be run as fast as possible due to limited access time. It is becoming apparent that this limitation may be partially overcome by tabletop High Harmonic Generation [133, 134], allowing the scale of experiments to be dramatically reduced. The HHG technique is not yet widely used as it is generally limited to producing VUV and soft x-ray wavelengths at relatively low photon flux compared to an XFEL, but is showing potential with recent advances including production of photons at 1.6 keV energy [135]. Devices suitable for performing diffractive imaging to such an extent that they are viable alternatives to using a synchrotron or XFEL are currently emerging [136], and lower resolution soft x-ray diffraction has been achieved [137].

A comparatively small vacuum system relative to synchrotrons and XFELs may be used and the entire system may be operated using a commercial Ti:Sapphire oscillator (although generally a more expensive regenerative amplifier and OPA are desirable when extensive sample pumping is necessary, see chapter 3). At present this is less true when high energy electrons of hundreds of keV or MeV are desired, which with current technology necessitates a larger vacuum system and complex electronics more suited to operation at a national facility (for example, the VELA accelerator at Daresbury Laboratory).

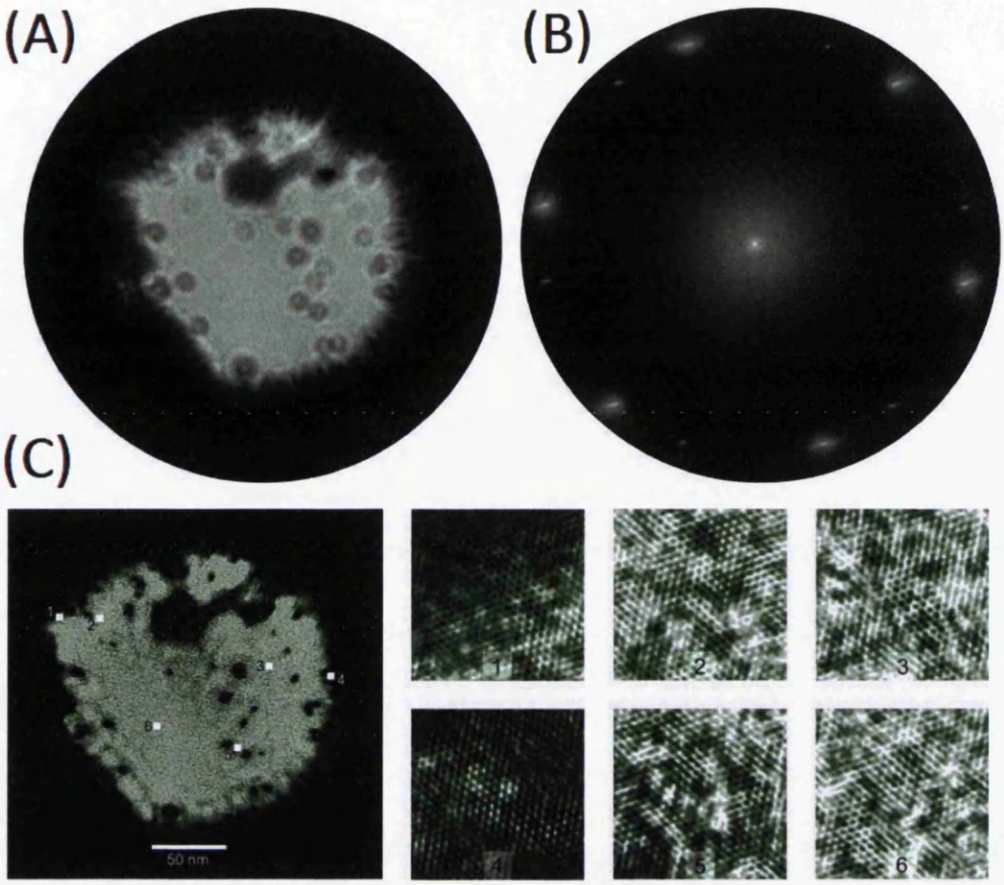

Figure 1.6: Experiment by Fink *et al* showing how electron microscopy and diffraction can be combined to accurately reconstruct an atomic scale image of graphene. Reproduced from [106]. (A) Inverted point projection microscope image of a graphene flake recorded at 58 eV. (B) Coherent diffraction pattern of the same flake recorded at 236 eV. (C) Combined reconstruction of the flake with 2 Å spatial resolution, with detailed view of the marked squares. The hexagonal atomic pattern is clearly visible.

Low energy ultrafast electron diffraction and microscopy, however, can readily be performed using apparatus on the scale (in both space and budget) of a university laboratory, as demonstrated both in this thesis and in the literature. Recent cutting edge work performed without the use of national facilities includes Ernstorfer *et al* constructing a novel electron diffractometer [138] and achieving sub-100 fs imaging of charge propagation in nanowires [132], and polymer structure dynamics being resolved by Gulde *et al* [139]. Baum *et al* have detected acoustic phonons with few-femtosecond temporal resolution through single electron diffraction with a comparable SNR to multi-electron experiments [140, 141]. Miller *et al* have employed electrons to image molecular motion and charge delocalisation [142], as well as imaging ring-closing reactions with femtosecond electron crystallography [143].

Gerbig *et al* achieved femtosecond electron diffraction through crystalline graphite [144]. Finally Siwick *et al* have reported using ultrafast electron diffraction to reveal photo-induced exotic phases of materials [145] and electron phonon coupling in graphite [146].

Chapter 2

Electron emission from nanoscale metal tips

In order to proceed with the goal of performing electron microscopy and diffraction with atomic spatial and temporal resolution, a suitable mechanism by which femtosecond electron pulses are produced must be determined. A combination of emission processes and, crucially, a photocathode capable of utilising this process effectively must therefore be selected. It was determined that nanoscale metal tips (often abbreviated to "nanotips" or simply "tips") were a suitable option with strong-field laser driven emission by a conventional femtosecond laser system producing optimal electron pulses. This chapter outlines the reason for this choice, giving a review of nanotips themselves as well as photoelectron emission processes, before outlining how the nanotips used in this project are produced and characterised. Emission from nantotips is already widely studied [147–154], often due to their additional uses in other techniques such as Surface/Tip Enhanced Raman Spectroscopy (SERS/TERS) [155–158], Scanning Tunneling Microscopy (STM) [159, 160] and Atomic Force Microscopy (AFM) [161, 162].

2.1 Photoemission in the ultrafast regime

Photoemission of electrons from metal surfaces may occur by a variety of processes, many of which may only be accessed by applying an extremely high local intensity, readily achievable with an ultrashort pulse. The use of such pulses allows bypassing of the naive approach, where emission is governed by the photoelectric effect and only permitted if the photon energy is above the work function of the surface in question, regardless of the intensity of the incident light [163–165]. By applying light in extremely short pulses very highly localised intensities may be created. In

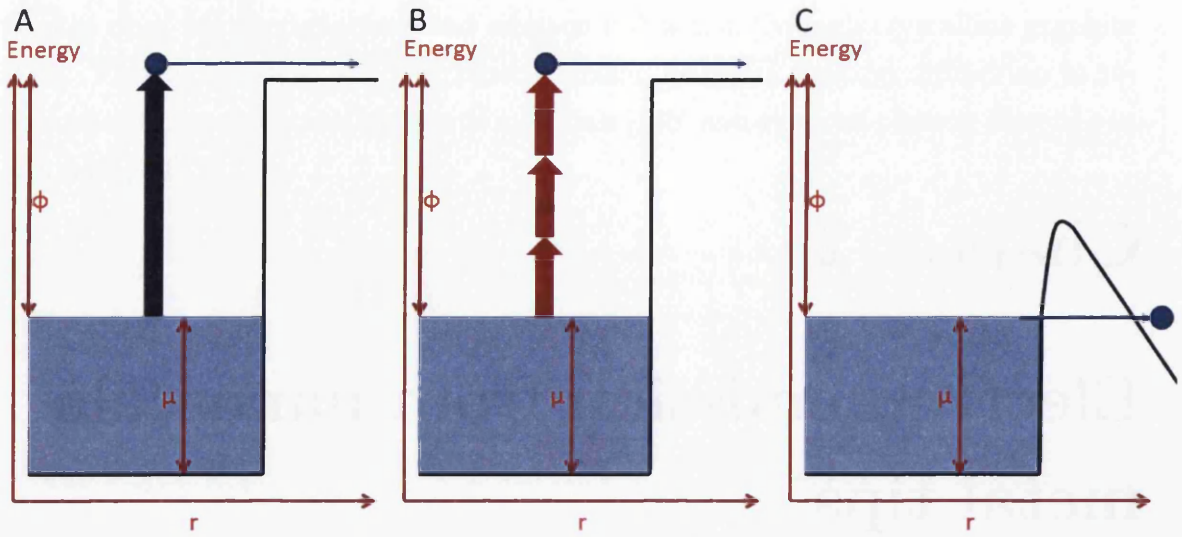

Figure 2.1: Illustration of the different mechanisms by which an electron may be emitted from a surface. (a) Single photon emission by a UV photon, commonly called the photoelectric effect. (b) Multi-photon emission by absorbing several photons until the electron has sufficient energy to overcome the potential barrier. (c) Tunnel ionisation, where the shape of the barrier is manipulated such that electrons at the Fermi level may tunnel through.

this regime the principle that emission is governed by the photoelectric effect breaks down, and it becomes possible to remove electrons from the metal by non-linear processes.

Emission may occur by either multi-photon emission [153, 166, 167], where a given electron absorbs several photons such that their combined energy is greater than the work function (as shown in figure 2.1(b)), or by the high localised and effectively instantaneous electric field generated by the laser pulse lowering the potential barrier keeping the delocalised electrons confined in the surface such that the electrons near the Fermi level can escape via tunnelling [149, 168] (figure 2.1(c)). These processes occur on the same time-scale as the incident laser pulse, however in addition the slower process of thermionic emission may occur, where the laser pulse creates a small localised region of extremely high temperature, which can grant electrons within the region sufficient energy to overcome the potential barrier over a period of picoseconds or nanoseconds. All of these processes may be further complicated by the addition of space-charge effects at the point of emission [167, 169, 170], as the field from the first electrons to leave the surface may modify the barrier felt by those following behind.

These processes, whilst distinct, often occur simultaneously from the same laser pulse. Thermionic emission and multi-photon are both relatively simple processes, although may be complicated by the brief lowering of the potential barrier caused

by the laser pulse. Strong-field emission is a more complex process, sub-divided into two further categories. The most common is tunnel ionisation, where the electric field from the laser both lowers and alters the shape of the potential barrier such that the probability of electrons performing quantum tunnelling to the continuum is no longer negligible. Manipulation of the barrier typically occurs when the applied intensity is of order 10^{14} Wcm^{-2} in the gas phase, however in the solid state the required intensity for barrier manipulation is dependent on the material structure and is generally lower by 3-5 orders of magnitude, due to both the increased electron density and field enhancements caused by the structure of the surface. In a single atom the barrier is defined by the potential between the electron and the atomic nucleus, whereas in a metal electrons at the surface are partially screened from the potential from the nuclei by other delocalised electrons. The second possibility requires extremely high intensities, and allows electrons to be liberated "over the barrier" if the applied field is strong enough to suppress the Coulomb potential to the extent that the highest point falls below the Fermi energy of the surface.

Whilst field emission and multi-photon emission tend to occur together in metallic surfaces, one process generally dominates the other, depending on incident laser intensity and wavelength. The transition between multi-photon ionisation and field emission being the dominant process was examined by Keldysh in 1965 [171], initially in the gas phase. Bunkin & Fedorov later demonstrated the applicability of the model to emission from a surface [172]. The Keldysh model explains ionisation when the photon energy is below the ionisation energy and the field is off resonance with atomic transitions, and so is applicable to electron liberation by an ultrafast laser pulse. The distinction between regimes is defined by the Keldysh parameter (γ), given by

$$\gamma = \sqrt{\frac{\phi}{2U_p}} \tag{2.1}$$

where ϕ is the work function and the ponderomotive energy U_p is defined as

$$U_p = \frac{q^2 E_0^2}{4m\omega^2} \tag{2.2}$$

which defines the energy of an electron (mass m and charge q) which exists in an oscillating electric field of peak magnitude E_0 and angular freguency w. The Keldysh parameter can be defined in simple terms as the ratio of the laser field frequency and the tunnelling frequency.

When $\gamma \gg 1$ multi-photon ionisation is the dominant process, for $\gamma \ll 1$ tunnelling emission is prevalent. Between these extremes both processes occur simul-

taneously. Increasing the intensity of the light causes the tunnelling regime to become dominant. At low intensities, where the multi-photon regime is dominant, the electrons may absorb energy from the minimum number of photons required to escape (the most common result) or they may absorb n additional photons, the probability of which increases with laser power. This causes some electrons to be emitted with greater energy, occurring in peaks separated by the photon energy. The Keldysh model has been criticised as the parameter is invalid under certain conditions [150, 173], although in most cases the model remains a valid starting point. It should also be noted that in the Keldysh theory applied to an atom the oscillations cause electrons to be emitted in both directions along the polarisation axis. This rule is clearly broken for emission from a surface, as only the parts of the oscillations where the field is directed to emit away from the surface will contribute.

The most accurate solution valid for all situations is to fully solve the time dependent Schrödinger equation, however for complex situations this is often infeasible due to the extreme computational requirements. Theoretical research into the mechanisms of photoemission is still developing, especially with regard to the surfaces of complex structures such as nanotips, with theories such as the semi-classical "simple man's model" (originally developed for gases but has proved applicable to surfaces [148, 151]) and time dependent density functional theory [148] being developed and applied to approximate the Schrödinger equation with numerical solutions.

2.2 Nanoscale metal tips as photocathodes

When producing femtosecond electron bunches a variety of photocathode options are available, with the most common variations being material and shape. The prospects of using metal nanotips, metal foil photocathodes, alkali coated metal photocathodes and semiconductor III-V based photocathodes such as Gallium Arsenide were examined [174]. Alkali coated photocathodes were deemed to be unsuitable due to their reactivity and the fact that they generally require light of wavelength shorter than 600 nm [175], which is inefficient to produce with a tabletop femtosecond laser system. Metal foil photocathodes require even shorter wavelength light (typically UV) or reliance on inefficient multi-photon emission. Semiconductor photocathodes are promising due to their high efficiency but are difficult to manufacture in-house. Furthermore all of these options have the issue that the emission area is large, being defined by the laser spot size. This precludes a high transverse coherence length of the electron bunch. Nanotips overcome these limitations as described below.

2.2.1 Motivation of using nanotips and review

Nanoscale metal tips are small cylindrical pieces of wire that have been etched electrochemically such that the end of the wire forms a conical taper (often curved) leading to a very sharp point, with a radius of curvature typically $\leq$100 nm. Nanotips can be manufactured from a variety of materials [176, 177], with metals such as gold [178–180], silver [155] and tungsten [181–184] being the most common, though other materials including PtIr [185–188] and ZnO [189–191] may be used. It is also possible to manufacture arrays of tip-like emitters from silicon [192] or carbon [193] though these are difficult to produce as a single tip.

Metallic nanotips make excellent photocathodes as they end in a region of extremely sharp curvature; most tips can be approximated as ending in a hemisphere with a radius of a few tens of nanometres. Even sharper tips are possible, up to and including those ending in a single atom. The small radius of curvature results in an enhancement of electric fields in this region [168, 194–196], whether they arise from an applied DC voltage (as discussed in section 2.2.4) or from an incident laser field. This allows nanotips to be used as either photocathodes or as DC field emission sources without the use of a laser, a key advantage over planar cathodes which require photons to produce electrons. Furthermore, the field enhancement effect allows laser driven strong-field emission to occur with relative ease, allowing photons with energy below the work function to be used [147, 151–154, 197]. This is significant from the practical perspective as it allows emission by the direct application of femtosecond laser pulses produced by commercial tabletop laser systems, which at present use either Ti:Sapphire (780-800 nm central wavelength) or tungstate compounds such as Yb:KGW (1030 nm central wavelength) as the gain medium as discussed in chapter 3. Production of femtosecond pulses with photon energy above the work function requires the use of more sophisticated techniques such optical parametric amplification or third harmonic generation which dramatically increases the scale and cost and reduces the efficiency of such systems, as a large amount of laser power is lost due to not all photons being converted to the desired frequency.

The field enhancement can be defined using the factor typically denoted as ζ, defined as

$$\zeta = max\left[\frac{|E_{nf}(r)|}{|E_{in}(r)|}\right] \tag{2.3}$$

where $E_{nf}(r)$ is the strength of the enhanced near field and $E_{in}(r)$ is the strength of the incident field. Field enhancement at nanotips has been studied theoretically by the group of Hommelhoff *et al*, who have performed extensive investigations into the magnitude of the effect as a function of tip radius, opening angle and material

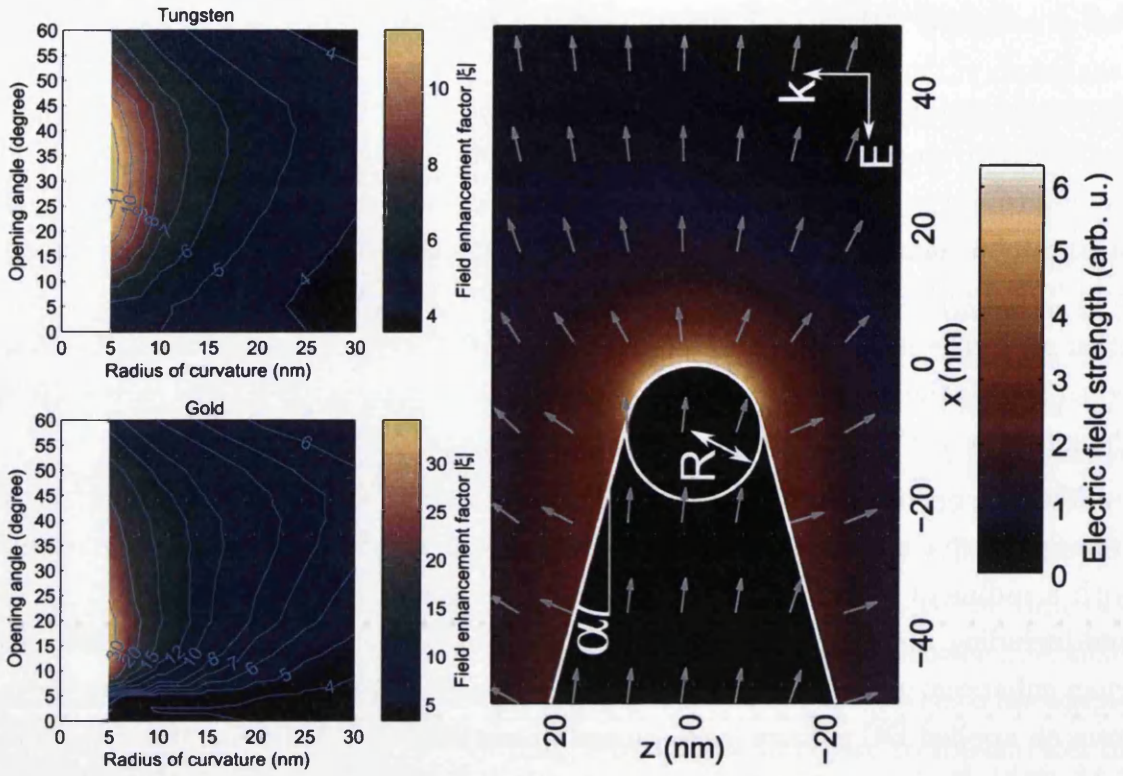

Figure 2.2: Results of a theoretical investigating the effects of tip material, sharpness and opening angle on the amount of field enhancement by Hommelhoff *et al*, adapted from [198]. They find that tungsten generates a maximum field enhancement factor of 12 at an opening angle of 35 degrees and that gold generates a maximum enhancement factor of 36 for 15 degrees. As expected the enhancement is greater for sharper tips.

[198]. A sample of their results is presented in figure 2.2. They concluded that the enhancement is not only dependent on radius of curvature at the apex, but also upon the opening angle of the tip. Sharper tips generate a stronger enhancement as expected, but there is a peak in the effect of opening angle at 35 degrees for tungsten and 15 degrees for gold. They also determined that the enhancement effect is a factor of 3 higher for gold than tungsten, likely due to the stronger plasmonic response of gold.

As the field enhancement only occurs at the nanotip apex, a sharp tip also approximates a point source of electrons, allowing their use as cathodes for point projection electron microscopy [105, 106, 199], both in the continuous DC emission and the femtosecond regime (see chapter 8). This is also advantageous for diffraction purposes as a collimated wavefront can be achieved with a relatively simple electrostatic or magnetic lens, or a sufficient approximation to flat can even be achieved simply by rapid acceleration which reduces the divergence of the beam. The small

emission area also results in a high degree of spatial coherence, with coherence angles up to 14.3 degrees being measured [200] and transverse coherence lengths larger than biomolecular scales being recorded [201]. The transverse coherence length ξ of an electron bunch can be defined [5] as

$$\xi = \frac{\lambda L}{2R} \tag{2.4}$$

where L is the distance of the bunch from the source, λ is the de Broglie wavelength of the bunch and R is the source radius, assuming the source is a circular disk or aperture. Using a source such as a nanotip where R is small therefore naturally leads to high coherence. This is a major strength over planar photocathodes where low coherence can be a significant obstacle to coherent diffraction experiments and may dramatically reduce the signal-to-noise ratio. The coherent nature of the electron emission is discussed further in chapter 6.

The small emission area is not entirely an advantage however, as it creates additional space-charge issues in femtosecond laser induced emission [169, 170], as a large number of electrons may be produced in a small volume. The resulting electron bunch will then undergo Coulomb repulsion. This requires images to be recorded by integration over many shots, with a small electron population in each shot. Attempting single shot images would require a large number of electrons to be present in the imaging bunch, $\geq 10^6$ as an optimistic minimum [2]. Emitting this number of electrons so close together (both spatially and temporally) results in extreme Coulomb repulsion and will make it extremely difficult to control and confine the electron bunch. This was achieved in chapter 8, where data collection over 10^6 laser shots with less than 10 electrons per shot allowed time-resolved electron microscopy to be performed without being limited by space-charge effects.

The final deciding parameter is that electrons emitted by strong-field photoemission from a nanotip will possess an energy bandwidth which is defined by the bandwidth of the laser pulse, and so as long as other emission processes such as thermionic emission are anticipated and prevented, the energy spectrum remains largely stable. It is important to note that the nature of the relationship between this spectrum and the shape and sharpness of a nanotip is yet to be categorically determined.

2.2.2 Production of nanotips

The standard method for production of nanotips relies on electrochemical etching [178, 180–182, 202, 203], where the material to be etched is placed in contact with a

reagent which does not normally interact with the metal unless a voltage is supplied to overcome the energy barrier to make the reaction energetically favourable and initiate transport of electrons and ions to the reaction sites. The starting material is a thin tungsten wire with a diameter of 250 μm. There are a variety of suitable etching chemicals, though sodium hydroxide (NaOH) was chosen due to a balance of ready availability, ease of working and effectiveness.

There are two standard methods for etching, known as the drop-off method [181] and the cut-off method [178], both illustrated in figure 2.3. Both methods may be used in a variety of physical configurations, but the common feature is that the wire to be etched is suspended vertically, with the bottom end suspended in a reservoir of the etchant chemical in solution. A counter-electrode is inserted into the etchant and often takes the form of a ring electrode centred on the bottom of the wire. This must be made of a material which, like the material being etched, is non-reactive with the etchant under normal circumstances but becomes a catalyst with the application of a voltage. It must allow the counter-reaction to the etching reaction to occur at this electrode for the given etchant. For the etching of tungsten, platinum works extremely well as a counter electrode, due to its non-reactivity with common etchants and compounds of tungsten, as well as its properties as a catalyst.

The difference between the drop-off and cut-off methods occurs in the way that the voltage is applied, and the way in which it is stopped when the etching is completed. In the cut-off method the positive voltage is applied directly to the wire itself (forming the anode), while the counter-electrode forms the cathode. The wire is then etched slowly into a tip at the surface of the liquid etchant, until the wire is broken leaving nanotips at the ends of both the suspended wire and the end which is now submerged and sinks to the bottom of the etchant. This method is simple but requires the voltage to the circuit to be cut off quickly if the suspended nanotip is to be used. After the wire breaks the nanotip remains in contact with the liquid surface and will continue to etch if the voltage is not quickly switched off, resulting in the end of the tip being blunted [204]. Manually switching the voltage off is not fast enough to prevent this, and to obtain a sub-100 nm tip a fast cut-off circuit is required utilising a transistor controlled by a voltage comparator to determine when the wire has broken.

The drop-off method requires that the suspended wire be passed through a second ring electrode above the surface of the etchant. The negative voltage is applied to this electrode and the positive voltage applied to the electrode submerged in the etchant reservoir. It is necessary to apply a thin lamella of etchant within the first ring electrode through which the wire penetrates. This lamella, held in place by

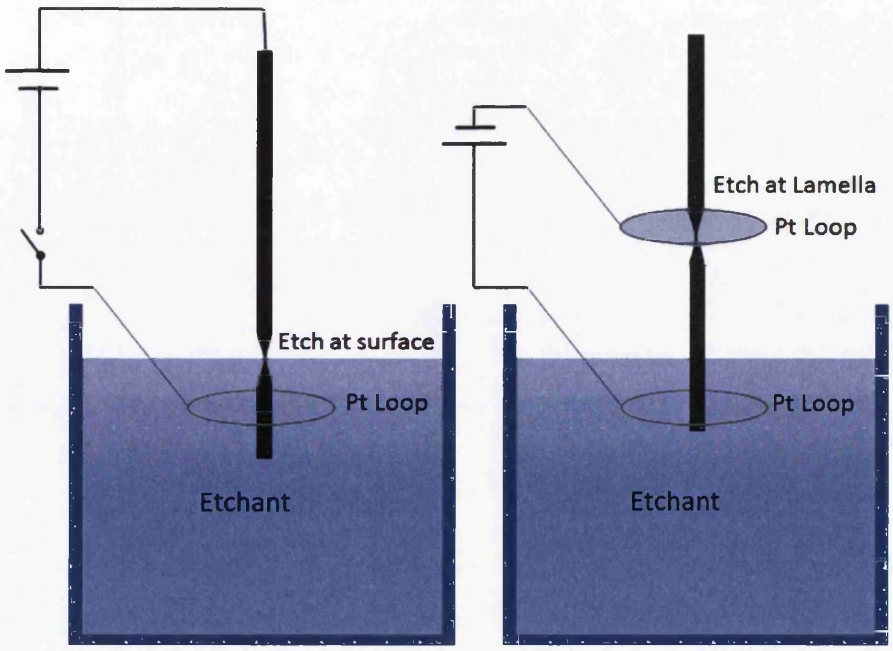

Figure 2.3: Illustration of the different methods for etching nanotips from a wire. Left: The cut-off technique, where etching occurs at the surface of the etchant and is stopped by a switch when the wire breaks. Right: The drop-off method where the etch occurs in a lamella suspended in a second loop above the etchant. The lower part of the wire is an integral part of the circuit, and so the circuit is broken when the wire breaks and falls.

surface tension, then performs the etching. As the wire is etched the gravitational force on the hanging part produces a taper, and a nanotip is formed when the wire eventually breaks. The act of breaking the wire breaks the electrical circuit and prevents further etching of the nanotip by the remaining etchant.

Tungsten nanotips are etched using the apparatus shown in figure 2.4, with a 2-molar solution of sodium hydroxide (NaOH) being used as the etchant. The negative voltage is applied to the upper platinum loop (cathode) and the positive to the loop submerged in the etchant (making the wire effectively the anode). This etchant was chosen due to its ready availability and high rate of occurrence in the literature, although generally any of the alkali metal hydroxides are suitable for etching tungsten as the alkali metal itself dues not feature in the reaction. The starting material was 250 μm diameter tungsten wire of 99.95% purity (Goodfellow W 005150).

Upon dissolution in water the sodium hydroxide separates into Na^+ and OH^- ions which dissolve in the water forming a naturally alkaline solution. When a voltage is applied the OH^- ions in the etchant are driven by the potential towards

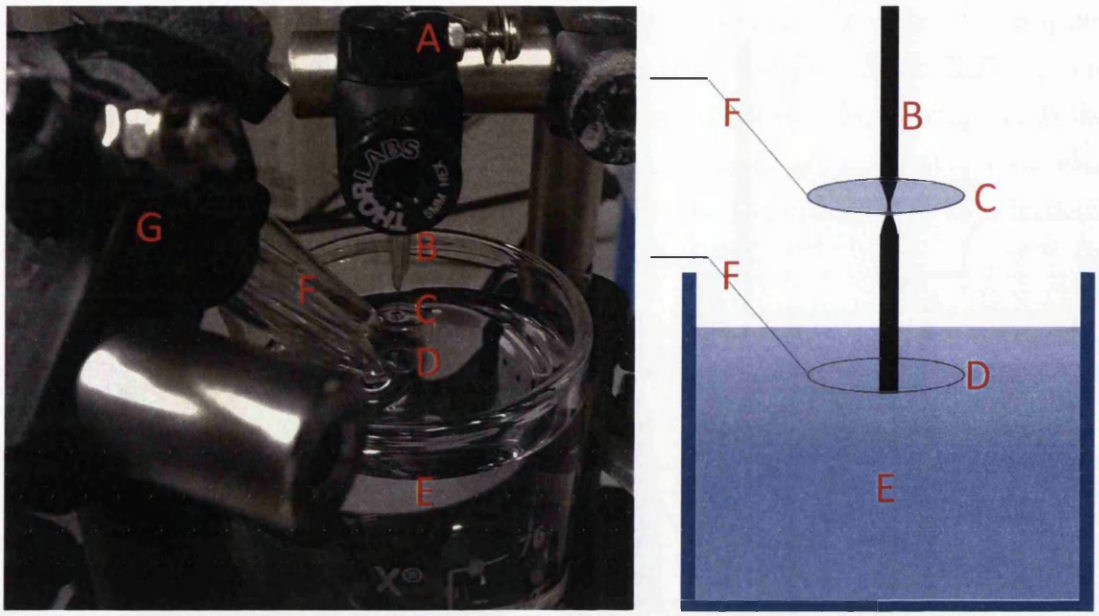

Figure 2.4: Photograph of the apparatus used for etching tungsten nanotips, with diagram of the etching region to clarify components. A) Wire fed through the top of the holder and secured by winding around the screw and tightening the nut. B) Wire holder formed from the end of a glass pipette to keep wire vertical and still during etching. C) Upper platinum loop filled with a lamella of etchant through which the wire passes. Etching occurs here. D) Lower platinum loop which forms the counter electrode, submerged in etchant. E) Beaker containing a reservoir of etchant which may be raised to replenish burst lamellas. F) Holders formed from the ends of glass pipettes to secure the platinum loops. G) 3-axis dovetail translation stages to allow accurate positioning of the loops to keep the wire central and account for any small bends in the wire. This apparatus may also be used in the double lamella drop-off configuration by lowering the beaker of etchant such that the lower loop is no longer submerged.

the tungsten wire, where the reaction

$$W + 6OH^- \rightarrow WO_3 + 6e^- + 3H_2O \tag{2.5}$$

can occur. The tungsten trioxide produced from the surface layers of the wire may then react with hydroxide ions already present in the etchant to form the reaction

$$WO_3 + 2OH^- \rightarrow WO_4^{2-} + H_2O \tag{2.6}$$

creating a soluble tungsten oxide ion and water. The overall reaction may therefore be denoted as:

$$W + 2OH^- + 2H_2O \rightarrow 3H_2 + WO_4^{2-} \tag{2.7}$$

which results in the release of hydrogen gas and removes the material of the etched wire into aqueous solution with the etchant. There is no deposition onto the platinum rings, as they take no part in the reaction itself and act only as catalysts, and only minor bubbling in the lamella. This is advantageous as excessive bubbling will break surface tension and cause the lamella to burst, interrupting the etching process significantly. The risk still exists that there may not be enough hydroxide ions present in the lamella to etch completely though the wire in one attempt, requiring replenishment. In the double-lamella technique there is also significant bubbling around the wire in the lower ring, which can cause regular lamella bursts and slow the etching process.

This method is generally effective at producing usable tips in reasonable time (approximately 30 minutes per tip) and without being labour intensive, but can be somewhat unreliable with regard to the consistency of both the taper and sharpness of the tips. A pair of tips produced under identical conditions, at least as far as macroscopic control of the system allows, are unlikely to be identical at the microscopic scale though are at least likely to be similar. A number of factors can affect the quality of tips, defined by parameters such as the sharpness/radius of curvature at the very end of the tip, as well as the taper length/aspect ratio and taper symmetry. These factors include:

1. The voltage applied, which affects the speed of the etch. A higher voltage causes a faster etch, which in turn results in a shorter taper and larger opening angle.

2. The length of wire present below the lamella, which defines the weight stretching the etching point. More wire results in a longer taper.

3. The angle at which the wire passes through the lamella. If the wire is not perfectly vertical to the lamella the taper will be a asymmetric and the wire may bend at the etch point resulting in a blunter tip.

4. The number of lamella replenishments required. Regular interruptions to the etch may result in ridged tapers and a bulbous zone near the apex.

Following production the tips are cleaned and stored ready for use. Whilst acid cleaning is sometimes used [205], the tips produced for this project were cleaned by rinsing first with running distilled water and then ethanol to remove any contamination and remaining etchant. Before being placed into storage tips are examined under an optical microscope. Tips may be reliably stored indefinitely provided they are handled carefully, although tungsten tips acquire a surface oxide layer under

exposure to atmosphere. It is therefore desirable to transfer the tungsten tips to vacuum as soon as possible once etching is complete, although it is possible to remove even thick oxide layers after they have formed (discussed in section 2.2.3).

2.2.3 Further refinement of nanotips

Once installed in the vacuum chamber there are methods of treating nanotips in-situ to enhance their usability by increasing their sharpness and removing surface contaminants. This is especially relevant for tungsten tips. Whereas most other tip manufacturing materials such as gold, silver or platinum-iridium are reasonably inert and once cleaned will generally acquire no further significant surface contamination provided they are stored under clean conditions, tungsten tips form a surface layer of tungsten trioxide upon exposure to air. In addition a layer will also be left coating the tip from the intermediate step of the tungsten etching process, as not all of the WO_3 ions formed by reaction 2.4 will be removed by reaction 2.5. This layer conducts poorly in comparison to the metal itself and provides both an impedance to emission and reduce the stability of emission when it does occur.

This may be countered by cleaning tungsten tips in vacuum conditions. Tungsten tips may be annealed at high temperatures. By heating the tip to $\geq$ 1000 K it is possible to efficiently remove this contamination layer. At these temperatures the tungsten trioxide (WO_3) will readily decay to tungsten dioxide (WO_2), expelling oxygen into the vacuum. WO_2 is comparatively volatile and at temperatures $\geq$ 1075 K will rapidly sublimate, leaving the surface of the tip as pure and uncoated tungsten. There is a distinct disadvantage with the annealing method in that if not correctly controlled (i.e. the tip is allowed to get too hot or the process run for too long) the tip may actually be blunted by surface diffusion, the migration of tungsten atoms from the apex to the shank, which increases the radius of curvature at the apex. It may be possible to reduce this effect by annealing in a low pressure oxygen atmosphere, although this raises the possibility of a small amount of oxide remaining. The annealing process can be technically challenging due to the requirements for a high localised temperature in vacuum and the careful control of the annealing time necessary to ensure that blunting does not occur. For this reason the idea of annealing tips was rejected for this project in favour of a pair of methods which, while perhaps less effective, are technically simple and, with practise, may be readily and remarkably reliably controlled by the intuition of the operator.

The first technique is to apply a high negative voltage to the tip to induce DC field emission [179, 185]. Direct observation of field emission of the tip using the electron detector assembly discussed in later chapters has yielded that the emission

from a tungsten tip which has not been annealed is often highly unstable, regularly undergoing sudden changes in flux and shifting direction, before eventually settling to a stable current and direction. It appears that this stable value is consistent with a relatively sharp tip as determined by techniques discussed in section 2.2.4. It appears, therefore, that a combination of the high the field present at the end of the tip and the electron flow from the field emission is effective at forcing contaminants away from the tip, effectively expelling large chunks of tungsten oxide. Independently verifying this is difficult, however, as the oxide layer is generally very thin (typically sub-10 nanometres), and the oxide is removed only from near the apex of the tip where the field enhancement is strong, as illustrated in figure 2.5(b). The emission of oxide is also not instantaneous, occurring in many small bursts over several minutes as successive layers are removed. These factors conspire to ensure that the volume of released oxide is not sufficient that it will readily be detected by a pressure gauge or residual gas analyser.

Over the course of this project it was also found to be possible to clean tungsten tips with laser pulses, as illustrated in figure 2.5(c). By applying a bias voltage to the tip marginally below the bias required to achieve field emission, and then applying the laser to the tip with slowly increasing intensity, it was observed that emission experienced a sudden activation after which field emission readily occurred at a lower voltage. This process appears to be repeatable until an equilibrium point is reached where stable emission is possible in either regime and any further increases in intensity only serve to damage the tip. This suggests that when emission is triggered by the laser two possible processes are occurring: the first possibility is that either localised heating or the sudden increase in electron current is causing the removal of contaminants such as oxides into the vacuum. The second possible process is the reshaping of the tip itself, such as the destruction of several emission sites and restructuring of the metal such that only one favourable and stable emission site remains.

No further in-vacuum sharpening of tips was performed, however options are available aside from annealing for actively refining tips with the aim of achieving a single-atom apex. The two most common of these are self-sputtering and bombardment. Self-sputtering requires injection of an inert gas around the tip and the application of a high negative voltage. Atoms of gas passing through the region of field enhancement near the very end of the tip may undergo ionisation, leaving a positive ion which is accelerated into the tip. The impact of the ion may remove material, and as a high negative voltage is used field emission may be induced and utilised as an indicator as to whether the tip is being sharpened or blunted.

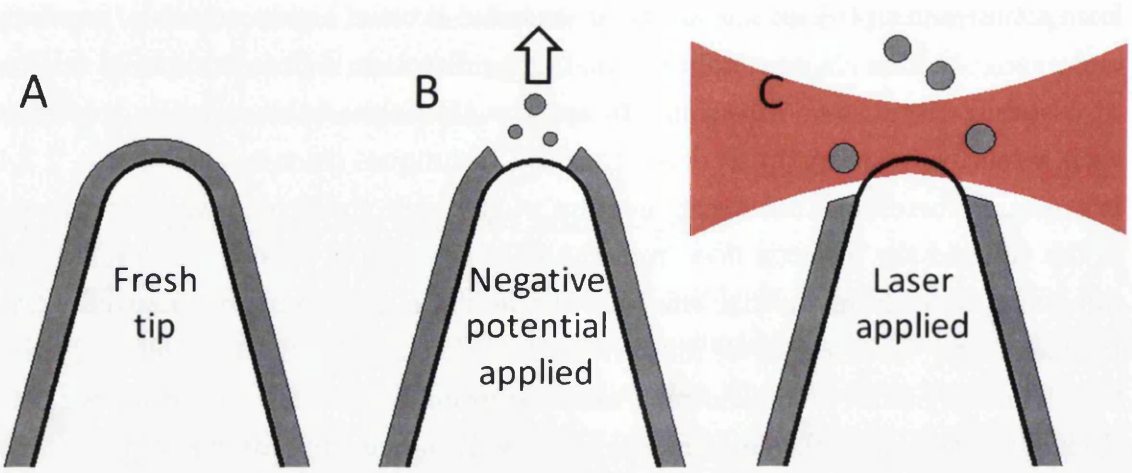

Figure 2.5: Illustration of the removal of the oxide layer from a nanotip. A) A constant thin layer around the apex of a fresh tip. B) Applying a negative potential causes emission of small pieces of oxide layer near the apex, pushing them into the vacuum. C) Application of a laser forces further cleaning, removing a substantial amount of oxide and leaving a relatively clean apex.

Bombardment is where the tip is deliberately impacted with ions or electrons which are not formed by the field of the tip itself in order to remove material. When these particles are applied as a beam the process is referred to as milling and is highly controllable, though difficult to achieve as it requires constant rotation of the tip to achieve even bombardment. It is less reliable though substantially simpler to provide free electrons or ions to the vacuum by, for example, heating a filament. These may then be directed into the tip by an applied voltage. This technique is risky and requires constant monitoring of the tip by field emission or field ion microscopy to determine if blunting if occurring from bombardment at the very apex of the tip. Single-atom tips are useful where extremely high electron coherence is required, and they are stable DC field emitters under clean conditions. Their emission properties combined with the small source size make them desirable for very high resolution STM and AFM, however in the case of this project however they are unnecessary, as a single atom apex is extremely vulnerable to laser damage, reducing their usefulness as photocathodes significantly.

2.2.4 Characterisation of nanotips through DC field emission

Once a tip is etched and cleaned the first step to determining suitability for use is to visually examine the tip under a microscope at 400x optical zoom, as shown in figure 2.6. Although it is not possible to see the very end of a sharp tip at this

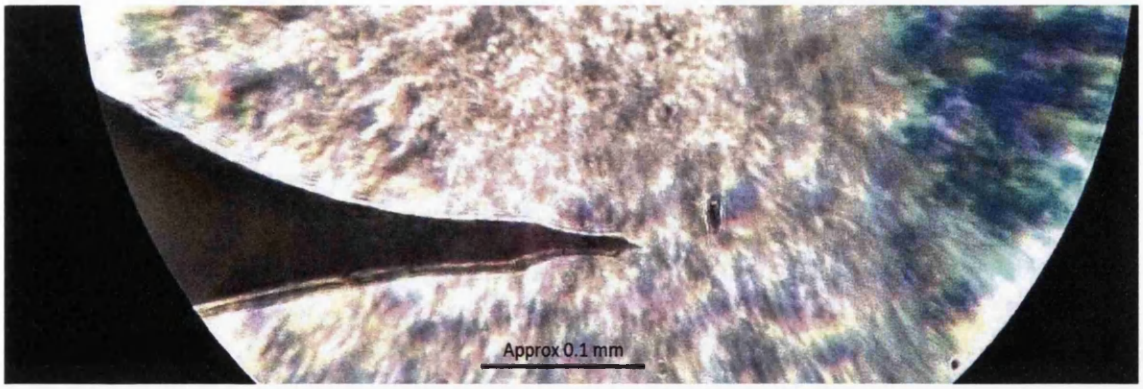

Figure 2.6: Photograph of a good newly etched tip under an optical microscope at 400x magnification, contrast enhanced to improve clarity. In this case there is no hook shape to indicate a crash and the end of the tip tapers to a point too small to observe any rounding, implying that the tip is sharp at least to the sub-micron level.

magnification it is easy to determine if the tip has been crashed into a solid object (in which case the end will appear as a hook), or if the tip has formed extremely blunt (i.e. end radius of curvature ≥ 1 μm). If neither of these features are present the tip may then be transferred to a vacuum chamber for further characterisation.

The preferred method for determining the sharpness of the tip is by using a technique based on the work of Fowler and Nordheim, by placing the tip in front of a grounded anode and applying a high negative voltage to the tip such that DC field emission may occur. The negative voltage reduces the potential barrier felt by delocalised electrons in the metal at the surface in an an inverse linear fashion, with the gradient directly proportional to the applied field strength. When this is sufficiently high the barrier may be lowered enough that the probability of a given electron at the Fermi level tunneling through the barrier becomes non-negligible [206], as in the case presented in figure 2.7. This is amplified for nanotips as the sharp curvature at the apex causes a localised enhancement of the electric field. The effect of the applied voltage V_{bias} on the field at a tip apex can be approximated as

$$E = \frac{V_{bias}}{kr} \tag{2.8}$$

where E is the effective electric field at the tip apex of radius r and k is a factor dependent upon the exact geometry of the tip. The amount by which the height of the barrier is reduced is given by

$$\phi_{reduction} = \sqrt{\frac{q^3 E}{4\pi\epsilon_0}}. \tag{2.9}$$

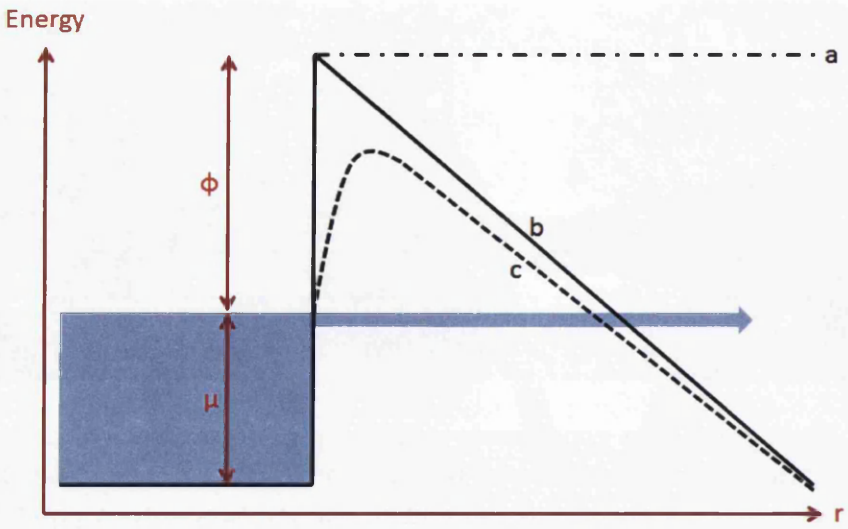

Figure 2.7: Illustration of the effects of applied fields and approximations on the potential barrier and tunnelling probability at the apex of a nanotip with work function ϕ and Fermi level μ. a) Barrier when treating the potential as a finite well resulting in zero tunnelling probability. b) Approximation of the barrier with gradient defined by an applied electric field E, making tunnelling possible. c) Barrier under electric field E with the image potential accounted for resulting in a rounded peak and a further increase in tunnelling probability.

Crucially, increasing the field further results in the electrons at the Fermi level being subjected to a narrower barrier, increasing the tunnelling probability and subsequently the emitted current. This is a process which may be macroscopically controlled, as fine control of the voltage can in turn yield a very fine control of the potential barrier and the emitted current. This relationship is given by an equation of the form

$$I = \frac{q^2}{2\pi h}\frac{\sqrt{\mu}}{(\mu+\phi)\sqrt{\phi}}E^2 \exp\left[-\frac{8\pi\sqrt{2m}\phi^{\frac{3}{2}}}{3hqE}\right] \tag{2.10}$$

referred to as a Fowler-Nordheim (FN) type equation, where the emission current density I released by a given electric field E is derived by taking the probability of quantum tunnelling through a barrier of height ϕ, accounting for the rate of electrons arriving at the barrier and integrating over all electron energies below the Fermi level μ. It is worth noting that whilst the form is roughly constant different assumptions and approximations yield many minor variants, mostly with alterations of factors of the constants.

Whilst this equation does not account for temperature, the dependence of field emission on temperature is sufficiently low as to be considered negligible in most circumstances. Fowler and Nordheim also developed this equation format with a flat plane as the emitting surface. The original derivation of this equation has

been criticised as containing inaccuracies and its validity has been questioned [207]. Despite this the FN type approach remains the most common in determining DC field emission properties, though some corrections are necessary before it may be applied to the case of tips. When the constants are replaced with numerical values the current density I is then given by equation 2.11.

$$I = 6.2 \times 10^{-6} \frac{\sqrt{\mu}}{(\mu + \phi)\sqrt{\phi}} E^2 \exp\left[-6.8 \times 10^7 \frac{\phi^{\frac{3}{2}}}{E}\right] \tag{2.11}$$

The constant of -6.8×10^7 within the exponent, is not obtained directly from Fowler and Nordheim who claimed the constant to be -2.1×10^7, instead resulting from a correction introduced to the model by Stern et al in 1929 [208]. These values require that the the units of I be Acm$^-2$, μ and ϕ be eV and that E be denoted in Vcm^{-1}. Fowler and Nordheim also dramatically underestimated the effect of the image potential induced in the surface by the electron tunneling, which has the effect of rounding the top edge of the potential barrier. Before applying this model to nanotips it is necessary to consider the image potential, though it can be approximated in the classical limit. Without considering the image potential a given electron approaching the barrier normally of height ϕ at distance r whilst an electrostatic field is applied will see an effective potential U of

$$U = \phi - Eqr. \tag{2.12}$$

Accounting for the image potential allows this to be to be adjusted to equation 2.13 where the additional term is given by the simple image potential in classical electrostatics

$$U = \phi - Eqr - \frac{q^2}{4r}. \tag{2.13}$$

It is obvious from equation 2.13 that the inclusion of an image potential reduces the barrier height and thickness seen by the incident electrons, naturally increasing the tunneling rate relative to the original FN-type model. A revised model was later developed separately by both Fowler and Gomer [209], who determined that the image correction should be applied as a multiplicative factor present in both the exponent and the denominator of the FN-type equation. This factor is commonly denoted as α and takes a value in the range $0 < \alpha \leq 1$, though the exact value varies as a function of the applied field. The issue remains that this model is primarily valid for an emitter consisting of an infinite flat plane, and does not account for the field enhancement induced by the extremely tight curvature at the end of a nanotip. In such a situation the electrostatic field on the surface is not simply given by a

value E as in the model above but by

$$E = \frac{V}{kR} \tag{2.14}$$

where V is the applied voltage, R is the radius of curvature of the tip and k is a correction factor to account for the fact that the tip is not a perfect spherical emitter. The value for k differs for every tip and receives contributions from a variety of sources, the most significant of which is the presence of the tip shank.

Equation 2.14 demonstrates that the field enhancement is greater for sharper tips. Replacing E in the FN-type equation with this expression and including the image potential creates expression 2.15 for which the suitability may be extended from infinite plane surfaces to finely curved structures, including nanotips with a total emitting area a:

$$I = 6.2 \times 10^{-6} \frac{a\sqrt{\mu}}{\alpha^2(\mu+\phi)\sqrt{\phi}} \frac{V^2}{(kR)^2} \exp\left[-6.8 \times 10^7 \frac{\alpha k R \phi^{\frac{3}{2}}}{V}\right]. \tag{2.15}$$

This equation now provides a direct link between the current emitted from a cathode and the voltage applied to it, and is now crucially valid for curved emitters including nanotips. Figure 2.7 shows the effects of considering these alterations on the structure of the barrier and hence on the tunnelling rate of the electrons. This allows the equation to be used as the base for a test where emitted current from the tip is measured at a series of known voltages, providing an indicator for the radius of curvature R at the end of the tip. The direct relationship is easier to visualise when the equation is rearranged into

$$\ln\frac{I}{V^2} = \ln\left[6.2 \times 10^{-6} \frac{a\sqrt{\mu}}{\alpha^2(\mu+\phi)\sqrt{\phi}(kR)^2}\right] - 6.8 \times 10^7 \frac{\alpha k R \phi^{\frac{3}{2}}}{V} \tag{2.16}$$

where R is in cm and a in cm^2. This equation may then be used to determine tip sharpness by plotting $\ln(I/V^2)$ vs $1/V$, the result of which should be linear with gradient $-6.8 \times 10^7 \alpha k R \phi^{\frac{3}{2}}$, as in the example given in figure 2.8. It is then therefore possible to retrieve R on the condition that α, k and ϕ are known. ϕ is trivial, being the work function for the emitting material in eV. α is more difficult to determine, although in most cases it is not an unreasonable approximation to take α as being 1 [202, 209]. Although taking α as unity ignores image charge, the correction factor is small and so in most practical purposes this approximation is valid, though will cause inaccuracy if R is sufficiently small that the tip approaches a single-atom emitter.

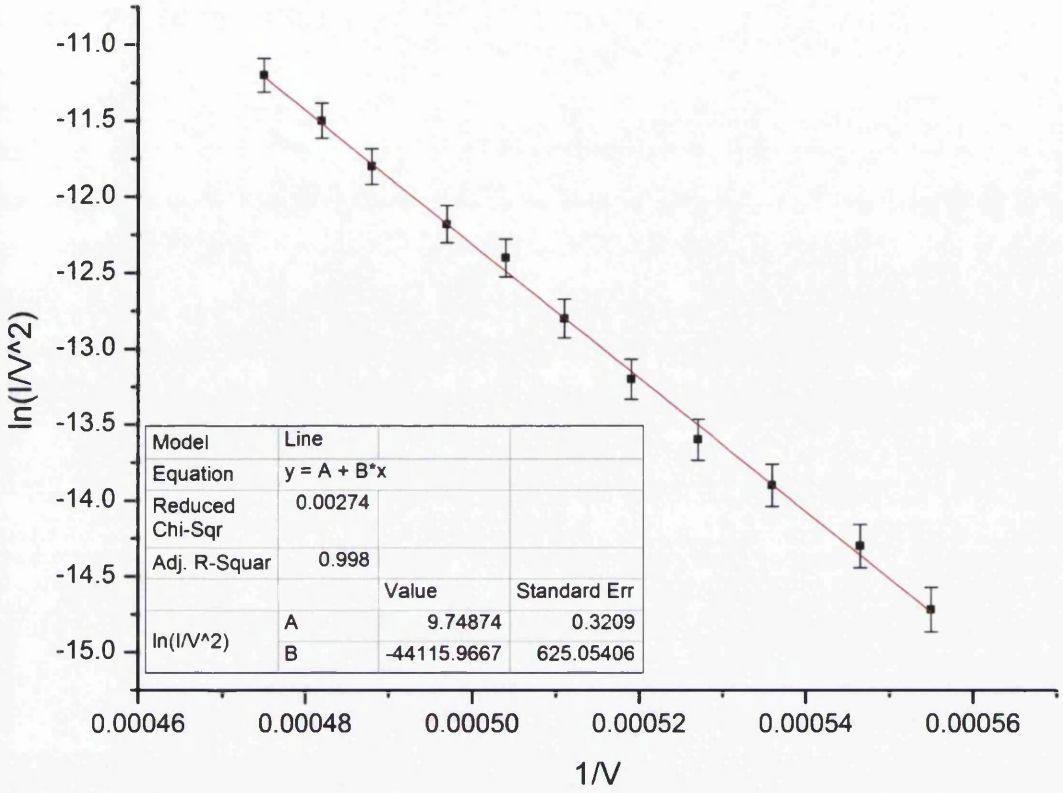

Figure 2.8: Example of how the Fowler-Nordheim technique is used to determine tip sharpness. In this case the gradient of -44115 gives a kR value of 680 nm. In the worst case scenario that k = 3 this gives an upper bound on the tip radius of 227 nm. This indicates a relatively blunt tip, though in reality it may be sharper than appears from this result as the Fowler-Nordheim method only provides an upper limit on tip radius, not the exact radius value.

The factor of k is harder to determine a suitable value for, as it is dependent on the taper length, curvature, symmetry and aspect ratio, as well as imperfections. For slender yet blunted tips k may be as low as 3 but is more commonly found between 5 and 8 [209, 210], though can be higher. This unfortunately gives a range of upper and lower bounds for the tip radius R. It is normally a reasonable approximation that k occupies the range $5 \leq k \leq 8$, however due to the wide range the Fowler-Nordheim technique is only truly reliable when used to obtain an upper limit for the radius of curvature of the tip rather than an absolute value, and becomes especially unreliable when R approaches that of a single-atom emitter. Such tips usually require further sharpening in vacuum to manufacture however, and so for good electrochemically etched tips where R is typically $50 \leq R \leq 100$ nm the technique remains useful.

2.3 Control of electron bunches after emission

Once emitted from the nanotip electrons are free to move around the vacuum, with their trajectories governed primarily by the local electric and magnetic fields. This allows the electron trajectories to be controlled at will by careful placement of electrostatic and permanently magnetic or electromagnetic components, such as steering plates/coils and Einzel/solenoid lenses. There are also two other significant contributions to the electron motion which must be contained or compensated for as much as possible. The first issue is that of global fields, either electric or magnetic, which can enforce a constant alteration of the electron trajectories. The second issue is the mutual interaction of the electrons themselves, as the Coulomb forces will naturally cause them to repel during free flight [211, 212]. Some expansion of the electron bunch will also inevitably occur due to an initial spread of the energy and momenta of the electrons, derived from both the bandwidth of the laser pulse and the shape of the photocathode, even in the single electron per shot regime where this spread will manifest as variations in the arrival time of the electrons at the target.

The first issue is equally disruptive to DC emission and photoemitted femtosecond bunches. Electric and magnetic fields must generally be accounted for separately but depending on the circumstances this is often easily achieved. The global magnetic field is usually composed of the Earth's natural field, which always adds a small deflection to the electron trajectories if left unchecked, and additional fields resulting from other items in the laboratory and in particular arising from any active turbomolecular pumps maintaining the vacuum. This can be solved in two ways; by encasing the entire electron path in a magnetic shield, or by using electromagnetic coils built around the chamber to generate an equal and opposite field to that of the global field. In this project both techniques are used. The use of coils built around the chamber is advantageous as they can also be used a steering device for the electron beam and do not affect the pumping properties of the chamber, however the disadvantage is that large coils are required which may still only produce a neutral field over a small section of the total beam path.

Encasing the entire electron path in a magnetic shield (generally manufactured from mu-metal) is a reliable way of ensuring that even for long flight tubes the field is effectively neutralised. This does come with a caveat, in the vast majority of situations it is not feasible to encase the chamber in a magnetic shield, hence it must be located inside the vacuum, which will negatively effect the pumping of the chamber by both dramatically increasing the surface area present and by constricting flow to the pumps. It is necessary to keep pumping holes in the shield relatively small to limit the depth to which the global magnetic field will penetrate.

It is obviously necessary to place all local steering and focusing components, both magnetic and electrostatic, inside the shield. It is also advisable to ensure that all metallic chamber components are manufactured from grade 316 stainless steel, which has a low magnetic permeability and as such exhibits sufficiently negligible generation of, or response, to magnetic fields for most purposes.

Global electric fields may be present from equipment in the lab and may not be static. A small oscillating electric field is generally present from the mains electricity supply and this may be overlaid with electrical noise generated from power supplies or computer equipment. This may be eliminated by surrounding the chamber in a Faraday cage, however this is often unnecessary. As vacuum chambers are metallic and generally electrically grounded at least by the power supplies to the pumps (and advisably connected to a clean Earth) the chamber itself often acts as a Faraday cage ensuring minimal penetration of unwanted electric fields. By using an internal mu-metal shield to control the magnetic field this is enhanced further as this can be electrically grounded further shielding the free electrons from stray fields of both kinds. For this reason a 316 stainless steel chamber and mu-metal internal shields were employed heavily in this project, although external neutralisation and steering coils were also used. No attempt was made to account for gravity as the trajectory deflection is negligible.

The issue of space charge again applies to both DC emission and photoemitted femtosecond bunches, but is much more prevalent in the latter. When a short laser pulse hits a nanotip a large number of electrons may be generated in extremely close proximity, as the emission occurs (ideally) at a single atom or few-atom site at the very end of the tip. In an ideal scenario this may be countered by emitting one electron per laser shot, however this is not always possible given either equipment limitations or the need for intense electron bunches. For a short time after creation, all emitted electrons may exist in a small region only a few nanometres across. For intense electron bunches the charge density may therefore be extremely high, leading to rapid Coulomb explosion due to the high repulsion forces at such close proximity. In any case this will result in a dramatic spatial expansion of the bunch and in extreme cases may render the temporal length of the bunch so large as to make it unusable. This is a particular issue when the desire is to keep the electron bunch as short as physically possible. Coulomb explosion will significantly lengthen the bunch along the axis of flight and may increase the length of a bunch from tens of femtoseconds to picoseconds or nanoseconds before the electrons arrive at their target.

Keeping electron bunches short is a difficult challenge and, given that some

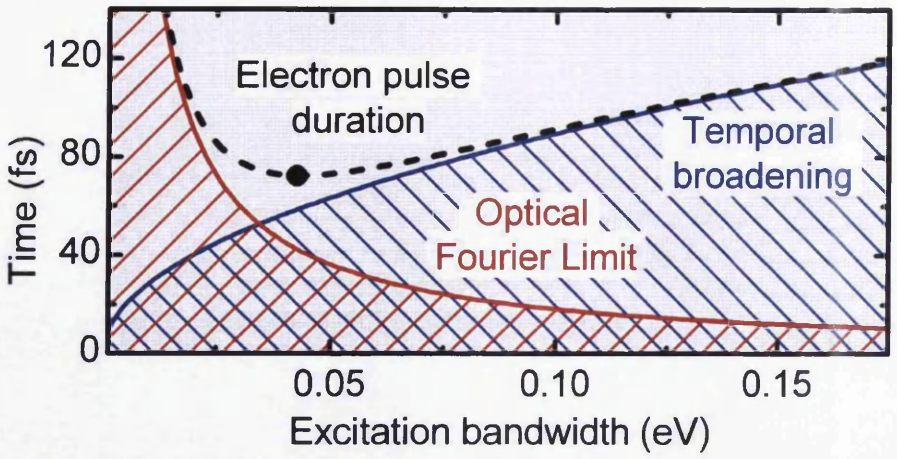

Figure 2.9: Illustration of the effects of temporal broadening and initial pulse length on the duration of an electron bunch at a target as calculated by Baum *et al*, reproduced from [174]. This demonstrates a "sweet spot" in the length of the laser pulse required to produce the shortest possible electron bunch.

expansion of the electron bunch as it flies is inevitable, is achieved in the simplest fashion of transporting the electrons to their target as rapidly as possible. There are two typical approaches to this, the first being to place the electron source and the sample extremely close as in the case of point-projection microscopy (as discussed in chapter 8) and when the electron energy needs to be kept low as in the case of low-energy coherent electron diffraction. The second approach is to accelerate the electrons as hard as possible within the breakdown limit[1] to ensure rapid delivery of the electron bunch to the sample in cases where deep penetration of electrons is required or where it is not possible to place the sample close to the source.

Alternative techniques to directly counter the spread of electron bunches may be used when compact systems are not possible or where the number of electrons in the bunch (and as such the repulsion from space-charge) is extremely high. This includes the suggestion of using shaped laser pulses interacting with the electrons in flight to form a ponderomotive potential well to create a temporal focus [213], as well the successfully implemented technique of creating a temporal focus using an RF cavity [122, 123] and eliminating the problem of space-charge by emitting an average of less than one electron per laser shot using a very low power but high repetition rate laser system [147, 151, 154].

Baum *et al* investigated mechanisms by which the shortest possible electron bunches could be achieved, in particular the space-charge free regime where one electron per shot (or less) is emitted [174]. In this case the length of the electron

[1]Typically taken as an electric field gradient of approximately 10 MV/m for a good vacuum, above which arcing is likely to occur

bunch after flying a given distance is dominated by three factors: The length of the emitting laser pulse, the initial energy bandwidth and the beam energy. In the ideal case of a transform limited laser pulse these factors are implicitly linked. As shown in their results presented in figure 2.9, they determined that there is an optimum length of a transform limited laser pulse that produced the shortest electron bunch length of a given geometry. An electron bunch emitted by a long laser pulse will be long at creation but, as the bandwidth needed to create a long laser pulse is small, the electron bunch will not broaden much whilst travelling to the target.

An electron bunch only a few femtoseconds long at creation will by necessity have a large energy bandwidth, causing it to exhibit substantial broadening during flight. Balancing these effects is therefore key to controlling the length of electron bunches even when no space-charge is present. The work of Baum *et al* is however limited to one configuration and energy, and so by itself is only useful as an indicator of the behaviour of the electron bunch and it is not viable to use their results to make quantitative predictions regarding any other scenario. This balance is investigated further in chapter 7.

Chapter 3

Production and characterisation of femtosecond laser pulses

The production of ultrashort electron pulses from nanoscale metal tips requires an ultrashort laser pulse to induce the emission. This chapter overviews how such laser pulses are produced, followed by a detailed discussion of the laser systems used in the work presented in this thesis. Finally, methods of controlling and characterising a laser pulse are discussed with particular reference to those techniques used both inside the laser systems and externally constructed. The background presented in section 3.1 is brief, as ultrafast lasers are complex devices and cannot be discussed in detail here, however comprehensive details on the theory and operation of a variety of ultrafast laser systems are presented in [214].

3.1 Ultrafast laser systems

The production of ultrashort laser pulses is a multi-stage process, but begins at an oscillator. This is a laser system that produces a train of short pulses of light at high repetition rate as opposed to a continuous beam. Most oscillators use crystalline titanium doped-sapphire (Ti:Al_2O_3, most often referred to as Ti:Sapphire) as the gain medium, though other media such as crystalline ytterbium-doped Tungstate (Yb:KGW being an example used in this project) are also used depending on the central wavelength and desired output power. Ti:Sapphire has a broad absorption spectrum ranging from 400 nm to 650 nm, peaking at approximately 500 nm. This spectrum is not Gaussian and reaches the half maximum at 450 nm and 600 nm with very steep rising and falling edges. The Ti:Sapphire florescence spectrum is also broad, ranging from 600 nm to 1050 nm, peaking at approximately 780 nm. This spectrum better approximates a Gaussian, with a FWHM of approximately 160 nm,

allowing a great deal of tunability of output with central wavelength selections most common in the range 780-800 nm. Yb:KGW has a narrow absorption spectrum centred at 981 nm with a FWHM of just 3.7 nm [215], and a reasonably Gaussian florescence spectra centred on 1023 nm with a FWHM of 20 nm, allowing tunability of laser output with 1028-1030 nm being a common selection.

The construction of a typical oscillator is similar in principle to most solid state laser systems, a continuous wave (CW) pump injects light into the gain crystal which is situated in an optical cavity. The crystal is chosen such that for the given pump wavelength the output is broadband over a known wavelength range instead of the monochromatic light utilised in CW systems. For Ti:Sappire systems commonly used frequency doubled Nd:YAG and Nd:YLF lasers satisfy this pumping condition excellently. The gain crystal is installed with the faces cut at the Brewster angle to the incoming light to minimise reflection. The central wavelength produced by the crystal may be manipulated by installing a separate thin birefringent crystal in the cavity; tuning is simply performed by rotating this crystal. When ultrashort pulses are desired the cavity must include compensation for the dispersion introduced as the light passes through the gain crystal, this condition is normally met by including a pair of prisms in a compressor configuration similar to the one constructed and presented in section 3.3.2.

The broadband output from the gain crystal is converted from CW light to an ultrashort pulse by modelocking. To facilitate this a modulator is placed in the cavity which synchronises losses from the cavity with the round-trip time of a cavity photon. This allows a mode to be found where the wavelengths within the cavity coherently interfere across the entire range such that they destructively cancel except at select locations where all of the waves are in phase, confining the energy in the cavity to the point on the waves where this condition is satisfied, creating a very short and bright pulse containing the entire spectrum. Modelocking may be active, where the modulator is generally electro-optic, or passive where a saturable absorber is used. In more powerful systems it is also possible to use the Kerr-lensing effect through the gain medium in place of inserting an additional component to perform modulation, in which case one of the cavity mirrors is often actively adjusted to "kick start" the effect.

The pulse energy produced by an oscillator is limited, even cutting-edge systems are limited to the order of 10's of nanojoules per pulse. By using a second crystal comprised of the same gain medium used in the oscillator it is possible to further amplify the pulse to much higher energies; greater than a millijoule in pulses shorter than 100 fs is easily achievable by many modern systems, and specialist systems are

capable of achieving tens of millijoules. Before amplification there are two considerations: Firstly amplification results in an extremely intense pulse being focused through the gain crystal; too intense and it is possible for the crystal to become damaged and for other unwanted effects such as white light generation to occur. Secondly, it is impossible to amplify each pulse in the incoming train (usually approximately 80 MHz) to the millijoule scale due to the enormous amount of power that would need to be injected into the gain medium to do this.

The first problem is solved by temporally stretching the pulse, usually using a grating stretcher to introduce negative temporal chirp (discussed in section 3.3.1). By stretching the pulse from a few femtoseconds out of the oscillator to a few nanoseconds, the peak intensity when focused is dramatically reduced. Chirping the pulse is by far the most effective way of avoiding damage to the gain crystal when amplifying to the millijoule energy scale. Negative chirp is used as additional negative chirp is also introduced by the gain crystal, so positively chirping the pulse would cause it to re-compress during amplification potentially damaging the crystal. When this method is used the amplification is referred to as Chirped Pulse Amplification (CPA) [39]. The solution to the second issue is to lower the repetition rate of the amplified pulses. Before entering the amplifier the pulse train is passed through a pulse-picker, which usually consists of a pair of linear polarisers and a $\lambda/2$ Pockels cell. Ordinarily the first polariser ensures that the beam has clean linear polarisation, and the second polariser blocks the beam completely. A pulsed voltage is applied to the Pockels cell at the desired repetition rate of the amplifier, timed to allow one pulse from the train to be rotated such that it passes through the second polariser. This lowers the repetition rate into the amplifier by any amount down to single shot on demand. Typically repetition rates on the kHz scale are used to ensure that the pulse has time to be amplified to the desired energy leave the laser before amplification of the next pulse begins.

Energy to the amplifier must be provided by a second pump laser. Unlike the CW pump used for the oscillator, CPA is much more efficient when the pump is pulsed and timed to arrive coincidentally with the seed pulse. Ideally the pump pulse should be a few nanoseconds long and highly intense; this makes Q-switched cavity-dumped Diode-Pumped Solid State (DPSS) lasers an extremely desirable source of pump light. Most Ti:Sapphire laser systems use one or more Nd:YAG or Nd:YLF lasers (frequency doubled to 532 and 528 nm respectively) as pumps, whereas Yb:KGW systems are typically pumped at 980 nm directly by laser diode output. As the seed pulse passes through the pumped gain crystal it gains energy via stimulated emission, however the interaction cross section is small and so even if

the crystal is pumped to inversion the gain is limited. Multiple passes through the crystal are required, with the pulse collecting more energy with each pass, before the millijoule scale is achievable. After a set number of passes is reached, typically between 5 -20 depending on the desired output power, the pulse is extracted either by missing one of the cavity mirrors (due to the path angle changing slightly each time, referred to as a "multipass amplifier") or more commonly by another Pockels cell (where the seed takes the same path through the gain crystal with each pass, referred to as a "regenerative amplifier"). The next seed pulse is then triggered to enter the amplifier and the pump laser is fired again.

Following extraction the pulse requires re-compression to compensate the both the effect of the stretcher and the additional dispersion introduced by multiple passes through the gain crystal. This is normally done by using a grating compressor, which allows the pulse to be shortened, potentially approaching the transform limited length, even with a high input power. Grating compressors are also generally highly compact, allowing the compression to be performed inside the laser rather than as a separate unit. Some laser systems use prism compression as an alternative, which is less compact and only viable at lower powers but results in less loss of energy during the compression process, making it a desirable option for dispersion compensation for oscillators in particular. Pulse compression is discussed further in section 3.3.

3.2 Specific laser systems used in this project

3.2.1 Coherent Libra-S

The Libra-S is an ultrafast laser system manufactured by Coherent Inc. and provided for this project via the EPSRC Laser Loan Pool. The system combines an oscillator with a regenerative chirped pulse amplifier and a high power pump laser into a single integrated unit. The combination of these components can produce output pulses of 100 fs length and 1 mJ energy at a central wavelength of 800 nm, although in practice the system generally delivered pulses of 120 fs length and 0.9 mJ energy. The shot repetition rate is variable but was normally used at the maximum rate of 1 kHz. The pulse energy is confirmed using a commercial power meter provided by the Loan Pool. The pulse length was confirmed by picking off approximately 1% of the beam using a thin silica wedge and directing it into a commercial pulse measurement device (A.P.E. *pulse*Check) also provided by the Loan Pool. This device is a compact auto-correlator with an attached controller which calculates and reads out the pulse length automatically.

The seed pulse is provided by a Vitesse Ti:Sapphire oscillator pumped by diode

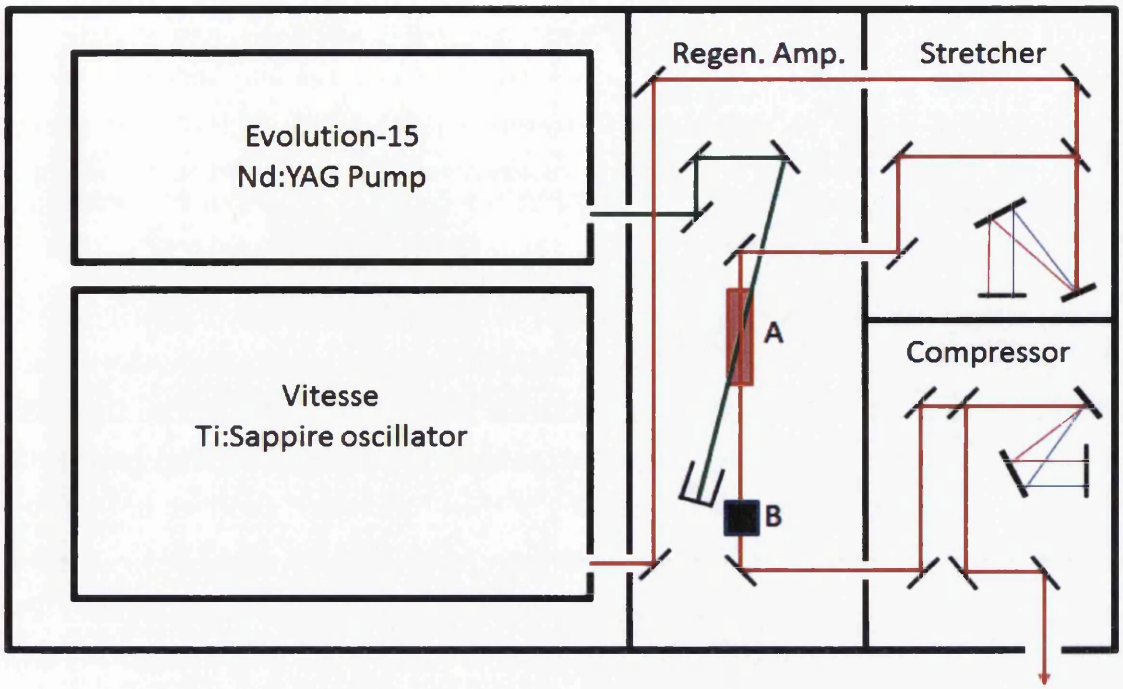

Figure 3.1: Optical layout of the Coherent Libra-S laser system. The pump laser and oscillator are sealed units with proprietary internal layout. The pump beam (green) has a simple path that takes it though a series of alignment mirrors, the last of which focuses it through the Ti:Sapphire crystal (A) in the regenerative amplifier, before being dumped. The seed beam (red) from the oscillator is aligned through a folded grating stretcher (shown expanded in this diagram) to facilitate CPA, before being focused through the crystal A in temporal and spatial overlap with the pump beam. The Pockels cell (B) reflects the pulse before being triggered to allow dumping after 12 passes. The dumped pulse is then directed to a grating compressor before exiting the laser.

bars located in the laser power supply. The oscillator is modelocked to produce a $\leq$100 fs pulse at 800 nm. The total output power is approximately 1 Watt at a repetition rate of 80 MHz, giving a pulse energy of around 12.5 nJ. A Pockels reduces the repetition rate to 1 kHz before amplification. A grating stretcher is then used to temporally spread the pulse to over a nanosecond to avoid damage to the regenerative amplifier.

The regenerative amplifier uses a 1 cm diameter rod of Ti:Sappire which amplifies the seed pulse over a total of 12 passes before an output Pockels cell is triggered to extract the pulse. The crystal is water cooled to provide stability, and operates with minimal Kerr-lensing such that the seed can be extracted when the amplifier is not running without adjusting the alignment. Energy input to the amplifier is provided by an Evolution-15 pump laser, specifically designed to act as a high stability pump laser for ultrafast systems. This is a diode-pumped Nd:YLF laser that operates in

the second harmonic (527 nm) and provides an output power of 12 W at 1 kHz in 300 ns pulses via Q-switching. Following extraction from the amplifier the pulse is passed through a grating compressor to restore a pulse length of 100 fs (at perfect alignment). After losses in the compressor the final output pulse has a maximum energy of 1 mJ.

The final output pulse is of reasonably high quality and retains an approximately Gaussian profile (in both apace and time) across a 6mm beam diameter ($1/e^2$). The profile is not perfect due to a horizontal dark fringe arising from the grating compressor, and no M^2 measurement could be performed to characerise the effect of the fringe. The energy stability is better than 1% RMS. The final bandwidth was approximately 17 nm FWHM (giving a time-bandwidth product of 0.8) and 40 nm at base and was reasonably Gaussian, as verified by the Libra's internal spectrometer. The temporal profile has a central Gaussian peak but retains wings containing a pre-pulse at a contrast of 1:1000 and a post-pulse at a contrast of 1:100 as determined by manufacturers testing.

3.2.2 Light Conversion Pharos

The Pharos is an extremely compact femtosecond laser system manufactured by Light Conversion Inc. and obtained via the EPSRC Laser Loan Pool. Like the Libra, the Pharos combines an oscillator with a regenerative chirped pulse amplifier and a high power pump laser into a single integrated unit, though in a more modular configuration that does not allow exposure of the internal optics to any contamination even when the main external cover is removed for maintenance. An approximate internal layout is presented in figure 3.2. Unlike the Libra, however, the Pharos is a tungstate-based system, using Yb:KGW crystals in place of Ti:Sapphire, giving the beam a central wavelength of 1028 nm.

The seed pulse is provided by a compact Yb:KGW oscillator which utilises Kerr lens modelocking to produce and output power of $\geq$ 700 mW at a 76 MHz repetition rate, giving a pulse energy of $\geq$ 9 nJ. The pulses length is typically $\leq$ 80 fs. Pumping for the oscillator is provided by a 980 nm diode laser module designed specifically for the Pharos and not otherwise commercially available. The seed pulses are passed through a Pockels cell which enables repetition rate selection from single shot to 200 kHz, before being passed through a grating stretcher in preparation for CPA. The stretcher utilises a double pass through a single transmission grating to facilitate compact construction whilst preserving high efficiency.

The regenerative amplifier again uses a tungstate rod which amplifies the seed pulse over multiple passes before an output pockels cell is triggered to extract the

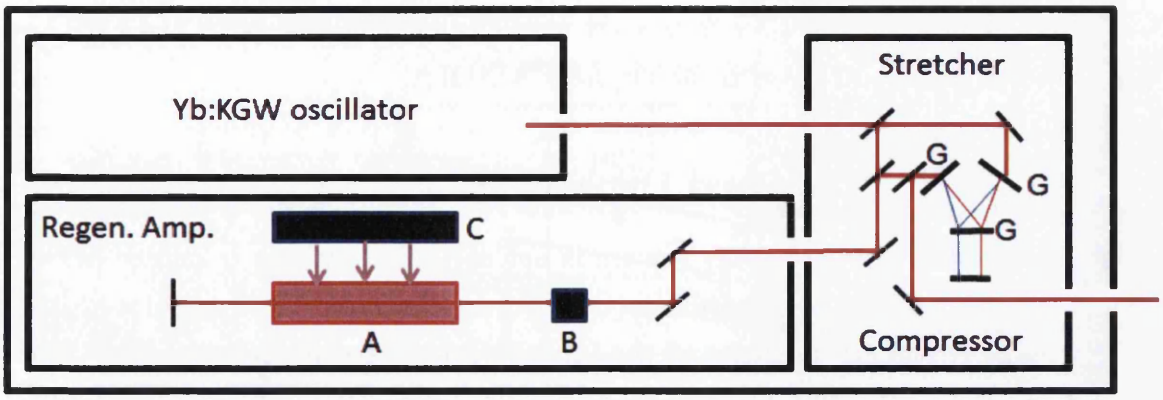

Figure 3.2: Internal layout of the Light Conversion Pharos laser system.The system is modular with the oscillator, regenerative amplifier and grating unit all separate and sealed units that bolt together. The oscillator cannot be opened outside the factory and so is not detailed. The Yb:KGW amplifier crystal (A) is directly pumped at 980 nm by a diode bar (C). The seed beam (red) from the oscillator is aligned through a grating stretcher (shown expanded in this diagram) to facilitate CPA, before being focused through the crystal (A) in temporal and spatial overlap with the pump light. The Pockels cell (B) reflects the pulse before being triggered to allow dumping after several passes. The pulse is then directed through the grating (G) compressor before exiting the laser.

pulse. The final pulse energy is tunable and the maximum achievable energy is strongly dependent on the repetition rate to avoid crystal damage. As with the Libra-S the crystal is water cooled to provide stability, although amplification does change the alignment and so seed pulses cannot be readily extracted without re-aligning the system. Energy input to the amplifier is again provided by a DPSS laser module designed specifically for the Pharos and not otherwise commercially available. Following extraction from the amplifier the pulse is passed through a grating compressor which utilises a transmission grating to restore a pulse length of approximately 290 fs. This is significantly longer than the seed due to a combination of effects introduced to the pulse during amplification, including loss of bandwidth as only the peak frequencies are properly amplified, and a significant amount of higher order dispersion introduced by the long optical path through the Yb:KGW crystal, Pockels cell and transmission gratings. Pulse lengths of 190 fs are achievable although 290 fs is preferred for use in optical parametric amplification to avoid damage.

The final output pulse retains a Gaussian spatial profile with TEM_{00} mode. The system is highly stable with an energy stability better than 0.5% RMS over 24 hours. A pre-pulse and post-pulse are unavoidably present at a contrast of 1:1000 and 1:200 respectively. The final pulse energy is a function of the selected repetition

rate, although for this project it was used at 200 μJ @ 20 kHz with the Orpheus OPA and 60 μJ @ 50 kHz with the Orpheus-N NOPA.

3.2.3 The Orpheus and Orpheus-N

The beam from the Pharos laser system is not used directly, but is instead passed into an Optical Parametric Amplifier (OPA) to be converted to an 800 nm central wavelength to match the output of the Libra in previous experiments. Two OPAs were used: the Pharos was supplied with an Orpheus, a system designed specifically to use the Pharos as a pump laser, and later an Orpheus-N, a non-collinear OPA (NOPA) which is a product under development and was supplied part way through the loan of the Pharos, at which time it replaced the Orpheus.

The Orpheus is a fully contained single-box OPA system, the internal layout of which is the proprietary property of Light Conversion and so is not presented, although can be discussed. The OPA is seeded by the 1028 nm beam from the Pharos, at which point a 515 nm pump beam is generated via second harmonic generation in a BBO crystal. The residual 1028 nm light is converted to a white light seed spectrum by a sapphire disk. This white light spectrum and the green pump beam are recombined spatially in collinear fashion at variable relative delay. The combined beam passes through a non-linear crystal whereupon the pump beam amplifies a selected part of the white light spectrum. As the white light seed is in a significantly longer pulse than the pump and is heavily chirped, the part of the spectrum to be amplified can be determined simply by altering the relative delay between pump and seed. The non-collinear version of this operation is shown in figure 3.3, which operates on the same principle.

Using this technique an output wavelength of anywhere between 630 nm and 2600 nm can be selected, as the collinear operation allows both the signal and idler outputs to be collected on the same path. At peak the energy conversion efficiency is 12 %, though this is assuming optimal input parameters and wavelength selection and in most cases the efficiency is approximately 6 %. As only a small selection of the seed is amplified the extracted pulse is shorter than the original seed, with a typical final length of approximately 190-200 fs. The output beam is directed through a second module, the Lyra, which features interchangeable filter slots to separate the signal and idler at the desired wavelength and polarisation combination.

The Orpheus-N that replaced the Orpheus part-way through the laser loan period was at the time an experimental product. Like the Orpheus it is a fully contained single-box OPA system, however the internal layout is significantly different. Again the exact layout is proprietary, however a simplified illustration is presented in figure

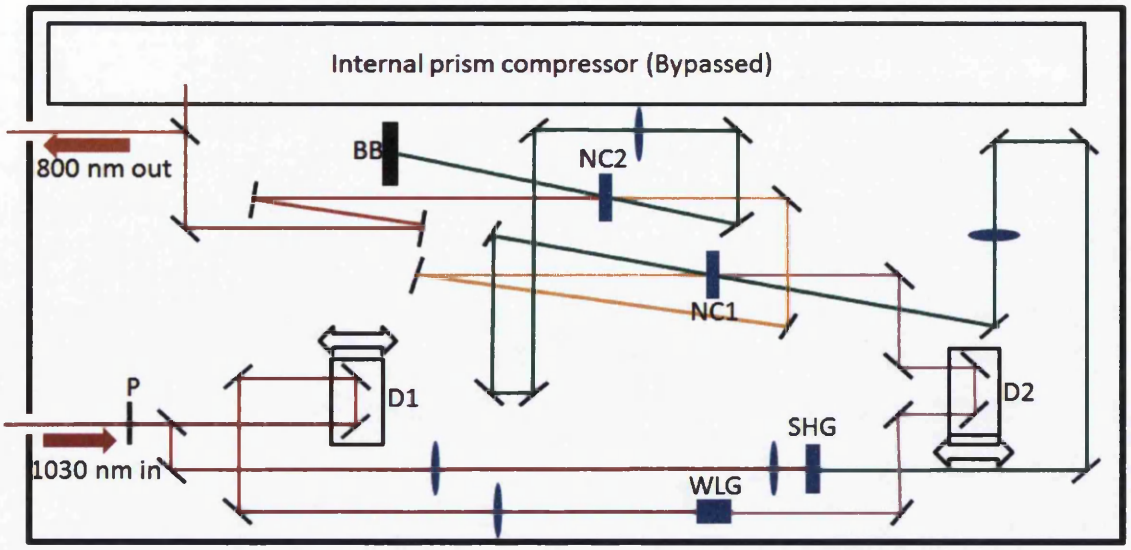

Figure 3.3: Simplified internal layout of the Light Conversion Pharos Orpheus-N NOPA. The standard Orpheus is in a collinear layout but operates on the same principle. The system is pumped at 1028 nm by the Pharos. The input light is split into a seed and pump, with the proportion of light in each determined by the rotation of the polariser P. The pump pulse is telescoped down and passed through a second harmonic generation crystal (SHG), before being focused into nonlinear crystal NC1 and then after a fixed delay into a second nonlinear crystal NC2, after which it is dumped into a beam block (BB). The seed pulse is passed through a delay stage (D1) before being focussed into a sapphire disk to perform white light generation (WLG). The white light is passed through a second delay stage (D2) before being passed through nonlinear crystals NC1 and NC2 in temporal and spatial overlap with the pump pulse at a small angle. The final amplified wavelength is determined by adjusting the delays D1 and D2, as well as rotating crystals NC1 and NC2. The Orpheus-N also features an internal prism compressor, however this was bypassed in favour of a custom external compressor.

3.3.

The Orpheus-N is again designed to be pumped by the Pharos laser system but with a reduced pulse energy of 6 μJ, and so the repetition rate was increased to 50 kHz. Again the input pulse is split, with one arm being converted to a 515 nm pump beam by second harmonic generation and the other being converted by a sapphire disk to a white light seed spectrum. The seed spectrum and the pump beam are again recombined spatially in a non-linear crystal, however they are no longer collinear, instead crossing at a narrow angle inside the crystal which is also tilted to preserve phase matching [216]. As before, the relative delay between the pump and the seed is used to determine which part of the seed spectrum is amplified to determine the new central wavelength.

The selection range is narrower than the standard Orpheus, with output wave-

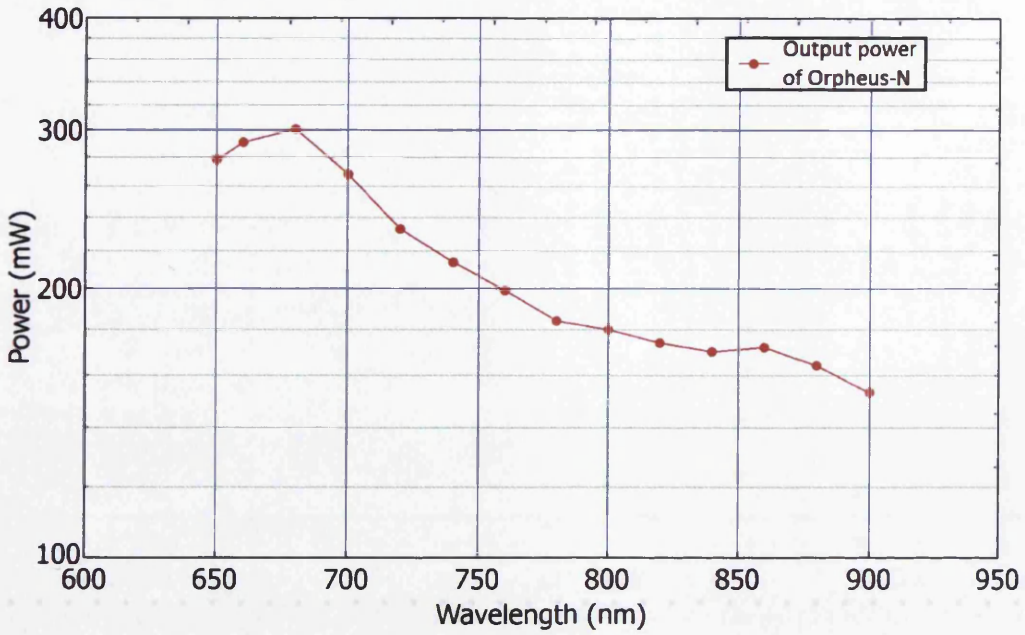

Figure 3.4: Recorded tuning curve of the Orpheus-N NOPA, with the Pharos pump laser power set to 3.0 W at 50 KHz with a pulse length of 250 fs. This is the optimised spectrum and the output power at 800 nm settled to 180 mW within the first week of use before remaining stable to within ± 5 mW.

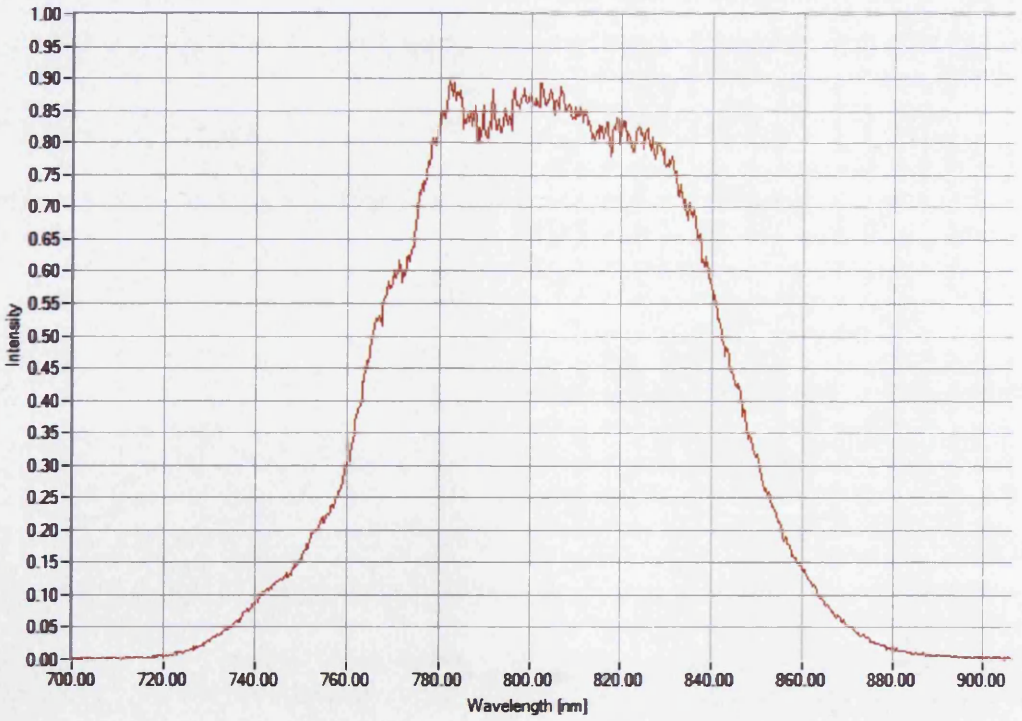

Figure 3.5: Recorded output spectrum of the Orpheus-N NOPA at 800 nm. Measured from the reflection from a piece of Teflon by a fibre-coupled spectrometer (Thorlabs CCS175), a FWHM of approximately 83 nm is demonstrated.

lengths between 650 nm and 900 nm available. The pulse is again of the order of 200 fs long but unlike the pulse from the standard Orpheus contains sufficient bandwidth to allow compression to approximately 20 fs. This is ordinarily achieved via a prism compressor built into the box of the Orpheus-N. This compressor can counter dispersion enough to achieve 20 fs at the exit of the NOPA but is not long enough to add positive chirp to counter the effects of glass further down the beam path. This compressor was therefore bypassed in favour of a custom built compressor discussed below. A measured output spectrum of the Orpheus-N at 800 nm and having bypassed the prism compressor is shown in figure 3.5, which if compressed to 20 fs would give a time-bandwidth product of 0.78.

3.2.4 Artemis

Artemis is a unique laser facility that forms part of the Central Laser Facility (CLF) located at the STFC Rutherford Appleton Laboratory (RAL) at the Harwell Oxford science and technology campus. The facility is constructed around a high-end commercial femtosecond laser system (KM Labs RedDragon), with several additional components to enhance the facilities capability in producing high repetition rate ultra-short pulses. Such additions include an OPA with a tuning range of 235-15000 nm, a hollow fibre compressor which can produce broad spectrum pulses, and the ability to generate VUV and XUV pulses via high harmonic generation.

The RedDragon is a Ti:Sapphire based laser system that integrates an oscillator with a two stage multipass chirped pulse amplifier. The central wavelength of the oscillator is 780 nm. A pulse picker reduces the repetition rate of the oscillator from 80 MHz to 1 kHz, after which the pulse is stretched by a grating stretcher to a few nanoseconds to enable a two stage chirped pulse amplification to be performed.

In the first amplifier a single Nd:YLF pump laser is used to amplify the stretched seed pulse to approximately 2 mJ over 14 passes. The Ti:Sapphire crystal used for amplification is encased in a cryo-cell and cooled with liquid helium to avoid damage from the heat delivered by the high power pump laser and to minimise the Kerr lensing effect. The beam is then passed into a second stage amplifier which utilises a pair of Nd:YLF pump lasers to amplify the pulse to approximately 14 mJ over several passes. This crystal is also cooled with liquid helium in order to avoid overheating from the high pump laser power.

After exiting the second compressor the pulse is finally passed through a half-wave plate and a polarising beamsplitter. Re-compression is achieved by a pair of grating compressors, with the waveplate and splitter used to determine what proportion of the total pulse energy enters each compressor. The final pulse parameters

are roughly the same regardless of which compressor is primarily used: The final pulse energy is tunable up to 14 mJ at 1 kHz and can be compressed to a final length of 30 fs.

Following the split through the compressors, one pulse is sent to an OPA (Light Conversion TOPAS), whilst the other is extracted at 780 nm and can be used as is, sent through a hollow fiber compressor and compressed further to 7 fs. A unique feature of Artemis is the ability to generate monochromatic XUV pulses. The 30 fs, 780 nm pulses extracted directly from the compressor may be focused in a vacuum chamber through a high density jet of inert gas, initiating high harmonic generation (HHG). This creates a series of photons at odd harmonics of the original photon energy, confined into pulses with roughly similar length to the initial pulse. By this method Artemis has produced photons with energies up to 100 eV. These pulses may be used in their broadband form or directed into a unique monochromator [217] which utilises a rotating grating and a slit to isolate a single harmonic whist maintaining a short pulse duration of ≤ 30 fs [218], although power must be sacrificed with a peak transmission of 30%.

3.3 Pulse compression and characterisation

3.3.1 Grating stretching and compression

In order to perform chirped pulse amplification in all three of of the laser amplifiers used in this project the pulse from the oscillator is first stretched using a pair of gratings and then re-compressed following amplification to its final length via the same technique in reverse. The principle behind such a device is remarkably simple, and in its most basic form requires only a pair steering mirrors in the input, a pair of reflection gratings, and a retro-reflector (often in the form of a roof mirror to allow the input and output beams to be vertically separated. Other variants exist utilising a single grating with multiple passes and even transmission gratings, however the principle remains fundamentally the same regardless of design.

The basic layout of a grating compressor is shown in figure 3.6. The grating compressor is advantageous for use within laser amplifiers as it can withstand extremely high powers. The damage threshold of the gratings is determined by the protective coatings, which are typically capable of withstanding several watts of average power. Furthermore grating compressors can be easily configured in layouts without any additional focusing optics, removing the issue of aberrations in lenses or white light generation. The disadvantage of grating compressors is that, as only the first diffraction order is typically captured, a large amount of the incident power is lost

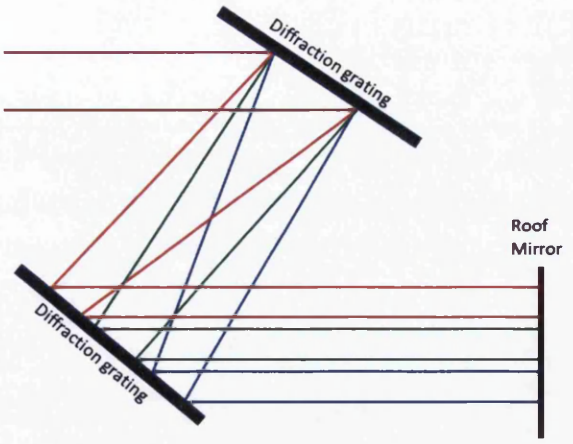

Figure 3.6: Basic layout of a grating compressor showing beam paths. The light enters negatively chirped, as is standard after having passed through the high refractive index gain medium. The collimated beam is scattered from the first grating to create a separation of the wavelengths. A second grating is positioned such that the first order diffracted light is captured and re-collimated after reflection, with the beam showing a high degree of spatial chirp across the beam profile. The collimated beam is then reflected back through the gratings along the same paths by a mirror or pair of mirrors which vertically separate the incident and reflected light. Passing back through both gratings collimates the beam which may be extracted for use. The short wavelengths at the rear of the pulse travel a shorter distance through the assembly than the longer wavelengths at the front of the pulse. When the pulse exits the compressor the chirp has been corrected such that all wavelengths overlap in both space and time. The amount of chirp to be corrected is adjusted by altering the separation of the gratings.

over the course of the compression in higher orders of the diffraction pattern (total transmitted energy is often as low as 35 % due to higher orders of diffraction not being collimated with the rest of the beam). These stray beams may also represent a hazard to users when operating the compressor without an enclosure e.g. during alignment.

Achieving a stretching effect with gratings is also relatively simple. An identical configuration to the compressor may be used if positive chirp is the desired outcome, useful for compensating glass further along the beam path which will induce negative chirp. Alternatively negative chirp may be achieved by mounting the gratings at an angle near perpendicular instead of the near parallel example shown in figure 3.6, the exact angle required being defined by the blaze angle of the gratings. This allows negative chirp to be achieved by passing the shorter wavelengths through a longer beam path than the longer wavelengths in the pulse. This is configuration typically used before the amplification process to avoid re-compression of the pulse by the gain medium.

3.3.2 The prism compressor

Whilst grating compressors are extremely useful for countering the effects of CPA, the power loss through a grating compressor makes them undesirable when the input power is low to begin with and needs to be preserved. Compression of the output light from the Orpheus-N NOPA therefore required an alternative compression technique, with prism compression being the obvious choice. The Orpheus-N contains a prism compressor which does not feature sufficient dispersion compensation to account for glass further along the beam path, so a custom external prism compressor was constructed.

Prism compression utilises the same principle as grating compression, however the dispersive optics are replaced with prisms and the light is transmitted rather than reflected, as shown in figure 3.7. In the standard configuration the light enters negatively chirped and is passed through the first prism at the Brewster angle of the material to minimise energy loss through reflection. Normally the beam diameter should be as small as possible (whilst keeping the intensity sufficiently low to prevent white light generation) and should be passed through the first prism as close to the tip as possible to avoid introducing too much second and third order dispersion.

As with the grating compressor achieving a stretching effect is also possible. When positive chirp is desired to compensate for the presence of glass further along the beam path this can be achieved by extending the distance between the prisms, as well as adjusting the extent to which the second prism is inserted into the beam. Conversely negative chirp may be induced by inserting the second prism from the other direction such that the shorter wavelength components must pass through more glass, though in reality this is very rarely used as grating compressors are generally preferred for stretching pulses due to their compact construction and because in the typical case of stretching before CPA the loss of energy in the seed can simply be countered with more optical power in the pump beam. Prism compressors are useful for countering dispersion in low power beams due to the low power loss they are unsuitable for most other purposes, in particular higher powers may induce white light generation in the prisms. A prism compressor requires a much larger distance between dispersive optics to produce the same dispersion compensation as a grating compressor. This distance makes building compact prism compressors extremely difficult, making them undesirable for directly building into an enclosed laser system. Additionally as the optics are transmissive it is inevitable that some second and third order dispersion will be introduced which cannot easily be compensated, meaning the output pulse will never quite achieve transform limited duration. However, the entire beam is captured at the second prism as there are no higher

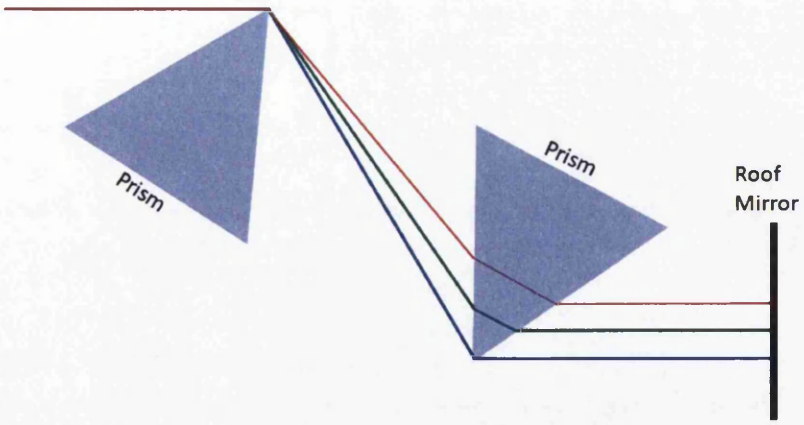

Figure 3.7: Typical layout of a prism compressor showing beam paths. Refraction through the first prism causes spatial separation of the constituent wavelengths of the incident light. This diverging beam is then passed through the second prism, which is angled such that the light is re-collimated by refraction, again with a high degree of spatial chirp across the beam profile. When the prisms are arranged as shown in figure 3.7 the longer wavelength constituents of the pulse pass through more glass in the second prism. The end result is that even though the physical beam path is shorter for the longer wavelengths than the shorter wavelengths, the optical path is longer for the longer wavelengths, allowing the shorter wavelengths trailing at the rear of the pulse to catch or overtake the longer wavelengths at the leading edge of the pulse. The collimated beam is then reflected back through the prism pair along identical paths by a mirror or by a pair of mirrors which vertically separate the incident and reflected light. Travelling back through both prisms re-collimates the beam which may be extracted for use. The amount of dispersion compensation provided by the compressor can be adjusted both by altering the distance between the prisms and by changing how far the second prism protrudes into the beam (although it should generally be positioned such that the shortest wavelength extent of the beam just touches the tip of the prism).

orders of refraction, hence the power loss is extremely low.

The compressor constructed to shorten the output of the Orpheus-N was built of standard opto-mechanical components on a dedicated breadboard also containing a FROG measuring device. The final construction is shown in figure 3.8 with the layout and beam paths detailed. Input to the compressor is determined by a pair of steering mirrors (not shown), before the beam is guided onto the dedicated breadboard by a 90 degree periscope (A) (extracted from the optical assembly of the Orpheus-N) to ensure correct beam polarisation. The beam is then passed over mirror (B) before being reflected by a final alignment mirror (C) through the first prism (D), which is mounted on a translation stage providing 3 axes of translation as well as pitch and yaw control. The beam is then guided by another mirror (E) onto a delay stage (F) used to set the amount of dispersion compensation to be

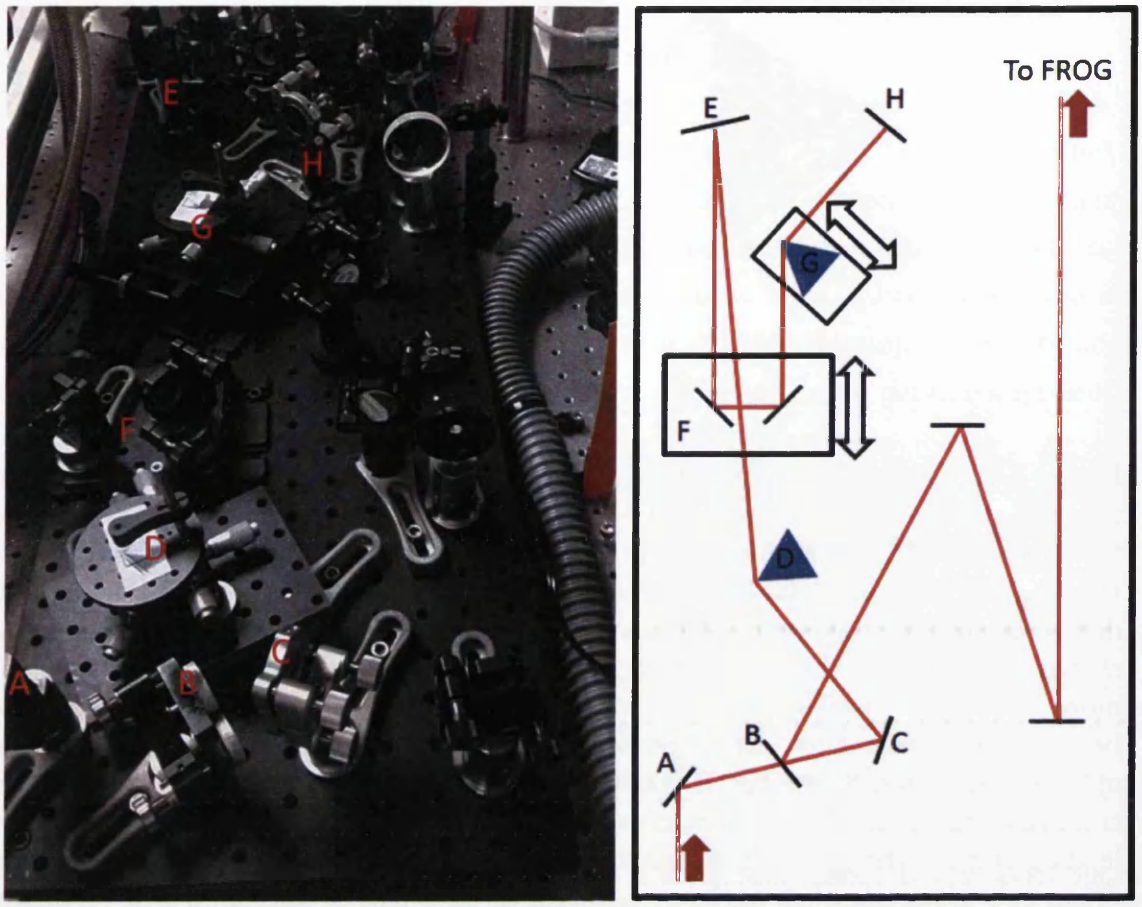

Figure 3.8: Photograph (left) and layout diagram (right) of the prism compressor used with the Orpheus-N with components and beam paths highlighted. The entire compressor was constructed using standard parts and achieved pulse lengths of 30 fs FWHM. (A) Periscope, (B), (C) and (E) Steering mirrors, (D) First prism, (F) Delay stage, (G) Second prism, (H) Angled retro-reflecting mirror.

applied. The exit beam of the delay stage is then passed through the second prism (G) mounted again on a 5-axis stage, and onto a mirror (H) which is slightly angled downwards to reflect the beam back through the prisms in a similar but vertically separated path. The exit beam passes below the input beam and so hits mirror (B) which extracts the pulse for use.

The distance between the prisms is set to entirely reverse the negative chirp of the pulse as emitted from the Orpheus-N, and then to add sufficient positive chirp to account for the dispersion introduced by 10 mm of fused silica, accounting for the beamsplitters, lenses and vacuum window through which the pulse must travel on the path to the vacuum chamber. Precise determination of the amount of positive chirp to introduce is finely controlled by the delay stage, which is manually moved but equipped with a differential drive capable of achieving movement in 10 micron

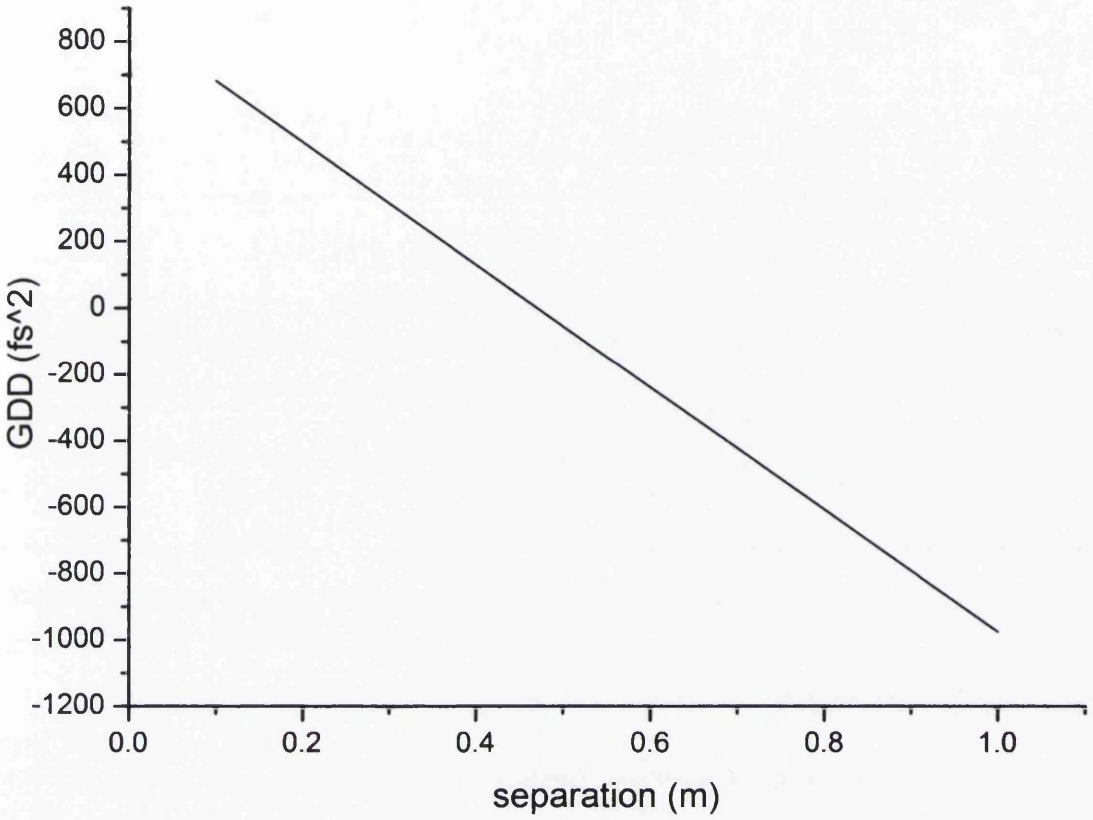

Figure 3.9: Calculation of the amount of group delay dispersion introduced by a prism compressor as a function of the distance between the prisms. The fitting equation is used to determine that an optimal separation of 1.14 m is required to compress the pulse from the Orpheus-N given the amount of glass through which it must pass.

steps. Additionally the two 5-axis stages provide 5-micron accuracy positioning of both prisms. The exact distance needed between the prisms was calculated based on equations determined by Fork *et al* [219], who showed that in the case of the double pass geometry used here the group delay dispersion introduced by the prism pair is given by

$$GDD = \left(\frac{\lambda^3}{2\pi c^2}\right)\frac{d^2P(\lambda)}{d\lambda^2} \tag{3.1}$$

where P is the wavelength dependent path length and is given by $P = 2L\cos\beta$, and where L is the distance between the apexes of the two prisms and where β is the angle taken by the beam after dispersion at the first prism. The parameter β can be estimated as

$$\beta \approx -2\frac{dn}{d\lambda}\Delta\lambda. \tag{3.2}$$

where n is the refractive index of the material.

It was also proven in [219] that equation 3.1 can be expanded to

$$GDD = \frac{\lambda^3}{2\pi c^2}\left(4L\left[\left[\frac{d^2n}{d\lambda^2} + \left(2n - \frac{1}{n^3}\right)\left(\frac{dn}{d\lambda}\right)^2\right]\right.\right. \\ \left.\left.\sin\beta - 2\left(\frac{dn}{d\lambda}\right)^2\cos\beta\right] + 4\left(\frac{d^2n}{d\lambda^2}\right)(2D)\right) \tag{3.3}$$

where the refractive index of the prisms is given by n and the beam diameter given by D. This equation is completely accurate, however can be approximated to

$$GDD = \frac{\lambda^3}{2\pi c^2}\left(-4L\left[2\left(\frac{dn}{d\lambda}\right)^2\right] + 4\left(\frac{d^2n}{d\lambda^2}\right)(2D)\right) \tag{3.4}$$

allowing a simple calculation of the separation L needed to compensate a given amount of group delay dispersion. A plot based on these equation is shown in figure 3.9. Extrapolating this graph using the shown fitting equation, and calculating the amount of dispersion compensation required for the amount of BK7 glass and fused silica in the beam path, it was determined that an optimal prism separation of 1.15 m was required to achieve the shortest possible pulse lengths. As this distance is adjustable it was then tuned to 1.14 m using the FROG as detailed below.

3.3.3 Pulse characterisation via FROG

Following compression of a laser pulse it is vital that a reliable method of measuring the resulting pulse be incorporated to determine whether the compressor is behaving as expected and to verify that the distance between the dispersive optics is correct to achieve the desired pulse length or level of chirp. Simply autocorrelating a split and recombined laser pulse allows a reliable measurement of pulse length to be obtained but is time-consuming and requires regular user interaction. The delay line must be manually moved across the full range of pulse interaction, which is inconvenient when attempting to use the measurements to optimise pulse length, as the measurement must be manually repeated each time an adjustment is made, making converging onto the optimum compressor length a relatively lengthy process. There exists the possibility of automating this process however it was not possible to do so with the resources available in this case.

When the pulse power is sufficiently high it is possible to perform autocorrelation measurements with a single shot rather than manually sweeping through a range of delays. The delay is positioned to provide perfect temporal overlap and the pulses are focused into the non-linear optic via a cylindrical lens or mirror. This

generates a third pulse of the second harmonic which is emitted along the sum vector of the two incoming pulses, which may be isolated using a slit and projected onto a CCD camera. By focusing in only one plane it is possible to generate a scenario where time delay is a function of position in the crystal. This technique can be refined further by using a single shot spectrometer as the detector of a single shot intensity autocorrelator, creating Frequency Resolved Optical Gating (FROG) [220]. If the cylindrical focusing is confined to one plane and is followed by a grating employed to disperse the frequency components of the pulse in the perpendicular plane, the resulting projection onto the CCD will feature temporal information of the pulse along one axis (as in the single shot autocorrelator) and wavelength information on the perpendicular axis. Intensity provides information as to the spread of components in each of these regimes. In a single shot, FROG provides a full pulse length and bandwidth characterisation, and allows near real-time tuning of both parameters, at a speed only limited by the refresh rate of the camera.

For this project a FROG was constructed to monitor the output of the prism compressor described above for use with the Pharos laser and Orpheus-N NOPA. This FROG was constructed on the same breadboard creating an integrated system for compression and measurement of ultrafast laser pulses, and is shown in figure 3.10.

The 2% of the beam from the compressor is extracted from the primary beam path to the tank and is passed through a 10 mm piece of fused silica (not shown) to replicate the effect of windows and lenses further along the main beam path. This beam is then aligned through the iris (A) before being passed through a 50/50 beamsplitter (B). The reflected beam is reflected by three mirrors to form the fixed arm of the delay line, the transmitted beam is reflected by two mirrors mounted on a delay stage (C) to form the variable arm which is adjusted to ensure good temporal overlap. Both of these beams are then aligned onto a cylindrical silver mirror (D) which performs focusing to a line in the plane perpendicular to the table. The beams then reach a piece of BBO crystal (E) which is sufficiently thin to preserve the phase matching condition and is mounted on a 1mm thick fused silica substrate The BBO itself has a thickness of 0.02 mm. When the two pulses are crossed at an angle (in this case 29 degrees) whilst temporally overlapped a third pulse along the sum vector is emitted with a horizontal spread determined by the autocorrelation time of the input pulses. The second harmonic beam is then steered though a lens (F) onto a card mask (G) positioned such that only the pulse along the sum vector is allowed to pass through a slit (H). The pulse is then focused by a lens (I) through a transmissive grating (J) which disperses the frequency components perpendicular

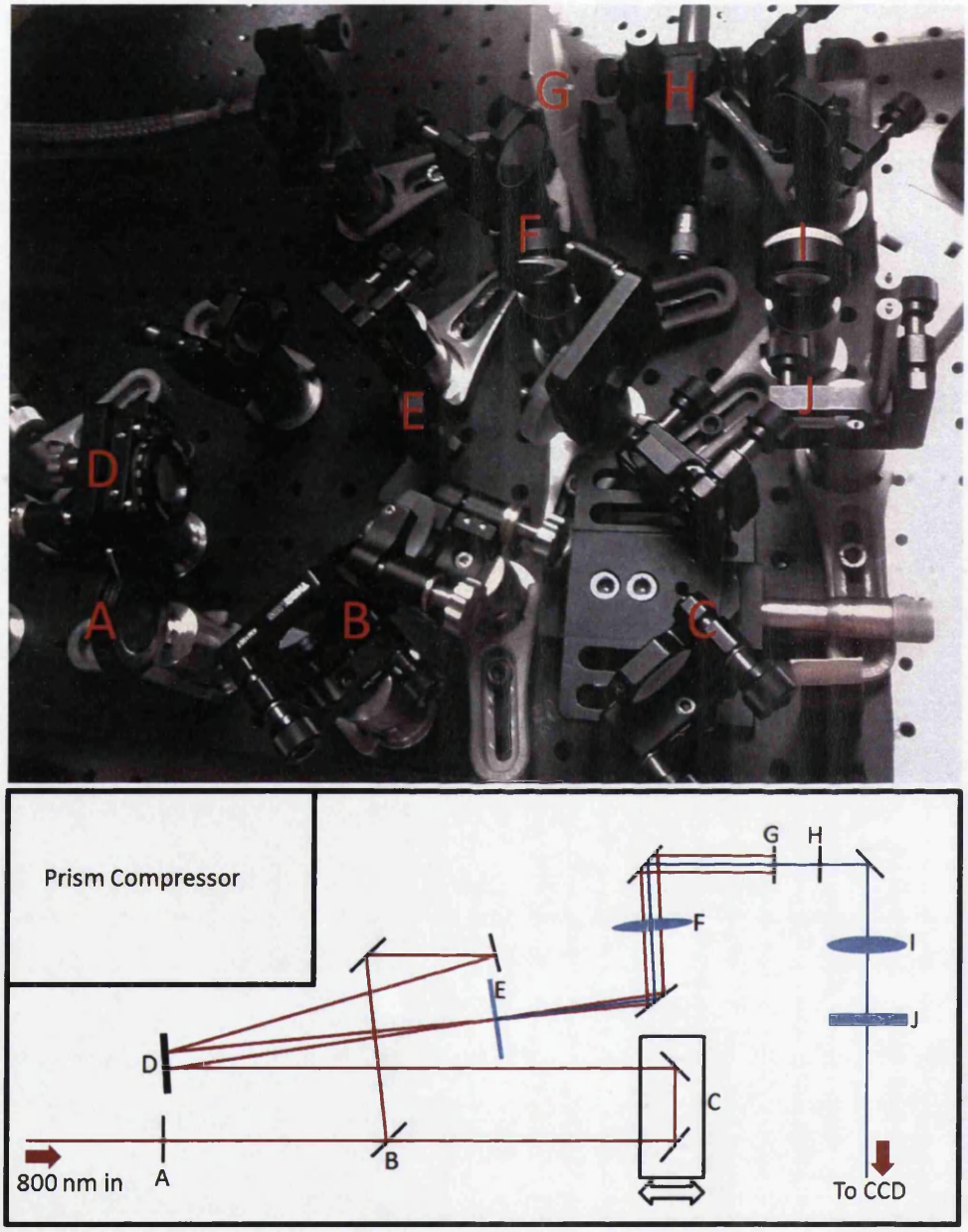

Figure 3.10: Photograph (top) and corresponding beam layout diagram (bottom) of the FROG pulse measurement device used with the Orpheus-N and prism compressor. The assembly was constructed using standard components. (A) Iris, (B) Beamsplitter, (C) Delay line, (D) Horizontal cylindrical mirror, (E) BBO crystal, (F) Lens, (G) Filter, (H) Horizontal slit, (I) Lens, (J) Transmissive grating (lines horizontal).

to the table, and onto a CCD chip (not shown) which is positioned to intercept the first diffraction order. The camera used was an AVT Marlin F146 (1392 x 1040 pixels, 17 fps) with no lens, the focusing onto the chip being done by the lens (I).

Whist the CCD image itself can be used as a tuning tool, extracting numeric values for pulse length and bandwidth requires a fairly complex phase retrieval calculation, although it is possible with a simple pulse shape and a very fast computer to run such algorithms almost in real time. Retrieving complete characterisation of complex pulses with nonlinear chirp may be substantially more time-consuming. To achieve full analysis of the laser pulse images from the AVT Marlin were saved and imported into a two stage MatLab algorithm developed by the group of Rick Trebino which is distributed freely [221]. This algorithm consists of two separate programs known as "Binner" and "Frogger".

The saved image must first be passed through the Binner code which bins the data contained in a grayscale image into a two dimensional histogram. This avoids the prohibitive computation cost of applying the calculation to every pixel of a high resolution image. The reconstruction accuracy will increase with the number of bins, however the computation time also increases dramatically. The code also allows the image to be centred to the brightest point, the removal of negative data points and the subtraction of a constant background. To supplement this a piece of LabVIEW code was used to background subtract the image by a dark image taken with the same number of camera shots. At this stage the user also inputs key parameters into the code such as the centre wavelength of the pulse and the calibration factors in both wavelength and delay. The delay calibration was performed by measuring the sideways movement of the image as the delay stage in the FROG was adjusted, then wavelength calibration was performed by measuring the vertical shift in the image as a function of changing wavelength, achieved by adjusting the output wavelength of the Orpheus-N.

The binned image is then imported into the Frogger code, which uses an iterative algorithm whereupon a sample FROG image is generated for the same central wavelength and calibration parameters using a random pulse length and bandwidth. This image is compared to the binned image and the difference measured at each bin. The duration and bandwidth parameters are then iteratively adjusted until the code determines that it has produced a reconstructed image which cannot be matched to the binned image any more closely than it already is within the rules of the code (i.e. preserving image symmetry). The algorithm also keeps track of phase information, although this aspect is somewhat unreliable. The inputs and outputs of this algorithm are shown in figure 3.11 and 3.12.

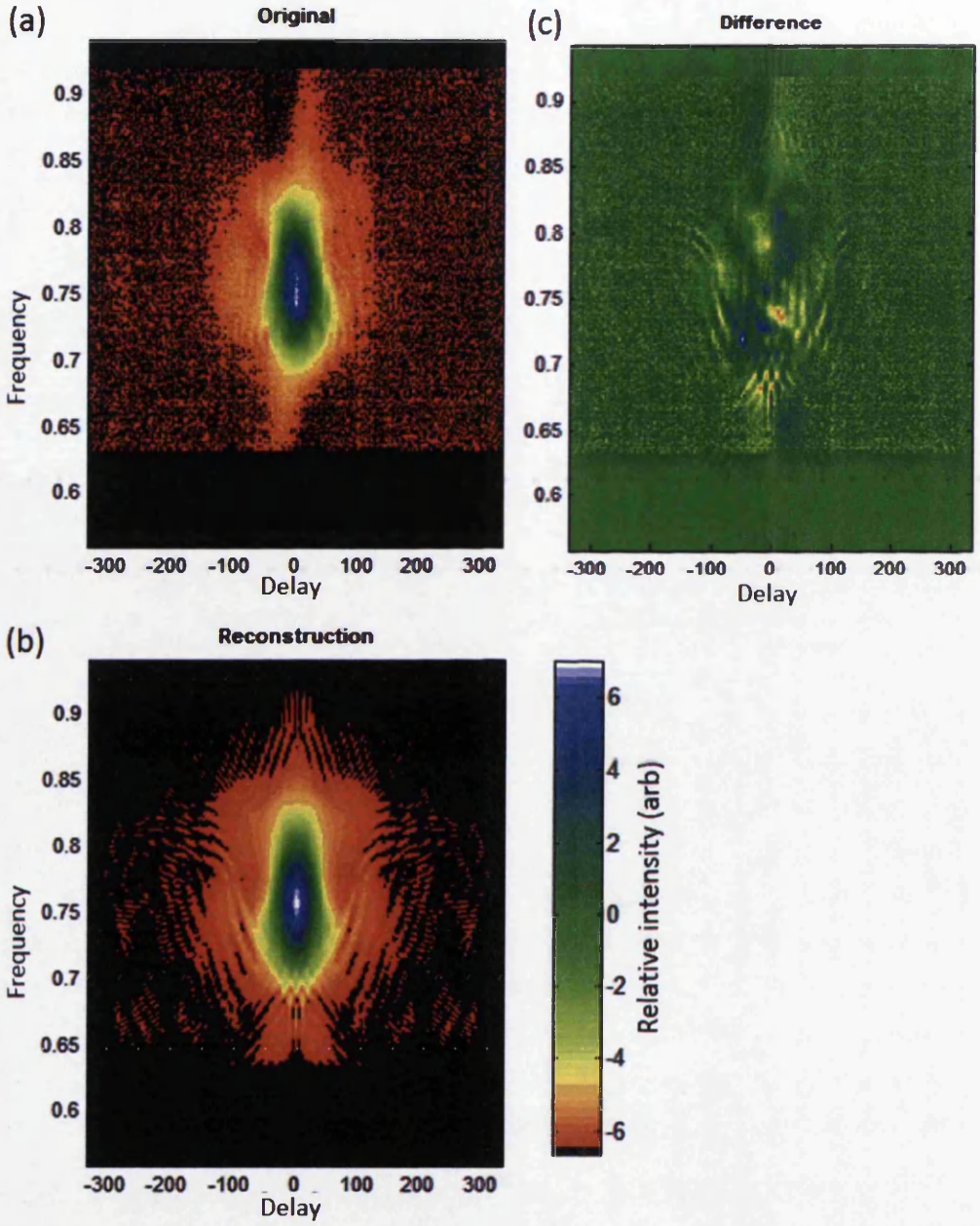

Figure 3.11: A recorded FROG trace presented alongside the calculated reconstructed trace and a plot of the difference. (a) recorded FROG trace from a real pulse produced by the Orpheus-N and optimised with the prism compressor, after being binned. (b) The optimum reconstructed trace calculated by the code. (c) A plot of the difference between the reconstructed and original trace. The scale bar is x10^5 for (a) and (b) and x10^4 for (c).

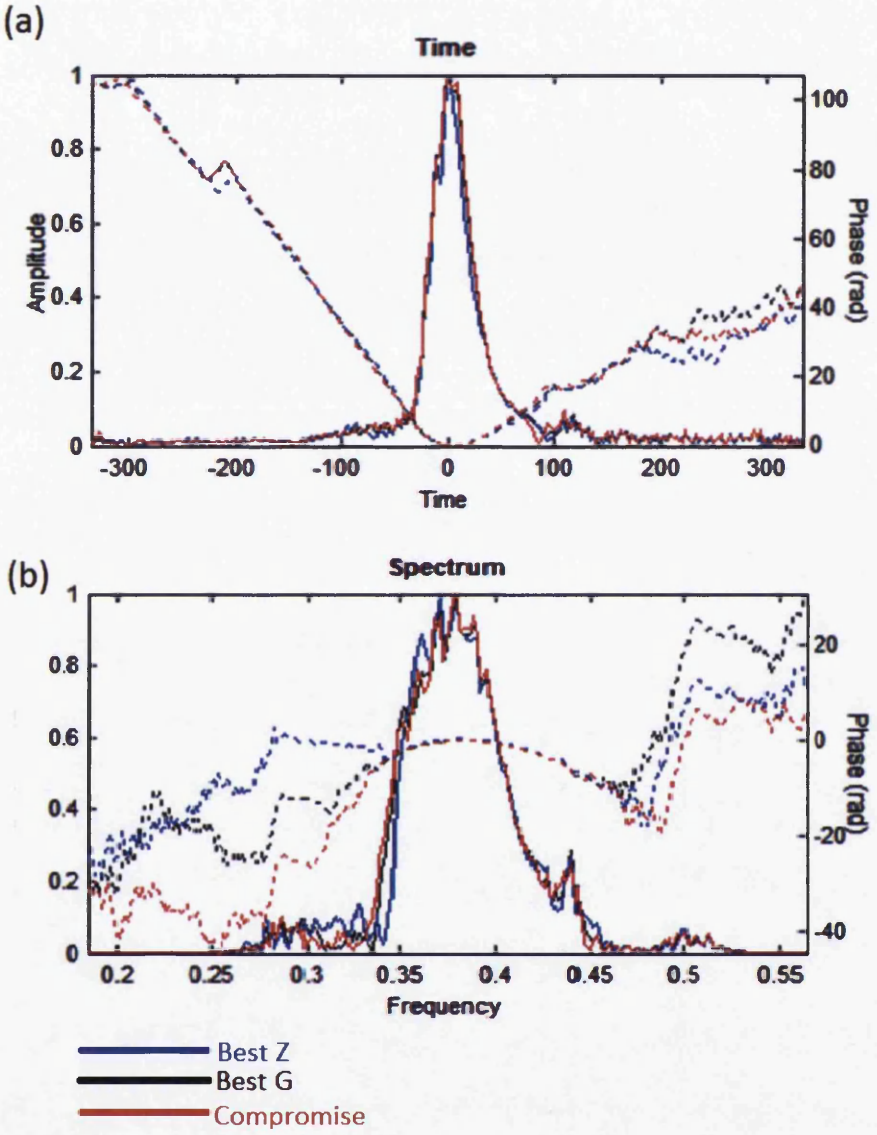

Figure 3.12: The calculated temporal and spectral profile of the reconstructed FROG trace in figure 3.11. (a) The reconstructed temporal profile of the pulse. (b) The reconstructed spectral profile of the pulse. The reconstructed values give a temporal length of 28.9 fs (FWHM) and a bandwidth of 85.9 nm FWHM. The different coloured lines are a result of the code converging to multiple solutions, where G and Z are fitting parameters used by the code over which the user has no control, both of which should be minimised to provide the optimum solution. It is generally not possible to have both values at zero and so the compromise results is used, where the sum of the G and Z parameters is minimised.

In the case presented here the Frogger code produced a reconstructed trace with temporal length 28.9 fs (FWHM) and a bandwidth of 85.9 nm FWHM from a pulse produced by the Orpheus-N and optimised with the prism compressor. This measurement reveals that although a short pulse is achieved the performance of the compressor is not perfect. At the measured bandwidth a transform limited pulse would be approximately 11 fs, which has been found not to be achievable. The likely reason for this is that whilst prism (and grating) compressors are highly effective at correcting first and second order dispersion, the pulse is also lengthened by third order dispersion which is not corrected (and is in fact worsened by the light passing through the prisms themselves). The amount of higher order dispersion is significant, arising from the nonlinear crystals in the NOPA itself, the prisms, the glass in beamsplitters and windows and, to a lesser extent, some is even introduced in reflection from the steering mirrors and the air.

Chapter 4

Magnetic bottle spectrometry of photoelectron emission from a nanotip

Reliably using a nanotip to produce ultrashort electron bunches for time-resolved diffraction and imaging purposes requires detailed knowledge of the energy spectrum of the electrons emitted under given laser and electrostatic conditions. A broad energy spectrum, or one where the distribution occurs over multiple peaks, will lead to a temporally stretched bunch or even multiple bunches in rapid succession, dramatically reducing the best obtainable temporal resolution of the image. Measuring the photoelectron energy spectrum from a tip before its use as an imaging source is therefore a vital requirement to understanding the limitations of electron imaging techniques. In order to examine the electron spectrum produced by the interaction of a laser pulse with a nanotip a magnetic bottle electron energy spectrometer has been constructed. This type of spectrometer traps released electrons in a strong magnetic field over a 2π capture volume, without changing their energy or speed. The electrons are then directed by the magnetic field down a flight tube to a detector, where the time-of-flight is used to determine the energy.

4.1 Principle of magnetic bottle spectrometry

Magnetic bottle spectrometry relies on electron emission occuring in a region of high yet well directed magnetic field, which is sufficiently strong to capture electrons of the highest energy produced by the laser-target interaction. These captured electrons may then be directed along the field lines without altering their kinetic energy. The magnetic field must initially decrease rapidly around the interaction region to

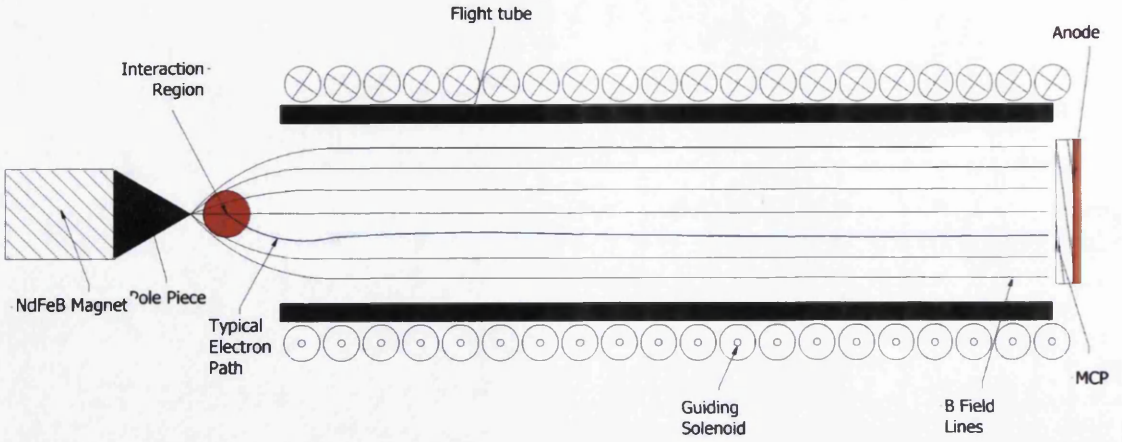

Figure 4.1: Layout and typical electron flight path through a magnetic bottle electron energy spectrometer. Electrons are emitted in a region of high magnetic field before their trajectories are parallelized by the field lines and are guided down a solenoid to a detector with high temporal resolution. The electrons are contained by cyclotron motion on the solenoid field and their arrival time at the detector is dependent on their kinetic energy.

spatially separate electrons of different energies, and then form a very low field strength plateau to allow the bunches of different energies time to separate before reaching the detector. The principle and typical electron flight through this kind of spectrometer is shown in figure 4.1.

This type of spectrometer was first proposed in 1983 by Kruit & Read [222], who studied multi-photon ionization of gases with an energy resolution of 15 meV. In the original design, the strong field at the interaction region was achieved using electromagnets which are excellent for producing an intense field but are cumbersome in a vacuum environment due to cooling and pumping requirements. High currents are required which often necessitates water cooling, as well as requiring large numbers of turns resulting in substantial trapped volume between the wires.

The first design to avoid these issues by using permanent magnets was created by Gillen and colleagues [223]. The spectrometer constructed for this experiment uses a more modern version of the Gillen design that has been commonly used for a variety of experiments [224–228]. A strong Ferromagnet, often NdFeB with a field-shaping paramagnetic pole piece, is used to generate a high strength field around the interaction region. The emitted electrons are immediately guided into a long flight tube with a solenoid adjusted to sustain a field of strength a factor of $\sim 10^3$ less than the interaction region field.

The resolution of this type of spectrometer is highly dependent on the structure of the magnetic field, as the electron trajectories parallelize with a time inversely

proportional to the field gradient. Upon release the electrons will immediately be drawn into helical cyclotron motion around an axis aligned with the sum vector of the magnetic field. This motion has a radius given by

$$r_i = \frac{m_e v \sin\theta_i}{qB_i} \tag{4.1}$$

with angular momentum

$$L_i = \frac{m_e^2 v^2 \sin^2\theta_i}{qB_i} \tag{4.2}$$

where m_e and v are the mass and magnitude of the velocity of the electron respectively, θ_i is the initial emission angle, q is the electron charge and B_i is the magnitude of the inital magnetic field. This angular momentum will be conserved on the condition that the magnetic field is adiabatic, which is met when the change in field experienced by the electron over one cycle of the helical motion is small. This requires that the field vary smoothly, as any sudden discontinuities in the field strength will violate this condition. When the condition is met the field gradient smoothly changes the angle of the electron velocity relative to the axis of the flight tube, such that over the course of the flight the angle is defined by

$$\frac{\sin\theta_f}{\sin\theta_i} = \sqrt{\frac{B_f}{B_i}} \tag{4.3}$$

where θ_f is the final angle from the normal of the electron motion in the drift tube with magnetic field B_f. The magnitude of the velocity remains unchanged, therefore the direction is changed with the transverse component being reduced and the longitudinal component v_L towards the detector being increased accordingly, from $v_L = v_i \cos\theta_i$ at emission to

$$v_L = v_i\sqrt{1 - \frac{B_f}{B_i}\sin^2\theta_i}. \tag{4.4}$$

This draws electrons into parallel trajectories along the flight tube regardless of their initial direction. When the field is adiabatic the radius r of the cyclotron motion naturally changes according to

$$\frac{r_f}{r_i} = \sqrt{\frac{B_i}{B_f}} \tag{4.5}$$

such that the total flux of the magnetic field encompassed within the radius of the cyclotron motion remains constant.

Assuming that all conditions regarding the field structure and adiabaticity are

met, this parallelization effect creates a flight time t of the electron bunch of

$$t = \frac{l_f}{v_L} \approx \frac{l_f}{v_i}\left(1 + \frac{B_f \sin^2\theta_i}{2B_i}\right) \tag{4.6}$$

where l_f is the length of the flight tube. If the field is optimally shaped such that $B_f \ll B_i$ and the transition between the 2 fields occurs over a length much smaller than that of the flight tube, the time-of-flight can be approximated as

$$t = \frac{l_f}{v_i} \tag{4.7}$$

in which case it is safe to assume that the parallelization has occurred sufficiently fast that all electrons of the same initial energy travel together, regardless of their direction of emission. In this case the conversion to energy can simply be given as

$$E = \frac{1}{2}m_e\left(\frac{l_f}{t}\right)^2 \tag{4.8}$$

rendering the analysis relatively easy, although there exists situations where this assumption may break down, such as when the magnetic field gradient is sufficiently large to render the motion non-adiabatic or too small to quickly parallelize the trajectories. The limit between adiabatic and non-adiabatic operation may be quantified using a quantity known as the adiabaticity parameter, defined by Kruit & Read [222] and generally denoted as χ_1, and is defined as

$$\chi_1 = \frac{2\pi m_e v}{eB_z^2}\left|\frac{\mathrm{d}B_z}{\mathrm{d}z}\right| \tag{4.9}$$

where z is the central axis of the flight tube. The ideal spectrometer is one where $\chi_1 \to 0$, though this is not realistically practical. The field may be assumed to be adiabatic when χ_1 is significantly smaller than 1. When $\chi_1 \ll 1$ is not satisfied but $\chi_1 \leq 1$ still holds, the electron bunch may move sideways, with the helical motion adopting a shifted orbital centre away from the original field line, which may alter the time-of-flight and disrupt the calibration, though likely not significantly. This causes an issue where position sensitive detection is used, though for a purely time-of-flight instrument it will only cause a slight delay in electron arrival time which may not be noticeable within the resolution of the detector.

At higher adiabaticities, however, more severe issues take hold. When $\chi_1 > 1$ the sideways shift is more significant, with the bunch jumping to orbit a different field line. The bunch also meets the new field line at an angle during transfer, which

may affect the orbital radius and thus the total path length, significantly increasing the flight time and giving an artificially low estimate of the bunch energy. It is also possible at very strongly non-adiabatic conditions for the electron bunch to lose integrity, resulting in a greater spread of arrival times reducing the energy resolution of the spectrometer.

This type of spectrometer has the advantages of being simple and has the capability to perform single shot measurements of the entire energy spectrum. It is also easy to adjust the geometry to optimise the detected spectrum. This allows for rapid and easy collection of data, and checks for repeatability by integrating over many shots. The disadvantages are that the detector suffers from an efficiency gradient, meaning that lower energy electrons may go undetected, and that a balance point must be found regarding the fields near the interaction region. A sharp field gradient is required to ensure high energy resolution, but in turn also increases χ_1. The balance point between maintaining a high energy resolution and a low adiabaticity parameter is therefore difficult to find.

4.2 Design and construction

4.2.1 Emission region and flight tube

In order to achieve good resolution in a magnetic bottle spectrometer two features are necessary. The electrons must travel for a long distance down a flight tube directed by a low but constant magnetic field, which must be the only field directing their flight requiring all other electric and magnetic fields including that of the earth to be shielded or actively countered. The longer the flight distance (and by extension time) that the electrons travel the more electrons of different energies will separate before reaching the detector, enhancing the energy resolution of the spectrometer. The second feature is an extremely strong static magnetic field in the region where the electrons are emitted, which captures and directs the electrons into the weak field of the flight tube. The field between the interaction region and flight tube must drop in a rapid but controlled fashion, with no local maxima or minima.

To ensure a strong field near the interaction region the field is generated by a Neodymium-Iron-Boron (NdFeB) ferromagnet, a mixture of materials that can generate extremely strong static magnetic fields. A pair of cylindrical magnets in sequence (20 mm OD x 10 mm deep, N42 strength) were used. Each of these magnets has an on-face axial field strength of approximately 0.5 T as measured by an axial hall probe. These are capped by a 45° conical pole-piece manufactured from Vim-Var core iron, which is highly paramagnetic with a relative permeability

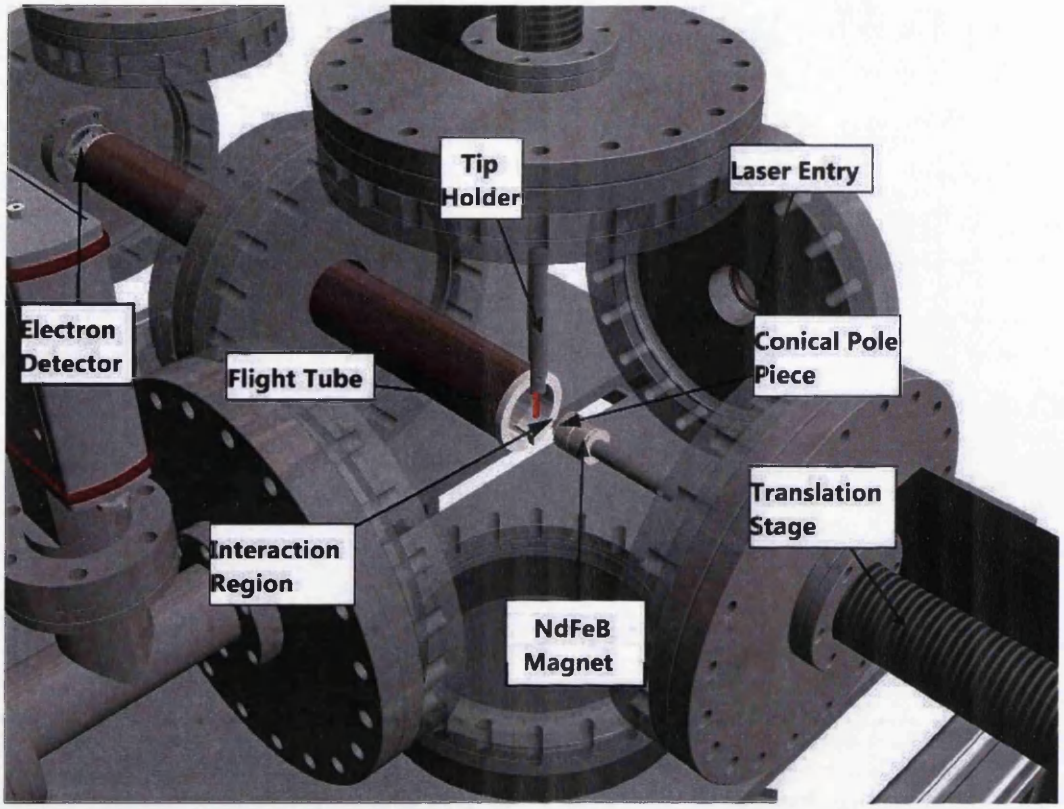

Figure 4.2: Illustration of the design of the interaction region of the magnetic bottle electron energy spectrometer. The red mark highlights the position of the nanotip.

on the order of $\sim 10^5\mu$. This focuses the field at the end of the pole piece, creating a feasible interaction region within approximately 1mm of the tip of the cone. The magnets are mounted on a 3-axis translation stage to allow full control over both the position of the interaction region and the strength of the magnetic field.

The flight tube is formed by a 316LN stainless steel pipe of length 464 mm, which includes a friction-fit cap that slots into the end nearest the interaction region. The tube has an outer diameter of 42 mm and a wall thickness of 2 mm to maintain rigidity. The edge of the end-cap typically sits within 15 mm of the tip of the conical pole-piece. A further 5 mm along the flight tube sits the inner edge of the end-cap, which provides a buffer to keep wiring in place. A solenoid begins at this point and runs 420 mm down the flight tube. The solenoid is only one layer deep with windings tightly packed, consisting of kapton insulated wire (0.76 mm OD, 0.5 mm core) rated to up to 4 A at 2 kV dc.

At the far end of the flight tube sits a channel electron multiplier (CEM, Burle 4830G Channeltron) to record the arrival of the electrons with nanosecond temporal sensitivity. The CEM operates on a similar principle to an MCP, but having only a single channel no spatial resolution is provided. With a high bias voltage, however,

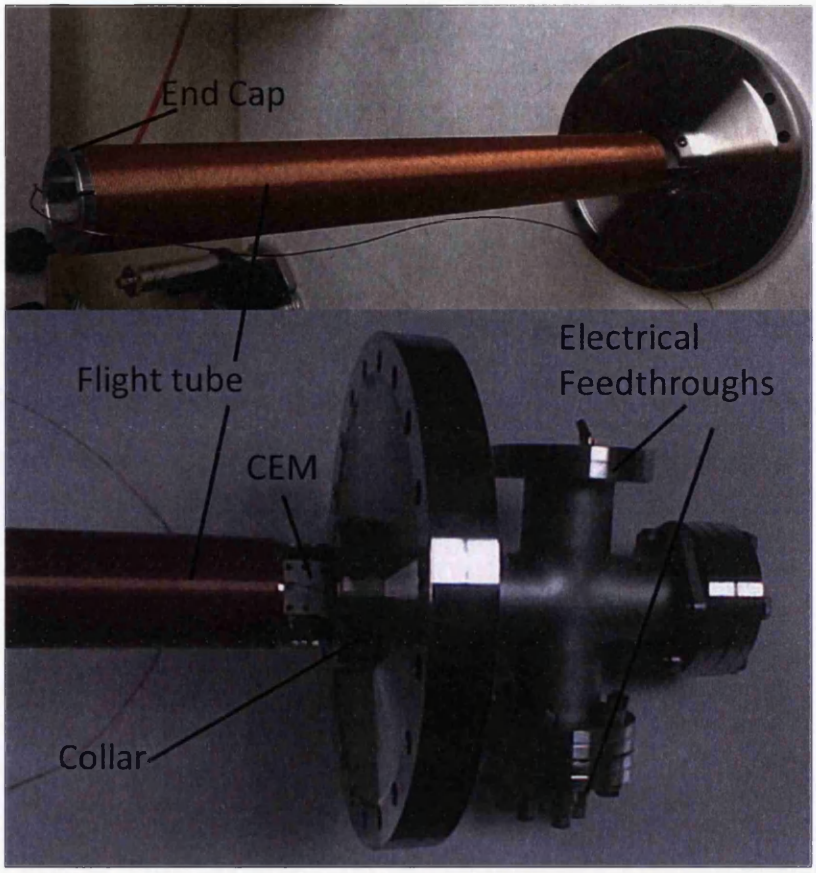

Figure 4.3: Photograph showing the flight tube and detector assembly for use in the magnetic bottle electron energy spectrometer.

it is possible to achieve extremely high gain using a CEM, and as spatial resolution is not required in a magnetic bottle spectrometer this is a suitable compromise. The CEM is 91 mm long with the back in line with the rear end of the flight tube, and so the front end of the CEM sits 373 mm from the entrance of the end-cap. This results in the solenoid carrying on past the point where the electrons enter the detector by nearly 50 mm, ensuring that no unwanted effects are produced by the non-parallel magnetic field at the rear end of the solenoid.

The entire tube is held in place by a collar at the detector end which is screwed to inside of the vacuum flange, as shown in figure 4.3. Radial screws in the collar are used to secure the tube itself. In front of the collar but behind the end of the solenoid is a 20 mm long 180 degree slot to allow pumping of the flight tube at both ends. A pair of small holes through the tube wall near the slot allow the solenoid wire to be secured, the other end of the wire being secured to the end-cap. The outer edge of the collar is kept smooth with the radial screw heads recessed, this allows a mu-metal magnetic shield to be friction fitted around the outside. For the experiments presented here this shielding was not present, as external manufacturing had not

been completed and proceeding with the experiment was forced by time constraints due to the use of the loan-pool laser system. The vacuum flange supporting the detector is a DN160CF to DN40CF adapter, with the port sitting directly behind the CEM. This allows a DN40CF cross to be attached containing the electrical feedthroughs which provide power to both the detector and the solenoid, as well as readouts of electron count.

4.2.2 Vacuum chamber design

The spectrometer was designed to be operated under ultra-high vacuum (UHV) conditions with pressures on the order of 10^{-9} mbar, in order to ensure that electrons would be able to travel the full length of the flight tube without significant interaction with background gas, which would not only reduce the overall signal but also cause the recording of flight time to be misleading. It is vital that the pressure is sufficiently low that the mean free path of the electrons is significantly longer than the distance from the interaction region to the detector. It must also be considered that the CEM requires UHV conditions in order to correctly function. Lower pressure is desirable, high gain is necessary to obtain clear signal when emitting a small number of electrons but also makes background noise more noticeable. This can be partially countered by keeping the ambient pressure as low as possible to reduce chance encounters between molecules of background gas and the detector and avoid ionising unwanted additional material present at the laser focus.

In order to achieve this low pressure a double-chamber configuration with a central baffle and differential pumping was employed, as shown in figure 4.4. A DN160CF 6-way cross (interaction area) was joined to a DN160CF to DN100CF 4-way reducer cross (detector area), with the joint formed by a central DN160CF double-sided blank flange with only two small holes, one central hole to allow the flight tube to pass through and another to enable easy wiring. This arrangement allows the chamber pressure in the two crosses to be nearly independent of each other, allowing low pressure to be maintained around the detector even when injecting gases into the interaction region. It does not, however, allow for independent venting of the two crosses. The top of each cross is occupied by a dual Pirani/Bayard-Alpert pressure gauge (Pfieffer HPT 100) read by a digital controller (Pfieffer DPG 109) for independent monitoring.

Pumping is performed through the bottoms of the two crosses by a pair of DN160CF turbo-molecular pumps (Pfieffer TMU 521 P) at 50000 rpm. These are backed by a pair of diaphragm pumps, which rough pump the chamber to a pressure of 2 mbar before the turbo-pumps are activated. The chamber typically reaches

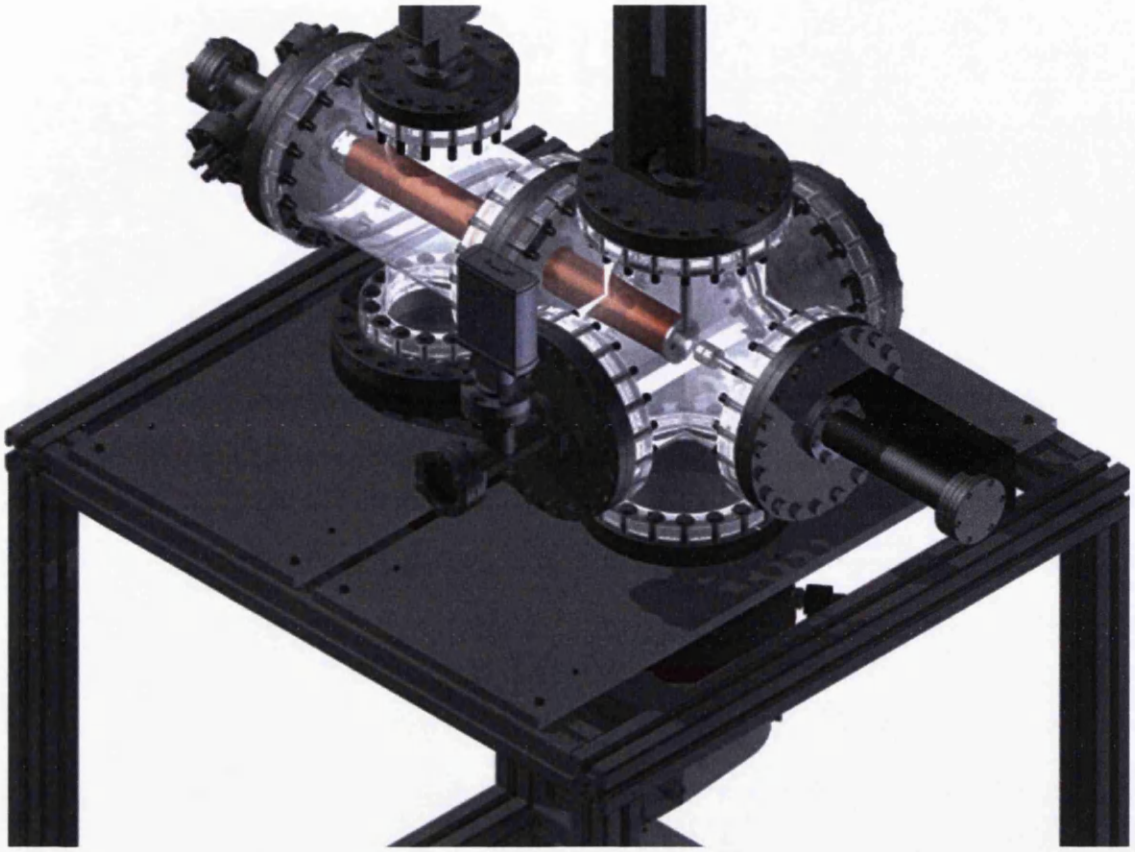

Figure 4.4: Illustration of the design of design of the entire vacuum chamber and frame housing the magnetic bottle electron energy spectrometer. The main crosses have been made transparent to show the internal components.

a pressure of $1x10^{-5}$ mbar in each side before the pumps have reached maximum speed, and then slowly drops towards base pressure over several days. Typically the chamber reaches a usable pressure of $1x10^{-8}$ mbar within 48 hours.

The sides of the 6-way cross consist of DN160CF to DN40CF adapters, to which fused silica windows are mounted to allow access for laser light. The exit window is mounted extended on a DN40CF T-piece, with the spare port being occupied by a pressure gauge (Pfieffer HPT100). The top port of the cross is again occupied by a DN160CF to DN40CF adapter which supports the target assembly, while the magnet assembly is supported via a translation stage mounted on an identical adapter on the port directly opposite the join between the two crosses. The top port of the 4-way cross features a DN100CF to DN40CF adapter with a second pressure gauge, with the remaining port opposite the join between crosses housing the solenoid and detector assembly.

The entire chamber is mounted on an extruded aluminium frame located beside the optical table. Secured to the top of this frame are aluminium plates featuring

apertures which close about the necks of the turbo-pumps to support the weight, as well as acting as extensions of the optical table for mounting lenses and steering mirrors close to the chamber windows. Locking rubber feet ensure stability and help to isolate the chamber from vibrations in the floor, most noticeably arising from the diaphragm backing pumps located beneath the chamber.

4.2.3 Final construction

In order to achieve the goal of UHV operation at a base pressure of 10^{-9} mbar, all components were cleaned with ethanol before being attached to the chamber. Smaller components such as screws and electrical connectors were also submerged in an ultrasound bath filled with methanol. All screws to be used in blind holes, such as those used to fix the collar at the base of the flight tube to the mounting flange were also filed flat on one side and cut washers used to remove any trapped volumes of air.

The frame, support plates and main chamber were assembled first, such that the pair of crosses, the baffle flange and the turbo-pumps were in place without the detector, flight tube, magnet or tip assembly attached. These were separately constructed around their respective adapter flanges outside of the vacuum before then being secured to the main chamber with all smaller components already in place.

The detector assembly was constructed as one unit outside the chamber. The CEM was connected to the MHV feedthroughs on the back cross via Kapton coated wire (0.76 mm OD, 0.5 mm core, 2kV dc rated) and attached with CuBe push-fit connectors. The other end of the wires were secured to the connection rods on the CEM by CuBe barrel connectors. The CEM was then secured in place by resting the mounting tabs on the back against the adaptor flange, before the flight tube collar was laid on top of the tabs and screwed into place, clamping the CEM in position. The solenoid was manually wound onto the flight tube outside of the chamber before the tube was inserted into the collar. It was then was secured by winding one end of the wire through the pair of holes in the friction-fit cap and the other end through the notches adjacent to the pumping slot in the rear of the tube. The entire detector assembly was then mounted on the chamber via the adaptor flange, with the front end of the flight tube sliding through the hole in the baffle flange. The connection wire was then pushed back through the top hole in the baffle and fed through the slot in the flight tube. The solenoid wires and detector wires were then extracted through the ports of the rear DN40CF cross as it was attached, before being linked to the MHV feedthroughs which were then secured.

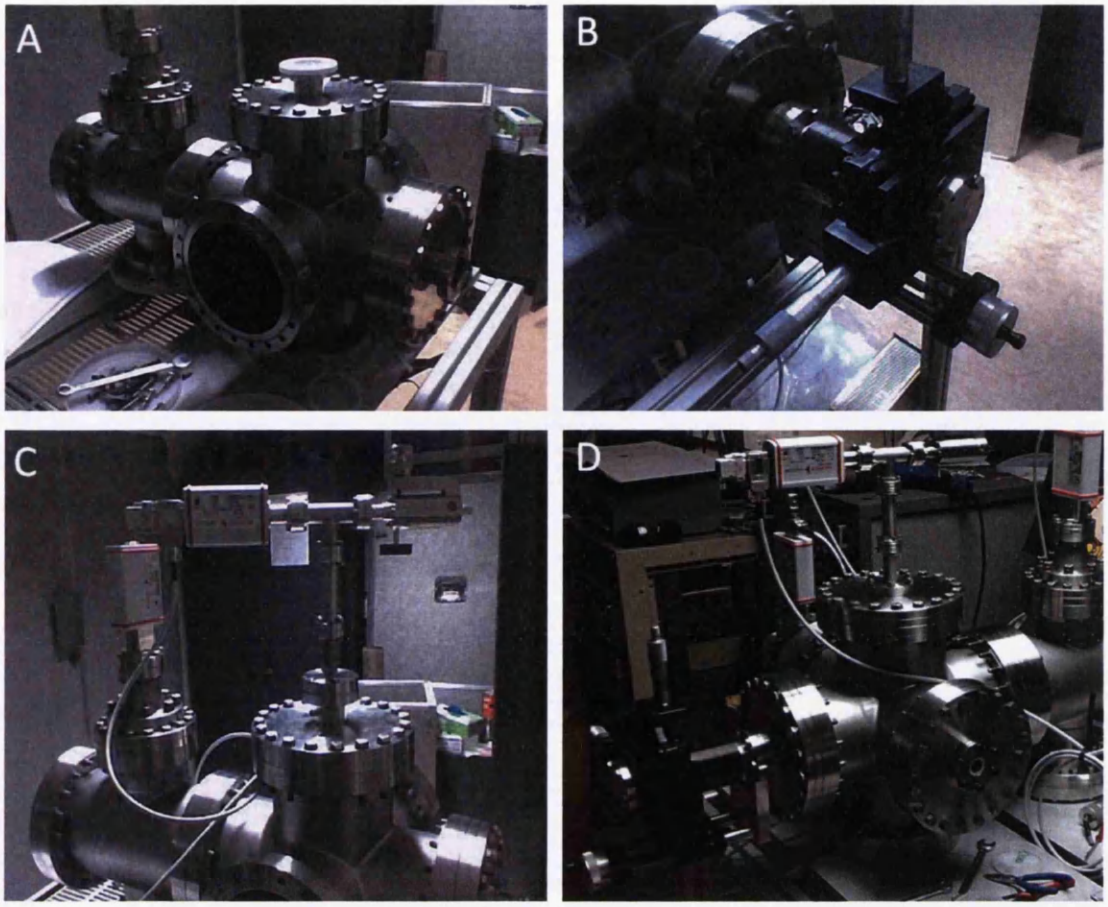

Figure 4.5: Photographs showing the stages of construction and outer components of the magnetic bottle electron energy spectrometer. (A) Construction of the frame and main chambers. (B) Attachment of the magnet assembly, manipulated using the 3-axis stage shown. (C) Attachment of the target assembly, in this case a gas line. The alternative nanotip assembly uses a similar 3-axis stage to that in (B). (D) The apparatus is fully assembled and pumping.

The magnet assembly was constructed by first bolting the support rod to the translation stage, then screwing the Vim-Var attachment piece to the end of the rod. The NdFeB magnets were brought into contact with the piece where they are both held and naturally centred by their own magnetic field. The pole piece was then attached by the same principle and the entire assembly attached to the adaptor flange, which was in turn bolted to the chamber. The target assembly consisted of a choice between a gas line and the nanotip holder. Both of these were assembled separately from the chamber such that they could be inserted as a unit and swapped with relative ease. The gas line was fixed, while the tip assembly featured a 3-axis translation stage similar to the one mounting the magnet assembly to allow the tip to be positioned at will.

4.3 Experiments and results

4.3.1 Emission from krypton for calibration

The spectrometer was pumped to an ambient pressure of 10^{-9} mbar with the gas line attached in order to inject krypton for testing and calibration purposes. This was done because it is possible to induce Above Threshold Ionization (ATI) in noble gases which produces electrons of several known energies spaced by the photon energy, allowing easy calibration of time-of-flight to energy. This technique is discussed further in chapter 5.

A sample time-of-flight spectrum from the krypton gas is shown in figure 4.6, and all spectra obtained followed this format. The early signal before 2.5×10^{-7} s is not part of the spectrum and is instead noise induced by the firing of the laser, likely arising from the high voltage trigger signal. After this time three distinct peaks followed by a relatively slow decay constitute the signal from the krypton calibration gas.

It is immediately obvious at this stage that the spectrometer was not behaving as expected. There are two significant issues, the first of which is the long decaying tail of signal which is not anticipated and suggests either a very slow decay time within the detector or an inability of the spectrometer to separate electrons at the lower energy scale. The second issue is a major indicator that the spectrometer is not working correctly: The three main peaks, if arising from ATI, should be evenly spaced in energy. As energy is directly related to the inverse square of the time-of-flight (by equation 4.8), one would not expect these peaks to be evenly separated in time, and yet this is exactly how they appear to be.

It quickly became apparent that the spectrometer could not be calibrated in this fashion and instead the approximation of equation 4.8 would be required, where the energy is assumed from approximating the velocity as the length of the drift tube divided by the flight time. Due to time limitations imposed by the use of the Coherent Libra form the EPSRC Laser Loan Pool, the decision was taken to proceed with experiments examining emission from a tungsten tip and use the approximated calibration as making the spectrometer work correctly would likely have taken sufficient time as to stretch beyond the deadline of the loan. The gas line assembly was therefore removed and the tip target assembly inserted.

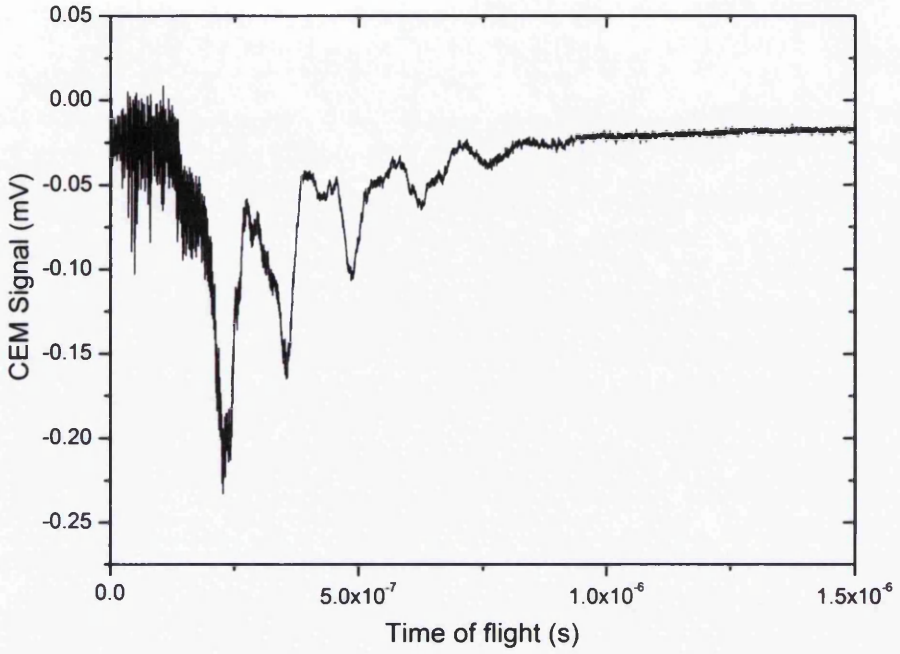

Figure 4.6: Sample time-of-flight spectrum from krypton in the magnetic bottle electron energy spectrometer. The dense signal at low time is shot noise from the firing of the laser. a series of distinct peaks are observed following a slow decay, this signal arises form the krypton, but the peak spacing being constant is not consistent with an ATI pattern, where the spacing should be constant in energy but not flight time.

4.3.2 Variation of applied bias voltage

The field enhancement around the end of a nanotip is convenient as it focuses the electric field delivered by the laser pulse to a high localised intensity, allowing the strong field emission process to occur even at relatively low incident laser powers. This effect, however, also applies to static fields. In practical situations where the tip would form part of an electron gun assembly it may be necessary to apply a bias voltage to the tip in order to produce the desired acceleration. The electric field around the tip generated by this bias voltage will also be subject to the field enhancement effect, as such photo-emitted electrons will be generated by a strong field which includes a time-dependent component from the laser and a static component from the tip. This static component is far from negligible, as the enhancement effect can generate fields of unexpected strength (enhancements of a factor of 12 are possible for tungsten, see chapter 2) which may account for a significant percentage (10% or more) of the total combined field present at the very end of the tip.

In a traditional flat photocathode enhancement does not occur (or is, at least, extremely limited depending on the surroundings), and as such it is expected that changing the bias voltage will alter both the acceleration and the final energy of

the electrons by a known value, preserving the energy spectrum which is exclusively defined by the laser pulse bandwidth and the properties of the material surface itself. With a nanotip, however, the enhancement of the bias voltage may create effects which are non-trivial to predict. In addition to the change in electron acceleration and beam energy, it is possible that the photoelectron yield may increase with the magnitude of the bias voltage. It is also unknown as to whether the enhancement from the bias voltage is capable of altering the energy distribution or bandwidth of the emitted electrons.

In an attempt to quantify the effects of the field enhancement at the apex of a nanotip an experiment was conducted where laser induced photo-emission was triggered from the tip with a variable bias voltage applied via the highly stable supply built into a Keithley electrometer (model 6517). Time-of-flight spectra were recorded for bias voltages ranging from +20 to -50 Volts, at intervals of a single volt. The bias voltage was the only parameter changed, with the positions of the tip, magnet and lens being held constant once suitable emission conditions were achieved. The Laser pulses were supplied by the Coherent Libra with polarisation aligned with the tip axis. Typical pulse parameters were 800 nm central wavelength with FWHM approximately 17 nm, a pulse length of approximately 120 fs, and an intensity at the centre of the focus on the order of 10^{12} Wcm^{-2}. The key results are presented in figure 4.7, with the electron yield presented in figure 4.8

One intriguing feature which unfortunately suggests that these results may be invalid is that even at a bias voltage of -50 eV the electron energy only extends up to 30 eV, seemingly violating the principle behind the acceleration away from the tip by Coulomb repulsion. This may be a function of the flight path of the electrons in our spectrometer, while the parallelization of trajectories is rapid it can still cause the flight path of the electrons to be longer than if they propagated straight down the flight tube. It is perhaps possible that the high energy electrons initially spiral with a very large radius and so their time-of-flight is increased dramatically, causing them to appear on a time-of-flight trace with unrealistically low energy. It is also possible that the magnetic field does not decrease sufficiently quickly to allow the time-of-flight calibration approximation in equation 4.8 to hold. It must therefore be concluded that the energy calibration is not correct, and that the results are somewhat untrustworthy.

It is curious that the spectra in figure 4.7 appears to show two distinct populations. At low bias voltages (0 to -10 V) there is a faint but possible band structure, suggesting multiphoton emission, up to a cutoff point in the general region of 12 - 15 eV, at least according to the apparent but likely incorrect energy calibration.

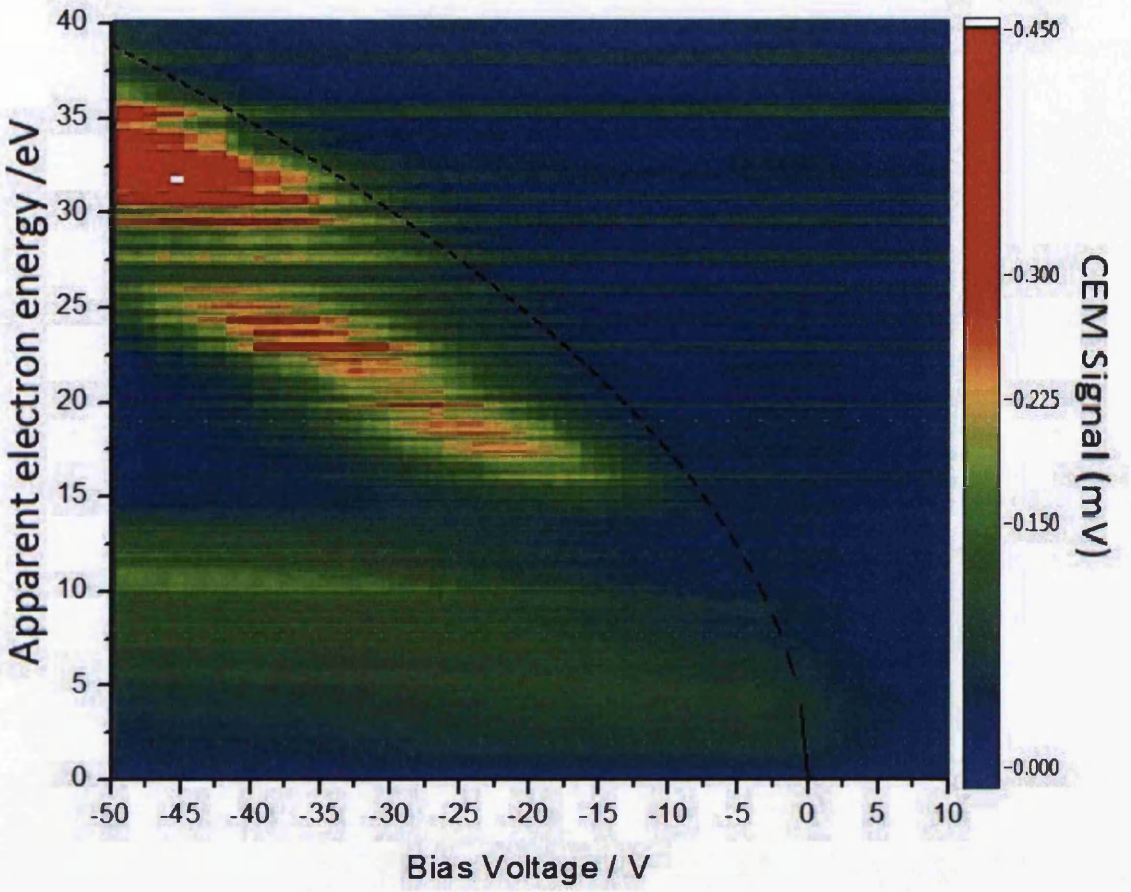

Figure 4.7: An example of measurements of the electron energy spectrum from a nanotip as a function of applied bias voltage. The dashed line demonstrates the $\sqrt{E}$ nature of the envelope, possibly indicating that the Schottky effect is occurring.

Above this region there exists a spread of electron energies that exhibits no real band structure. If the results were not so inconclusive and the confidence in the calibration so low, it might be suggested that these electrons are liberated through tunnelling, where the bias voltage is sufficiently high as to reshape the barrier (as discussed in chapter 2) such that the tunnelling probability becomes non-negligible. They therefore enter the vacuum from the Fermi level and are subjected to the potential gradient caused by the voltage of the tip behind them. It is also possible that this regime is caused by plasma forming on the tip surface as the result of the enhanced field, or by recollision effects, or a combination of said processes. The apparent existence of a $\sqrt{E}$ dependency may indicate the Schottky effect becoming applicable.

At positive bias voltages the electron yield on the detector was extremely low as to be expected (figure 4.8), with the electric field likely pulling emitted electrons back towards the tip and therefore into the hemisphere which is not captured by the

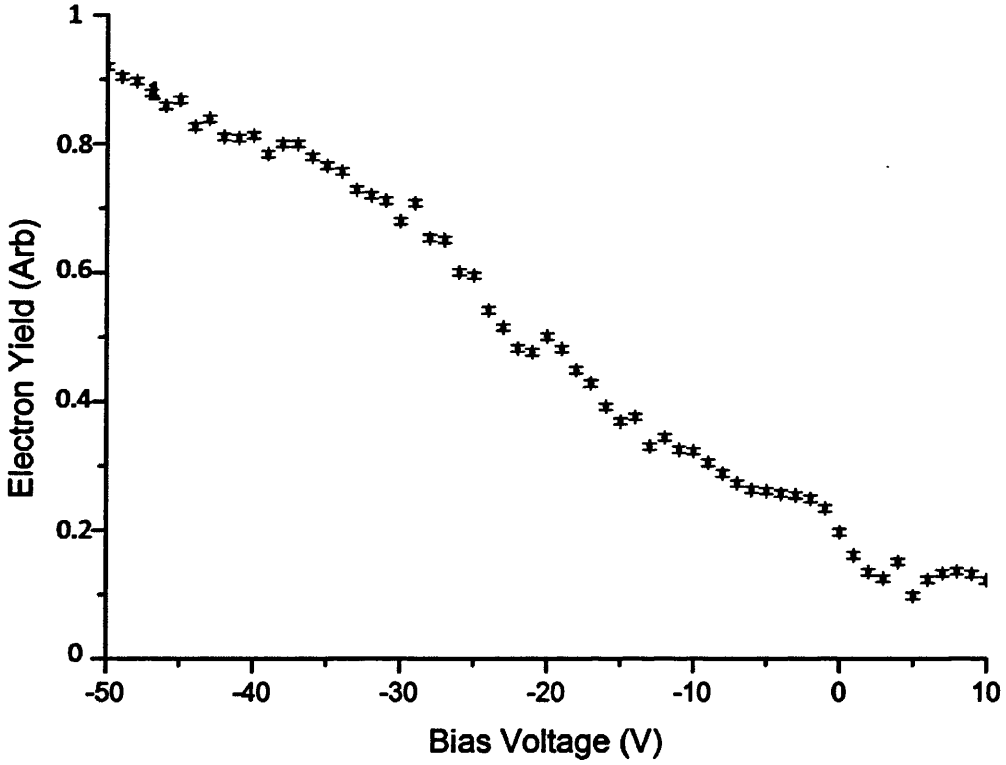

Figure 4.8: Effect of changing bias voltage on electron yield. The effect seems predominantly linear with the exception of certain local variations which are to be examined in more detail to determine if they are real or experimental anomalies.

spectrometer. The yield follows what appears to be a vaguely linear relationship with bias voltage, however there are too many hints at a structured relationship to warrant applying a linear fit, and insufficient data to resolve the nature of this structure, or indeed whether this structure is a real electronic effect or is arising from vibration or movement of the laser beam.

4.3.3 Variation of laser polarisation

An experiment was performed to quantify the effect of the polarisation direction of the incident laser light on photoelectron emission. This was done to examine the principle that the field enhancement is greatest when the polarisation vector is directed along the tip axis. It is anticipated that this leads to a greater occurrence of strong-field emission, creating a high flux with a well defined energy spectrum. Alternatively, a laser polarisation perpendicular to the tip axis will lead to a much less substantial field enhancement. In this situation it is likely that both a lower overall flux will be produced and that the energy distribution will be poorly defined due to thermionic emission.

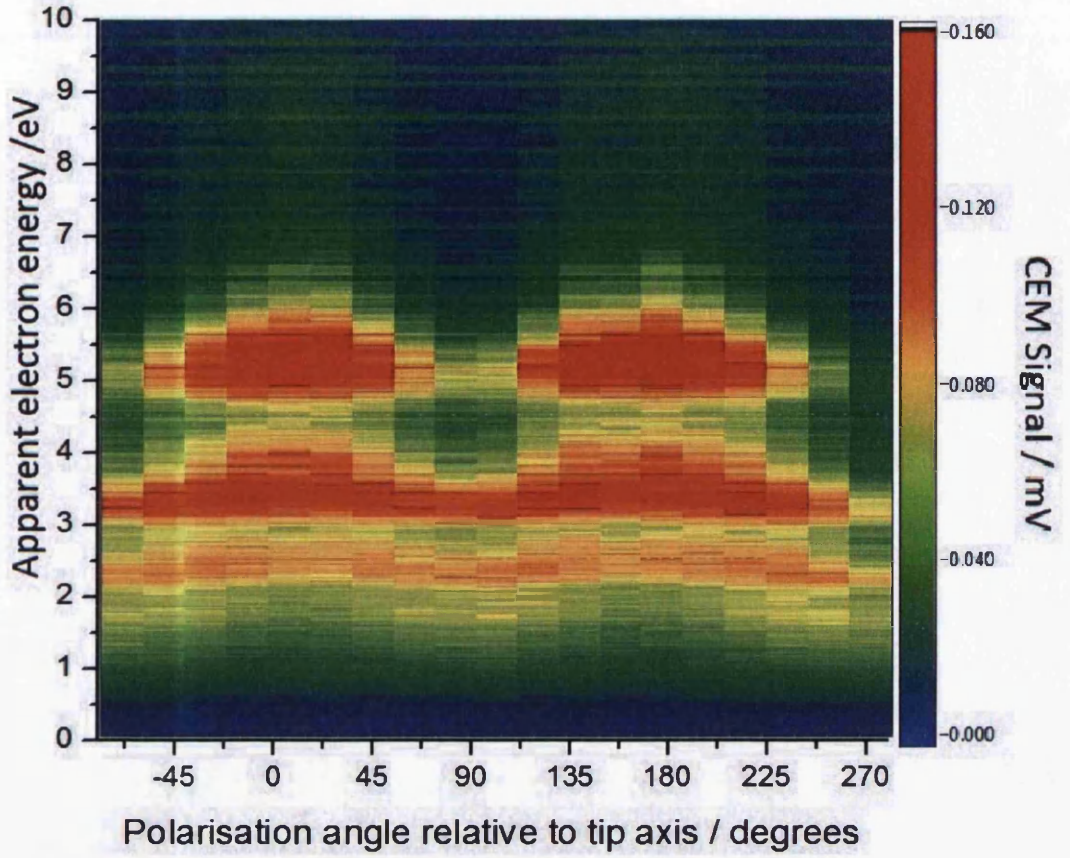

Figure 4.9: An example of measurements of the electron energy spectrum from a nanotip as a function of incident light polarisation. As expected the strongest emission occurs when the polarisation is aligned with the tip axis. A band structure is observed suggesting multi-photon emission, although it appears out of the ordinary that the largest population seems to exist in the higher energy band, a curious result which does not agree with the results obtained by velocity map imaging in chapter 5, in which the lower bands do not appear.

An 800 nm $\lambda/2$ plate (zero-order) was used to rotate the laser polarisation in systematic steps of 20 degrees over one full 360 degree range. Figure 4.9 shows an example of an electron energy spectrum obtained by this method. The spectrum shows clearly that the most intense and most energetic emission occurs when the polarisation is aligned with the tip, as is expected. The concerning result here is the structure of the "bands" in the electron energy, which alter their energy value depending on polarisation. This may be the result of a Stark shift caused by the differing nature of the field enhancement for different polarisations, however their presence contrasts with both the literature and the results obtained by velocity map imaging in chapter 5, which are considered to be significantly more trustworthy.

Furthermore the total electron yield emitted from the tip, as measured via the charge-sensetive pre-amplifier, changes sinusoidally with polarisation as shown in

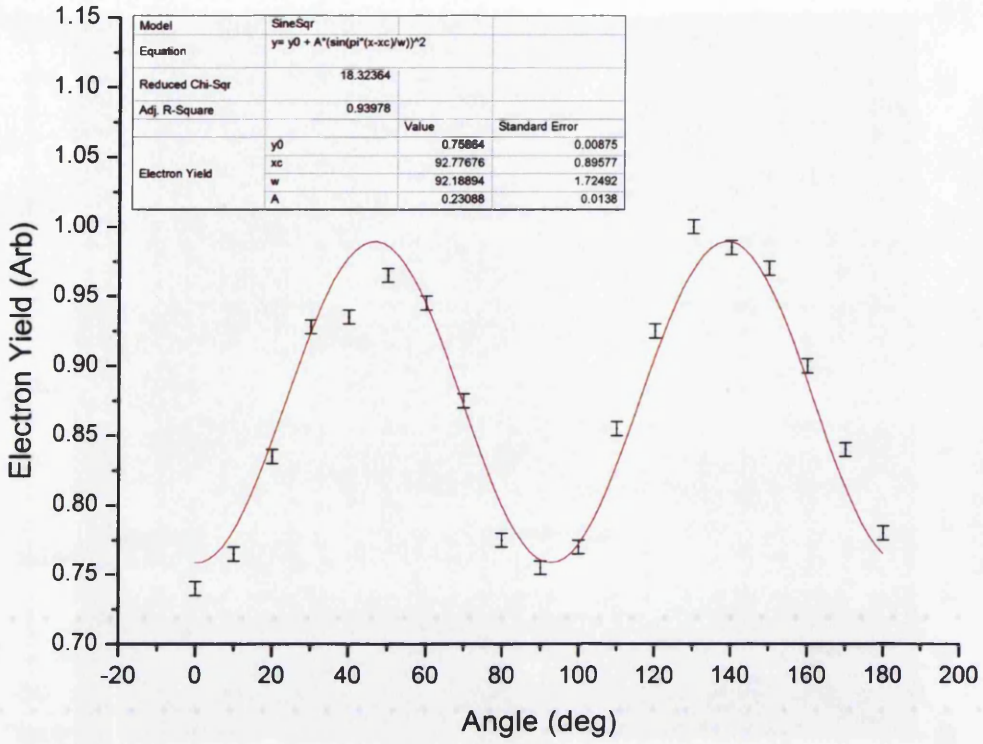

Figure 4.10: Total electron yield from a tungsten nanotip as a function of incident light polarisation. As expected the highest yield is obtained when the polarisation is aligned with the tip axis. The emission does not, however, drop to zero when the polarisation is aligned perpendicular to the tip axis. This suggests that a large number of electrons are still being emitted. It is possible that a significant number of thermionic electrons are being produced.

figure 4.10. This again shows that the emission rate is highest when the laser polarisation is aligned with the tip as expected, and confirms the signal intensity pattern recorded at the detector. It is curious, however, that the signal drop is not as significant as expected when the polarisation is aligned away from the tip axis (it should be noted that the scale of figure 4.10 is linear, and normalised to the most intense signal measured when the polarisation is aligned with the tip). It is expected that the emission intensity should drop to near zero when the polarisation is aligned perpendicular to the tip axis, however the observed emission only drops to 75% of the peak value, suggesting that a substantial number of electrons are still being emitted regardless of the polarisation of the incident light. Whilst the source of these is unconfirmed, it is likely that the optical power applied to the tip is too high and that most of the emitted electrons are thermionic in nature.

It has previously been demonstrated that polarisation can be used to control the emission characteristics of nanotips by Yanagisawa *et al* [229, 230]. Unfortunately the results obtained here again do not match entirely the expected pattern.

It is expected that, as shown in both figure 4.9 and figure 4.10, the highest electron yield will occur with the polarisation vector along the tip axis, due to the increased plasmonic response of the nanotip when this condition is met. It is not, however, anticipated that the energy spectrum would appear to shift as the polarisation changes. This may be an indicator of sub-par performance in the spectrometer, particularly where parallellizing trajectories is concerned. The apparently lower energy when electrons are emitted perpendicular to the tip axis may be due to their trajectories being changed relatively slowly, leading to a longer flight path and so apparently lower energy.

4.4 Conclusions and outlook

Whilst some useful information has been obtained in this experiment, in particular relating to how the tip responds to light of different polarisations, it must ultimately be considered a failure. This is due to the disagreement between the results obtained here and those in the literature, in particular relating to the observed band structure, and the fact that the energy calibration approximation is clearly wrong due to the unphysical result of measuring an electron energy below the bias voltage applied to the tip.

There are two major complications regarding the energy spread in the presented spectra. The first issue is the energy resolution of the spectrometer, which is currently significantly below optimal. At present the magnetic field strength along the flight tube decreases relatively slowly in comparison to the original spectrometer design of Kruit & Read. This in turn causes the trajectories of the electron bunches to parallelise slowly, resulting in bunches of electrons with the same energy but a wide spread of flight times caused by the initial angular spread. Following the experiment the magnetic field was measured with an axial hall probe as a function of distance, with the results shown in figure 4.11. This field drops to 1/10 of its original value at 35.6 mm from the magnet end and 1/100 of its original value at 170 mm from the magnet end. By contrast, Kruit & Read's spectrometer had a field which dropped to 1/10 of its original value at 5 mm from the point of strongest field and 1/100 of its value at 13.5 mm from the point of strongest field. It is likely therefore that the spectrometer was far too slow parallellizing electron trajectories to be effective, as all approximations require that this process be rapid.

The second issue is that of space-charge effects. In this experiment large numbers of electrons have been simultaneously liberated from a very small volume, and forced to travel in close proximity. These electrons will strongly repel each other,

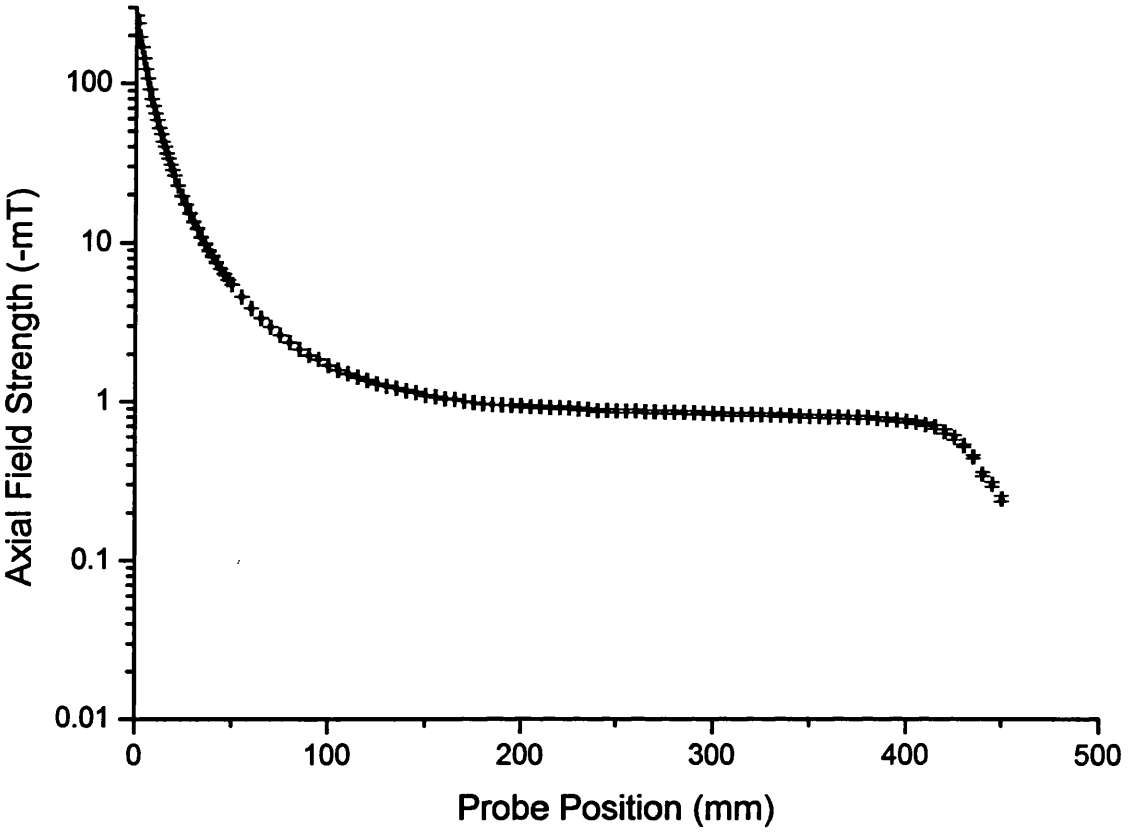

Figure 4.11: Measured magnetic field profile of the magnetic bottle electron energy spectrometer. Zero is defined to be at the tip of the magnet.

with electrons at the front of the bunch being pushed along the flight tube to a shorter flight time, and electrons at the rear of the bunch being slowed down by the repulsion of the preceding electrons, leading to longer flight times. This will give the impression of a bunch of electrons containing a much larger energy spread than it actually does. This effect is demonstrated in recent work by Passlack and colleagues [170], who examined photoemission from a surface under femtosecond laser pulses produced by an oscillator and a regenerative amplifier. They found that despite the amplifier producing shorter pulses than the oscillator, the measured time-of-flight spectrum from the amplifier appeared significantly broader than that from the oscillator, with the broadening following a $\sqrt{N}$ dependence, where N is the number of electrons in the pulse. They confirmed the cause to be space-charge by also observing a change in the angular distribution of the electron pulse. The issue of space-charge was originally treated theoretically by Siwick and colleagues [212], who investigated theoretically the propagation of femtosecond electron pulses using an N-body numerical simulation. They found that such pulses are highly susceptible to space-charge broadening of both the pulse length and the kinetic energy bandwidth.

The simulated pulses were lengthened to several times their original length and the kinetic energy bandwidth was increased by eV within nanoseconds. As our flight tube is sufficiently long to generate flight times of 10^7 s, and our pulses are generated from a very small volume, it is certain that our pulses are susceptible to these effects and that our time-of-flight spectrum is dramatically stretched. In a magnetic bottle spectrometer this effect could be countered by using smaller population pulses produced by an oscillator. For other applications it could be countered by a shorter flight path, and accelerating voltage or a means of compression by reversing the velocity chirp of the pulse such as an RF cavity)

In addition the efficiency of the detector is far from 100% and may in itself be somewhat energy dependent, leading to a skew of apparently higher signal at high energies, when in fact the signal may be at or below the level of signal at lower energies. The entrance to the channeltron is significantly smaller than the diameter of the flight tube, hence even if electrons are not brought onto parallel paths rapidly it is possible for some to miss the detector. It is not possible from the evidence collected to determine if this is indeed the case.

There are three key possible improvements to the spectrometer to improve performance, besides the use of a higher repetition rate, lower energy laser system to reduce space-charge issues. The first is the addition of a magnetic shield which, as mentioned in section 4.2.1, was planned to be included but was delayed due to manufacturing issues requiring the experiment to be performed without shielding. The second improvement would be the addition of vibration isolation and beam stabilisation to ensure that the intensity applied to the tip remains constant over the course of a long[1] data collection run. The final possible improvement and the most important is the addition of a high magnetic permeability pole piece with a pinhole on the end of the flight tube. Whilst this may reduce the collection efficiency, it should control the magnetic field such that a sharp decrease in strength can be achieved through the pinhole. This could lead to dramatically increased trajectory parallelization speeds, hopefully increasing the energy resolution to the order of 10 meV.

[1]Data collectoin runs for this experiment were at least tens of seconds for trial runs where only a few data points were required, and on the order of an hour or more for systematic runs with few femtosecond resolution.

Chapter 5

Velocity map imaging of tungsten nanotips and inert gas

Photofragment imaging, where a laser pulse is focused onto a target to induce a sufficiently strong electric field to initiate ionization and fragmentation, is a powerful tool for examining the geometric and energetic characteristics of systems [231, 232]. The initial state of the system is imprinted on the fragment electrons and ions modulated by the interaction with the laser pulse. The imprinted information may then be retrieved by detecting the fragments by a variety of methods that use temporal and/or spatial resolution to infer energy and direction of emission. Velocity Map Imaging (VMI) is a powerful technique which allows the initial fragment distribution in both energy and initial velocity vector to be observed simultaneously. Combined knowledge of both of these distributions is necessary when determining suitable applications for photoelectrons, such as being directed through a lens assembly for microscopy or diffraction through a target to be imaged. It also allows for diagnosis of the suitability of a particular tip for these purposes, for example observing emission over a wide-angle distribution may be indicative of a blunt nanotip.

In this chapter the development of a VMI spectrometer and its application to a tungsten nanotip is discussed. Whilst this is not the first VMI apparatus to be designed to examine solids [233], to the authors knowledge it is the first to successfully do so by simultaneously obtaining calibration and focusing information from a noble gas.

5.1 Principle of velocity map imaging

VMI requires that the laser-target interaction take place in a region of high potential consisting of cylindrically symmetric electrostatic fields, which direct charged

fragments of a selected polarity towards a position sensitive detector, often a Micro-Channel Plate (MCP) and phosphor screen recorded with a CMOS or CCD camera.

The potential is shaped by electrodes to create an electrostatic lens along the path of the charged particle such that electrons or ions of a particular momentum arrive at the same point in the detector plane independent of the point of creation. The volume of emission for which this condition holds is dependent on the size of the VMI apparatus. It is straightforward to have this volume relatively large; a VMI apparatus with an electrode diameter of hundreds of millimetres will successfully momentum image over of the order of millimetres to tens of millimetres, much larger than the Rayleigh range of a typical laser focus.

Developed in 1997 by Eppink & Parker [234], the traditional design of a VMI spectrometer consists of the detector and 3 flat electrodes; a repeller and extractor either side of the interaction region and a focusing electrode between the extractor and detector. This simple configuration has been widely used with minimal variation until relatively recently, a number of variations on the standard design have been developed by various groups, using alterations such as shaped electrodes (generally conical or tapering to a plateau) or additional focusing electrodes [235]. Further designs have used gas injection integrated into one of the electrodes to increase the target density [236], allowing use with low photon flux systems such as XUV or attosecond pulses [237–241], as well as CEP stabilised pulses [242].

The three-dimensional distribution of charged particle momenta is projected onto a two-dimensional detector which can result in a variety of image types but in most gas phase experiments results in a series of flattened spheres, with energy defined by the radii and the circumferences filled according to the initial direction distribution. If the flattened sphere distribution is maintained with cylindrical symmetry then an Abel inversion or iterative reconstruction may be used to convert the distribution into a 3-dimensional map of the initial momentum distribution [243].

VMI is particularly effective at obtaining information revealed by strong-field ultrafast laser dynamics, whereby a laser pulse is focused down to a beam waist on the order of microns, causing nonlinear processes such as tunnel ionization, recollision excitation and ionization, formation of rotational and vibrational wavepackets and molecular fragmentation. Furthermore, the dynamics of electronic wavepackets can be directly driven by manipulating the carrier-envelope phase (CEP) of the laser pulse if it is of a few optical cycles in duration [244, 245]. The laser spot size and Rayleigh length is often much smaller than the collection region of a VMI instrument, and if the laser pulse duration is picoseconds to few femtoseconds, dynamics relevant to gas-phase atomic and molecular systems become observable [240].

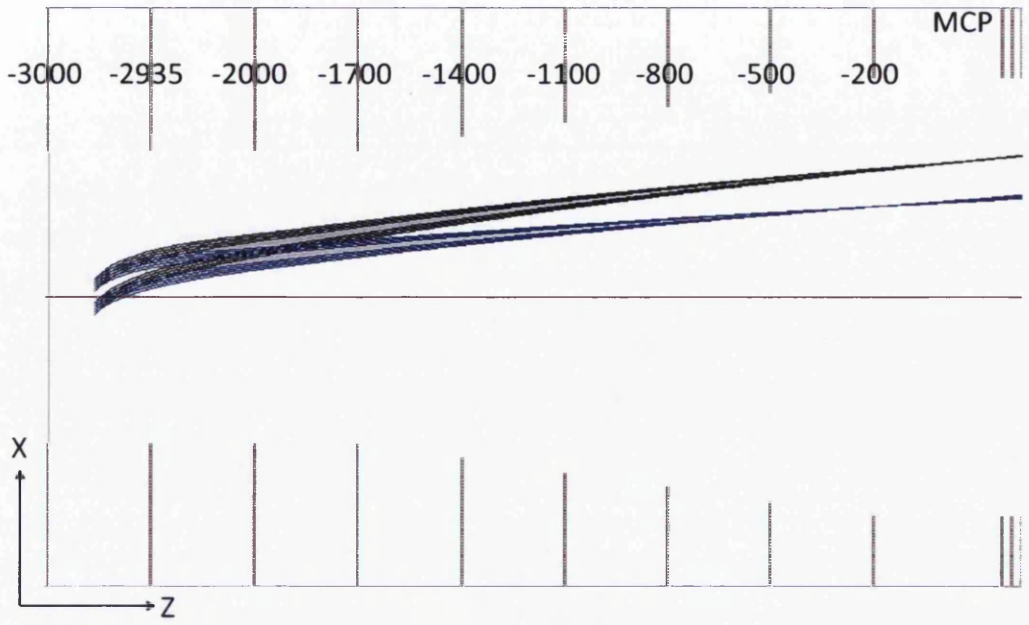

Figure 5.1: SimION simulation demonstrating velocity focusing through a stack of electrodes. Electrons of 25 eV (blue) and 40 eV (black) were emitted in a line distribution with momentum vector (x=1, z=1). The focusing voltages are optimised for 40 eV, hence the 25 eV electrons are slightly diverging at the detector. In this example the electrode aperture is 80 mm at the detector and 50 mm at the interaction region. This example differs from the final design presented in section 5.2 in that it has 9 electrodes at a spacing of 20 mm.

The primary disadvantage of VMI is the requirement for carefully balanced and rotationally symmetric electric fields, which are difficult to maintain if placing a conductive solid into a region of high potential. This has to date prevented the use of VMI as a tool for analysing photoelectrons from solids, as emission must take place from a non-floating conductor to allow replenishment of the emitted electrons and prevent the sample from charging. This has to date limited the applicability of the technique to gaseous targets, although recently experiments exploring aerosol [246] and nanoparticle [247] samples have been successfully conducted. This work outlines the first successful application of this technique to a solid target with macroscopic components.

5.2 Design and construction

5.2.1 Electrode stack design

The spectrometer developed for this project follows from the work of Suzuki *et al* [235], who determined a relationship between the number of focusing electrodes and the maximum achievable resolution. The spectrometer therefore uses 8 electrodes instead of the traditional three separated by 22mm, as shown in figure 5.2, with the objective of achieving higher resolution through tighter velocity focusing. This has the additional advantage of allowing for a more open interaction region, as the aperture in the extraction electrode can be large given that subsequent electrodes can compensate with additional field control. The larger aperture assists in pumping and allows a large detector to be used to enhance resolution.

The nanotip is mounted on an insulating Poly-Ether Ether-Ketone (PEEK) arm placed between electrodes E1 and E2, with the remaining electrodes used to ensure correct focusing. The arm is mounted on a 3-axis translation stage to freely allow the sample to be positioned relative to the laser focus. The electrode aperture diameter is 50 mm at the interaction region, and increases to 75 mm towards the detector to accommodate the curved electron trajectories. Electrode E1 has a fine mesh applied across the aperture to manage the field flatness at the interaction region. All electrodes are flat Oxygen-Free High Conductivity (OFHC) copper with a thickness of 1 mm.

In order to evaluate the effectiveness of the VMI design prior to construction, finite element modelling of the electric field structure was performed using the model exported from Autodesk Inventor 2013 and imported into SimION 8.0.4, allowing real geometry and sizes to be used rather than relying on the typically rotationally symmetric approximations that are often used in such cases. With all insulating elements ignored and optimised potentials applied, SimION was used to calculate electron flight trajectories through the electrodes, and so allows any unwanted areas of localised field gradient to be quickly highlighted. Initial modelling of the VMI revealed the necessity of using insulating rods to support the electrodes; it is was apparent that using metal support rods would pull the electrons into arcing paths that disrupt the VMI conditions, despite the large distance of the rods from the central axis. The electrodes are therefore mounted on four rigid insulating PEEK rods, with spacing and location defined by a stack of male and female ceramic spacers. PEEK was used because of its relatively high stiffness, vacuum compatibility and electrical insulation properties.

In a further simulation, with the nanotip and contact wire removed from the

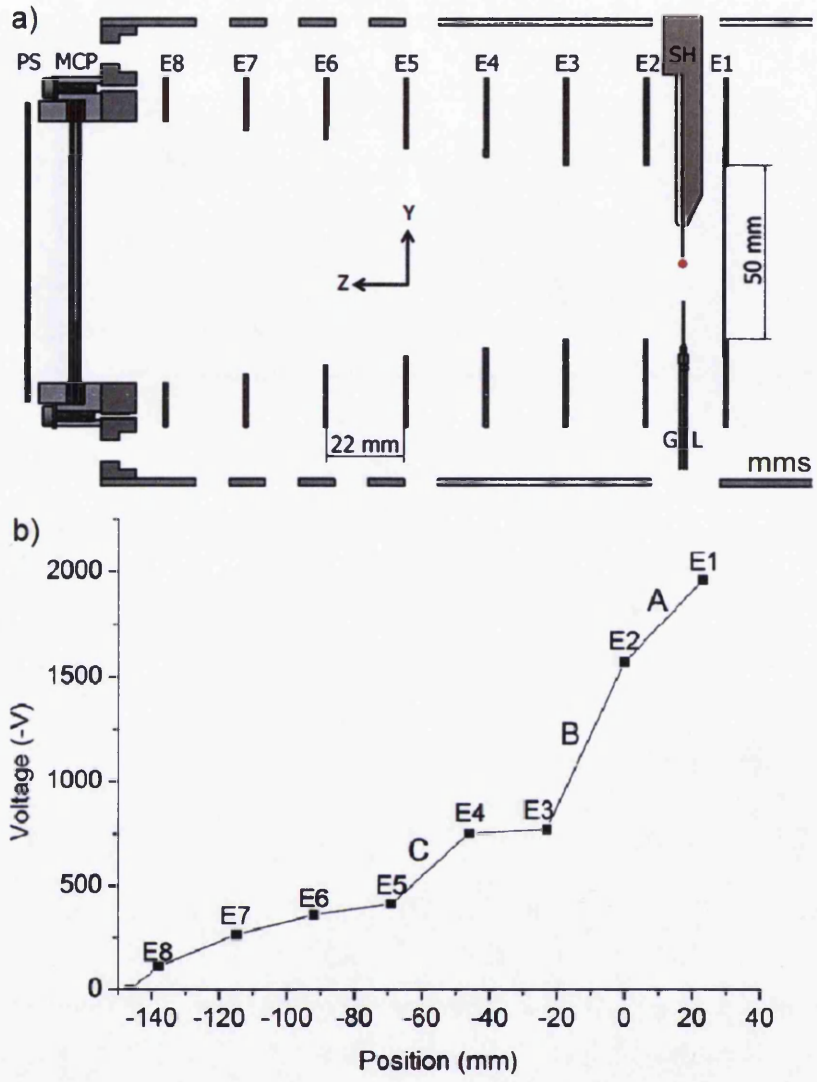

Figure 5.2: a) Slice view schematic of the VMI spectrometer. The interaction region lies between electrodes E1 and E2, with the laser propagating perpendicular to the image plane as denoted by the red dot. The sample holder (SH) holds the tip electrically isolated from the rest of the chamber on a 3-axis translation stage, and can be retracted for gas phase operation. A wire contained within the holder connects the tip to an external power supply. The gas line (GL) is held electrically floating and stationary. E3 retains a 50mm inner diameter and is used for focusing, whilst E4 through E8 have an expanding inner diameter in 5mm steps to 75mm and are used to further refine the focusing and enhance resolution. The entire stack is enclosed in a grounded mu-metal shield (MMS) with pumping holes. b) Typical electric potential of the VMI as a function of position. The zero point coincides with E2, the dots coincide with the electrode positions. Region A is the extraction area, where the sample must be kept at a potential that sits close to the line in order to avoid field disruption. Region B is the focusing region of a traditional VMI and reprises the same role in this adaptation. The remaining electrodes provide further focusing, with region C being a second major lensing area.

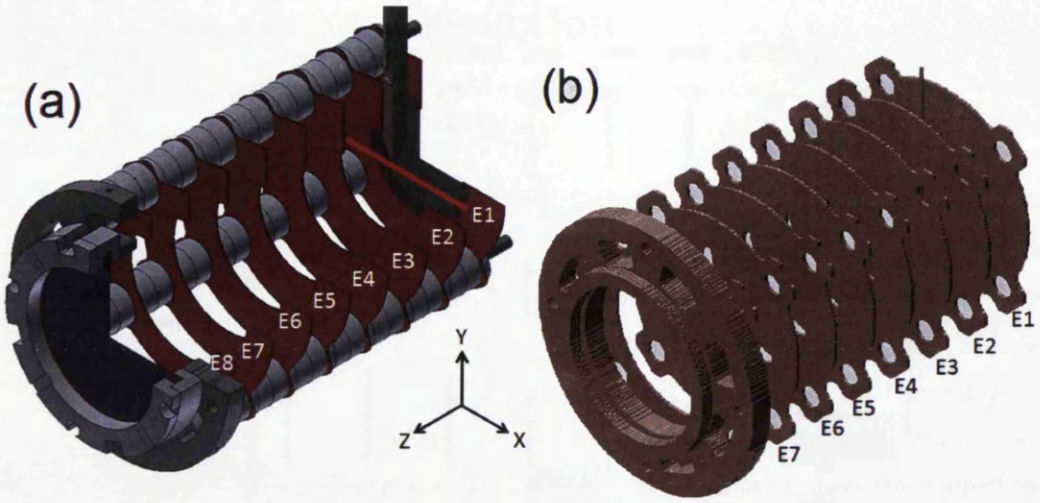

Figure 5.3: (a) Section view of the CAD model used for the simulations, including insulating components. (b) Actual SimION configuration imported from (a), showing all conducting components including electrodes, tip connection wire, mounting collar and detector electrodes. The model resolution is 2 grid squares per mm, sufficiently high to achieve convergence. The 100 fs laser pulse propagates along X between E1 and E2 as shown in red, and is linearly polarised along Y. The electrode spacing is 22 mm.

SimION model (shown along with the Autodesk Inventor in figure 5.3), an optimization of the electrode voltages demonstrated the velocity mapping condition could readily be achieved with the 8 electrode configuration detailed in figure 5.2. Optimization of the applied voltages on electrodes E1 to E8 allowed focusing characteristics to be found, and demonstrates the ability of the 8-electrode stack to achieve velocity focusing for a variety of electron energies at realistic voltages.

As a test of the ability of the electrode stack to velocity focus for a wide range of initial energies simultaneously, non-interacting electrons were simulated with kinetic energies of 2, 20, 30 and 40 eV and propagated to the detector plane as shown in figure 5.4. 1000 electrons at each of these energies were emitted from the centre of the interaction region over a filled sphere of 1mm radius. The electron momentum vectors were defined by an opposing pair of 3D gaussians centred on and rotationally symmetric about the Y axis to simulate the effect of linear laser polarization along that axis, albeit with an exaggerated FWHM of 75 degrees to enhance the clarity of any defocusing effects, and ensure that the effect of focusing a specific energy to a specific radius is met over full rotational symmetry. It is clearly demonstrated that focusing of different electron energies to different radii is achieved, whilst preserving the angular distribution.

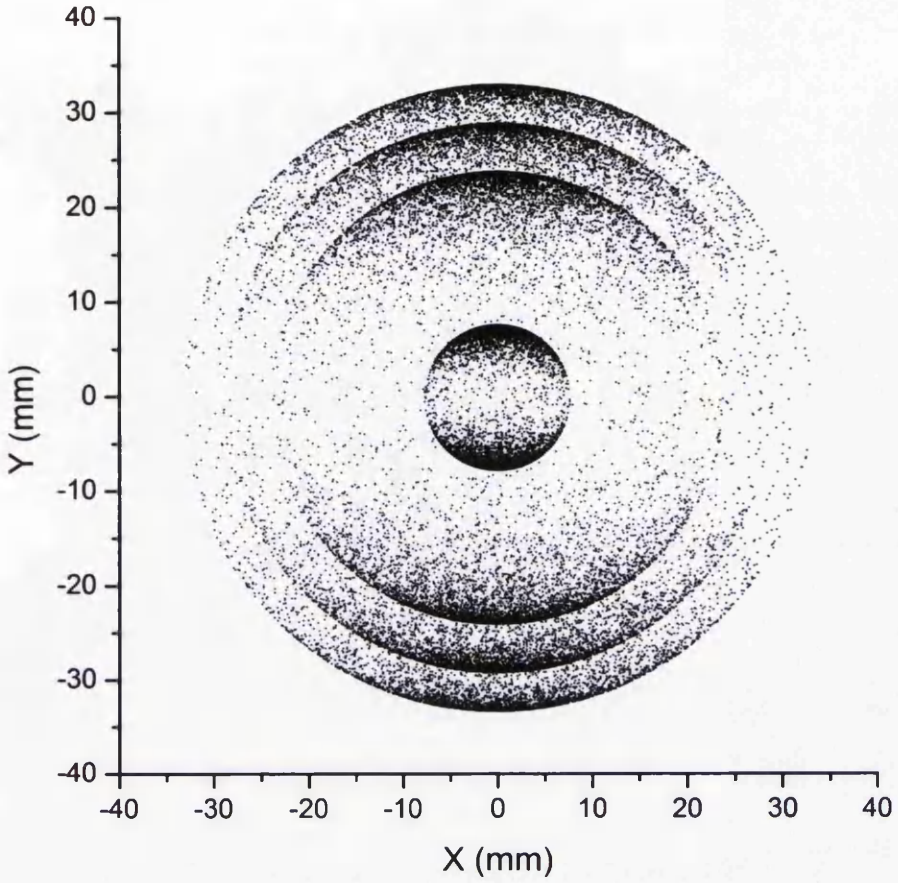

Figure 5.4: Simulation demonstrating ability of the multi-electrode VMI design to achieve simultaneous focusing of a variety of electron energies. The electrons originate at (0,0) in rotationally Gaussian distributions about the y axis, with discrete energy populations of 2, 20 30 and 40 eV. Electrons of the same energy are successfully focused onto the same radius.

5.2.2 Vacuum chamber design

Ultra-high Vacuum (UHV) is required when operating a VMI instrument; it is necessary to ensure that only the desire target is present in the volume of the laser focus, as any material present in the focus is liable to be ionised. The flight path of the electrons is also relatively long and their interaction with background gas is strong, high pressure may prevent many of the generated electrons from reaching the detector. In addition, detectors using MCPs to provide gain will interact with background gas when switched on at high pressures, which may induce breakdown within the detector at high gain and pressures above 10^{-6} mbar.

To meet this requirement the apparatus is integrated within a vacuum chamber (shown in figure 5.5), capable of being pumped down to a base pressure 10^{-9} mbar. The chamber is first roughed to a pressure of 10^{-1} mbar by a scroll pump (Edwards

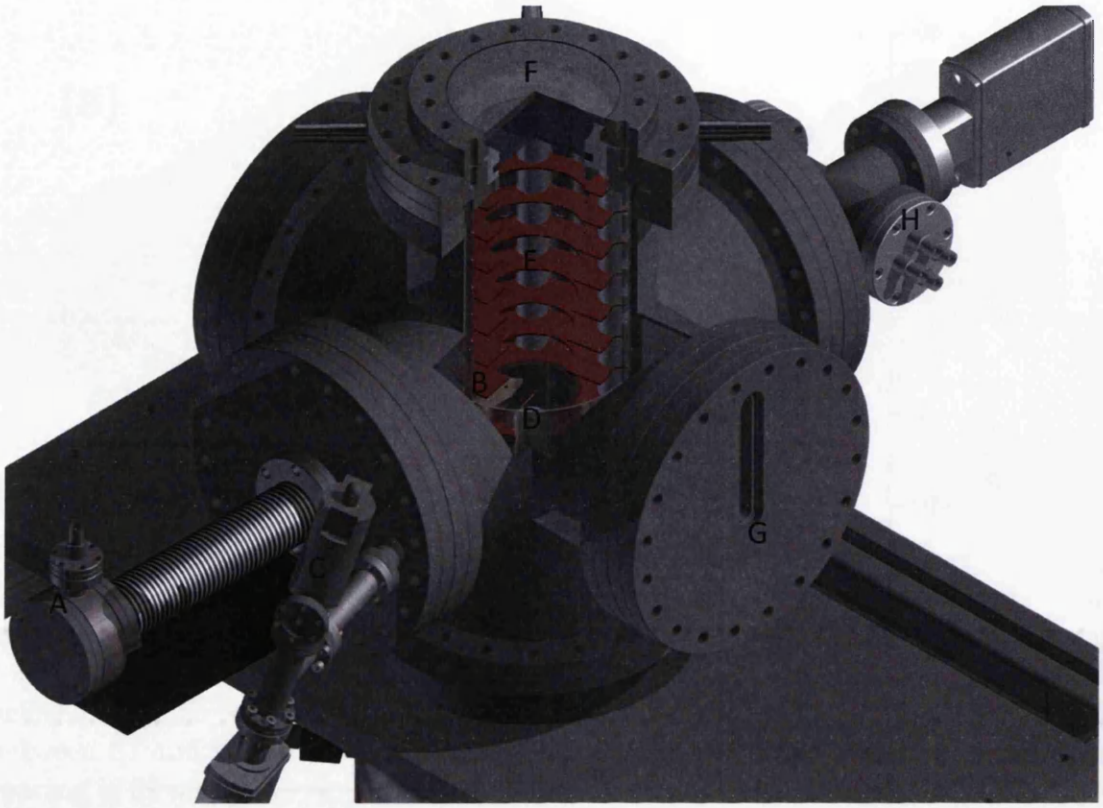

Figure 5.5: Render of the final design of the VMI chamber, with cutaway to show key internal components. The mu-metal shield is rendered transparent for clarity. A: Tip control stage with feedthrough for for application of a controllable potential. B: Nanotip at end of support rod. C: Gas line for injection of an inert calibration gas. D: End of gas needle near interaction region, held electrically floating. E: Main electrode stack. F: Position sensitive electron detector. G: Letterbox windows to allow access for laser light. H: Feedthroughs for application of voltages to the electrode stack.

XDS10), at which point a DN160CF turbomolecular pump (Pfieffer TMU 521 P) is switched on and accelerated to a speed of 50,000 rpm. The chamber typically reaches a pressure of $5x10^{-6}$ mbar before the pump has reached maximum speed, and then slowly drops towards base pressure over several days. Typically the chamber reaches a usable pressure of $5x10^{-8}$ mbar within 48 hours. The pressure is recorded with a dual Pirani/Bayard-Alpert gauge (Pfieffer HPT 100) read by a digital controller (Pfieffer DPG 109).

The main section of the chamber is a DN160 CF 6-way cross, which is large enough to accommodate the outer diameter of the mu-metal shield with 6 mm to spare. The electrode stack hangs from the top of the chamber; the rods are screwed into a collar which is bolted onto the top flange. This flange is a zero-length 8" to 6" adapter which accommodates a viewport and 4 radial SHV10 electrical feedthroughs

that are used to power the detector. This configuration is preferable to mounting the VMI from the side as it prevents the support rods from sagging under the weight of the electrodes and spacers, an issue that was revealed during the initial construction. The collar also has threaded holes radially which allow for mounting of the mu-metal shield.

Two sides of the cross are occupied by flanges equipped with letterbox windows which allow for light to be sent through the chamber level whilst allowing for versatility in tip position. These were made in-house and consist of 1 mm thick UV grade fused silica secured to a DN160CF flange using Torrseal UHV adhesive sealant, and have a clear aperture of 10 mm x 90 mm with rounded corners. The other two side flanges are occupied by adapters. One mounts three DN40CF flanges, each with four SHV10 electrical feedthroughs, two of which are used to apply voltages to the VMI electrodes with one redundant. The opposing flange is also an adaptor which mounts an angled DN16CF port as well as the DN40CF stage used to manipulate the tip. On the end of this stage sits a double faced flange with a radial feedthrough used to connect the tip to an external power supply (Stanford PS350, up to 5 kV at 330 μA). This is capped by a flange into which the tip mounting rod is screwed. The angled port supports a gas line incorporating a 200 μm capillary and a leak valve (VG Scienta ZLVM940) through which calibration gas may be injected to approximately 6mm from the interaction region.

The bottom of the chamber is occupied by the turbo-pump. The entire chamber sits beside an optical table mounted on a custom frame, with locking rubber feet to ensure stability. Support is provided by a pair of aluminium plates with an aperture that closes around the neck of the turbo-pump. These plates can also act as a table upon which steering and focusing optics may be mounted. The scroll pump sits beneath the frame. The gas bottle is mounted to a leg of the frame and attached to the gas line by a flexible Swagelock hose.

5.2.3 Detector design

The detector mounting was custom designed and built round a pair of MCP's that had been already obtained prior to the commencement of this project. The MCP's were made to order by Photonis and are imaging quality, with a thickness of 1 mm, and a pore size of 25 μm with a separation of 32 μm. The diameter are of the plates is 86 mm; the high diameter to thickness ratio makes the plates extremely fragile, requiring support around the entire circumference.

The holder consists of 2 Polytetraflouroethylene (PTFE) pieces which close around the front and back of the plates to electrically isolate them from their sur-

roundings whilst maintaining vacuum compatibility. A 75 mm aperture front and back allows a sufficiently large active area to be useful whilst also covering enough of the outer area of the plates to provide strong support. The centre area of the PTFE holder forms a cavity where the plates sit with a copper electrode between them and the pieces and a third electrode separating the plates. The electrodes are OFHC copper with thickness of 1 mm and tabs which allows a connecting wire to apply voltages the MCP's. The PTFE pieces have slots in the side to accommodate the tabs such that they do not protrude beyond the outer diameter of the PTFE whilst allowing easy access to the connection hole.

The PTFE pieces are machined such that when pressed together the depth of the cavity they form matches the depth of the plates and electrodes to within 0.2 mm, to ensure that the plates are locked in place and are unable to move within the holder. As PTFE is a soft material and compressible, the pieces cannot be screwed together due to the risk of over tightening and applying uneven force to the plates, which could lead to cracking. Instead 4 slots are machined into the pieces which locate 4 sprung metal clips which press lightly on the PTFE in a controlled fashion and are held in place by friction.

The whole assembly is mounted to the back of of the same collar that anchors the rods which support the VMI electrode stack, and sits inside the bore of the feedthrough flange that provides the current and voltage to run the detector. Between the feedthrough flange and the viewport sits a phosphor screen, custom made by Kimball Physics. The screen consists of P22 phosphor mounted on a piece of Indium Tin Oxide (ITO) coated glass (80 mm diameter) which sits 13 mm behind the rear MCP, and is electrically isolated from the surrounding chamber via ceramic breaks on the mounting clips. P22 phosphor has a decay time of 60 μs and glows blue upon an electron impact with energy 500 eV or higher. The screen is then observed through the viewport by a camera outside the chamber (AVT Pike F-505 CCD, 14 bit, 2452 x 2054 pixels) equipped with a flat-field lens (Pentax C30811 8.5mm f/1.5 2/3").

In this configuration the detector produces enough gain to observe clear signal on the camera at a bias of +4 kV on the phosphor screen, with the front of the channel plates (the side of electron impact) held near ground and the rear held at a bias of between +1 kV and +1.3kV depending on the desired gain and the density of incident electrons. Potential is applied by a pair of external supplies (Stanford PS350, identical to the supply used to power the tip). One supply is reserved for the phosphor screen, the other supply applies power to the back of the MCPs and then to the middle and front of the plates via a resistive divider. To protect the detector

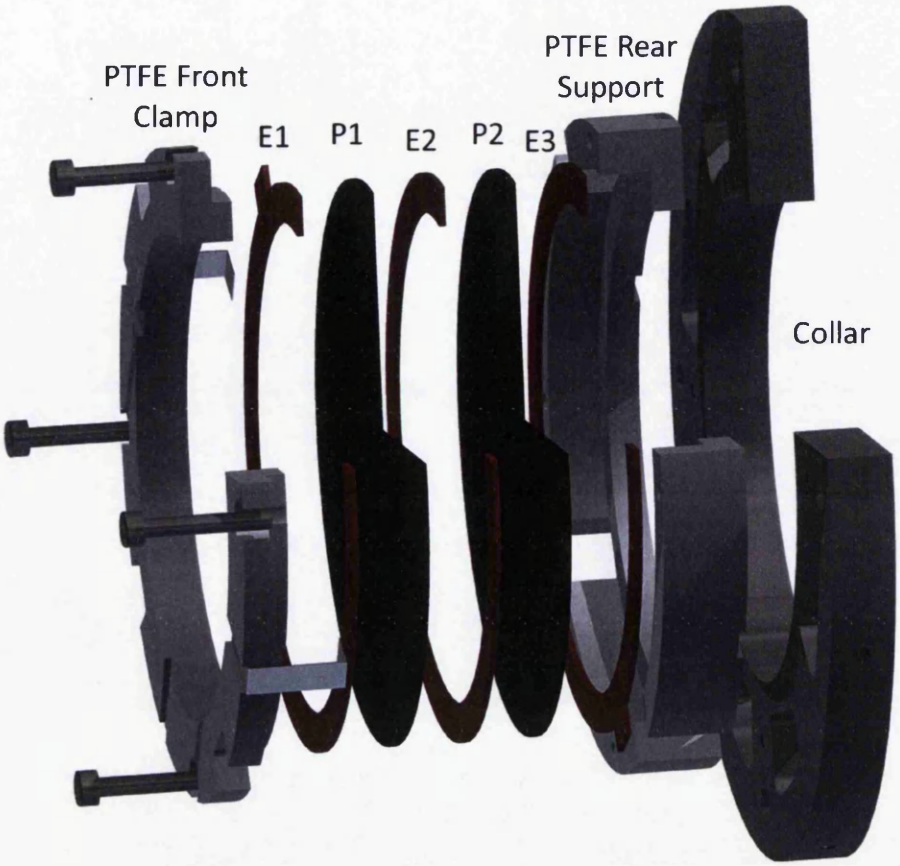

Figure 5.6: Exploded Illustration of the position sensitive electron detector designed and constructed for use with the VMI, with quarter section cut. The PTFE rear support sits on the collar, in turn screwed to the 8" side of a DN160CF to DN100CF adapter flange (not shown). The electrodes E1-3 and the channel plates P1 and P2 sit inside the rear PTFE piece, before the front PTFE clamp piece is lowerd into the assembly and attached to the rear piece by spring-clips to avoid applying pressure to the MCPs. The mounting screws then pass through openings in the front PTFE piece before securing the rear PTFE piece to the collar.

from damage the Stanford supplies were set to trip at a current of 150 mA.

5.2.4 Final construction

The spectrometer was assembled to full UHV standards with all components being cleaned with ethanol before being inserted into the chamber. Smaller components, especially those with threaded parts, were also cleaned by soaking in an ultrasound bath filled with methanol. The screws used to fix the collar to its mounting flange were also filed flat on one side to remove any trapped volumes of air.

The detector was connected to the feedthroughs via Kapton coated wire and attached with CuBe push-fit connectors. The other end of the wires was stripped

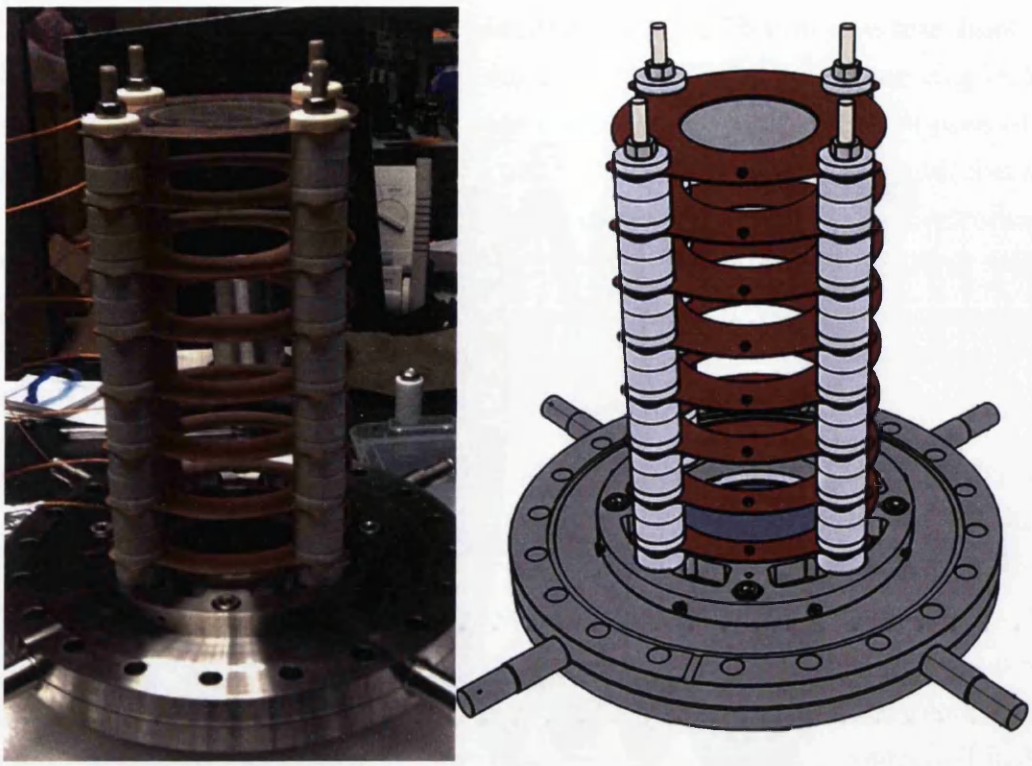

Figure 5.7: Final rendered design of the VMI and the assembled instrument (both without the mu-metal can).

and pushed through the holes in the connection tabs, where they were tied ensuring contact with the copper. The assembled detector was then screwed into the mounting collar. The screen was then mounted and the viewport attached.

The rods were then inserted into the collar upright and the electrode stack constructed using alternating male and female ceramic bushings to separate the electrodes. The inner diameter of the bushings is slightly larger than the outer diameter of the rods to ensure that there is no trapped volume. The rods were threaded at the top, nuts were used to lock the electrode stack in place. Kapton wires were attached to each of the electrodes by compression under a washer, held in place by a screw through a small outer hole. The wires were than carefully fed through the pumping holes in the mu-metal shield, some of which were deliberately positioned to line up with the electrodes, as the can was lowered over the stack and onto the outside of the collar, where it was screwed into place.

5.3 Focus testing through ionisation of krypton

A typical technique for checking that an electron spectrometer is functioning correctly is to examine emission from a noble gas. When sufficient intensity is applied

the gas undergoes Above Threshold Ionization (ATI), an extension of the multiphoton emission process explained in chapter 2 where a sufficient number of photons to overcome the ionization potential are absorbed. As part of this process the electron may absorb more than the required number of photons, leading to peaks in the photoelectron energy spectrum separated by the photon energy. These peaks appear at energies given by

$$E = (N_\phi + s)\hbar\nu - \phi \tag{5.1}$$

where ϕ is the ionization potential or work function and N_ϕ is the number of photons required to reach ϕ and trigger ionization. The value s then represents the number of photons above the minimum that are absorbed. The energy spectrum of electrons from a noble gas therefore consists, given sufficient laser power, of a series of peaks separated by the photon energy as a result of ATI.

The energy structure and spatial spread of such emission is well understood [248, 249] and allows the correct operation of the VMI to be confirmed. The highly discrete nature of the energy spectrum and high zero-momentum population from such a target allows easy convergence onto the correct velocity focusing conditions. For this testing the noble gas used was krypton. The expected pattern from Kr is a bright central momentum spot with "wings" along the laser polarisation direction. These wings contain ridges of signal from electrons with energy $nh\nu$ (where n=integer and $h\nu$ is the photon energy), demonstrated in the recorded pattern presented in figure 5.8. This is highly convenient as the ridges occur at known energy and so allow easy calibration of the detector position as a function of energy for the given set of focusing voltages. The filled area between these ridges is a result of the emission not being in a flat plane but being conical. Application of an Abel inversion to account for this has not been performed in this case.

Initial tests using linearly polarised 100 fs 1 mJ pulses at 800nm from the Coherent Libra Loan Pool laser system (UFL2) highlighted slight disruption to the images by the presence of the gas needle. The original needle was made entirely of stainless steel and so was grounded to the rest of the chamber. The extension of the needle inside the magnetic shield caused an asymmetry in the electric field and subsequently the smearing of the signal in the direction towards the needle. This needle was then replaced by a needle with a ceramic break outside the shield which left the end electrically floating.

The resulting images were of sufficient quality to enable a definitive calibration of the VMI. Figure 5.8 demonstrates a typical gas signal image and a calibration slice. The ATI ridges allow easy calibration of axis position to energy, the peaks occurring at known energy allows an energy to pixel relationship to be determined

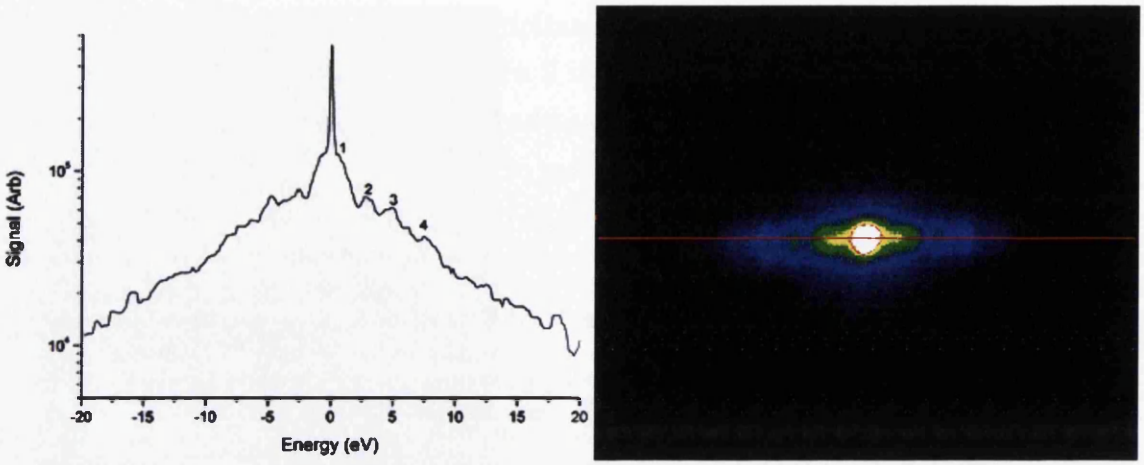

Figure 5.8: Slice view of a recorded VMI pattern from Krypton gas, showing the intense zero-momentum spot and ATI fringes which are clearly visible as peaks at the marked positions. These can be dramatically enhanced by applying an Abel inversion to the image to account for the electrons emitted non-parallel to the detector plane. A rank 2 median filter is employed to reduce signal noise.

provided at least three peaks are measurable with sufficient spatial resolution. This relationship will change as the focusing conditions change, therefore changing any voltage within the spectrometer requires the calibration to be renewed.

5.4 Verification of 3D applicability using krypton

To further refine the operation of the VMI and verify that it can work over all emission directions a tomography-like measurement was done of the krypton gas. In the case of emission from a noble gas, this can be done by rotating the linear polarisation of the laser. In a correctly operating VMI focusing should be maintained over a tomographic measurement with the image appearing to rotate about the laser path. In full tomography the rotational images are used to reconstruct a 3D object, which was unnecessary in this case.

To perform the tomographic measurement the tip was retracted as far from the interaction region as possible and left grounded. The chamber was pumped to a base pressure of $5x10^{-8}$ mbar to minimise signal from the background gas. Krypton was then injected through the gas needle to raise the pressure in the chamber to $4x10^{-7}$ mbar.

Laser pulses from the Libra laser system then ionised the krypton. Pulses 120fs long at 800nm were delivered into the chamber via a 25cm focal length lens. The pulse energy into the tank was 230 uJ leading to a peak intensity of just below 10^{14} cm^{-12}. An achromatic half-wave plate was used to rotate the polarisation

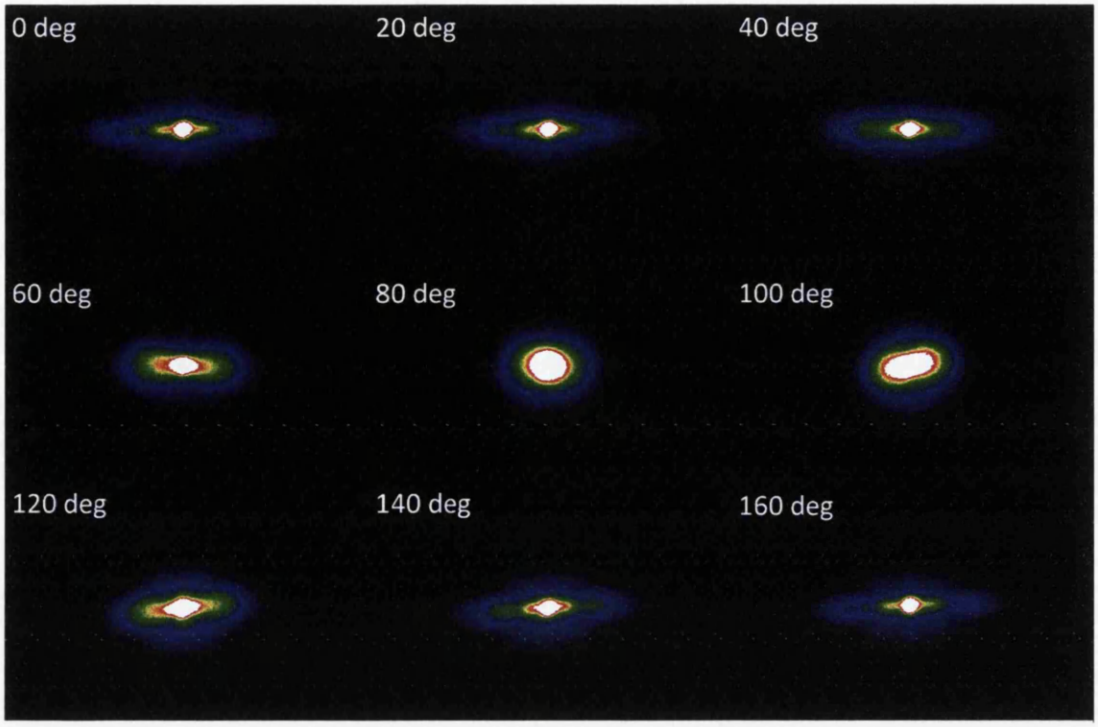

Figure 5.9: Tomographic images of Kr used to verify that the VMI is functioning as expected. The laser polarisation is rotated with 0 degrees being in the plane parallel to the detector and 90 degrees being towards the detector.

of the beam. Although this introduces dispersion to the laser pulse the effect is anticipated to be negligible as the pulse is already relatively long (approximately 120 fs) at this point. The results of the tomographic measurements are presented in figure 5.9. The crucial point is that these results look exactly as one would expect for a tomographic image of a gas, with "wings" occurring when emission is parallel to the plane of the detector and all signal confined into the central spot when emission is directly towards the detector. This successfully demonstrates that the VMI conditions picked are suitable for resolving the emission direction of electrons. It should also be noted that the emission is slightly tilted so that the wings do not face directly along the detector axis at the correct polarisation, this is due to the beam not passing through the tank perfectly perpendicular to this axis.

5.5 VMI of electron emission from a nanotip

5.5.1 First simultaneous observations of photoelectrons from a nanotip and a calibration gas

Once the correct operation of the VMI had been verified with krypton allowing appropriate focusing voltages to be found, attempts were made to obtain a velocity map spectrum of the electron emission from a tungsten nanotip. This was done by focusing on the krypton signal and slowly moving the tip towards the interaction region. At regular steps the tip was stopped and the distortion of the gas signal from the new field asymmetry observed. The tip voltage was then adjusted until both symmetry in the wings of the gas signal and the circularity of the zero momentum spot was restored. As the tip approached the interaction region the advance was paused at steps of reducing size as the asymmetry changed more rapidly with tip position. Laser power was also reduced such that only the zero-momentum Kr spot was visible to reduce the risk of destroying the nanotip on contact with the beam. The tip was then very slowly and carefully advanced to the edge of the beam until electrons from the tip were visible.

Most results were taken with the laser power lowered such that no gas signal was present, to facilitate the alteration of various parameters without the risk of the laser destroying the tip, though this does introduce the risk that the spectrometer could defocus without the defocusing being obvious. By very carefully and finely positioning the tip on the very edge of the laser focus, it was possible to emit electrons from the tip whilst keeping the laser intense enough to observe ATI signal. This allowed us to verify that we were observing electrons from the tip which were properly focused. At this point the electrons from the tip and gas are emitted from distinct sites, with electrons from the gas being produced at the center of the focus and electrons from the tip being released approximately 20 μm from the center. This does not introduce any distortion as this distance is an order of magnitude smaller than the large acceptance region of the VMI.

Examples of VMI images as the tungsten nanotip is moved into the laser focus are shown in figure 5.10(b). To demonstrate that velocity mapping conditions are maintained, the nanotip was very carefully inserted into the low intensity edge of the laser focus whilst ATI signal from Kr was present. A small lateral shift of the zero momentum point is observed, however this can be corrected by adjusting the tip voltage. Once electron emission from the nanotip was first observed, the laser intensity was lowered by a factor of three before advancing. This is clearly necessary for three reasons: the field enhancement caused by the nanotip is anticipated

to increase the effective intensity by around an order of magnitude. The density of the nanotip is also many orders higher than the gas, and the ionization potential of tungsten is 6 eV lower than Kr. The combination of these effects means that exposing the tip to such an intensity would immediately generate a plasma, evaporating the tip.

With the new lowered laser pulse energy of 70 μJ and the nanotip advanced approximately 100 microns into the focus, it is possible to simultaneously observe the zero momentum electrons from ATI of Kr at an estimated intensity of 8×10^{12} Wcm^{-2} and electrons from the nanotip at an intensity of $\simeq 10^{11}$ Wcm^{-2}. This allows focusing to be maintained as sub-optimal focusing appears to cause the zero-momentum spot to become distorted. The electrons from the tip typically form a semicircular band on the detector, as shown in figure 5.10(c), suggesting an initial conical direction distribution centered along the tip (Y) axis (as defined in figure 5.3), and a reasonably consistent energy across the entire distribution. When rotating the laser polarization the zero momentum spot remains essentially unchanged, while the emission from the nanotip switches on and off. This is an important result from this experiment: the 2 modes of operation are not mutually exclusive, and that it is possible to emit electrons from a solid target whilst also observing electrons from a calibration gas in order to adjust the focusing voltages in real time. This only requires the solid target to be smaller than the laser focus, and crucially this was done without any temperature control of the nanotip or gas.

The laser intensity is then reduced to approximately 10^{10} Wcm^{-2} via reflective ND filters, and the nanotip advanced further to approximately ten microns from the centre of the focus. The corresponding electron VMI image is shown in figure 5.10(d). A clear signature of strong field emission was then observed: an almost semi-circular band of electron momentum centred at the zero momentum point. Identification of this structure as having an origin in strong field emission comes through agreement with previous work [250], which indicated that the majority of electrons emitted from a nanotip via the strong field regime have a specific and narrow energy spectrum, with the primary peak in energy occurring at approximately 5 eV. In addition, whilst the emission process as compared between an atom and a nanotip has a number of similarities, zero momentum signal is not expected as a result of strong-field emission from a tip. The results in figure 5.10(c) and (d) replicate these expectations remarkably well.

As an additional diagnostic, observations of the laser exit beam are useful in assisting to verify that the band structure is a a result of strong-field emission. Even though the tip is small its size relative to the focus still causes it to block

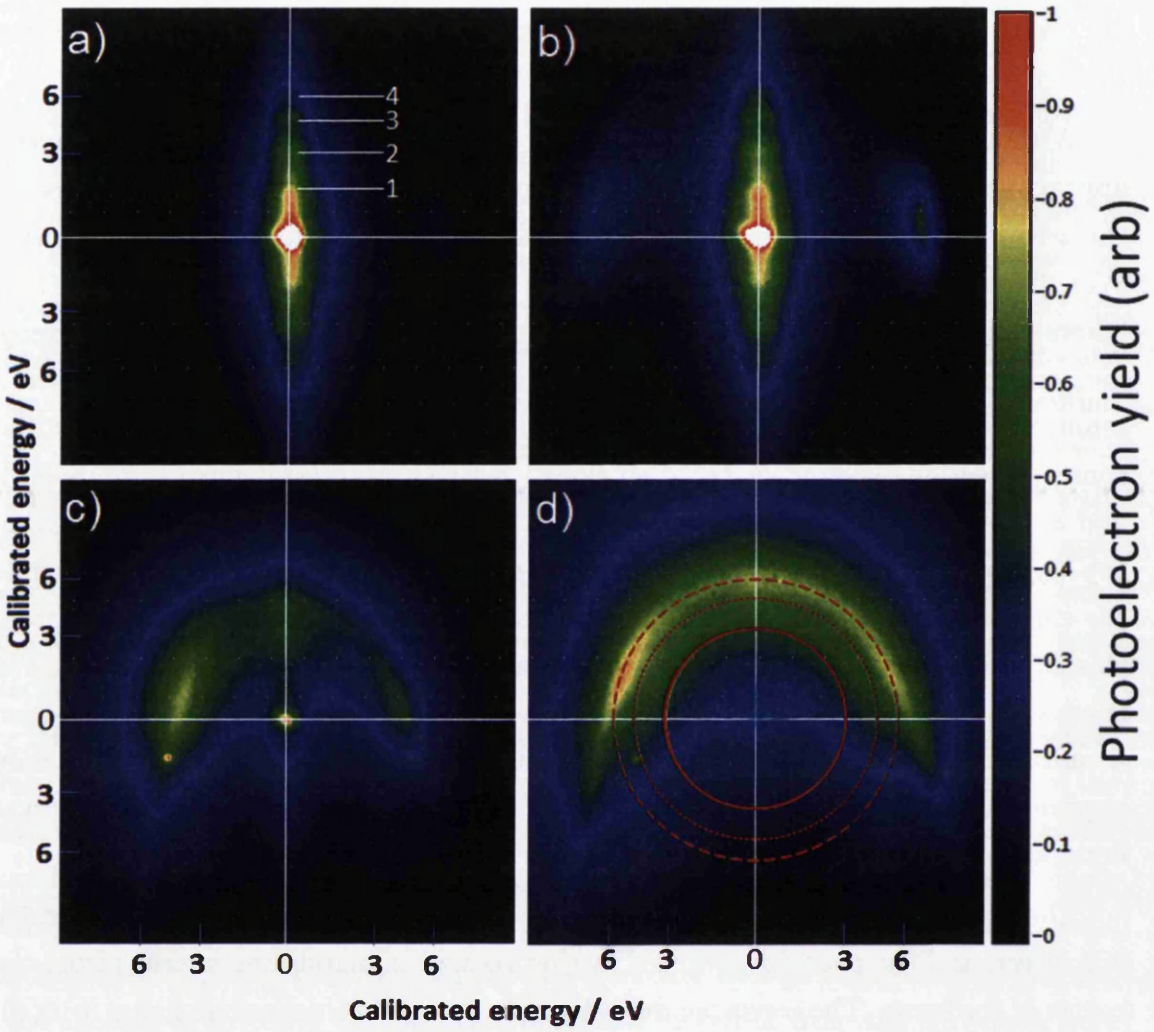

Figure 5.10: Colour enhanced images of real VMI patterns obtained with the VMI apparatus as shown in figure 5.2. In all images the tip is oriented along Y. Laser propagation is along X, with linear polarisation along Y. (a) Image of krypton gas with ridges showing ATI. The marker numbers n indicate the position of n-photon emission. (b) Electrons present from both gas and nanotip, with tip at edge of beam. (c) Electrons from both gas and nanotip, with beam attenuated to allow tip signal to be highlighted. Some smearing is visible due to a sub-optimal Vtip. (d) Image of electron emission from nanotip only. The inner ring shows the lowest momentum where electrons were detected, followed by rings indicating the 2nd (dotted) and 3rd (dashed) photon energies as calibrated from the ATI ridges in (b). The off-center bright spot on (c) and (d) is a result of contamination on the MCP. The energy scale is calibrated using the ATI fringes in image (a).

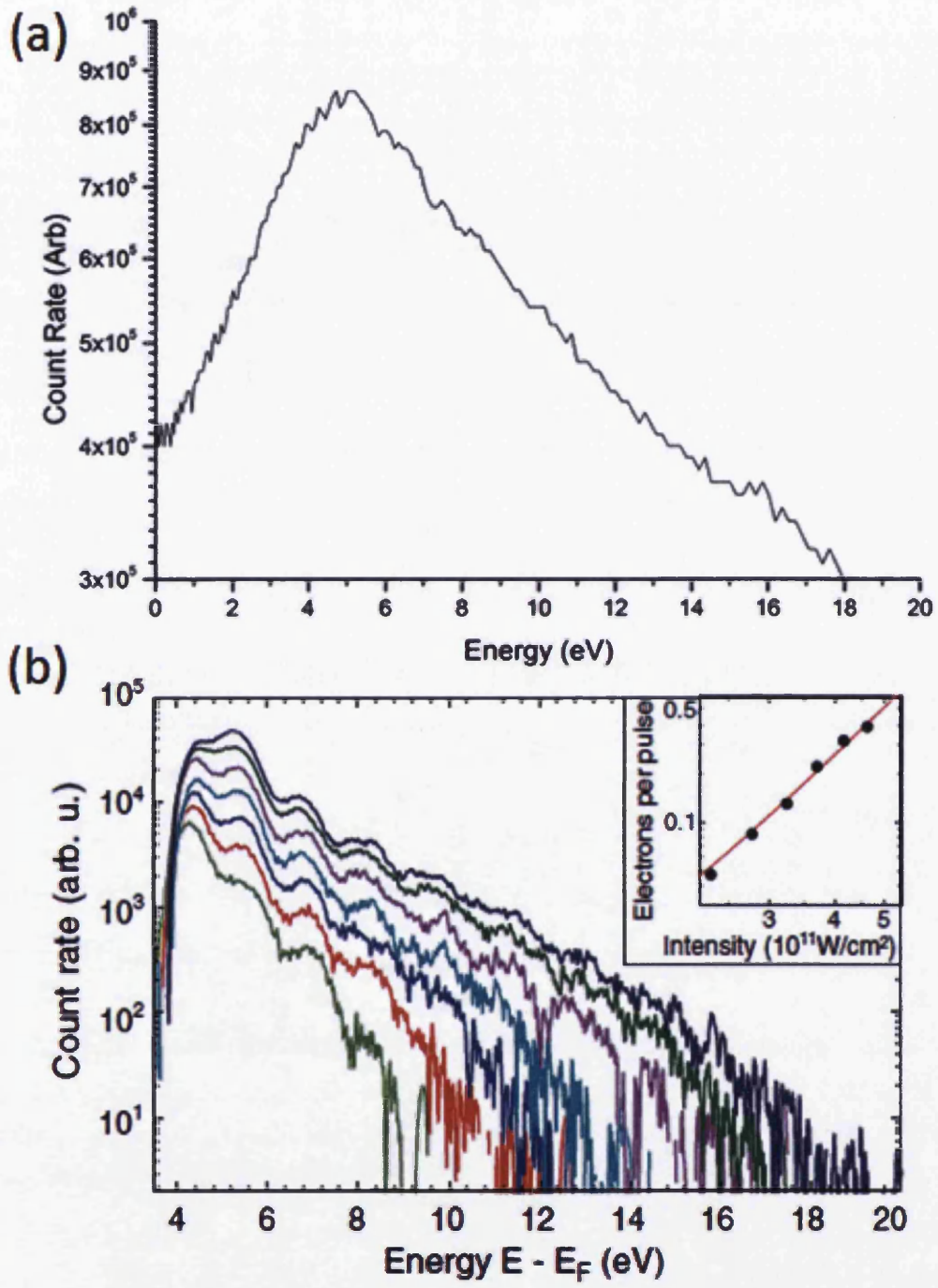

Figure 5.11: Comparison of the measured photoelectron energy spectrum for electrons emitted directly from the apex with the literature. (a) Slice along the tip axis through the recorded VMI pattern presented in figure 5.10(d). (b) Results from Hommelhoff *et al* reproduced from [251]. These results were obtained from a tungsten nanotip using a retarding field spectrometer, at an 80 MHz repetition rate with CEP stable pulses.

a significant part of the beam when near the centre of the focus, and to imprint diffraction into the beam when only the very end of the tip is touching it. As the tip is translated slowly into the focus, the semicircular band becomes the first major structure visible and occurs when a hint of diffraction but no shadow is visible in the exit beam. This strongly suggests that the semicircular band is made of electrons emitted from the very apex of the tip. Furthermore, this band is the only achievable structure which contains electrons of a very specific energy (as is expected with strong-field emission) rather than a random or thermal distribution, whilst being sure that velocity focusing is maintained. It is possible to verify that the very end of the tip is neatly in the focus by translating the tip vertically and observing a reversal of the diffraction pattern as the tip sweeps through the centre of the focus.

With the strong-field nature of the emission established the validity of the VMI as a means of measuring the photoelectron energy spectrum from a tip can be confirmed by comparing the results to those obtained from a similar tip by a different method. Such methods include time-of-flight measurements and retarding field spectrometers, both of which provide excellent spatial resolution but lack the ability to resolve direction of emission. By taking a slice of the VMI image along the axis of the tip a direct energy spectrum of the electrons emitted from the apex is obtained, which may be calibrated using the energy to pixel relationship determined by the ATI fringes of the krypton as in figure 5.10(a).

A slice from figure 5.10(d) is presented in figure 5.11(a) where it is compared to results taken by Hommelhoff *et al* [251] in figure 5.11(b). The results from Hommelhoff *et al* are highly sensitive due to their use of an oscillator to produce an average of less than one electron per shot, eliminating the issue of space-charge before the detector. It was not possible for us to emit in this regime and retain a usable signal due to the low (1 kHz) repetition rate of the Coherent Libra laser system. Furthermore Hommelhoff *et al* used a CEP stabilised laser system allowing fine features in the energy spectrum resulting from recollision effects to be resolved. This is not possible with the long pulses from the Libra, which are not stabilised causing such effects to be washed out.

The main peak in energy occurs at the same location (approximately 5 eV but relatively broad) in both datasets presented in figure 5.11, visible in figure 5.10 as the main band of strong-field emission. The rise into this peak is slower in the data from the VMI and the contrast is lower. This may not be a factor in the emission itself, rather it is likely an issue with the nature of the detector. Use of a CCD to image the phosphor screen allows the signal registered from one area of the detector to be altered by light pollution arising from another bright area, which will not

be corrected with background subtraction. The trailing edge of the peak follows a similar shape as the results from [251], but at a much shallower gradient. Following the pattern of the results in figure 5.10(b) where the gradient becomes shallower with higher intensity and increasing numbers of electrons per shot, this indicates that the VMI is suffering from significant space-charge at the point of emission, and would benefit from the use of an oscillator to emit fewer electrons per shot. The results from the VMI do not resolve the ridged structure seen in figure 5.11(b). It is likely that these ridges appear due to recollision effects, and so would not be present in the VMI results due to lack of CEP control.

5.5.2 Obeservations of transition between thermionic and strong-field emission regimes

By observing just the nanotip and altering the intensity of the incident light we have observed the transition between electron emission in the strong-field and thermionic regimes. This transition defines the boundary at which electrons from a nanotip become usable for coherent diffraction purposes. Those emitted in the strong field regime will generally be coherent and emitted in a conical distribution centred about the tip axis. Thermionic electrons induced by a laser pulse are less coherent due to emission from a larger volume, occur in a much longer pulse and are emitted in a much less predictable distribution. They are therefore generally useless for most purposes and steps should be taken to ensure that the strong field regime is prevalent.

The dominant band of electron emission is almost symmetric around the y axis (along the length of the tip), indicating the surface enhancement effect is having a clear influence on ionization, however a hotspot of electron emission in the direction that the laser pulse arrives from is also observed, which is most likely due in part to thermionic emission. The volume of the focus is sufficiently large that when the apex of the tip is near the centre a portion of the shank may be illuminated. It is this that produces thermionic emission, rather than from the tip apex, and can readily blunt a nanotip due to melting effect caused by extremely high local temperatures.

A systematic measurement was performed where the tip translated was swept in gradual steps of 5 μm through the focus along the x axis, with the apex of the tip approximately halfway between the center and edge of the laser focus. Images were recorded at each step. This has the effect of varying the intensity at the apex of the tip, whilst also increasing the amount of the shank that is illuminated as the intensity increases. The results of this sweep are shown in figure 5.12. This shows a clear transition between regimes, although it is apparent that the transition is

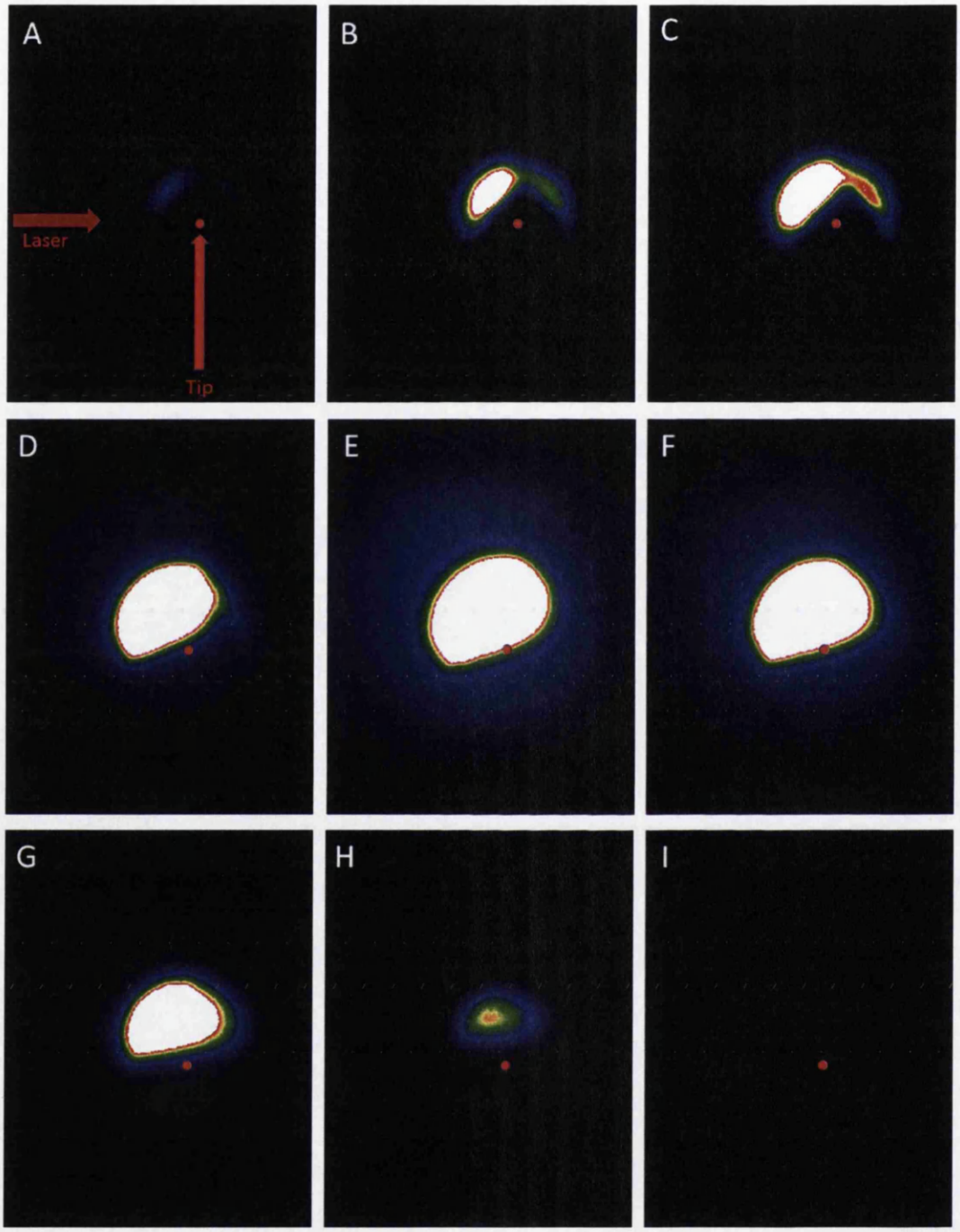

Figure 5.12: Observations of the transition between thermionic and strong-field emission regimes of a tungsten nanotip using velocity map imaging of tip being moved through the laser focus along the axis of the VMI, with panel E being where the tip is closest to the centre of the focus. In each panel the tip is moved by 5 microns, although as this is at the limit of the resolution of the micrometer this value may not be trustworthy. The tip in this figure enters from the bottom, with the laser incident from the left. The red dot shows the estimated position of the apex of the tip.

gradual rather than a direct switch on/off process. The point at which thermionic emission overtakes strong-field to the point where the tip becomes unusable appears to occur at approximately 10^{11} Wcm^{-2}, although this is an estimation as the nature of this experiment unfortunately makes obtaining an exact value nearly impossible. Furthermore the intensity is not the only factor at play, with the shape of the tip and the amount of the tip taper and shank under illumination also playing a key factor. It is therefore apparent that any experiments attempting to use a tungsten nanotip as an electron gun should retain both a tight focus (sub-10 microns) and an intensity below 10^{10} Wcm^{-2} value in order to ensure that the tip is not damaged by the laser or that the detector is swamped by non-coherent electrons.

That these electrons are thermionic was confirmed through destructive testing where the tip was moved further into the VMI such that it blocked a significant portion of the exit beam. Doing so causes the semicircular band structure to by suppressed and the thermionic feature to become dominant, forming a much broader momentum distribution with no discernible internal structure. Being thermionic it would be reasonable to expect an approximately Boltzmann-like distribution, although actually confirming this is difficult due to saturation of both the detector and the camera. Returning the tip to its original position reduces the thermionic component but generally yields a significantly weaker strong field emission structure, or none at all. This is indicative of the thermionic electrons being emitted during a one-way evaporation or heating process that permanently alters the tip shape.

5.6 Modelling of electron flight through the VMI

Following collection of the above results, a systematic study of the VMI focusing conditions was performed with all elements (nanotip, supply wire, VMI electrodes, detector mounting collar, detector electrodes) defined with independent voltages. This investigated the effect of tip voltage and position on the parameters of the resulting focus. The simulation includes the added asymmetric potential caused by the presence of the tip and its contact wire, which was placed at realistic positions within the spectrometer by varying the distance between the tip and electrode 2, accounting for the limitations of the real geometry and testing the ability to momentum focus despite the freedom to move the tip. Electron flight through the spectrometer was then modelled for a range of tip voltages.

There are three approximations of note:

(1) The initial electron distribution was modelled as a small sphere (radius 0.1 mm) with zero energy. This replicates the observed strong-field behavior of gas

phase photoelectron emission, which can be used as a diagnostic even when ignoring the "wings" caused by above threshold ionisation. Minimising the ellipticity of the central zero-momentum spot has in practice proven to be a surprisingly reliable indicator of correct velocity focusing.

(2) It was necessary to approximate the tip (and the connection wire) as a simple cylinder with a flat end, as SimION is incapable of dealing accurately with undulating geometries due to the lack of an adaptive grid, and was not able to accurately refine the taper of the tip into the grid due to the small size of the tip relative to the grid size. To use a grid size small enough would have rendered the simulations too computationally expensive for our current resources. We anticipate that the microscopic geometry of the tip and the resulting field will have an influence on the resulting velocity map distribution, and is an area of future investigation where we expect to see the structure of the VMI image reflecting the distribution of emission sites across the curvature of the tip. Investigation of the extent of this influence is ongoing.

(3) Space-charge is ignored, again due to the availability of computation resources, but this is not an unreasonable approximation as it is possible to emit an average of the order of 1 electron per laser pulse from a tip with sufficiently low intensity [251, 252]. This is advantageous as by integrating over a large number of single electron shots it is possible to severely reduce or eliminate disruption caused by space-charge. Even when releasing multiple electrons per shot this approximation may still hold, as the large geometry of the VMI and the strong static fields present will naturally allow and encourage a large separation between electrons, where the field from the VMI will totally dominate space-charge effects, although not for the case of the results above where it is estimated that several hundred electrons per shot were released. The area where this approximation becomes a real experimental issue is at the plane of the detector, as the simulation cannot account for the action of the MCP and the resulting Coulomb expansion between the MCP and phosphor screen. This results in a simulated distribution that is accurate upon arrival at the detector but appears more tightly focused than the results observed on the screen due to spreading of the distribution within the detector. It is anticipated the accounting for mutual repulsion during the flight through the electrodes would lead to some smearing of the image upon arrival at the front of the detector, which would be normally be sufficiently minor as to be unobservable in comparison to the smearing caused within the detector itself, only becoming a major problem upon the release of $\geq 10^5$ electrons per shot.

The results of this simulation are shown in figure 5.13. For a series of nanotip

positions with respect to E2, the applied nanotip voltage V_{tip} was scanned through the correct focussing voltage and 5000 electrons were flown individually through the VMI. The coordinates in the detector plane of all electrons were recorded and the mean and standard deviation in the detector plane (x and y, where y is along the tip) used to quantify the parameters of the final focus.

Figure 5.13(a) shows the displacement, defined along the y-axis, a measure of the deflection of the mean coordinate of the electron bunch from the center of the detector caused by the potential on the tip. Positive displacement is defined as away from the tip (indicated in figure 1). Only y displacement is considered as for a symmetric nanotip and straight contact wire there should be very little X-axis displacement. As is clear from the shape of the curves in figure 5.13(a), it was found that the dependence of displacement on V_{tip} was remarkably independent of tip position, with the only changing factor being the intersect with zero which shifts by 21.5±1 Vmm^{-1} of tip translation for the given electrode voltages.

The spatial spread of electrons arriving at the detector plane (effectively the electron focal spot) is quantized by the standard deviation from the mean along both the x- and y-axes. As shown in figure 5.13(b), the standard deviation along the x-axis (σ_X) passes through a clear minimum which occurs at the same tip voltage (to within ±2V) as the point of zero displacement shown in figure 5.13(a). Again the shape of the curve remains remarkably similar as the tip position is changed, with the voltage of best focus shifting again by 21.5±1 Vmm^{-1}. The spot size is in the x dimension is also symmetric about the minimum, which remains constant as the tip is moved. The symmetry of this observation is a result of the additional axis of symmetry around the z axis.

The most interesting prediction occurs when the electron spot standard deviation along the Y-axis is considered. A minimum in the standard deviation along the y axis (σ_Y) is observed, shown in figure 5.13(c), which occurs at approximately the same voltage as the minimum in x and the point of zero displacement, figures 5.13(a) and (b), however the function is highly asymmetric. When the tip voltage is too low such that a negative displacement occurs the defocusing of the spot is extremely rapid as it expands along the tip axis. The minimum, whilst clear, is less well defined and is predicted to be a factor of 35 larger on the y axis than the x axis. When the tip voltage is above the required focusing voltage the defocusing occurs much less rapidly, expanding faster along the X axis than the Y axis. Fluctuations in the data in figure 5.13(c) is a result of small statistical variation in the simulation.

The measurement of spot size on the y axis does not follow the same pattern as the x axis and displacement as the tip position changes. Although again the

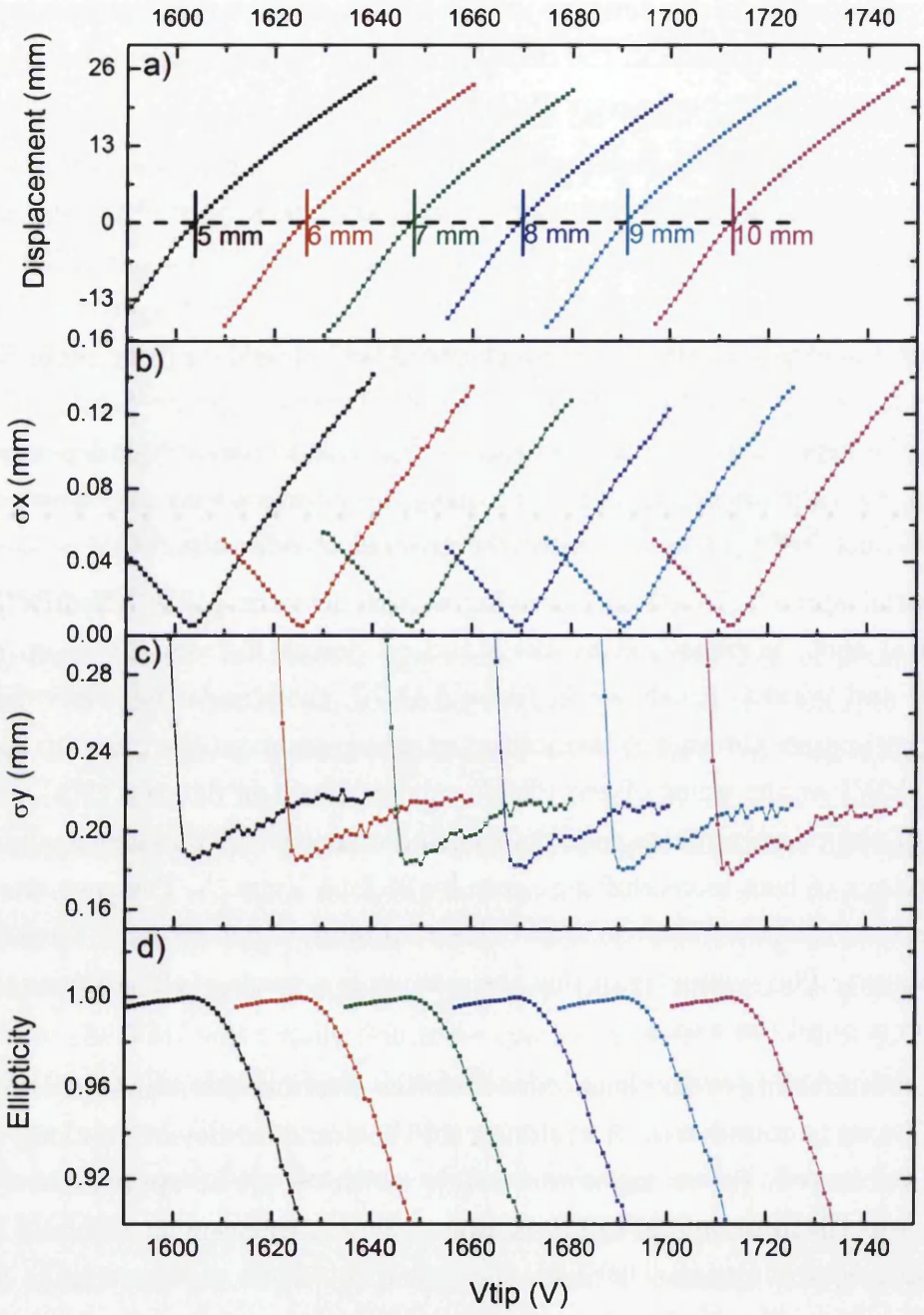

Figure 5.13: Results of simulation of electron flight through the VMI as a function of tip voltage and position. a) Displacement of the center of the electron bunch from the center of the detector along y. b) and c) Standard deviation of the electron bunch along the detector in x and y respectively. d) Predicted ellipticity of the bunch arriving at the detector. Tip positions are defined relative to E2 in the z axis, and are chosen to reflect tip positions used in the real VMI, where the tip typically sits closer to E2 than E1 due to the geometry of the vacuum chamber.

functions remain similar as the tip moves and the minima again shift by 21.5±1 Vmm^{-1}, the value of the minimum point shifts slightly lower as the tip moves further away from the detector. This effect shows that it is advantageous to have the tip far from electrode E2. It was not possible to fully utilise this for the initial measurements presented below due to the geometry of the vacuum chamber, which required that the tip is closer to electrode E2 than E1.

Whilst there is a predicted variation in the resolution in the x and y directions, it is anticipated that this will not be an experimental limitation. The smallest σ_X is predicted to be of the order of 10 μm, resolution of which is not achievable with the current MCP and phosphor screen combination. With the current MCP parameters achieving a spot on the phosphor with a diameter comparable to the predicted minimum of σ_Y (approximately 200 μm) is reasonable.

The simulations predict a very high ellipticity at the point of best focus due to the spot size in the x axis being dramatically smaller than in the y axis. This suggests that the point needs to be both large and at high displacement in order to achieve a round spot from a spherical distribution. In this aspect the simulations disagree from our observations, which showed that with careful handling of the tip position and voltage it is possible to obtain a circular spot at low displacement and with usable focusing of both the spot and ATI fringes. It is likely that this is due in part to the effect of the MCP's spreading the electron distribution before arrival at the phosphor screen, and is modified in future experiments (discussed in chapter 8). Furthermore, as shown in figure 5.10(d), no zero momentum signal from the nanotip is expected. Electrons with a non-zero momentum will spend significantly less time in the vicinity of the tip, so their trajectories may be influenced to a lesser degree, resulting in less disruption to the maximum achievable resolution. Experimentally there are strong indications when the correct VMI conditions are found. It was observed that when the tip voltage was too low the zero momentum distribution expanded rapidly towards the tip along the tip axis, replicating the steep gradient seen in figure 5.13. It was also observed that at increasing tip voltage the distribution expanded more rapidly in the axis perpendicular to the tip, again replicating the prediction of the simulation.

5.7 Concluding remarks

A novel adaptation to the traditional VMI spectrometer design was constructed that allows simultaneous observation of the momentum distribution of photoelectrons from gas and solid targets. The effectiveness of this revised design has been demon-

strated by examining above threshold ionization from krypton gas and tunnelling emission from a tungsten nanotip. Conditions were found that allow photoelectrons from the tip to be observed whilst using the structure of the zero-momentum spot from Kr to verify velocity focusing. This capability allows easy calibration of electrons emitted from a solid by comparison to those emitted from a noble gas under the same velocity focusing conditions. The spectrometer is unique in this regard.

This instrument gives direct access to three dimensional emission characteristics from metal nanotips illuminated with femtosecond laser pulses. Knowledge of the momentum distribution will be decisive in the design of next-generation femtosecond electron diffraction and microscopy instruments. Using the instrument as a diagnosis of the nature of photoelectron emission from a nanotip is reliable in terms of discerning between emission regimes, and determining the usability of the electrons for diffraction and microscopy experiments.

The agreement between the SimION predicted VMI focusing conditions and the appearance of the symmetric structure in the observed distribution demonstrates that the instrument is operating in the velocity mapping regime, however it is well known that the enhancement of both DC and laser fields has a dominant influence over hundreds of nanometres, a smaller length scale than is possible to simulate with SimION. These simulations show that it is possible to maintain the VMI conditions over a wide range of configurations, crucially it is possible to retain the condition that the velocity focusing is independent of the emission location. When moving the tip closer to or further away from the detector it is possible to restore a velocity focusing condition only by adjusting the potential applied to the tip for a given set of electrode voltages, whilst returning to a focus of very similar parameters. Such a condition could be very influential if this instrument is employed for examining overlapping laser foci, as will be required in pump-probe experiments.

The resolution of these results is sub-optimal due to the construction of the detector leaving a large gap between the back of the MCP and the phosphor screen, allowing for coulomb explosion of the signal. Even so, these results are a major success because until now the requirement for symmetry had restricted the use of the VMI technique to the gas or aerosol phase. Only one previous attempt has been made at velocity map imaging from a macroscopic solid, which was unable to demonstrate focusing [233]. Here it has been proven that focusing is maintained by simultaneously recording electrons from both the gas and the tip, and furthermore the results are validated by those already present in the literature obtained by retarding field spectrometry [251]. This therefore represents the first time that VMI has been successfully demonstrated not just from a nanotip, but from any solid.

Chapter 6

Holography as a means of measuring electron coherence and bunch length

A key advantage of using nanotips is that producing electrons from a point-like source greatly increases the coherence angle (as discussed in section 6.1.1), or transverse coherence length (as discussed in section 2.2) of the emission. A high degree of coherence between electrons in a bunch is essential if the bunch is to be used for diffraction studies of a target [253–255], hence nanotips are the preferable photocathode type for such studies [256–259]. When an electron bunch is passed through a sample, those within the coherence angle may undergo diffraction as their wavefunctions interfere during scattering. Electrons outside the coherence angle will not contribute to the pattern but still scatter elastically or inelastically, adding random events to the detector and decreasing the signal-to-noise ratio. It is therefore desirable to ensure that as many electrons as possible are coherent, a goal which may be achieved by making the coherence angle large. Nanotips achieve this but knowledge of typical coherence angles is useful to determine what targets may be imaged, hence an experiment has been designed using holography attempting to quantify the coherence of emission from a tungsten nanotip.

6.1 Principle of holography

6.1.1 Introduction to holography

Measurement of coherence can be performed by means of holography [200, 260–263], where a wavefront is forced into overlapping with another wavefront from

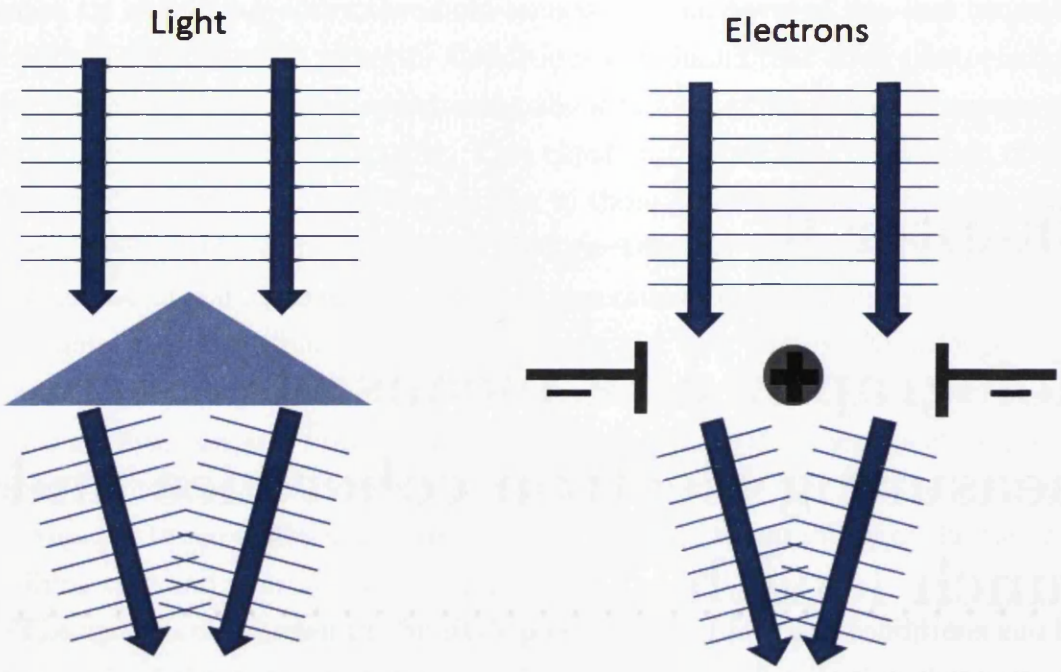

Figure 6.1: Similarities between biprism configurations using both light and electrons. In both cases a flat incoming wavefront is split in half and each half is steered inward to produce a crossing of wavefronts and the production of interference fringes.

the same source. If there is coherence, an interference pattern will occur, from which information can be obtained allowing the transverse coherence length to be determined. The process may be done with any beam that is at least partially coherent, be it a particle beam or laser light. The beam can be made to interfere with itself by splitting and recombining using a device known as a biprism (as shown in figure 6.1). The idea of performing electron holography is not new, having first been proposed in 1948 by Gabor [264], and a number of different experiments have been performed since by several variations on the basic technique [256, 259, 262, 263, 265].

When the incident wave is light this may be achieved by a variety of collinear interferometer types, however the technique most closely related to the method when using electrons is a simple glass prism with a shallow apex angle and with the apex pointed toward the incoming wavefront. Light through each of the angled faces of the prism is refracted inward, leading to a crossing of wavefronts and subsequently an interference effect, if the incoming light is coherent. The electron analogue to the biprism was invented in 1956 [266], achieving splitting with a central thin wire aligned orthogonal to the electron path. In order to complete the effect the electrons must pass between the anode wire and a cathode, usually in the form of a pair of conducting plates as shown in figure 6.1. These must be held negative relative to

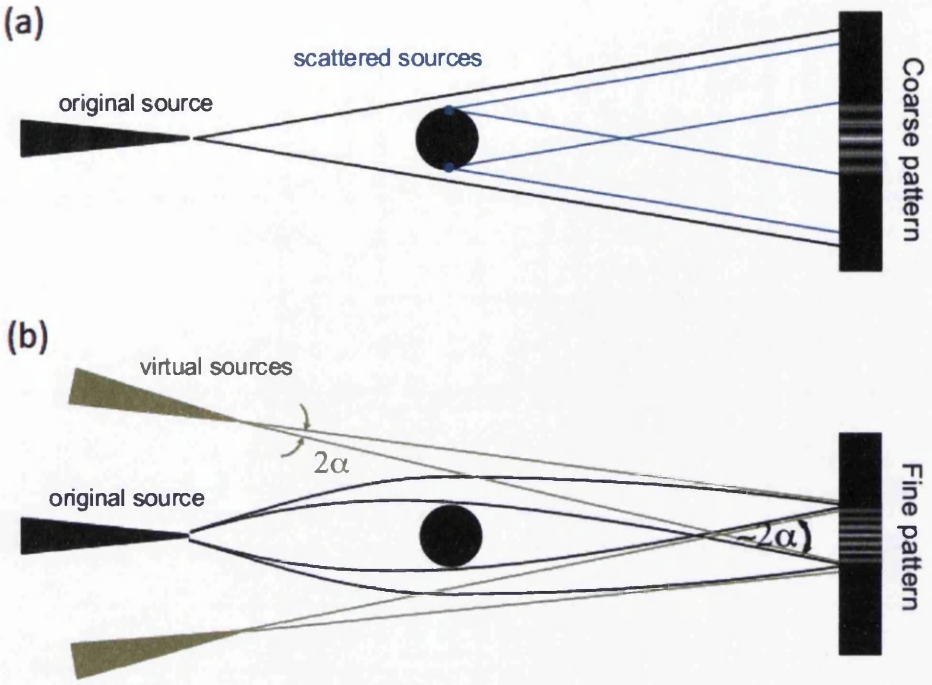

Figure 6.2: Comparison and highlight of differences between the biprism effect and the classic double slit experiment. Reproduced from [200]. (a) Presenting the electrons with neutral voltages on the biprism results in a simple coarse interference as is expected in the double slit arrangement, arising from Fresnel effects from electrons passing close to the wire. (b) A set of fine interference fringes arises from the birprism effect when voltages are applied to the wire and to plates either side of it that lead active crossing of the electrons beams. The overlap angle α represents the lower bound of the coherence angle of the beam, defined in more detail below.

the anode, and so grounding them is usually sufficient to achieve the desired effect. When this wire is held at a positive voltage the incoming electron wavefront is attracted and electrons passing each side of the wire are bent inwards towards each other, again leading to a crossing of wavefronts and an interference effect if there is a degree of coherence amongst the incoming electrons. This may be detected by observing constructive and destructive interference on a position sensitive detector such as an MCP-Phosphor screen combination or photographic plate. The idea of the electron biprism is closely related to Young's double slit experiment, where electrons passing each side of the wire act like they have passed through separate slits as a result of Fresnel effects [267], as shown in figure 6.2.

The contrast between the light and dark biprism fringes is proportional to the percentage of coherent electrons within the beam, with a contrast of unity implying that the beam is completely coherent. Holography via biprism also allows other coherence properties to be measured. It is also possible to quantify spatial and

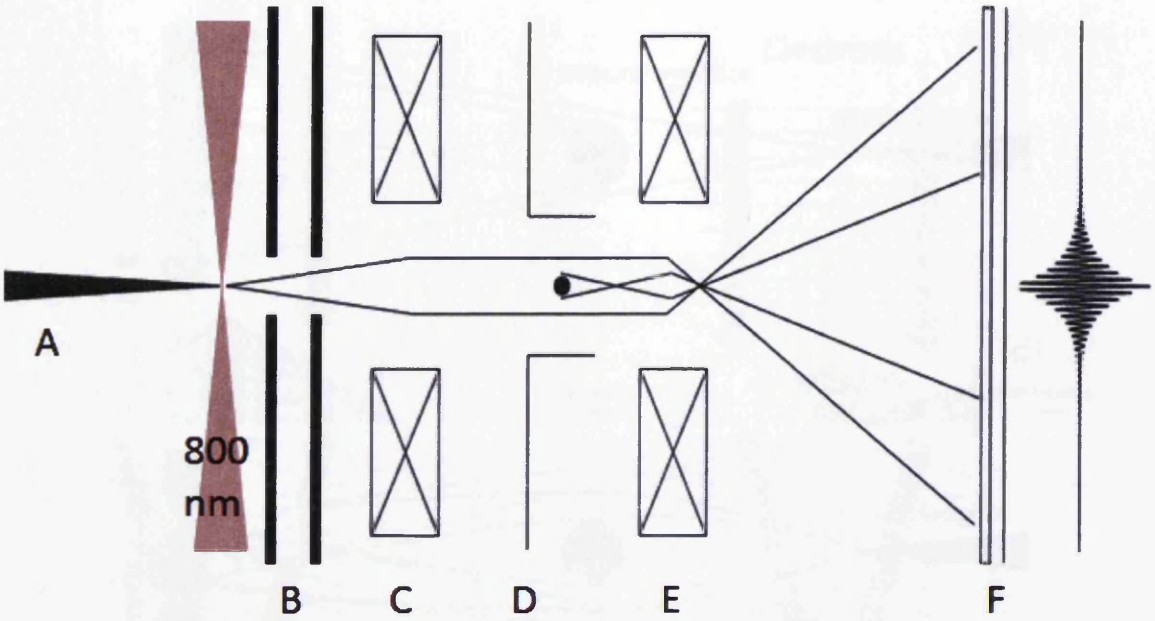

Figure 6.3: Illustration of the typical requirements and electron paths to achieve holography for measuring coherence of electron emission from a nanotip. A) nanotip, B) accelerating structure C) collimation lens (optional except at very low beam energies, D) biprism consisting of positive wire and grounded plates, E) lens necessary to achieve high magnification, F) position sensitive detector.

angular coherence using the derivation presented in [263]. The parameter α as shown in figure 6.2 gives a quantification of the angular coherence. It is possible to calculate the parameter α directly from the fringe pattern using the relationship

$$\alpha = \tan^{-1}\left(\frac{\omega}{2L}\right) \tag{6.1}$$

where L is the distance between the source and detector, and where ω is the width of the fringe pattern. Using this technique coherence angles as high as 14.3 degrees have been measured from highly structured nanotips [200], though normally nanotips are limited to approximately 5.5 degrees [105].

Whilst the production of an interference pattern allows a wealth of information to be obtained regarding the coherence of the initial wavefront, holography is also a useful imaging technique because the beam briefly exists as two separate arms before being recombined. A perturbation (which may take the form of an object to be imaged) may be introduced to one of the arms resulting in a disruption to the interference pattern. The other arm is retained unperturbed as a reference beam. Observation of this disruption may be used to reconstruct the nature of the perturbation. A schematic of a typical configuration to achieve this is presented in figure 6.3.

6.2 Design and construction

The apparatus developed for this project was newly designed and does not follow directly from the work or designs presented in the literature, although does take inspiration from the literature [260, 265, 268]. UHV conditions are a necessity for electron holography, due to both the operational requirements of the detector and the high scattering probability between free electrons and background gas. In addition the high voltages present in this experiment present a significant arcing risk when even low pressure gasses are present, hence the best possible vacuum is a necessity for electrical safety. The equipment was designed to use the same basic vacuum chamber and the same detector as the VMI experiment discussed in chapter 5. The instrument simply slots onto the same detector flange as the VMI in place of the electrode stack, and may be inserted vertically into the 6-way DN160CF cross in identical fashion. The key differences are the absence of the mu-metal shield, which does not have holes positioned to allow access to the ponderomotive grating beams, and the replacement of the feedthroughs for the VMI electrodes with a pair of single 40kV ceramic feedthroughs to provide high voltage to the accelerating structure. The loss of the mu-metal shield is a potential issue and so performing holography at high energies is necessary to minimise the disruption to electron trajectories due to the Earth's magnetic field.

The apparatus follows the idea presented in figure 6.3 but omits the optional collimation lens (part C) which is generally not required for keV beam energies as the acceleration will naturally lead to a relatively flat wavefront. The final design consists of an accelerating structure, the biprism and a magnetic lens, and is presented in figure 6.4.

The accelerating structure consists of the tip itself and a pair of circular OFHC copper electrodes, 1 mm thick with an outer diameter of 50 mm and a concentric hole of diameter 1 mm. A second pair of electrodes was also created with a central hole of 2 mm diameter, which is easier to align but not quite as effective at collimating the electron beam. These are held at a separation of 9 mm and encased in PTFE holders allowing them to be used at high voltages without arcing. The electrodes feature extended tabs with a small hole allowing a wire to be attached linking them to high voltage feedthroughs. Typically the nanotip is held at -30 kV with the first electrode held at around -29.7 kV to direct the electrons and the second electrode held at ground to provide an acceleration stage. The PTFE mounting pieces are secured in place by the same mounting rods that support the VMI stack, separated by the same ceramic bushings and secured by nuts on the threaded end of the rods.

Above the accelerating structure sits the biprism. This consists of 3 PTFE

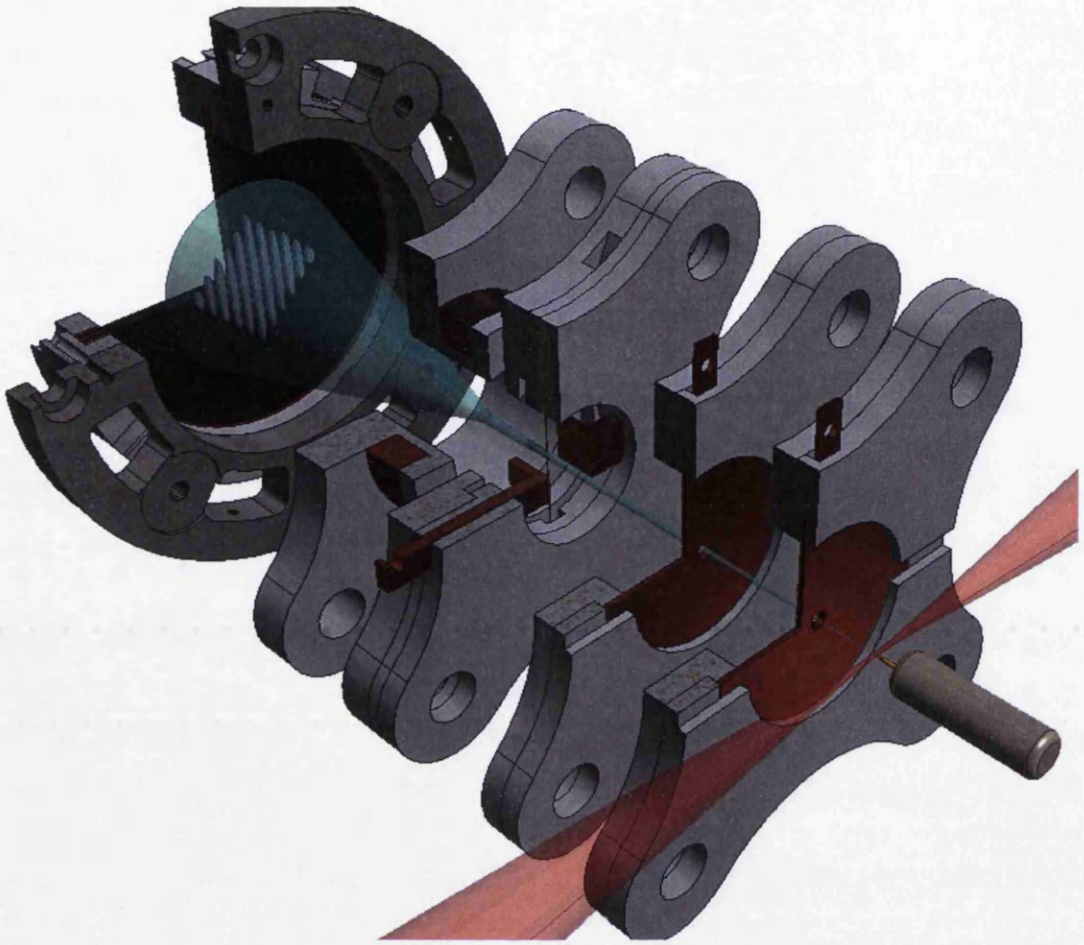

Figure 6.4: Rendered design of the biprism assembly showing the electron path and electrode structure with PTFE mounting pieces. The supporting rods are omitted for clarity.

holding and insulation pieces mounted using the same technique as the accelerating electrodes. The first and second of these pieces hold the grounded plates, which are inserted into grooves on the faces of the pieces and held in place by friction as the PTFE is secured. The grounded plates are L-shaped as per figure 6.3 and are manufactured from OFHC copper, featuring holes through which connection wires may be secured to ensure grounding. The second and third PTFE pieces hold and OFHC copper ring to which the biprism wire is secured by using colloidal graphite as a conductive adhesive. The wire itself is 4 μm diameter tungsten wire (Goodfellow). Voltage to the wire is supplied by the supporting ring which is connected to a feedthrough and to an external power supply (Stanford PS350).

The final stage is the magnetic lens, which consists of a solenoid of Kapton wire wrapped around a PTFE holding piece, with one side of the solenoid resting against the main body of the piece and the other secured by a lip protruding from the PTFE which forms a bed for the solenoid. The ends of the solenoid feed through a pair

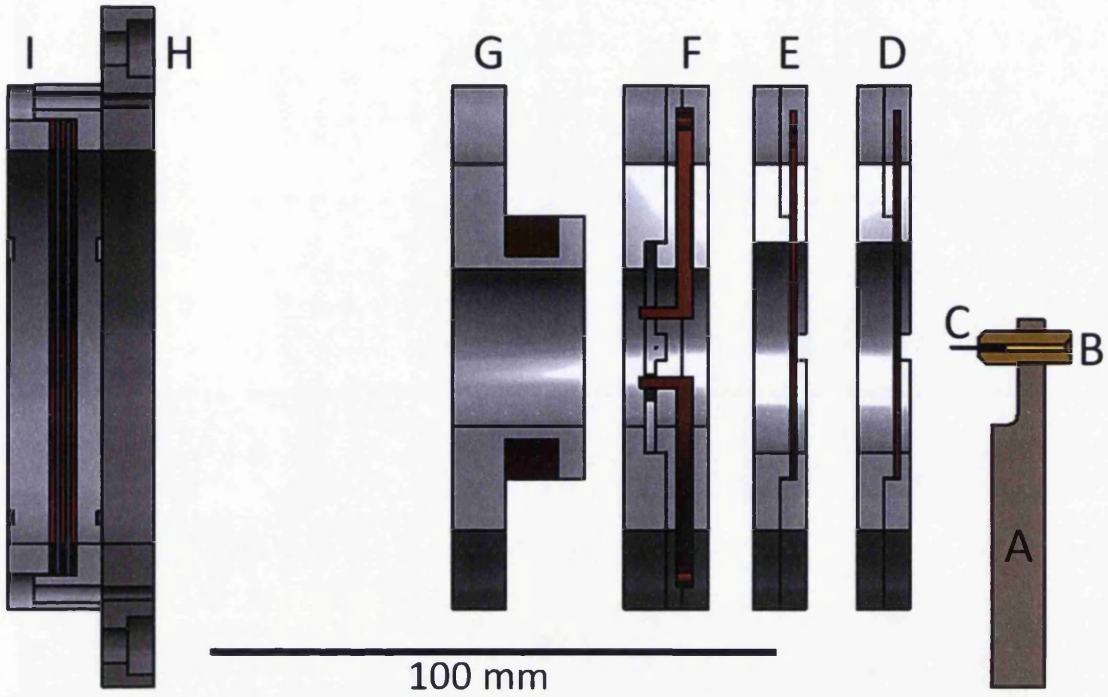

Figure 6.5: Section view of the completed biprism assembly to scale. The nanotip (C) is mounted pointing directly though the apparatus as opposed to perpendicular as in the case of chapter 5. The nanotip is supported by a BeCu push-fit connector (B) inserted into a PEEK insulating piece (A) with the connection wire entering the connector from behind. This is then in turn connected to a 316 stainless steel rod welded to a flange mounted on a 3-axis translation stage which is bolted via an adapter to the main cross, allowing free positioning of the tip to enable alignment to the electrode apertures. (D) and (E) are the accelerating electrodes, (F) the biprism and holder and (G) the magnetic lens. The grounded collar (H) supports the detector (I).

of holes in the mounting piece which secures them, and connected to an external power supply (Thurlby-Thandar QL355T) via feedthroughs to provide current. The completed apparatus is shown in figure 6.6.

High voltage to both the tip and accelerating structure is provided by a pair of high voltage DC power supplies (Spellman MP30N24). These are capable of delivering a maximum of -30 kV at 100 μA and a stability of 0.007%. The output of these supplies is determined by a programming voltage, delivered by a pair of Thurlby-Thandar QL355T low voltage supplies chosen for their precision (better than 1 mV with 0.35 mV rms noise) and transferred via custom made series of resistors that allows one control voltage to be used to raise the output of both high voltage supplies together, and the other control voltage to set the difference, minimising the risk of arcing between the tip and first electrode.

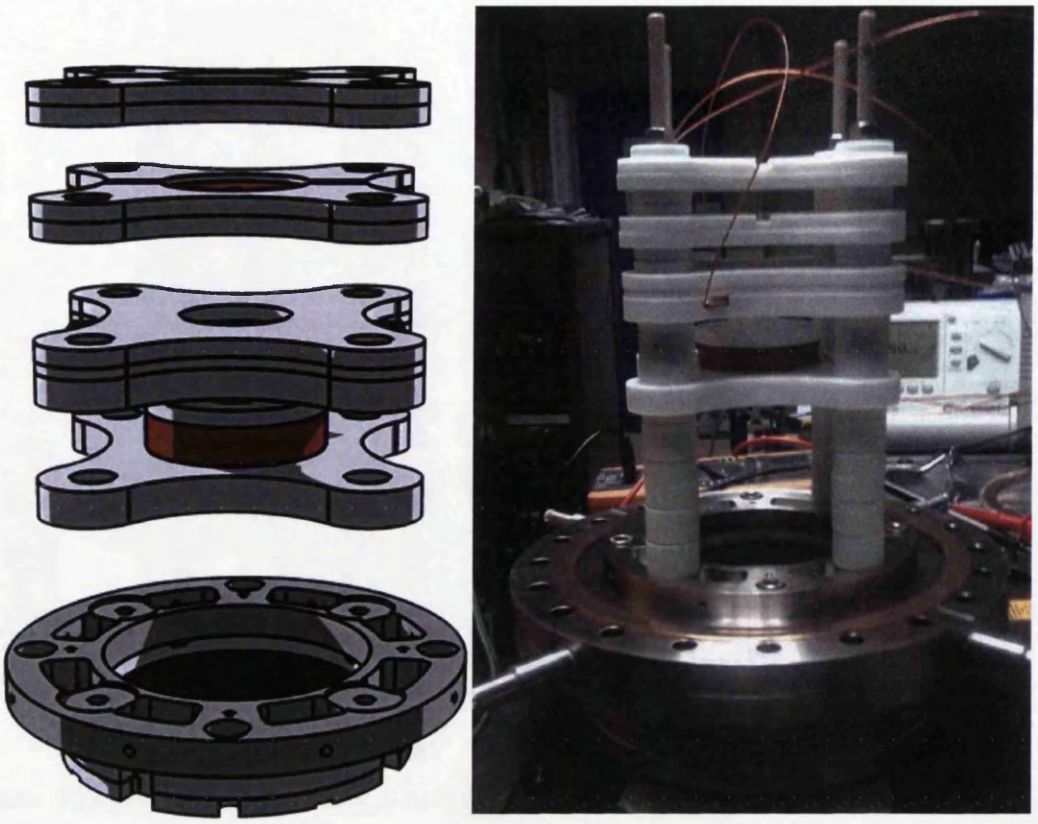

Figure 6.6: Rendered design of the biprism modules for off-axis holography with the constructed instrument for comparison.As with the VMI, the assembly process was conducted to full UHV standards with all components being treated with solvent before being inserted into the chamber. The detector itself was assembled in identical fashion to the procedure described in chapter 5. As with the VMI assembly the rods were then inserted into the collar upright and alternating male and female ceramic bushings used to define the separation of the components from the detector. The separation of the components is chosen to be convenient to assemble using standard bushings. Nuts were used at the end of the rods to secure the stack in place. Kapton wires were attached to each of the accelerating electrodes via the small hole on the tab, and connected to the appropriate feedthroughs after insertion into the chamber. The solenoid on the magnetic lens was manually wound.

6.3 Experimental procedures and results

The apparatus was initially tested by applying a high negative voltage to the tip to induce DC field emission. The first electrode was used as a grounded anode with current measurements being performed by a high resistance electrometer (Keithley 6517A) to verify field emission and provide a mechanism for Fowler-Nordheim measurements to verify tip sharpness as discussed in chapter 2. This allows alignment if the tip to the electrode apertures to be performed by manoeuvring the tip into position such that the signal received by the electrometer drops to zero and the

beam becomes clearly visible on the detector.

The main experiment was conducted at the Artemis Laser Facility as discussed in chapter 3. Following installation at the facility a new tungsten nanotip was inserted and, following pumping to 10^{-7} mbar a Fowler-Nordheim test was performed using electrode E1 as the anode, as shown in figure 6.7 A. This verified that the upper limit on the tip radius of curvature was $R \leq 163$ nm with a predicted real value $R \leq 54$ nm. As the Artemis beam had not been used to generate electron bunches from a nanotip before, this tip was then treated as sacrificial to determine the range of pulse energies at 30fs over which the tip could be made to stably produce electrons before damage occurred. Following destruction of the stable tip laser driven emission was obtained from the remaining wire (albeit without the coherence of a point-like source) and used to check the alignment of the beam through the biprism by altering the wire voltage and observing the effect for a variety of tip positions.

A second tip was then inserted and verified by the Fowler-Nordheim technique (shown in figure 6.7(b)) to have a maximum possible radius of $R \leq 241$ nm with a predicted real value of $R \leq 80$ nm. Laser driven emission from the tip was induced by lowering the laser power to 170 mW with a combination of an aperture and neutral density filters. A lens with a highly reflective coating was used to focus the beam, reducing the power onto the tip to 40 mW (giving a pulse energy of 40 μJ) in a beam of 3 mm FWHM diameter. The lens had a focal length of 25 cm and the laser grating compressor wasadjusted to produce an optimised pulse with a duration of approximately 30 fs giving an intensity of 1.9×10^{10} Wcm^{-2}. The beam was aligned through the letterbox windows with crosshairs and then onto the tip using the shadow in the exit beam. The focus was positioned such that the diffraction pattern in the laser exit beam arising from the tip (which appears as dark fringes in a diagonal cross) was barely visible, avoiding placing the full intensity squarely onto the tip and reducing the risk of damage.

As with the initial testing it was necessary to verify that it was possible to produce a stable laser driven pulsed electron beam aligned centrally onto the biprism wire. This was verified by applying a voltage to the wire; a negative bias splits the electron beam in half and causes the resulting beams to diverge, making the position of the wire easily visible. A positive voltage will result in crossing of the split beams. Both of these scenarios are displayed in figure 6.8 for a variety of bias voltages, demonstrating the effectiveness of such a wire. These images of the beam are not magnified to best display the effect, so no fringing is visible.

Unfortunately conditions under which fringes could be viewed were not achievable for this configuration due to vibration issues, a lack of magnification and sig-

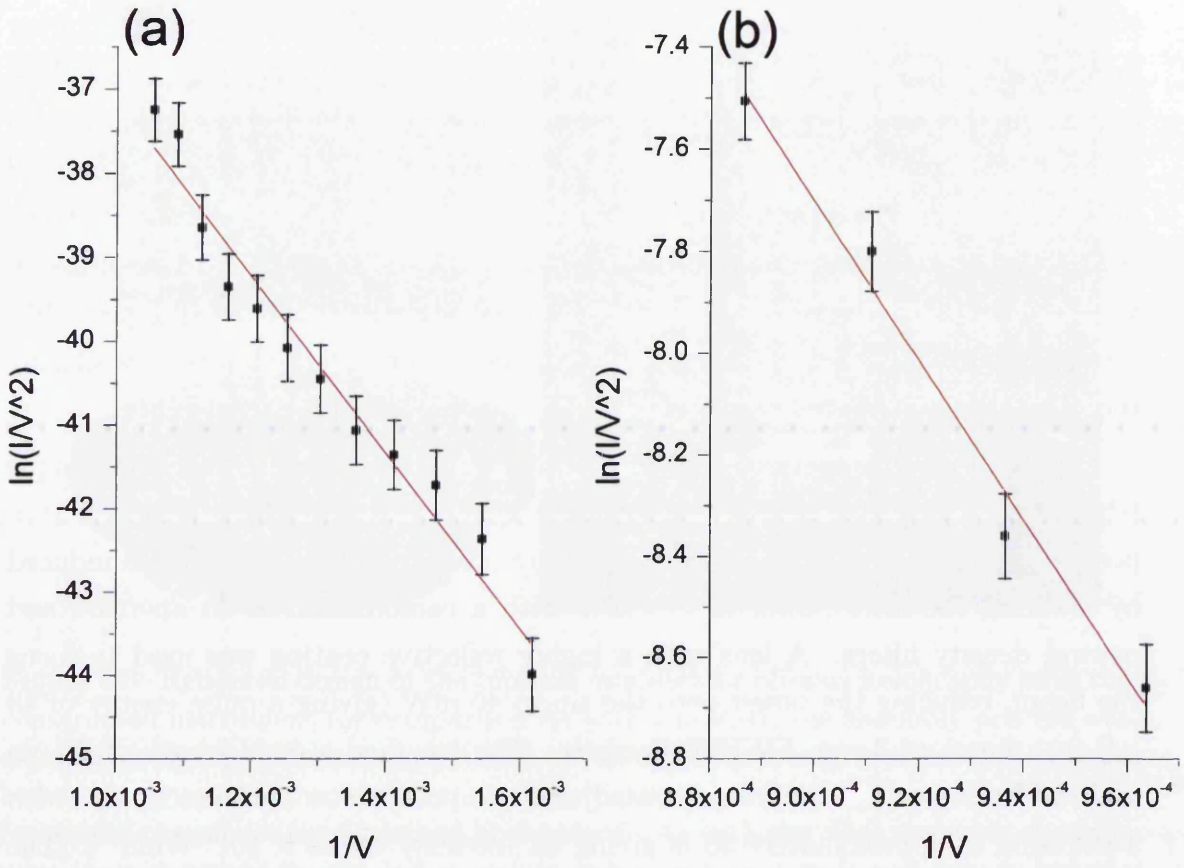

Figure 6.7: Graphs showing Fowler-Nordheim measurements used to characterise tip sharpness before attempting high energy off-axis holography. (a) Measurement of the first tip, with a gradient value of -10551.1 V suggesting a kR of 163 nm and, assuming in the worst case scenario that k=3, a value of R of 54 nm. (b) Measurement of the second tip, with a gradient of -15686.4 V suggesting a kR of 241 nm and, again assuming in the worst case scenario that k=3, a value of R of 80 nm. Only four points were obtainable from the second tip due to the field emission being particularly unstable. There are significant fluctuations in the measured current, although they are difficult to quantify due to the changing nature of the signal. The data above was collected at points of unusual stability where possible i.e. where fluctuations were less than 1% for at least 10 seconds. Currents were recorded via a high precision electrometer (Keithley 6517), with each data point representing the average of 100 current readings to minimise inaccuracy caused by fluctuations.

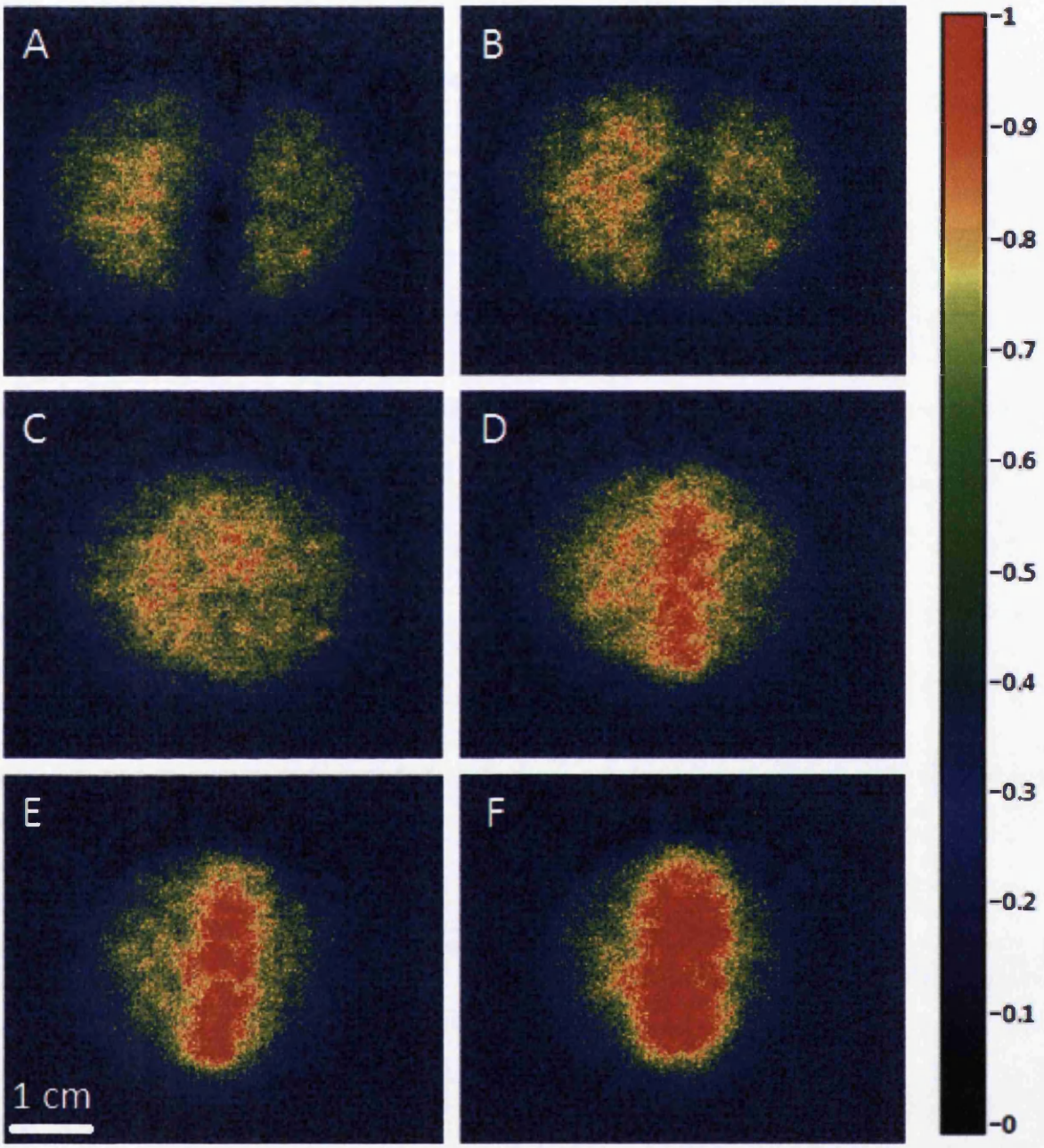

Figure 6.8: Image of electron beam for a variety of biprism wire voltages: A= - 60 V, B= -30 V, C= 0 V, D= +30 V, E= +60 V and F= +90 V. The negative voltages clearly allow the position of the wire to be seen, and the positive voltages clearly show the resulting split beams being overlapped. No fringing is visible due to a combination of insufficient magnification from the magnetic lens and space charging effects within the detector. It is also possible that a significant component of the electron emission was thermionic in nature, which is less coherent.

nificant space-charge issues within the detector. The magnetic lens did not have sufficient focusing power to enlarge the image enough to make the fringes visible due to the large aperture, achieving significant magnification required a large current which in turn led to rapid heating of the coil making the lens unusable within seconds, as evidenced by a sudden rise in chamber pressure. The detector could not be reconfigured to eliminate this problem due to the limited beam time available at the Artemis facility, however the limitations were noted and corrected using the detector design presented in chapter 8.

The space-charge issue arises from two sources, space-charge during flight and smearing due to the large distance between the micro-channel plates and the phosphor screen, replicating one of the issues listed in chapter 5. The issue with space-charge during flight was ultimately caused by the need for a large number of electrons per shot to be emitted in order to facilitate a usable detection rate due to the relatively low repetition rate (1 kHz) of the Artemis laser. This experiment highlighted, even more so than the work presented in chapter 5, the devastating effect that significant space-charge has on the ability to actually use an electron bunch for imaging, as well as issues caused by space-charge within the detector.

There were three key decisions made as to the future direction of the project based on the outcomes of this experiment. The first was that it was decided to redesign the detector to enhance the spatial resolution, as the original design as detailed in chapter 5 features large tolerances and could be significantly miniaturized to improve spatial resolution (discussed further in chapter 8). The second was the decision to switch to a higher repetition rate, lower energy laser system to produce fewer electrons per shot. The lower pulse energy of such a system would also make damaging the nanotip source significantly less likely, as well as reducing space-charge both at source and in flight. For this experiment the use of a 1 kHz repetition rate system necessitated the emission of a few hundred electrons per shot to achieve a usable signal, although the exact number is unknown. Reducing this to ten or fewer electrons per shot at higher repetition rate would allow an equally bright signal at the detector with minimal space-charge disruption.

The final outcome was the highlighting of the need for vibration isolation. The emission from the tip was generally very unstable and this has been attributed to the long arm upon which the tip is held which is linked directly to the vacuum chamber and is therefore susceptible to carrying vibrations originating form the pumps. A revised design to reduce this issue is detailed in chapter 8.

6.4 Ponderomotive holography

6.4.1 Principle of ponderomotive scattering

Ponderomotive holography is the name given to a holography technique where the perturbation is ponderomotive in nature, in that it consists of the force of an electric field arising from a laser pulse acting on an electron in flight. The nature of this interaction was first determined by Kibble in 1966 [269], who determined that the ponderomotive potential is given by [270]:

$$U_P(\vec{x},t) = \frac{e\vec{A}_0^2(\vec{x},t)}{4m_e} = \frac{e^2\lambda^2}{8\pi^2 m_e \epsilon_0 c^3} I(\vec{x},t) \tag{6.2}$$

where $\vec{A}_0$ is the peak vector potential, leading to a ponderomotive force of

$$F(\vec{x},t) = -\frac{e^2\lambda^2}{8\pi^2 m_e \epsilon_0 c^3} \nabla I(\vec{x},t) \tag{6.3}$$

where e and m are the electron charge and mass, and λ and I are the laser wavelength and intensity. It is immediately obvious from equation 6.3 that the ponderomotive force is extremely small, for a typical 800 nm laser pulse the constants combine to approximately 10^{-36}, indicating that an extremely high gradient of intensity is required to produce a noticeable force acting on an electron. The ponderomotive effect induces a phase shift between the paths of electrons in the vacuum and those in the laser focus. This difference is given by [270]

$$\phi_A - \phi_{A=0} = -\left[\hbar \frac{e^2 \vec{A}_0^2}{4m_e} T\right]^{-1} \tag{6.4}$$

where ϕ is the phase and T is the time spent by the electron in the laser focus.

Ponderomotive scattering is difficult to perform, as it relies on precise timing of the arrival of the electron bunch and laser pulse at the chosen interaction site, as well as careful spatial control of both beams. As there is generally no reliable indicator of overlap (such as a noticeable shadow in the laser beam) other than observing a change in the pattern caused by the electrons upon arrival at the detector, the overlap points in both the spatial and temporal regimes can be extremely difficult to determine. Furthermore when overlap is not achieved it is non-trivial to determine whether the discrepancy lies in the spatial or temporal alignment, or indeed in which direction adjustment needs to occur. The final issue is that, as is clear from equation 6.3 inducing a noticeable perturbation to the electron bunch requires an extremely

high laser intensity, with a single laser pulse of the order of 10^{16} Wcm^{-2} required as an absolute minimum to produce a significant detectable deflection (on the order of a millimetre) for 800 nm light [271]. It is also therefore possible that overlap is achieved but that the laser intensity is too low such that the resulting perturbation is not noticeable.

This may in part be solved by using the creation of a ponderomotive grating [272] as shown in figure 6.9(b), an object which arises when a pair of counter-propagating laser pulses are used in place of a single high intensity pulse. When the pulses are coherent (readily achieved by being derived from the same laser) the electric fields combine to form a series of constructive and destructive fringes. For the few femtoseconds in which these fringes exist they form a grating structure where incoming electrons may scatter from the constructive fringes, known as the Kapitza-Dirac effect [273–275]. The ponderomotive force arising from the counter-propagating pulses is approximated [272] by

$$F(x,t) = \frac{I_0 e^2 \lambda^2}{8\pi^2 m_e \epsilon_0 c^3} \exp\left(-\frac{t^2}{2\omega_t^2}\right) \exp\left(-\frac{x^2}{2\omega_t^2 c^2}\right) \sin(2kx) \tag{6.5}$$

where the two laser pulses are assumed to be identical, I_0 is the peak intensity of each laser pulse, $k = 2\pi/\lambda$ and $\omega = 2\pi c/\lambda$. Equation 6.5 considers only the force in the lateral direction of electron travel, which dominates over the forces in the longitudinal direction and the vertical direction defined as parallel to the fringes. In this case the ponderomotive force can be a factor of 10^2 higher than in the case where a single pulse is used, allowing lower intensities readily producible with tabletop femtosecond laser systems to be used. The distance is drastic, in the single pulse case laser energies on the order of 10 mJ are required to achieve sufficient intensities, whereas by using counter-propagating pulses measureable deflections have been recorded using pulse energies as low as 135 μJ [272].

Both of the single pulse and the grating method can be used to measure the length of the temporal electron bunch [271, 272]. Applying a single pulse to the electron bunch should cause a change in the profile of the electron bunch allowing extraction of the bunch length by sweeping through a series of delays between the arrival time of the laser and electrons, albeit with significant uncertainties [271]. Using a ponderomotive grating follows a similar method. As the grating is short lived relative to the length of the electron bunch, the bunch length can be measured by scanning the relative delay between the creation of the grating and the arrival of the bunch, and measuring the range over which a perturbation to the bunch arises from the ponderomotive effect of the grating [272]. As detailed in the sections below,

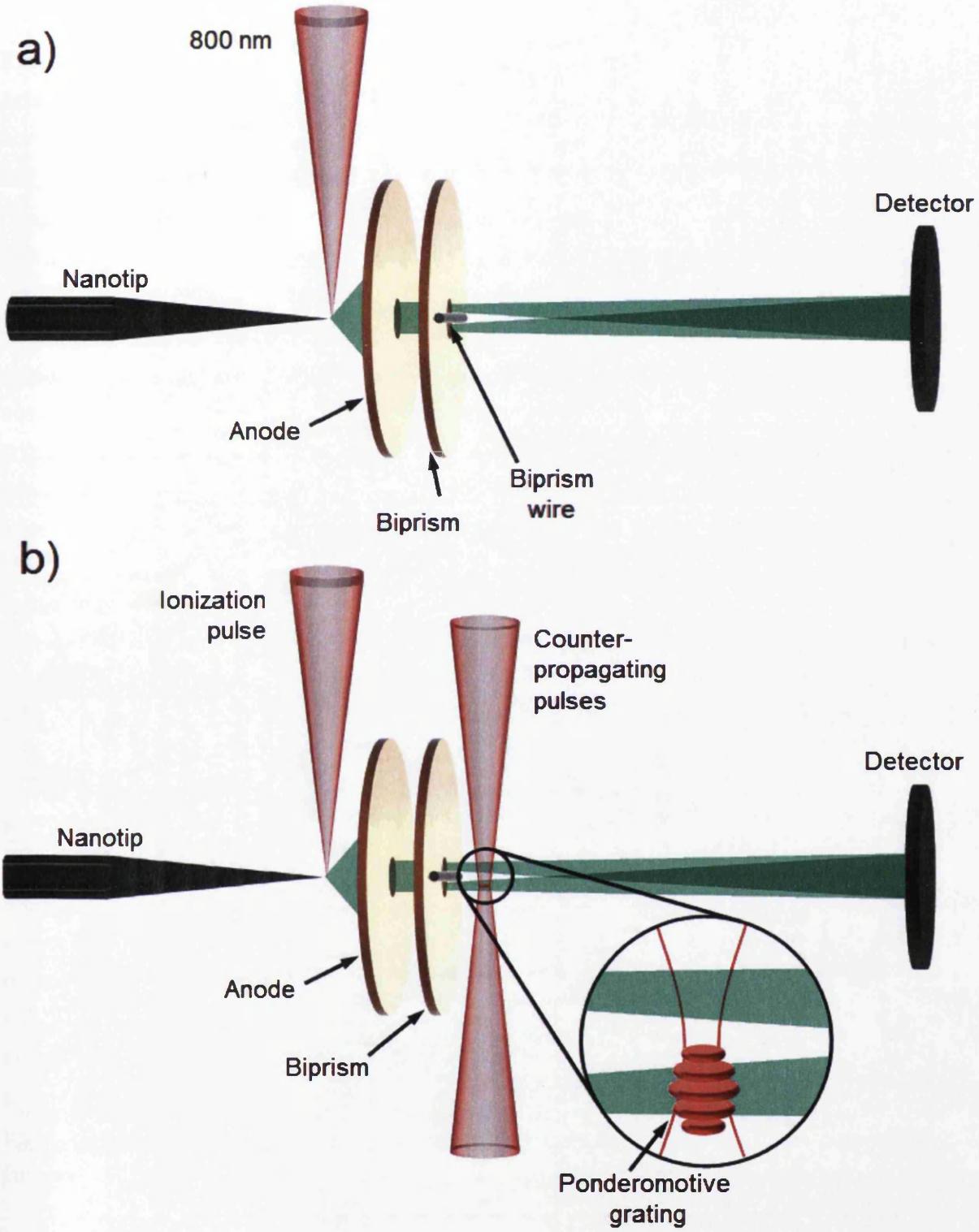

Figure 6.9: a) Illustration of the principle of laser driven electron holography from a nanotip. b) Illustration of the principle of using counter-propagating pulses to introduce a ponderomotive perturbation into one arm of the split electron beam.

however, we were unable to replicate the effects detailed in [271] and [272].

6.4.2 Attempted ponderomotive scattering

The optical path was reconfigured to the layout shown in figure 6.10. This arrangement is slightly simplified from the one used in the experiments which featured additional alignment mirrors after the delay stages, these are omitted for clarity. The vertical alignment of the apparatus within the chamber made it necessary to align the two beams forming the ponderomotive grating via periscope and a pair of mirrors on a table each side of the chamber, with access via thin elongated windows.

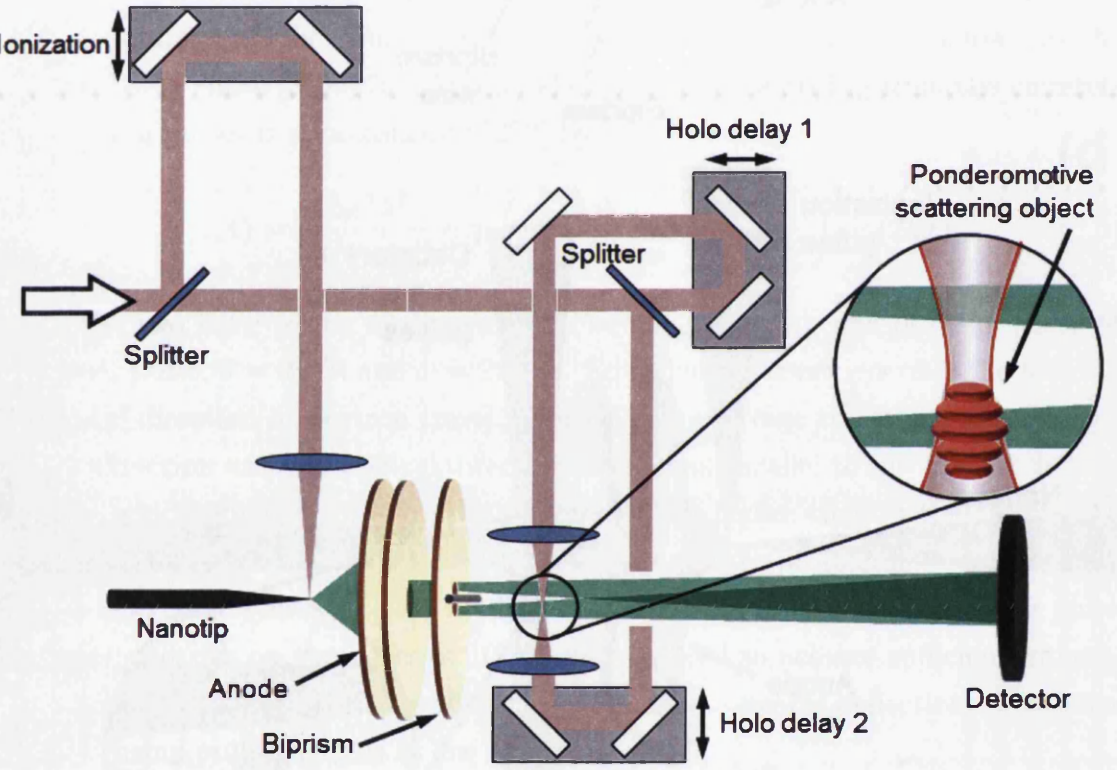

Figure 6.10: Illustration of the beam layouts used for attempting to perturb electron holography using a ponderomotive grating. The beam paths are simplified to show only key components and omit additional alignment mirrors for clarity.

The previous attempts at splitting and recombining the electron beam by adjusting the voltage on the biprism wire were repeated, with the addition of the pair of gating pulses. The delay stage designated "Ionization" is used to define the arrival time of the electrons at the desired interaction point with the grating. The two holography delay stages than define the relative arrival times of the two grating pulses, allowing the spatial position of the ponderomotive grating to be adjusted.

Unfortunately no usable results were obtained for this part of the experiment as it was impossible to determine whether successful spatial and temporal overlap was achieved between the arrival of the electron bunch and the creation and position of the ponderomotive grating. The search for an effect arising from the grating relied on trying to observe a change in the image on the detector as delays were scanned. With the image on the detector relatively blurry and lacking fringes arising from the holography any change may have been far too small to observe.

Despite the lack of results this experiment proved useful as it narrowed the options for keeping the electron bunch length short for future experiments. Of the various techniques discussed in chapter 2, ponderomotive compression was actively considered as a viable option as it would have allowed countering of space-charge without the need for expensive RF compression systems, easing the restriction of having a small number of electrons present in the bunch and allowing the use of a lower repetition rate laser system. As a direct result of this experiment highlighting the difficulty of ponderomotive control, and in combination with the issues highlighted when attempting to obtain interference fringes, the idea was abandoned in favour of using a higher repetition rate laser system and lower population electron bunches to limit space-charge in future experiments, in particular those detailed in chapter 8.

6.5 Conclusions and Outlook

This experiment cannot be considered a success due to the inability to resolve interference fringes in the electron beam. This has prevented this experiment from obtaining a value for the coherence angle. In addition no reliable measurements of the length of the electron pulse could be made due to lack of a visible effect from the ponderomotive grating. This is the result of a combination of issues which could not have been solved within the time available for the experiment, although several improvements to the apparatus have been suggested to overcome these issues in future.

The issue of space-charge may be solved on two fronts. Smearing due to charge within the detector may be reduced by reducing the distance between the exit of the MCP and the phosphor screen, this gap is a region of high charge density and minimizing the time spent by electrons in this region can only improve the final image resolution. The details of this modification to the detector are discussed in chapter 8. Repulsion between electrons during flight can be resolved by dramatically reducing the number of electrons in the bunch, ideally approaching the single

electron emission per shot regime. This may be naively performed by simply reducing the laser intensity, however the subsequent reduction in signal may is so drastic that even with extremely long integration times the signal is indistinguishable from the noise. This in turn may be solved by increasing the repetition rate of the laser by several orders of magnitude. The Artemis laser is locked to a 1 kHz repetition rate demanding that several thousand electrons per shot must be emitted in order to provide a suitable detection rate. Using a system with a repetitions rate of tens of MHz, such as an oscillator, may allow single electron pulses to occur frequently enough that sufficient signal is obtained in a usable integration time.

In addition there may be some smearing present from vibration of the tip itself. For convenience the tip was mounted on a 3-axis translation stage bolted to the main chamber. Whilst this allows free and easy movement it also couples any chamber vibrations such as those from the vacuum pumps directly to the flange supporting the tip, which may result in a regular oscillation of tip. This may be exacerbated by the long arm leading from the flange on which the tip was supported, as well as the joint between the insulator to which the tip was connected and the metallic arm welded to the flange. This increase in stability would also allow a shorter focal length lens to be used; the resulting tighter focus will reduce the thermionic component of the emission, reducing background signal and allowing the effect of the ponderomotive grating (which will only affect strong-field electrons due to the short time for which it exists) to be more readily observed. This issue has been solved by an adaptation to the chamber discussed further in chapter 8, where the tip mount is secured to the chamber only by a bellows and secured to the optical table upon which the translation stage is mounted. This achieves superior vibration isolation but required a large scale redesign of the chamber and frame.

Finally the lack of magnification requires a new magnetic lens design. The re-

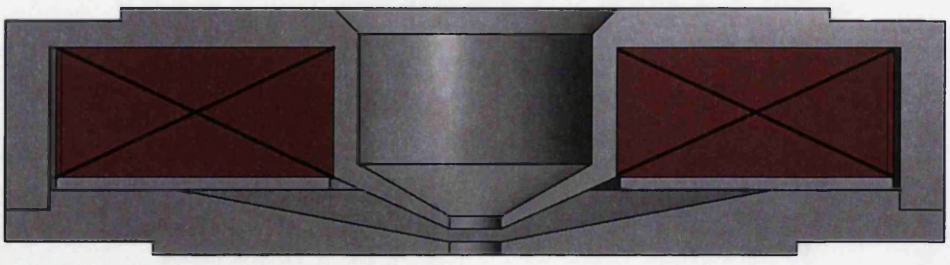

Figure 6.11: Cross-section view of the new magnetic lens design to achieve focusing and magnification of the electron beam after the biprism. The shaping pole-pieces focus the magnetic field, compressing it from being spread over the coil diameter to confined within the central aperture, resulting in an increase in field density of over an order of magnitude.

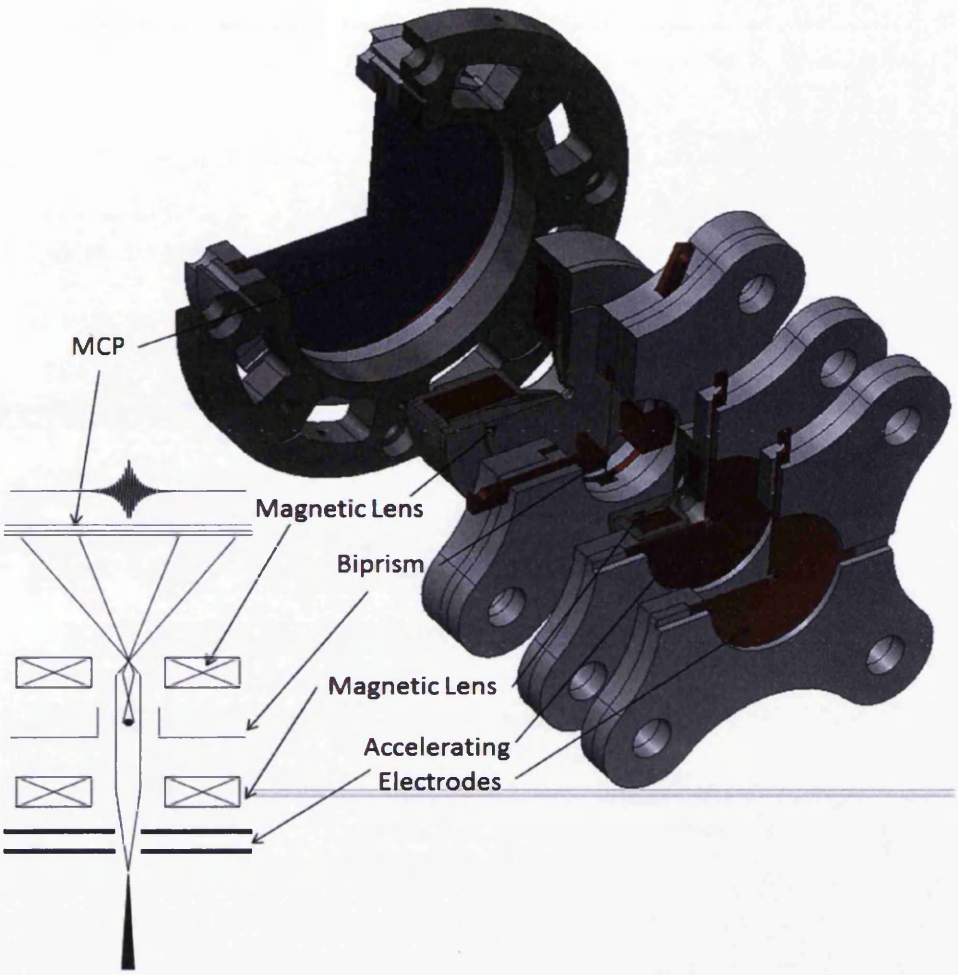

Figure 6.12: Schematic and design of the new biprism assembly showing the positions of the new magnetic lenses and their effect on the electron beam path with optimal focusing fields.

quired magnetic field to achieve the magnification required to resolve fringes in high energy holography is far too large for the current magnetic lens to produce, which was originally designed with a much lower energy experiment in mind. To resolve this issue a pair of new magnetic lenses have been designed capable of achieving a much higher focusing field. These lenses consist of a wire coil encased in a high magnetic permeability metal (Vim-Var) which is shaped to focus the magnetic field into a small region of high density. The design cross section is shown in figure 6.11. The pole piece design is based on immersion lenses commonly used in TEM, which are designed to channel the magnetic field along the arms of the pole piece to achieve maximum flux density in the central hole where the field jumps from one side of the lens to the other. To verify that this pole-piece design is effective a simulation using the Superfish (LANL) suite of codes discussed in detail in chapter 7 has been performed to plot the magnetic field strength on the central axis of the magnet

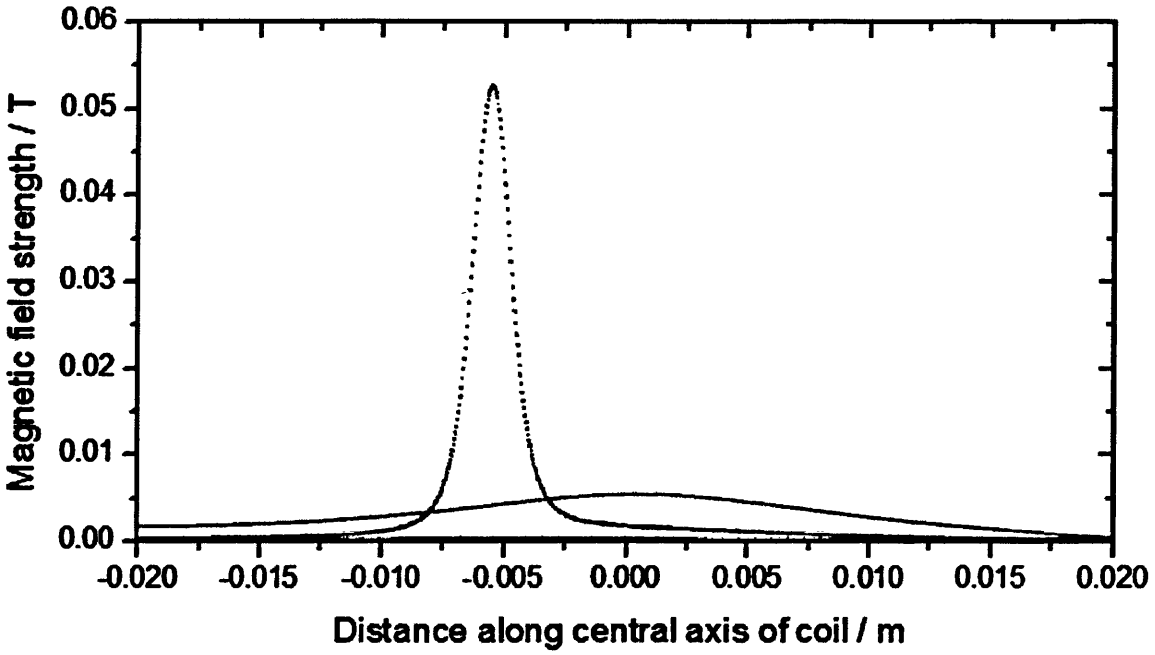

Figure 6.13: Comparison showing the effect the high permeability pole-pieces in figure 6.11 on the strength of the magnetic field. The sharp peak arises when the pole pieces are used, whereas the flatter distribution originates from the coil itself with no additional components.

in comparison to the field produced by a simple coil without the assistance of the Vim-Var. This is shown in figure 6.13.

Two of these lenses have been designed, one to achieve the required magnification and a smaller scaled version to fulfil the optional requirement of being placed between the accelerating structure and the biprism to assist beam collimation and provide additional focusing options. These lenses integrate seamlessly into the existing biprism and mounting design, as shown in figure 6.12, and it is anticipated that these will allow a high enough magnification to obtain interference fringes large enough to be resolved by the detector should this experiment be repeated in the future.

Chapter 7

Modelling of a micro-lens for beam collimation

Coherent Diffractive Imaging (CDI) is a highly effective technique for imaging molecular targets in either ensemble or individual form, and is regularly performed using x-ray photons. The technique is not limited to light however, by passing a beam of coherent electrons through a sample a diffraction effect may be generated given the de Broglie wavelength of the electrons is sufficiently short, as detailed in chapter 1. A key requirement for simplifying the reconstruction of diffraction patterns is that the imaging wavefront be flat, implying that the electron beam must be well collimated, hence when using a nanotip as a source (which produces a diverging beam) a lens assembly near the tip is required to achieve collimation. A suitable lens configuration to achieve this requirement has been designed and preliminary simulations verifying its ability to maintain a sub-100 fs electron pulse under the right conditions have been performed.

7.1 Primary considerations

As demonstrated in chapter 5 the application of a femtosecond laser pulse to a tip produces an electron pulse by strong-field emission. This emission is centred on a well-defined energy but with a substantial bandwidth, defined by the bandwidth of the laser pulse. This causes the electron bunch to undergo temporal broadening in flight, as well as spatial broadening due to being emitted conically over a reasonably large half-angle (the exact value being dependent on the geometry of the tip and the amount of tip surface under illumination). Divergence management (both temporally and spatially) is extremely important as the beam must be well collimated in order for a suitable diffraction image to be obtained, and must be

confined to short bunches to achieve useful temporal resolution. The requirement for collimation arises from the need to have a flat incident wavefront at the sample to ensure efficient diffraction, especially when imaging a pumped process which may be propagating across the face of the sample. In reality a good approximation to a flat wavefront is sufficient, and so diffraction is best achieved with a beam focused in the plane of the detector to minimise the size of the spot arising from the zero order beam.

By placing a lens assembly in front of the tip this pulse may be adequately manipulated in order to perform time-resolved diffraction studies. The purpose of the lens is three-fold: To manipulate the divergence of the beam, to manage the spatial profile of the beam, and perhaps most importantly of all to ensure delivery of the beam onto the target with minimal temporal broadening of the pulse. It is necessary to achieve collimation by altering the initial conical distribution. The lens must also define the beam size when collimated, which should generally be only a few microns across to ensure that only the target is imaged whilst still being large enough to encompass many unit cells if the target has a regular structure.

The broad energy spectrum of the pulse causes a natural temporal broadening during flight, even in the single electron per pulse regime, which may be minimised by ensuring that the pulse arrives at the target as rapidly as possible from the time of emission. Outside of this regime space-charge is the dominant factor, though rapid delivery to target is the primary method of keeping the pulse short regardless of the cause of the broadening. This may be achieved by either accelerating the electrons to high energy (hundreds of keV is common for flight paths on the metre scale, tens of keV are common for paths on the cm scale), or by ensuring that the target is as close as possible to the tip (hundreds of microns for beam energies of a few hundred eV). Either way, this requires that the flight path between the tip and the lens be short to achieve rapid early acceleration and that the lens be extremely compact, allowing electrons to go from the entrance to the exit of the lens as quickly as possible.

Both of these options are fundamentally limited by the need for electrostatic components which must be supplied with a low enough potential to avoid electrical breakdown (which occurs at approximately 10 MV/m for a clean vacuum at 10^{-9} mbar), and a balance where both are partially achieved is a viable option. The initial energy bandwidth arising from the spread of wavelengths in the incident laser pulse can be significant; regenerative Ti:Sapphire amplifiers will produce bandwidths of several tens of nanometres, and the shortest pulse oscillators can produce bandwidths as high as 200-300 nm centred on 800 nm. This can led to an initial energy

spread on the order of 0.5 eV when using a particularly short incident pulse. An electron bunch with this energy bandwidth allowed to propagate unchecked would rapidly expand, causing a significant reduction in the theoretical maximum temporal resolution obtainable.

The above considerations are not necessarily at odds with each other. The requirement that the lens be close to the tip can be advantageous, as confining the collimated beam to a diameter of a few microns is easiest when the lens aperture is small. Ordinarily this would make perfect alignment ensuring 100% electron capture difficult, but ensuring capture of the whole beam become less difficult as the separation reduces. Additionally the requirement that the lens be very compact to get the beam through with minimal temporal expansion matches well with the ability to control divergence; having the components of the lens close together creates a stronger field gradient, allowing easier steering of the electrons from a diverging cone to a collimated beam.

Whilst it is advantageous in terms of maintaining a short pulse length to have the lens and tip as close as possible, there are other considerations which enforce a minimum distance. The first is that if the lens is to be used in a time-resolved configuration there is a necessity that the incident laser pulse onto the tip is not obscured in any way. The exact minimum distance in order to meet this requirement is defined by the focal length of the optics in the incident beam. The positioning must allow the full diameter of the focus to exist between the lens and tip, and the outer diameter of the lens electrodes must be sufficiently small that the edges of the beam are not clipped (creating a non-Gaussian focus).

The second major configuration is the necessity of avoiding electrical breakdown between the tip and the lens. The beam energy may be tailored by adjusting the voltage between the tip and lens; a higher voltage will accelerate the electrons harder and assist in both shaping the beam and maintaining a short pulse, however the field must not exceed the breakdown limit, which varies with pressure but is widely assumed as 10 MVm^{-1} for UHV conditions. This value assumes that the field exists between planar components, and does not account for the field enhancement of sharp objects, and as such a tolerance of a factor of 10 in distance or voltage is advisable for components near the tip. For high beam energies it may be necessary to increase the distance to avoid breaching this limit. Furthermore a large tolerance to the vacuum breakdown limit is required as the commonly quoted figure of 10 MVm^{-1} does not take into account the "lightning rod" effect, where the sharpness of the nanotip and the resulting field enhancement may allow electrical arcing to be triggered at a field strength below the 10 MVm^{-1} limit, with the reduction in the

breakdown voltage increasing with tip sharpness which may change with use.

7.2 Lens Configuration

In order to match the above considerations a relatively simple yet highly compact configuration was designed which utilises components with features on the micron scale yet which are still realistically constructable with modern micro-machining and laser cutting techniques. Whilst many designs were investigated a basic electrostatic arrangement was chosen in order to keep the lens compact. Magnetic lenses are extremely effective at manipulating electron beams, though the need for a coil of wire generally makes the lens too large to facilitate use on femtosecond timescales.

The lens design consists of five elements, built around a pair of circular plates with small central apertures. The other two elements are an insulating divider, the tip and the sample; in order to generate the field structure needed for collimating the diverging electron beam the sample itself forms part of the electrostatic structure. The lens is designed to be static whilst the distance between the lens and tip is adjusted by moving the tip.

The circular plates used in the design are based on commercial models readily available in large quantities for use in transmission electron microscopy, and in practice would likely be manufactured from molybdenum. Such plates would be suitable for a micro-lens due to their stiffness even at extremely low thickness (although stainless steel would be a viable alternative). In order to avoid clipping the incoming laser beam the plates would be limited to $\leq$3 mm outer diameter, not including tabs used to apply voltages, though cutting the plates smaller would allow the tip to be located even closer, to within a few tens of microns. A thickness of 25 μm was chosen to achieve a balance between the need for a thin electrode and the requirement for sufficient stiffness to maintain a flat surface. The plates are separated by 127 μm, a distance chosen to conveniently coincide with an existing ceramic disc whilst also fulfilling the primary considerations of lens design as given above.

The full structure of the lens is displayed in figure 7.1. The design incorporates the sample at a distance of 200 μm from the back of the second plate, which completes the electrostatic structure. The field between the sample and the second electrode plate is the final stage in collimation of the beam. The distance allows the collimation effect to be achieved with relative ease, and yet is large enough to allow a laser to pass between the sample and second electrode plate at such an angle as to allow optical pumping of the sample for time-resolved measurements.

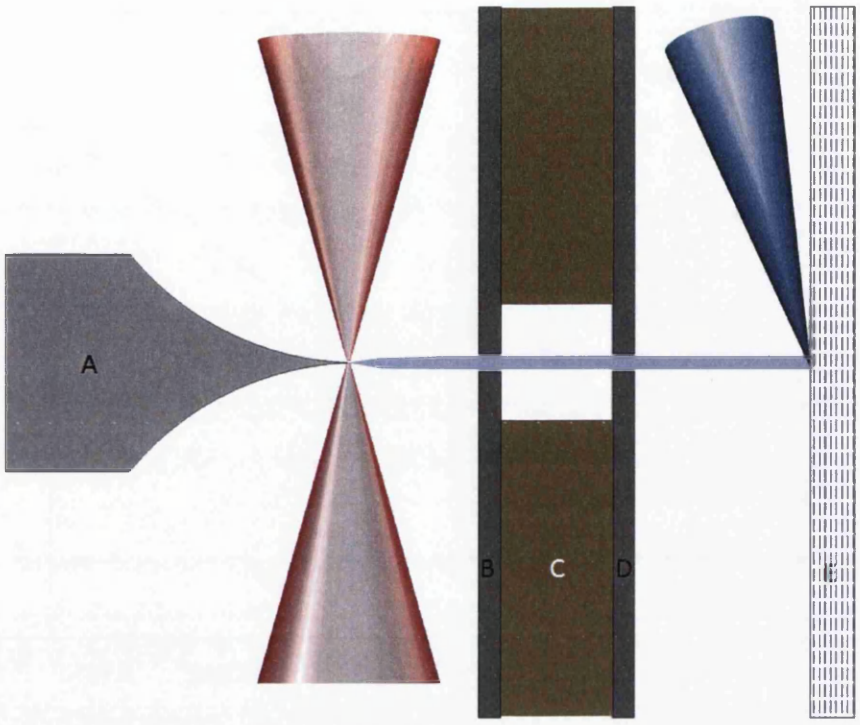

Figure 7.1: Illustrated layout of the proposed electron micro-lens. An electron beam (light blue) is generated from the nanotip (A) by a femtosecond laser pulse (red). Steering and collimation is achieved by a pair thin metallic electrodes (B and D) separated by a ceramic insulator (C). The beam is then directed onto a grid containing the sample (E), which may be optically pumped by another femtosecond laser pulse (Blue). The model is cylindrically symmetric about the central axis of the tip.

For the design given in figure 7.1 to achieve collimation and acceleration of the beam the tip must be held at a high negative voltage. Whilst it is possible to narrow the beam such that collimation is approximately achieved by having decreasing negative voltages through the assembly, much finer control may be achieved by holding the first electrode at a positive voltage and the second at a negative voltage. The sample should then be held electrically grounded to complete collimation.

The typical velocity profile of an electron directed through this electrode stack is shown in figure 7.2. In this case the electron is accelerated rapidly between the tip and the first electrode, with the compression of field lines near the tip causing a nonlinear field and hence nonlinear acceleration. This results in most acceleration happening whilst the electron is near the tip, and is already at 85% of its final velocity before reaching the halfway point to the positive electrode. As the second electrode is negative, the velocity peaks at the first electrode and decreases relatively linearly between the electrodes. It is this sudden switch in the direction of the field gradient where the lensing effect is greatest, pulling electrons from their diverging

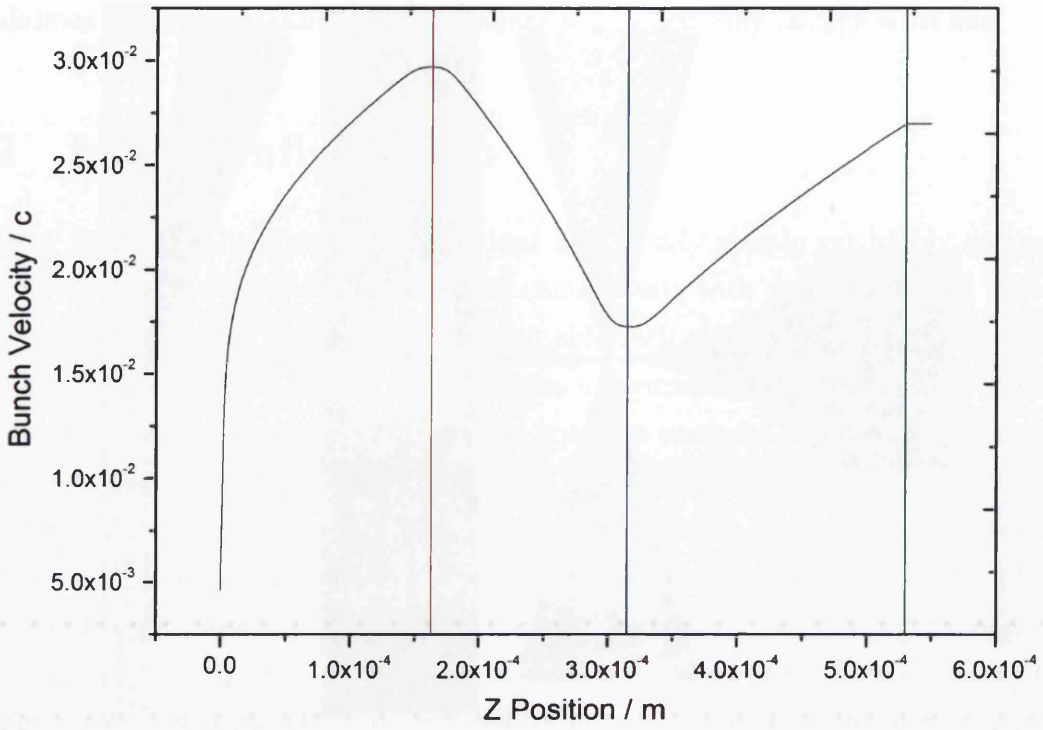

Figure 7.2: An example velocity profile of an electron passing through the proposed electrostatic microlens design. The bunch velocity is given as a factor of c. This calculation was performed using the General Particle Tracer code for a tip voltage of -250 V, a first electrode voltage of +40 V and a second electrode voltage of -110 V using the lens geometry discussed below. The red line shows the position of the positive electrode, the blue line marks the negative electrode and the green line marks the sample.

trajectories into a collimated or focussed beam. After passing through the second electrode the electrons are again accelerated linearly toward the grounded sample, helping to keep the pulse short. This velocity simulation was performed using the lens geometry defined in detail in the following sections.

7.3 Construction of simulations

7.3.1 Building the geometry

The design in figure 7.1 was recreated using the Superfish suite of codes developed by the Los Alamos National Laboratory (LANL). This process utilises four separate codes from the suite (known as Automesh, Poisson, SF7 and WSFPlot) to produce a physical and field geometry through which particles may be flown by finite element trajectory calculation software. These codes are run in sequence by a batch file, calling a series of user created input documents.

The first stage is to use the Automesh code, which take a user-defined geometry and applies a triangular mesh, with the vertices defining the points taken for field calculations. The geometry is defined in terms of conducting objects and empty space, with static or oscillating voltages applied to objects and the mesh applied to empty space. Insulating solids may be defined as empty space. Crucially, the size of the mesh may be defined as a function of position within the geometry. In this case the geometry is created as a two-dimensional plane with rotational symmetry about Y axis as defined by the code, which is chosen to align with the tip axis. The position of the components within the Automesh input is set for all simulation scenarios. Typical output of the Automesh code is displayed in figure 7.3(a).

The second stage utilises the Poisson code, which is a field solver. Its function is to use the mesh structure created by Automesh and the user defines voltages on each object to calculate the magnitude and direction vector of the electric field at each vertex of the mesh. An example output of Poisson is displayed in figure 7.3(b).

The third stage applies the SF7 code, which is a field interpolator used to convert the field produced by the solver into a format which may be used by finite-element software. The mesh and field value information is imported, along with a user created instruction file, which defines a spatial range over which to operate and a set number of points along each axis. The code then measures the field value at these points and creates a two-dimensional function to fit the values by interpolation between the points. The result is a file which matches (in content though not format) a three-dimensional graph with the 2 spatial axes and the electric field magnitude as the third axis, with the local gradient defining the overall field direction at any point. The higher the number of points chosen in the input file, the more accurate the interpolation will be, though at the cost of computational resources. The output of this rectangular interpolation is encoded in such a way as to not readily be displayable, although the contour lines as shown in figure 7.3(b) are a reliable indicator.

The final stage uses the WSFPlot code. This code creates a visual representation of the created mesh, along with field contour lines and directional arrows based on the calculation of the field solver code. This step is not strictly necessary but is an extremely useful diagnostic; the input to the previous steps is text based and the code runs through a batch file (or command prompt) with no visual interface. The output file formats are unique to these codes and may not be readily plotted with most spreadsheet or graphing software. Therefore this code allows the user a simple visual check as to whether the codes have behaved as expected and whether any simple mistakes have been made in the input files causing, for example, objects to

be misplaced or field directions reversed. Figures 7.3(a) and 7.3(b) are taken from the outputs of the WSFPlot code.

The key advantage to using the Superfish suite in this simulation is that it has the ability to accurately account for curved geometries, on the condition that the curve radius is at least an order of magnitude larger than the separation between mesh points. When this condition is met the software is capable of simulating the bunching of field lines around high regions of curvature of the electrodes. This makes Superfish ideal for simulating the field around a nanotip where having a straight or stepped taper in place of a curvature would be too much of an approximation to allow the simulation to retain its validity. This condition may however be violated at the very apex of the tip, where in the single atom approximation the software treats edge of the tip as coming to a point.

7.3.2 Defining electron flight calculations

Whilst previously used codes such as SimION as used in chapter 5 are extremely useful for modelling particle flight through electrostatic systems, even extremely complex ones, the relatively long time-steps used make them unsuitable for situations where measurements such as bunch lengths are anticipated to be on the femtosecond timescale. To solve this issue the code chosen to perform the electron flight calculations was the General Particle Tracer (GPT, Pulsar Physics), specifically developed for designing systems such as particle accelerators and radio-frequency bunchers, where accurately simulating short electron bunches at a variety of energies is required.

GPT, whilst capable of constructing its own basic field layouts, is designed to interface with other geometry and field solving codes, and contains built-in algorithms specifically for utilising the outputs of the Superfish code suite. The first step is to run an import algorithm which takes the interpolated output of the SF7 code and converts it to a format which GPT can use, creating a field map file which the GPT code may the apply to calculations of the forces and field acting on a particle at each time and position step.

The code then utilises an input file which details the initial parameters of the simulation. At this stage the number of particles in the bunch, their initial central energy and a suitable energy spread are defined in both extent and structure, the values of which are discussed in section 7.4. An initial spatial distribution of the bunch is defined as a function of radius and angle to match the photocathode; a curvature of the cathode may also be applied. For photoemission a laser pulse length may be defined to select the emission time, as well as a temporal spread matching

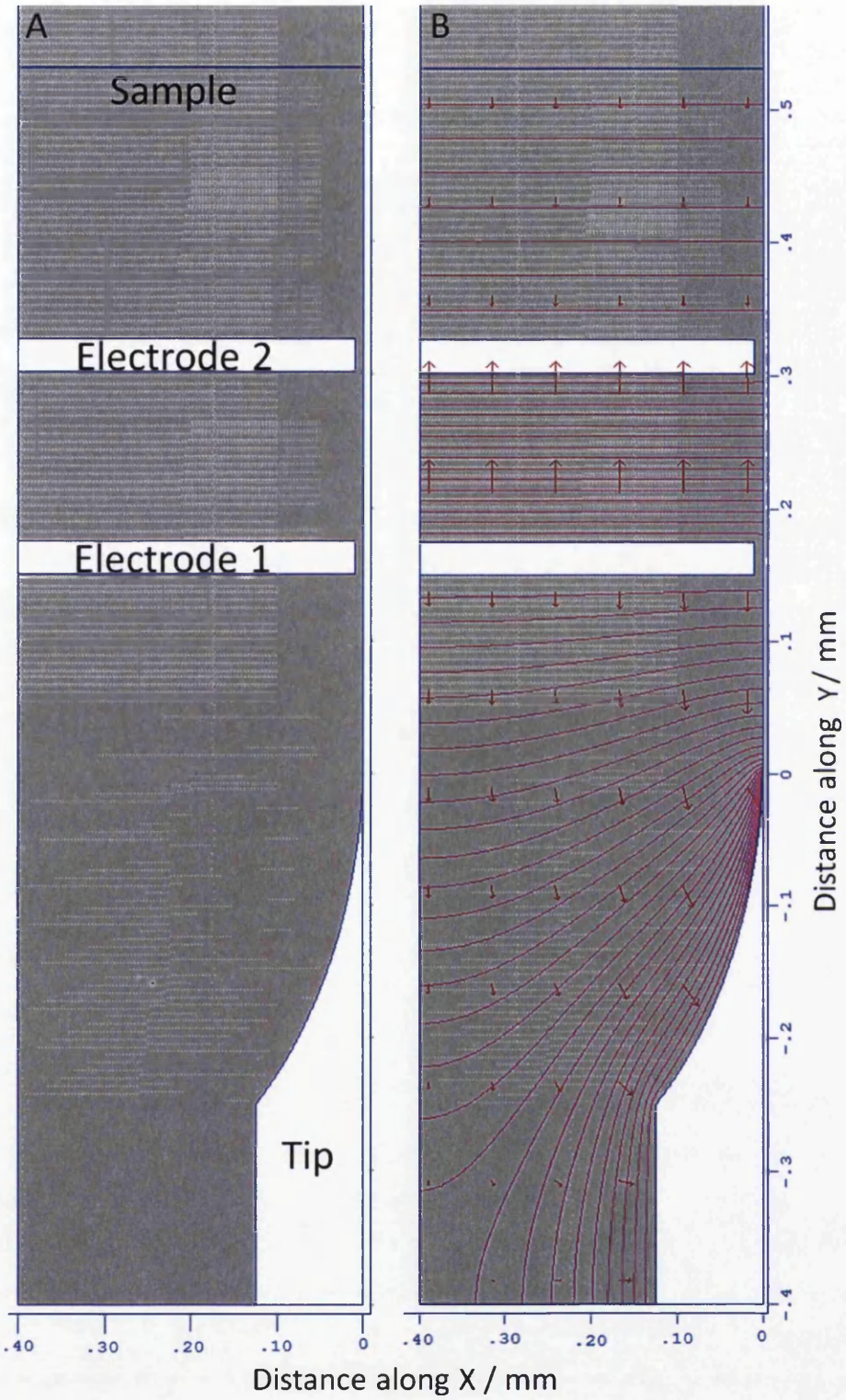

Figure 7.3: (a) Typical output of the Automesh code, showing objects in white, boundaries in blue and the triangular mesh in grey. The mesh is extremely fine relative to the sizes of the objects to ensure accuracy, although the increasing size of the mesh with distance from the point of the tip can be seen in the striping at the top left of the image. The geometry is rotationally symmetric about the right boundary. (b) Typical output of the Poisson code using the mesh presented in (a).

the structure of the laser pulse (typically Gaussian). Other simulation parameters defined at this stage include the algorithm used to calculate space-charge, if any, and the numerical accuracy of the simulation which affects the number of significant figures used at each time step. Finally, the form of output is defined. GPT is capable of recording the output at a plane, or by recording all particle parameters at regular time intervals, necessary if particle trajectory information is required, hence output at each time step was recorded for these simulations.

The GPT code also includes multiple post-processing algorithms that may be applied to the results of the simulations, three of which are used. The first algorithm applies a transpose operation to the results file (if it contains time step data) which allows plotting of the position of each of the electrons in any spatial axis or time against any other. The second algorithm is an averaging code which calculates combined parameters of the bunch at each time step, such as central position of the bunch and average spatial spread (as standard deviation) along each of the axes. Crucially, the average velocity of the bunch may also be recorded, which when combined with measurements of the standard deviation allows the temporal length of the bunch to be calculated. The final post-processing code is a file converter, allowing the results file and outputs of the other post-processing codes to be converted from GPT's own file formats to an ASCII based text format, allowing analysis to be performed in other commercial graphing and spreadsheet software.

7.4 Simulation parameters

In order to simulate the complete system under a variety of relevant circumstances two key parameters were chosen; The laser pulse length and bandwidth as linked parameters defined by the Fourier limit, and the beam energy (adjusted by altering the voltage applied to the tip). For each beam energy, a range of voltages on the electrodes were simulated in order to refine the exact point of collimation. For each of the beam energies the collimation conditions were set and a sweep was performed of the laser parameters.

The laser pulse length and bandwidth is swept through a realistic series of values for a modern Ti:Sapphire system. The values used were 5, 10, 20, 30, 50, 100, 200, 300, 500, and 1000 femtoseconds. This incorporates the range of lengths used in this project from near single-cycle pulses produced by the Artemis hollow fibre, through the 20-30 fs pulses produced by the Orpheus-N, the 100 fs pulses produced by the Libra to the 250-300 fs pulses produced by the Orpheus. As the pulse length is changed in the simulation the bandwidth is also altered accordingly, important as

the energy spread of the electron bunch is defines by the bandwidth. The bandwidths are chosen to be a transform limited match to the pulse-lengths (i.e. the minimum bandwidth which can produce a pulse of given length), defined for a Gaussian pulse such that the time-bandwidth product is 0.44. This is an idealised case, for example the final time-bandwidth product of an Orpheus-N pulse is ≈ 1.17 as reconstructed from the FROG. This discrepancy arises from the assumption that 0.44 is the Fourier limit for a perfectly Gaussian pulse subjected to only first order dispersion which may be readily corrected, whereas real laser pulses are generally not perfectly Gaussian, in both frequency and time domains, and are subjected to second and third order dispersion when passing through materials both inside the laser and compressor and during transfer from the laser to the tip.

Certain parameters as set in the GPT input were common to all simulation runs. The number of particles was set constant at 1000, enough to provide reliable mean and standard deviation values without being too computationally expensive. The central energy of the electrons was set at 5 eV, corresponding to the main peak of emission observed in the results from the VMI in chapter 5 and the work of Hommelhoff *et al* [151]. The electrons were set to be emitted from a curved photocathode chosen to match the parameters of a realistic tip; a hemisphere with a radius of curvature of 20 nm. The centre of the hemisphere was positioned at the same coordinate as the very end of the tip in the field imported from Superfish. The emission sites of the electrons are distributed across hemisphere uniformly as determined by a Hammersley point set. The temporal spread of the pulse was defined as Gaussian centred on t=0 and permitted to extend to $\pm\infty$, with the FWHM being varied according to the laser pulse lengths from 5 to 1000 fs as listed above.

The accuracy parameter used by GPT to control the execution of the simulation was set at 12 (allowing up to 12 significant figures even in exponential notation) to ensure a sufficiently high accuracy. As the accuracy parameter is increased so does the precision of the calculations of electron flight, until results typically converge at parameters of 8-10 and above. Choosing 12 therefore ensures convergence, and is convenient as an initial test demonstrated that 12 was not significantly more computationally expensive than using a lower parameter on a modern processor, making a difference to the simulation runtime of less than 5 seconds.

In all cases the simulation was run from time -500 fs (to allow for the preceding wing of the longer pulses) to a variable end time (altered for each beam energy) to allow easily sufficient time for the electron bunch to pass through the plane of the sample. The GPT code automatically chooses a fine timestep to ensure simulation accuracy, but a step of 100 fs was manually specified for the interval at which results

should be written to the output files, creating of the order of 1000 steps over which to interpolate the trajectories (exact value again varying with beam energy due to the differences in time taken to arrive at the sample).

In all simulations space-charge was neglected, treating all electrons as flying independently. This is a legitimate approximation as with low pulse intensity (on the order of 10^9 Wcm^{-2}) it is possible to achieve an average of a single electron per pulse from the tip, readily achievable using an oscillator to induce photoemission [250] and discussed further in chapter 8. Use of this approximation not only reduces the computational resources required but is desirable for practical purposes, as if the laser intensity is sufficiently high to generate a dense bunch of electrons then Coulomb repulsion is inevitable. This is an extreme disadvantage if the lens is designed to keep an electron bunch temporally short, electron-electron repulsion can only lengthen the bunch, with the magnitude of the effect dependent on both the the initial size of the bunch and the number of electrons. For intense laser pulses the effects of repulsion on the bunch length will far outstrip the effect of the energy spread resulting from the laser bandwidth, and the spatial repulsion along the axis perpendicular to electron flight will affect the final diameter of the bunch and, in extreme cases, whether or not collimation is achieved at all for a given set of voltages. This is a trade-off, however, as using single-electron bunches requires integration over a large number of shots to achieve usable CDI. In this case the length of the bunch at the target is better defined by differences in the arrival time of the electrons due to their initial energy bandwidth.

7.4.1 Determining collimation

A number of beam energies were found for which collimation is achievable with the lens design as given. These were found by setting the tip voltage from -100 to -350V in 50V steps, and altering the electrode voltages until collimation was achieved. This was determined by visually checking the trajectories of the electrons through the lens (an example of trajectories displaying suitable collimation is shown in figure 7.4), and examining the beam size at both the exit of electrode 2 and in the sample plane. A divergence of less than 1 degree between the 2 points is deemed to be suitable collimation.

The simulations demonstrate that collimation of the electron beam into the target is readily achievable with this lens design for a variety of beam energies, using realistic voltages that do not breach the vacuum breakdown limit. These conditions are presented in table 7.1, and were found initially using a 5 fs laser pulse. There is an approximation used with regards to divergence, the electrons were produced

Tip Voltage / V	E1 Voltage / V	E2 Voltage /V	Beam energy / eV
-100	+10	-48	52
-150	+20	-68	82
-200	+30	-90	110
-250	+40	-110	140
-300	+40	-130	170
-350	+55	-155	195

Table 7.1: Table of lens collimation voltages for a variety of beam energies for the configuration given in figures 7.1 and 7.3.

from the end of the tip with initial momentum directly away from the tip along the tip axis. They then obtain a divergence from the shape of the electric field around the tip itself. This discounts the effect of emission site on the initial direction of the electrons.

It should be noted that each tip voltage will provide multiple solutions of the two electrode voltages that satisfy the collimation condition, albeit at different beam energies. It was found that a positive voltage on the first electrode and a negative voltage on the second, such that a velocity profile similar to that in figure 7.2, gave collimation conditions like those displayed in figure 7.4. The set of results presented here follows a regular pattern of solutions. It appears that for every -50 V change to tip voltage the collimation condition is satisfied by a +10 V change to the first electrode voltage and a change of approximately -20 V to the second electrode voltage, with some variation as shown in table 7.1. This combines to give a beam energy increase of approximately 30 V for a -50 V change in tip voltage whilst maintaining the collimation conditions.

These energies and voltages are chosen to be usable in the small dimensions of the lens configuration as proposed. Whilst these beam energies seem unusually low for an electron diffraction experiment, where normally even in the low-energy range several hundred eV is considered desirable, this is a necessary trade in order to keep the lens system compact enough to ensure that the shortest possible pulse is maintained. As the gap between the tip and the first electrode is only 0.13 mm, it is necessary to keep the voltage difference low enough to avoid triggering continuous field emission, which would disrupt the ability to obtain time-resolved diffraction measurements.

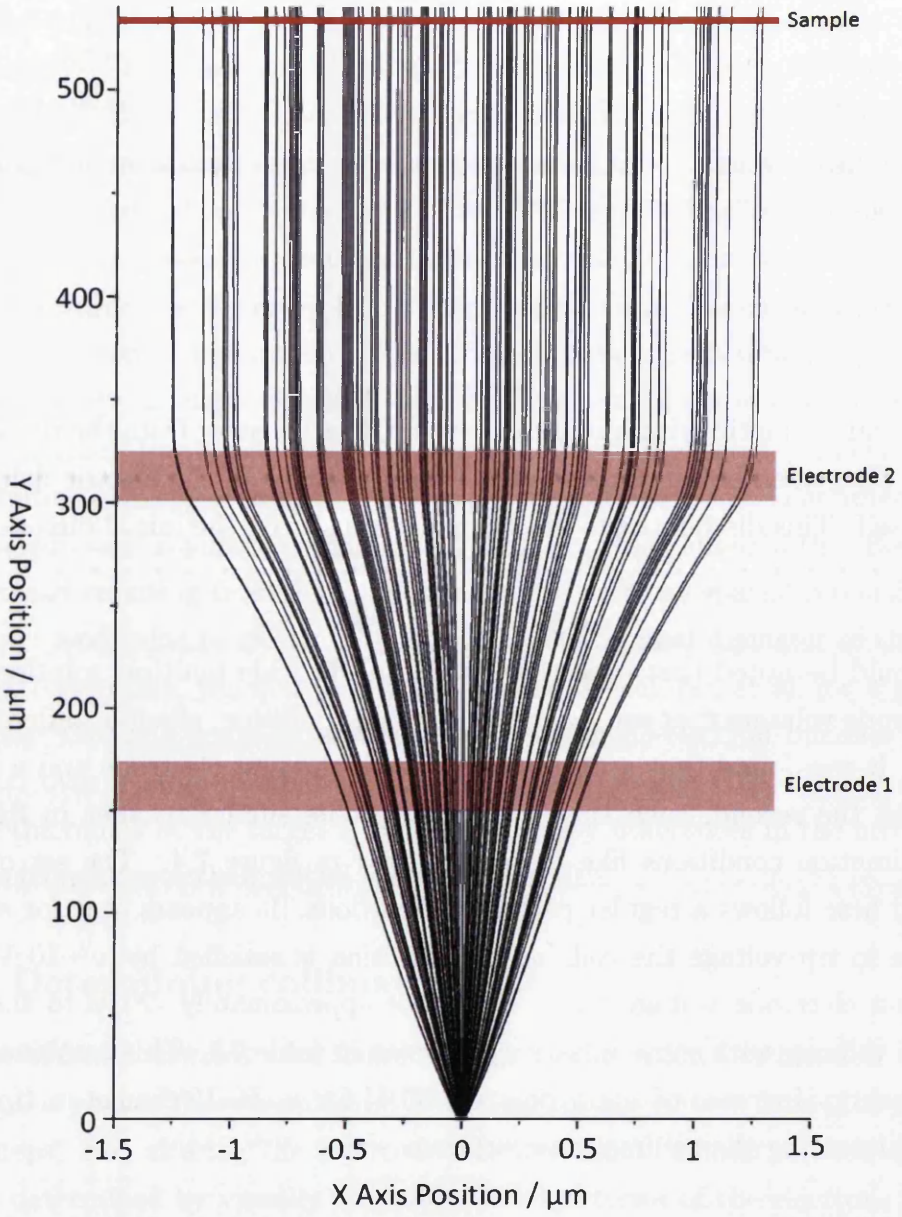

Figure 7.4: Top-down of the electron trajectories as the collimation condition is met. The end of the tip is at (0,0), with the back of electrode 2 at sample at 327 μm and the sample at 530 μm where the trajectories end. The positions of the main lens components are highlighted. The beam is narrow enough that the electrode aperture diameter is larger than the width covered by the figure, so electrode positions are shown as semi-transparent overlay.

7.5 Systematic variation of beam energy and laser pulse length and bandwidth

An extensive simulation was performed whereby the electron bunch length was calculated at the sample plane following emission by laser pulse lengths of 5, 10, 20, 30, 50, 100, 200, 300, 500, and 1000 femtoseconds. This was repeated for the beam energies and voltages given in table 7.1. The mechanism of electron emission was treated in the most simple manner possible; that the emission occurs directly from the field of the incoming laser pulse in such a way that the FWHM of the electron bunch at creation is identical to the FWHM of the laser pulse.

The results of these calculations are presented in figure 7.5. Again the electron bunch length is defined by the standard deviation along the flight axis divided by the mean bunch velocity, and the FWHM definition of the bunch length may be obtained by multiplying this value by 2.3548, omitted here to avoid crowding the graph. It can be clearly seen that for each beam energy there is a definite minimum, suggesting that there is an optimum laser pulse length (and corresponding bandwidth) that produces the shortest possible electron bunch at the sample. Crucially, the laser pulse that produces this minimum is dependent on the beam energy.

The simulations reveal that the optimum laser pulse for producing a short electron bunch in this lens configuration occurs at approximately 20-50 fs, depending on beam energy. This is the balance point between the length of the electron bunch at production and the amount the bandwidth causes it to stretch during flight. The beam energy affects the flight time through the lens, and thus the overall effect of the bandwidth on the length of the bunch. For longer laser pulses, where the bandwidth is small, it is natural to expect (and confirmed by the results) that the bunch length arriving at the sample should have little to no dependence on the beam energy, being created long and expanding only a small amount relative the initial bunch length. At laser pulses shorter than the optimum, however, the bandwidth is large and so is the dominant effect on the length of the electron bunch, causing rapid expansion during flight. In this scenario it is anticipated that reducing the flight time would strongly affect the length of the electron bunch and therefore the effect of beam energy will be highly noticeable at shorter laser pulses, a result again confirmed in figure 7.5.

It is intuitive to expect that for a higher beam energy, the high bandwidth of an ultrashort pulse becomes less disruptive, as the bunch has less time to expand during flight, allowing production by a pulse with a larger bandwidth. This naturally leads to a minimum which occurs at both a shorter bunch length and shorter laser pulse

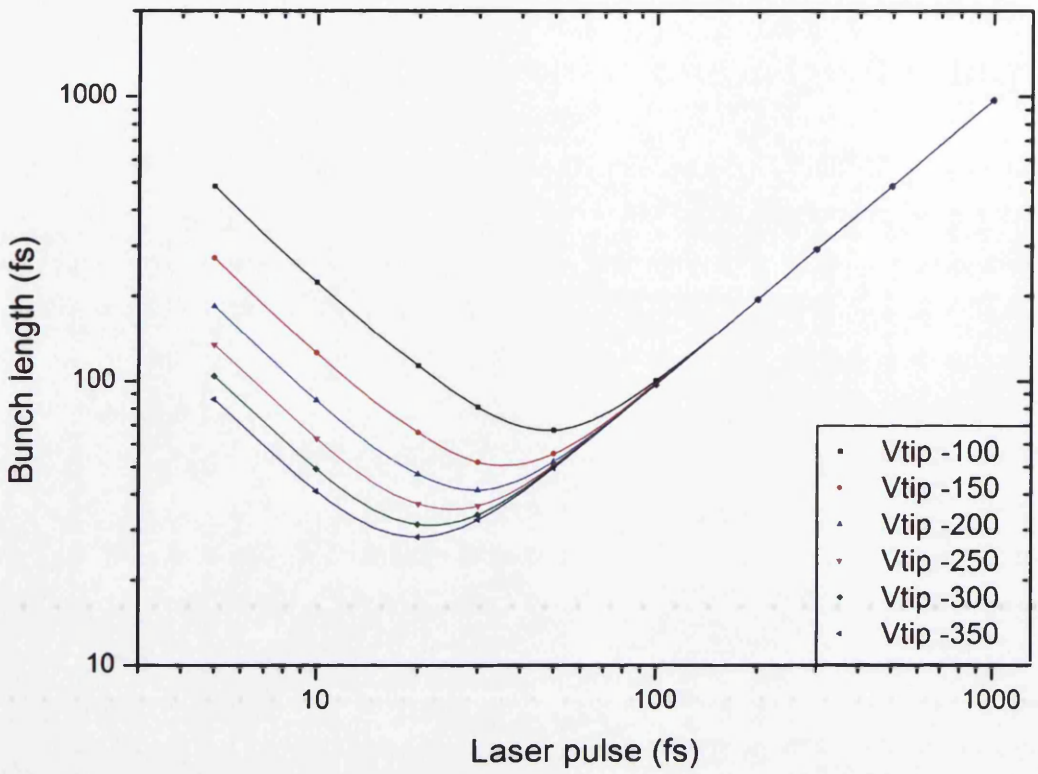

Figure 7.5: Electron bunch length at the sample as a function of laser pulse for a number of beam energies provided by the electrode voltages in table 7.1. Spline fits (500 points, cubic) are included to highlight minimum values and differences at short laser pulses.

as the beam energy increases. Characterizing how this minimum moves as the beam energy is scanned reveals the most efficient set of circumstances under which the lens may be used, as generally it is always desirable to use a laser pulse and beam energy that converge onto the minimum.

Figure 7.7 shows how minimum achievable bunch length for each beam energy scales with the laser pulse used. Each point is the position of a minimum in figure 7.5, with lower beam energies having their minima occur at longer laser pulses. This representation highlights the linear appearance of the dependence. Figure 7.6 shows the data in complete fashion, and the black line in figure 7.7 may be interpreted as running along the minimum of the surface in figure 7.6. It is apparent from the fitting equations to figure 7.5 that there is an issue with the simulation data. The fitting parameters suggest a negative value for the intercept, which is entirely unphysical. This suggests that the linear fit is an approximation, with a subtle deviation from a perfect line warranting either a polynomial or exponential fit to achieve an accurate fitting equation. In order to confirm this simulations were continued by Connor Barlow-Myers, who examined the electron bunch behaviour at

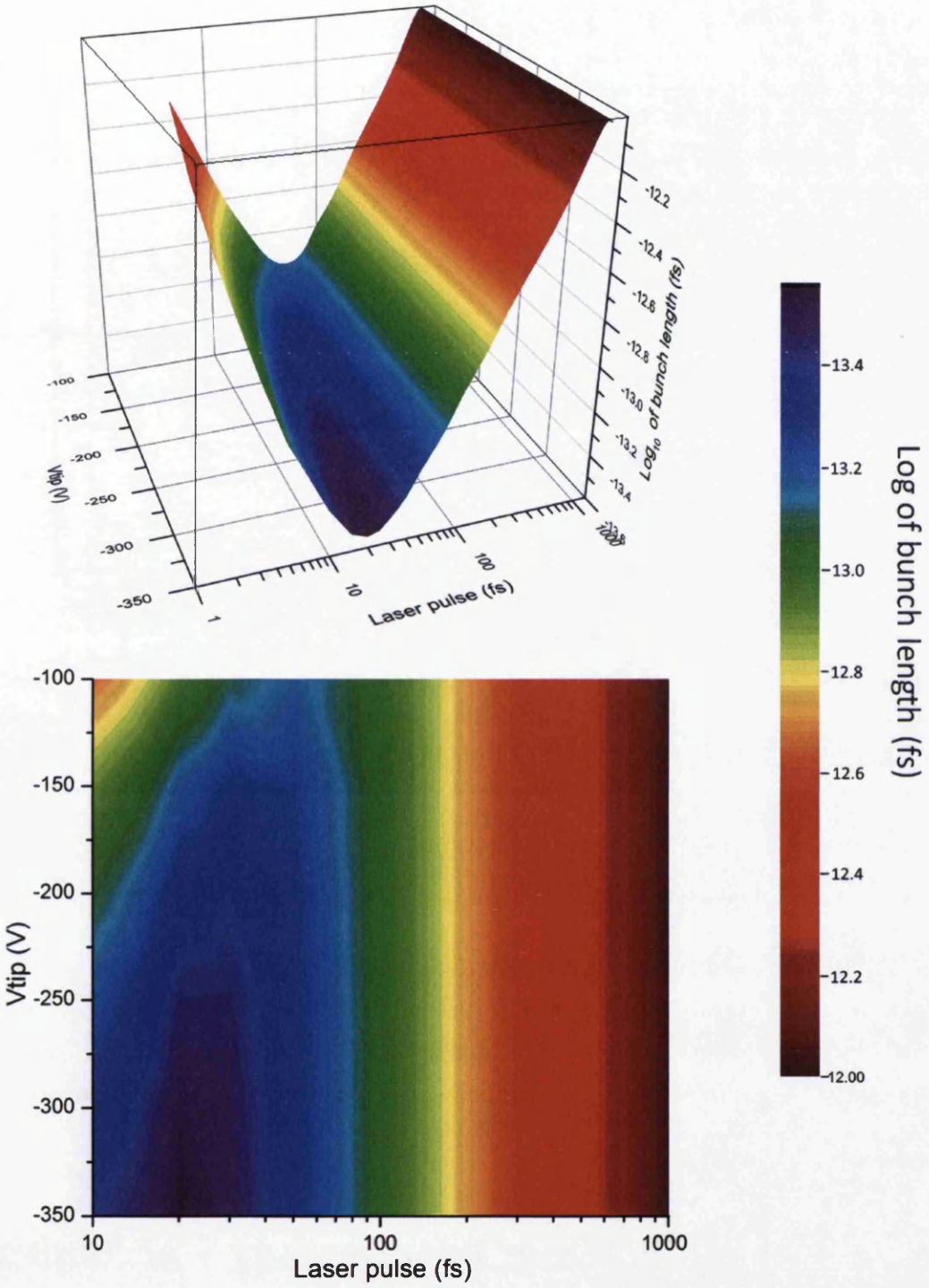

Figure 7.6: Best achievable electron bunch length at the sample as a function of laser pulse and beam energy. The bunch length is defined again using standard deviation, and is presented as the logarithm of the value in seconds, due to a limitation in the graphing software. Both images are of the same surface, the top image highlights the valley shape and the bottom image is a flattened map from above.

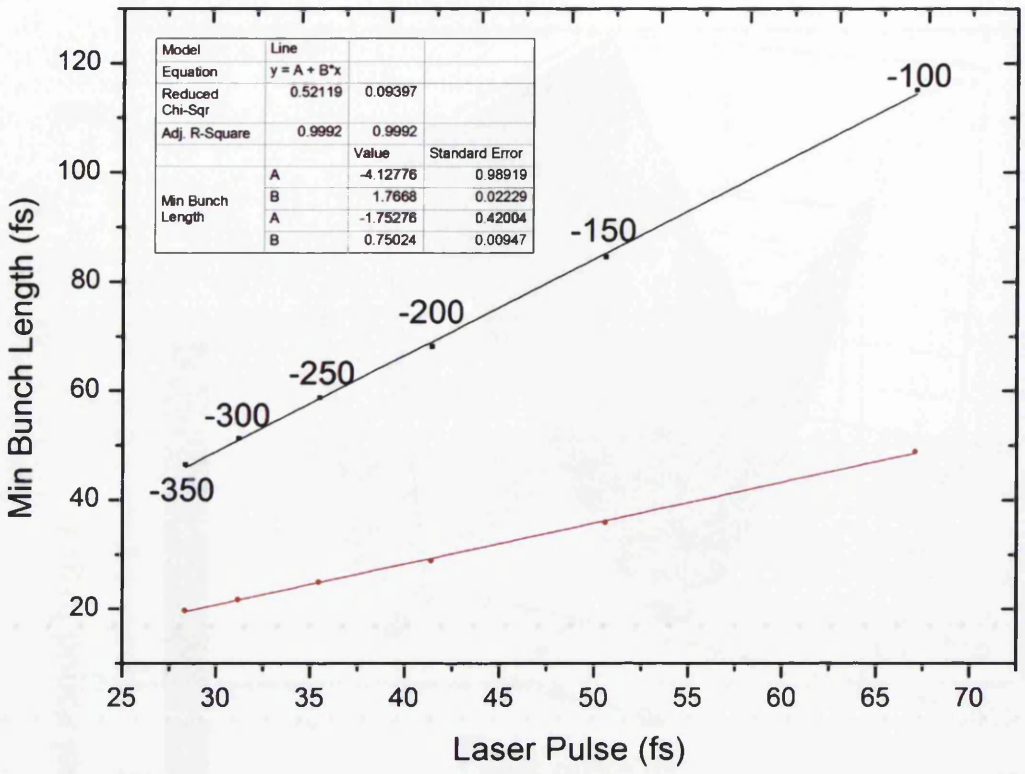

Figure 7.7: Best achievable bunch length at the sample as a function of laser pulse, each data point is the position of a minimum in figure 7.5. The red line represents a direct value of bunch length using the standard deviation divided by the bunch velocity, the black line is scaled to represent the FWHM length of the electron bunch. The point labels represent tip voltage at that point according to the voltages in table 7.1.

higher beam energies, including those unfeasibly high such that breakdown would occur is used, to extrapolate the graph further. This work is ongoing however the preliminary conclusion is that the relationship is indeed slightly nonlinear and with more points taken into account even a linear fit begins to exhibit a positive intercept value.

7.6 Effect of changing beam energy - accounting for 3-photon emission

Whilst treating the electron emission time as being directly correlated to the laser pulse temporal profile is suitable for determining the existence of an optimum point, the work in chapter 5 and work by others [151, 250] suggests that a common mechanism of emission from nanotips by 800 nm light is by the absorption of 3 photons. In multi-photon emission processes the effective laser pulse causing the emission is

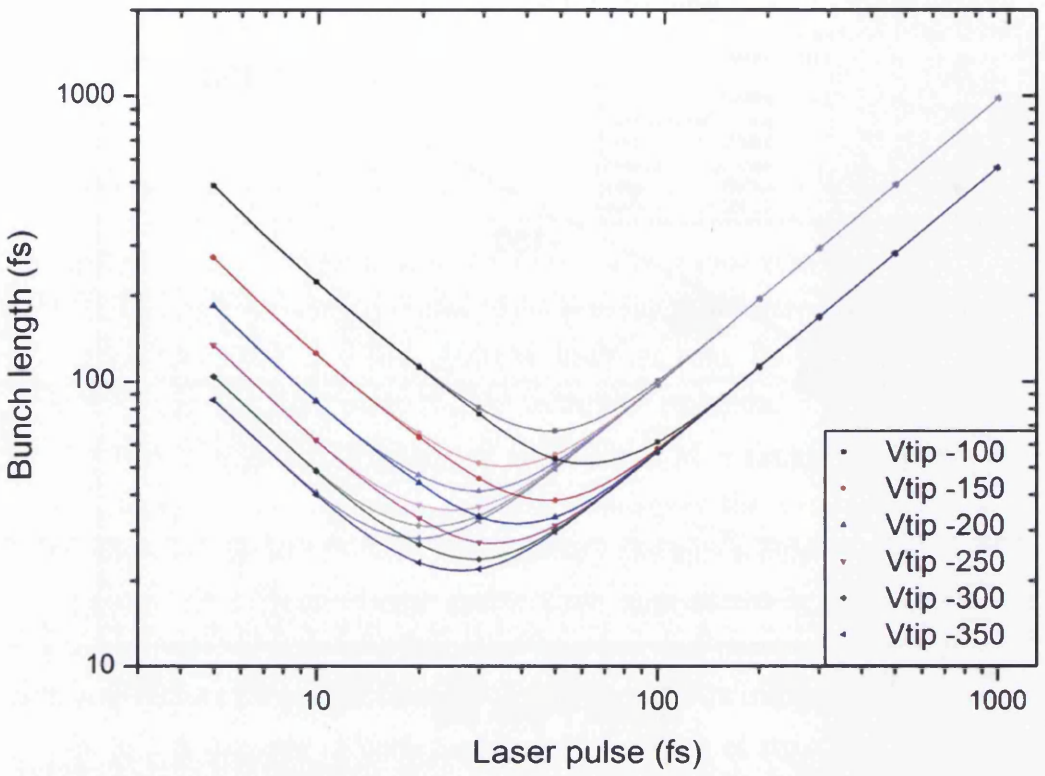

Figure 7.8: Electron bunch length at the sample as a function of laser pulse for a number of beam energies provided by the electrode voltages in table 7.1, when 3-photon emission is accounted for. Spline fits (500 points, cubic) are included to highlight minimum values and differences at short laser pulses. Included in semi-transparency are the results from figure 7.5 for comparison.

adjusted such that the effective FWHM is equal to the FWHM of the laser pulse divided by $\sqrt{N}$, for N-photon emission. The result of this is a laser temporal profile seen by the photoelectrons that has been shortened such that a 10 fs FWHM laser pulse causes photoemission to occur over a FWHM of just 5.77 fs.

To account for this, the simulations in section 7.5.2 were repeated over the same parameters, but with the FWHM of the emitted electron pulses being reduced accordingly for a given incoming laser pulse, such that a laser pulse with the same bandwidth as a 10 fs pulse produced a 5.77 fs electron bunch. The results of this scan are presented in figure 7.8. Again the electron bunch length is defined by the standard deviation along the flight axis divided by the mean bunch velocity, and the FWHM definition of the bunch length is omitted here to avoid crowding the graph.

Again it can be seen that the optimum laser pulse for producing a short electron bunch in this lens configuration occurs at approximately 20-50 fs, depending on beam energy.and the same general dependence on bandwidth is observed. However

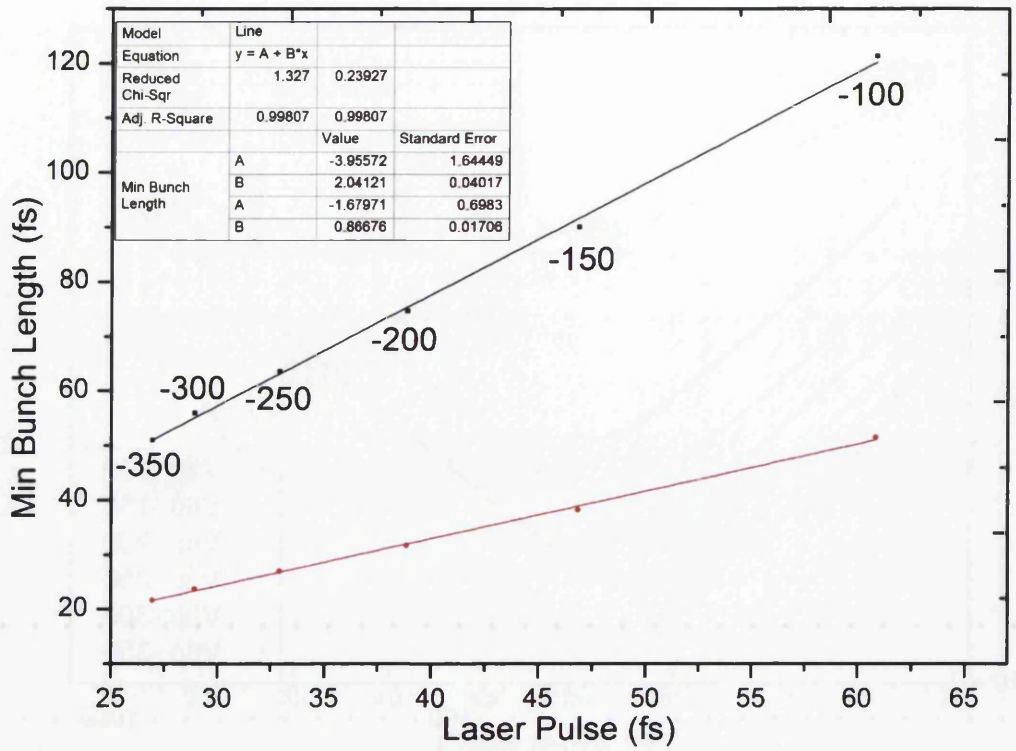

Figure 7.9: Best achievable bunch length at the sample as a function of laser pulse with the shortened emission time due to 3-photon emission taken into account. Each data point is the position of a minimum in figure 7.5. The red line represents a direct value of bunch length using the standard deviation divided by the bunch velocity, the black line is scaled to represent the FWHM length of the electron bunch. The point labels represent tip voltage at that point according to the voltages in table 7.1.

for long initial laser pulses the electron bunch at the sample is made significantly shorter by taking the 3-photon consideration into account. This makes intuitive sense, as for long laser pulses with short bandwidth the primary dependence of the bunch length is on the length at creation rather than expansion during flight. Conversely, it is also therefore to be expected that the results from the two sets of simulations converge for short laser pulses where the bandwidth is far dominant over the initial length in determining the length of the pulse arriving at the target.

It is worth noting that the 3-photon approach demonstrates decreased minimum values, allowing for shorter electron bunches to be delivered to the target. These minima are also shifted such that they occur for slightly longer laser pulses, in essence making it easier to produce shorter electron bunches at the sample if the 3-photon emission process is prevalent.

7.7 Suitability of the micro-lens for time-resolved electron diffraction

It can be concluded from the simulations that the lens idea presented in figure 7.1 is a valid and suitable design for conducting ultrafast electron diffraction experiments. The lens is constructed using realistic dimensions which would allow for laser access to both the nanotip and the sample whilst keeping the electron flight path sufficiently short that sub-100 fs FWHM electron bunches may be deployed to the sample provided a suitable laser pulse is used to induce emission.

The lens is capable of achieving collimation at a range of low beam energies using entirely realistic voltages that are well below the vacuum breakdown limit, commonly taken as 10 MV/m. Unfortunately the lens is only suitable for low energy experiments, as a beam energy grater than approximately 150 eV would require sufficiently high voltages to achieve collimation that continuous field emission from the tip would would render time-resolved experiments impossible.

The lens is capable of being used with a variety of tip sharpnesses and aspect ratios; the small distance between the tip and first electrode results in a high electric field even at low voltages that rapidly pulls electrons into a collimated path. This renders the lens performance independent of initial divergence angle, defined by the tip parameters, allowing sharp or blunt tips to be used without requiring adjustment. It should be noted that a sharp tip is still preferable for diffraction due to higher coherence, an issue unaffected by the use of the lens.

The lens is capable of achieving an extremely short electron bunch to the sample. Pulses of sub-30 fs standard deviation and sub-80 fs FWHM are readily achievable provided that a suitable laser pulse and set of voltages are used. The correct laser and voltage conditions to achieve these optimum results have been presented. There is a balance point identified at which the best laser pulse exists to produce a short electron bunch, between the initial length of the bunch and the expansion in flight of the bunch caused by the energy spread applied by the bandwidth of the laser pulse.

Constructing the micro-lens as detailed above would be difficult but possible. Whilst thin commercial plates with apertures of 10-20 μm are available, they are typically designed for use in transmission electron microscopy and often have an outer diameter of $\approx$ 3-5 mm. This is too large to avoid blocking part of the incoming laser beam (to both tip and sample) when the tip is kept close to the front of the lens. A further problem with utilising commercial apertures is alignment during construction. Both apertures must be aligned perfectly concentrically to each other

and to the tip to facilitate best operation of the lens assembly. Aligning a pair of holes of 20 μm diameter (or less) represents a significant technical challenge, and any misalignment will make it virtually impossible to position the tip in such a way that extracted electrons may still be directed onto the sample.

It is possible to solve both of these issues by custom manufacturing the apertures by laser micro-machining. As an alternative to purchasing commercial apertures, blank, flat thin plates with outer diameters on the order of $\approx$ 3-5 mm are readily available. Sufficiently thin metal plates may be cut relatively easily by a high-repetition rate femtosecond laser system such as the Pharos. By rotating the plate in smooth mount whilst applying the laser at a fixed point off-centre using a short focal length lens, the plate may be cut completely circular to any desired diameter. Once cut to the desired diameter the blank plates could be mounted together, and the central aperture made by drilling through the plates with the laser. The aperture is definable by the size of the focus, adjustable by using different focal length optics, and the amount of shots applied. Crucially, it may be possible to drill through both plates simultaneously whilst they are in final mounting position, as they sit close enough that the laser Rayleigh range extends through both (as machining can be performed with a focal length as long as 75 mm for large apertures). This allows the holes to be created already aligned and eases the process of ensuring that the holes are concentric. It also allows adding additional holes near the outer edges of the lens to assist in pumping the region between the two electrodes.

7.8 Future simulations

Following the extension of the simulations from the naive model to the 3-photon model, it would be possible to extend them further to include the full cycling electric field of the laser pulse. These simulations have not been performed as with the vast majority of femtosecond laser systems, including the Libra and Pharos, the effect would be washed out over several shots and would return to the envelope approximation used in the 3-photon simulations, as the Carrier-Envelope Phase (CEP) of the pulse is not actively stabilised and will naturally vary shot to shot. The most important reason they have not been performed, however, is that the preliminary simulations have revealed that the use of a CEP stabilised system would be undesirable; few cycle pulses with lengths shorter than approximately 8 fs are required for CEP stabilisation to be noticeable. The simulations have revealed that a transform limited pulse of this length would not produce an optimum electron bunch length at target, due to the high energy bandwidth, and would produce an equivalent

result to a non-CEP stabilised pulse of length several hundred fs (dependent on beam energy), which would be much easier to employ than a CEP stable system.

It is anticipated that for a pulse where the relative phase between the carrier and the envelope field is zero, emission occurs in a series of peaks with width and separation defined by the central wavelength of the laser and intensity bound by the field envelope. The effect of chirped pulses could be simulated using this principle by smoothly altering the width of the peaks across the laser pulse, though this effect would not be visible in real-world terms in the vast majority of cases, requiring a CEP stabilised system and the ability to keep the electron emission peaks arising within the same laser pulse separated during flight, a virtually impossible task.

Perhaps the largest barrier in practise to achieving the extremely short pulse lengths obtained in these simulations is the problem of space-charge. The simulations assume that an average of 1 electron per shot is emitted and that subsequent shots do not interact. The non-interaction of subsequent shots is a valid approximation, as at the distances involved and the repetition rates of current laser technologies each bunch would already have passed through the sample before the next emission event occurs. Non-interaction within electron bunches, however, is a less solid approximation. Whilst emitting on the order of one electron per shot is certainly possible by using an oscillator, it lengthens the time needed to take a diffraction image (and thus the time for which the system must be held completely stable) significantly.

Stability is difficult to achieve, often due to vibrations from vacuum pumps and similar sources, and it is often beneficial to increase the number of electrons emitted in order for a clear pattern to be obtained by integrating only a small number of shots. This in turn will introduce space-charge effects, making this approximation invalid. It is anticipated that the loss of this approximation will have effects on both the spatial and temporal structure of the bunch. The bunch length would no longer be defined by the shot-to-shot jitter in the arrival time as a result of the initial energy bandwidth, and the effective bunch length is expected to dramatically increase with the number of electrons in the bunch. The exact relationship between the number of particles in the bunch and the bunch length with space-charge considered is currently under investigation. It is also anticipated that lateral repulsion will increase the spot size at the sample, and may even override the collimation conditions to produce an expanding beam for the same voltages that achieve collimation under the approximation, and even produce focusing aberrations if the size of the electron beam at the electrode apertures becomes close to the aperture size.

Finally these simulations are currently being expanded to remove two key yet

unphysical approximations. The first approximation is that the tip comes to a single atom point. A new Automesh code has been developed which not only allows the radius of the curvature at the end of the tip to be taken into account, but also allows for an adaptive mesh spacing to ensure that the field in the region at the very apex of the tip is properly resolved. The second approximation is that the beam has no initial divergence, with the electrons being emitted directly away from the tip and gaining a natural divergence from the field in flight. This is somewhat unrealistic as any electron not emitted form the very end atom of the tip will have an off-axis velocity vector defined by the radius of curvature of the tip. The GPT code is currently being expanded to take this feature into account and examine the effect of different beam divergence angles.

Chapter 8

Point projection electron microscopy and time-resolved imaging.

Following on from previous chapters, and the accompanying lessons learned, the final stage of the project involved taking electron bunches generated from tungsten nanotips and utilising them for point-projection electron microscopy. This involved developing a new dedicated apparatus capable of examining a sample at higher spatial resolution than optical methods using femtosecond laser driven photoelectrons. This experiment advanced to the point of performing time-resolved pump-probe electron microscopy on a tungsten nanotip using a laser pump and electron probe with sub-picosecond temporal resolution.

8.1 Development and theory of point projection microscopy

Point Projection Microscopy (PPM) is a remarkably simple form of shadow microscopy where the object to be imaged is viewed as a shadow in the imaging wavefront which is projected onto a position sensitive detector. The technique requires that the wavefront used for imaging is produced from a point source; in practical situations this is not realistically applicable though approximating a point source is generally sufficient. The requirement for achieving the approximation that the source be much smaller than the smallest object to be imaged, something which is readily achieved with a pinhole in the case of light or a sharp nanotip when using electrons. Unlike diffractive imaging the wavefront should not be flat and no addi-

tional electron optics to achieve collimation should be employed. It is required that the wavefront be expanding radially as it passes through the sample to achieve a high magnification.

The magnification achieved by point-projection microscopy is determined by the ratio of the distance between the electron source and the sample to be imaged and the distance between the sample and the detector, as given by equation 8.1.

$$M = \frac{X_{detector} - X_{sample}}{X_{sample} - X_{source}} \tag{8.1}$$

where X denotes the coordinate of the component along the central axis of the system.

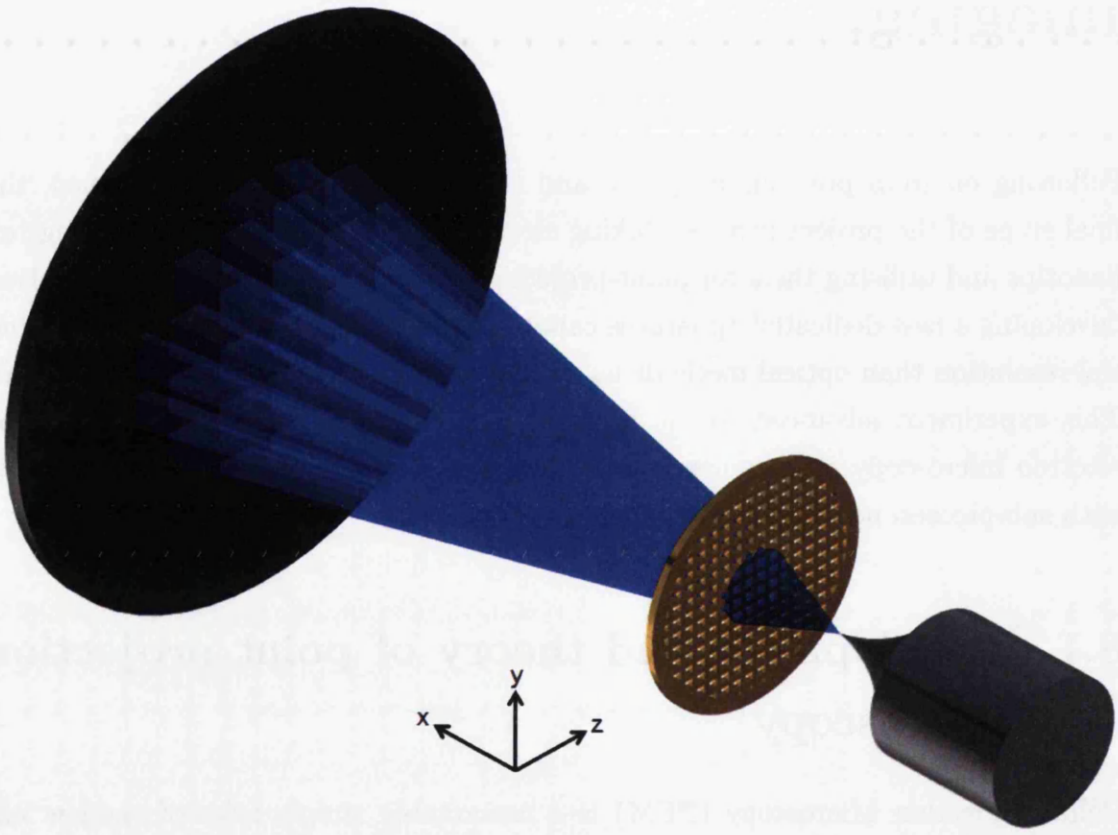

Figure 8.1: Illustration of the principle of electron point projection microscopy of a grid target using a nanotip source. This is applicable to continuous operation for static imaging or laser-driven operation for time-resolved imaging. The laser path is omitted for clarity but follows the Z axis.

The use of electrons in Point Projection Microscopy (ePPM) was originally developed in 1989 by Fink and colleagues [276, 277] as a static imaging technique, the basic premise of which is illustrated in figure 8.1. This follows from an idea originally

proposed by Gabor [264], who proposed an experiment similar to ePPM to remove focusing aberrations in holography experiments. This simple arrangement consists only of a point source, the sample and the detector along with their supporting mechanisms. It is necessary to minimise disruption to the image by ensuring that all conducting components are rotationally symmetric about this axis and that all background magnetic fields are negated. Due to the simplicity of the geometry this is readily achievable. The lack of focusing optics also removes the primary source of aberrations, helping to maintain a clear image of the sample, which is the key attraction that lead to the original proposal of the idea.

Modern ePPM equipment routinely satisfies the point source requirement by using a metal nanotip [278, 279] which allows the apparatus to double as a simple means of conducting holography due to the high coherence of the emission [105, 106, 278, 280], with interference fringes becoming visible at a magnification of approximately 10^4. By finely controlling the distance between tip and sample and using an extremely sharp tip with effective vibration isolation it has been reported that resolutions as high as 2 nm are possible [281].

It is not possible to achieve the sub-angstrom resolution potentially possible with diffractive imaging using ePPM, as the emission point would have to be closer to the sample than is practically possible whilst maintaining a usable electron energy. In addition temporal resolution may be limited as electron bunch compression is not practically feasible in such a small space. There are, however, features which make ePPM the preferable technique in certain situations. The apparatus is much simpler to design, construct and align than the collimation equipment necessary for diffractive techniques such as electron Coherent Diffractive Imaging (eCDI). In addition no reconstruction of the image is required to derive the sample as ePPM directly produces an easily interpretable real-space image [139, 199, 282]. This makes ePPM a useful tool for combining with eCDI, the reconstruction processes for which require some prior knowledge of the sample in order to guarantee convergence. This requirement can be met by performing ePPM and eCDI on the same sample [105].

In addition to ePPM it is relatively simple to use a similar arrangement to perform a process know as "in-line" holography, an alternative to the off-axis holographic technique detailed in chapter 6. In-line holography uses a typical ePPM arrangement where a point electron source and the sample to be imaged are brought into close proximity to project a highly magnified image onto the detector. The sample in question must be a thin object about which electrons can be bent in order to form two paths which can interfere with each other. The key difference is that instead of being positioned in front of a grid to flatten the electric field the sample

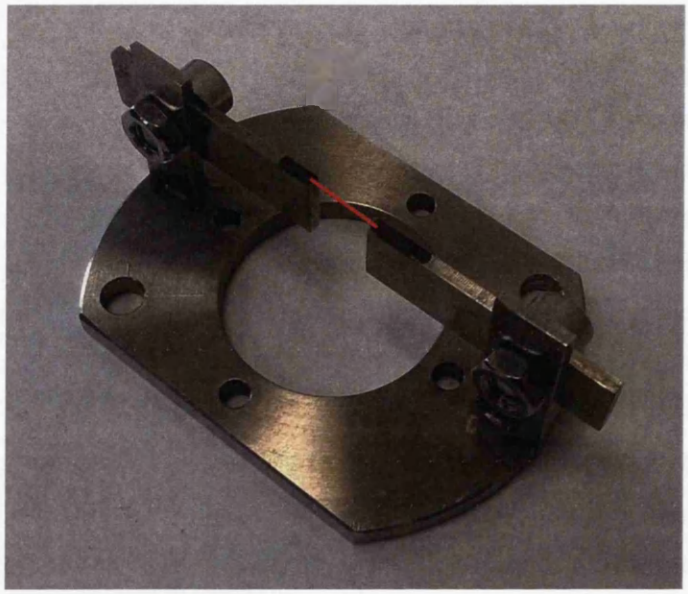

Figure 8.2: Photograph of the wire holding system used to support a 4 μm tungsten wire to be imaged by point-projection electron microscopy. The wire is secured at both ends by the black colloidal graphite. The wire itself is too small to be visible in the photograph and so is overlaid by the red line.

wire itself acts as the reference voltage, which need not necessarily be grounded. This creates an electrostatic lensing effect that bends electrons passing either side of the wire into overlapping with each other, creating an interference pattern.

8.2 Further attempts at holography through point projection microscopy of a wire

The experiment detailed in chapter 6 was ultimately unsuccessful using the technique of biprism-based off-axis holography. A final attempt was made to obtain fringes using the alternative method of in-line holography, a variant of ePPM descibed above. The same 4 μm diameter tungsten wire used in the biprism detailed in chapter 6 was employed as the sample. This wire was pulled taut and mounted onto a shaped aluminium holder as shown in figure 8.2. Colloidal graphite was used as a conductive adhesive to secure both ends of the wire and allow electrical grounding or voltage application. The electrical connection is provided by a thin gold wire wrapped around one of the screws and clamped by tightening the nut.

The wire holder is sandwiched between two PFTE holders recycled from the biprism holder described in chapter 6, and is mounted on the same rods extending from the detector collar but sits at the end of the rods within a few mm of the

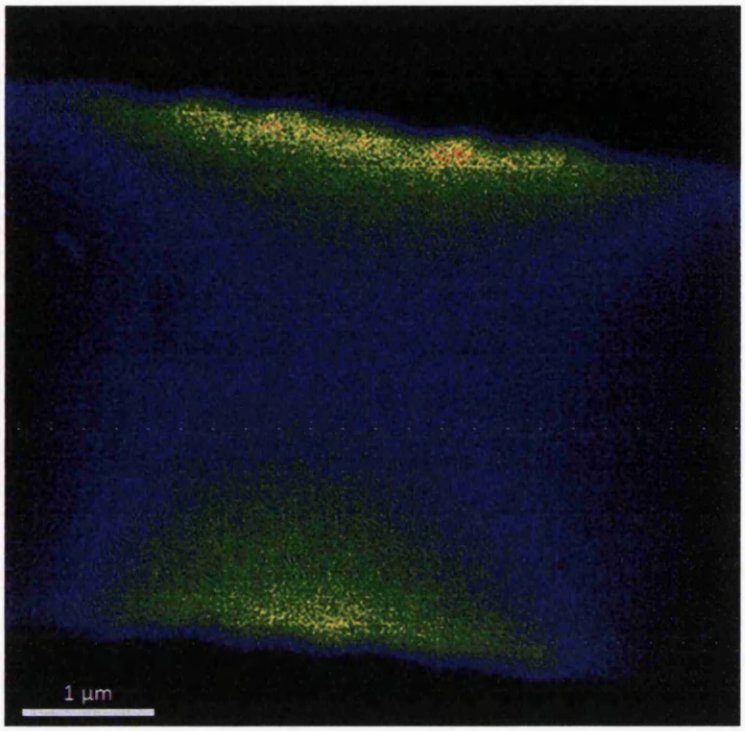

Figure 8.3: In-line hologram of a 4μm tungsten wire using DC field emitted electrons.

tip. The tip itself is mounted and manoeuvred in the same manner as in chapter 6, with power provided by a Stanford PS350 supply linked to the rear of the BeCu tip holder which is inserted to a PEEK insulating piece.

The tip was advanced towards the wire with a high negative potential applied until field emission was observed. The tip was then advanced closer to the wire with the voltage being adjusted to maintain field emission until it was observed that the vibration in the tip was rendering the image so blurry as to be unusable. The tip was then retreated until blurring was no longer observable to the naked eye. Images were then recorded of the hologram, an example of which is presented in figure 8.3. It is clear that the magnification is far too low to observe interference fringes, in this case a magnification of 960 is estimated, whereas 10^4 is necessary to observe fringes [263]. Higher magnifications could not be achieved due to the vibration issue being exacerbated by the tip being mounted on a long arm and the chamber not being vibration isolated. This exercise highlighted these issues as a major obstacle to performing point-projection electron microscopy and as a result of this the decision was taken to redesign the vacuum chamber to include vibration isolation features.

8.3 Development of a dedicated point projection microscopy apparatus

The experiments detailed in chapters 5 and 6 highlighted a number of design issues in need of correction. Foremost among these are the need for vibration isolation of the tip. The frame and chamber were therefore redesigned as detailed below to reduce vibration and create an optimised environment for electron point-projection microscopy. A new interaction region was constructed featuring fine control and fulfilling the requirement for vibration isolation at the tip itself, and the detector was remodelled to enhance spatial resolution and sensitivity. Finally a series of coils were added around the chamber to provide magnetic field negation not limited by a mu-metal shield and to provide a degree of beam steering.

8.3.1 The interaction region

The key consideration for a point-projection microscopy arrangement is that the emitting nanotip and the sample must be freely positionable such that the distance between them can be adjusted at will. Relative vibration between them must also be minimised or eliminated entirely, as to achieve a magnification of 10^4 or better the distance between them may need to be a few tens of microns depending on the distance to the detector, at which even a small vibration will cause the image to constantly shift or blur. There must also be a highly controllable voltage between the tip and the sample to provide acceleration and define the beam energy, which must be adjusted as the distance is changed to avoid electrical discharge.

Furthermore it is advantageous to mount both the tip and sample such that if any vibration of the interaction region does occur it is synchronised with the vibrations of the optical table. Failure to do this can cause the tip and the laser focus position to oscillate out of phase, resulting in highly unstable emission. If vibration cannot be completely eliminated, synchronising the laser movements caused by vibration of optics with the vibration of the source ensures a stable level of emission, provided long term drift is accounted for or is too slow to affect the system over the course of a data collection run.

The interaction region is designed such that control of position is achieved by mounting both the tip and sample on 2-axis translation stages such that they can be manipulated freely from outside the vacuum. The translation stage on the tip provides motion along the x-axis (defined in this case as along the tip) to control the relative distance between the tip and sample, and the z-axis (defined as being along the laser path) to ensure concentric alignment with the sample and detector. The

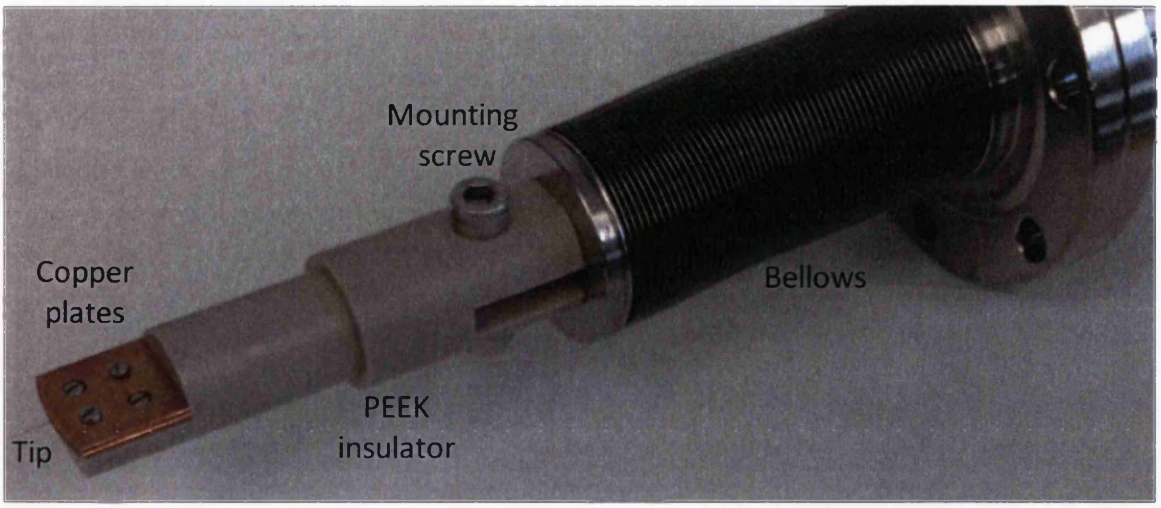

Figure 8.4: Photograph of the tip mounting system for use in the point-projection electron microscope, designed in conjunction with Helen Lewis.

sample position is fixed in x but mounted on a 2-axis translation stage providing control in the y and z axes to select the region of the sample to be imaged.

The tip is secured between two copper plates which screw together to hold the tip in a clamp, as shown in figure 8.4. The screws are secured by nuts on the underside, one of which also clamps the end of a kapton wire (rated to 2kV DC) which leads to a feedthrough, through which a negative voltage is applied to the tip by a Stanford PS350 power supply. These same screws secure the two copper plates to a piece of PEEK which provides an insulated link to a metal connector, which is in turn connected to a flange by highly flexible vacuum welded steel bellows to allow freedom of movement. A metal rod welded to the air side of the steel connector allows manipulation of the tip assembly and is connected to a linear translation stage aligned along the x-axis equipped with a manual micrometer of 10 μm resolution and a manually adjusted stepper motor capable of steps as small as 5 μm. An identical stepper motor provides fine control along the z-axis. These stages are secured to the optical table.

The sample mounting is designed around a conical piece of PEEK designed to hold the sample electrically isolated from the surroundings, the choice can then be made to ground the sample or apply an independently controlled bias voltage. The mount is designed in two parts, a support rod which screws into a flange and extends into the chamber through a bellows, and a conical head piece which fits into the rod and holds the sample. This allows the sample to be fixed to the end of the head piece cone without the piece being attached to other cumbersome components, a useful feature when handling delicate samples such as coated TEM grids. The combination of these pieces is shown in figure 8.5.

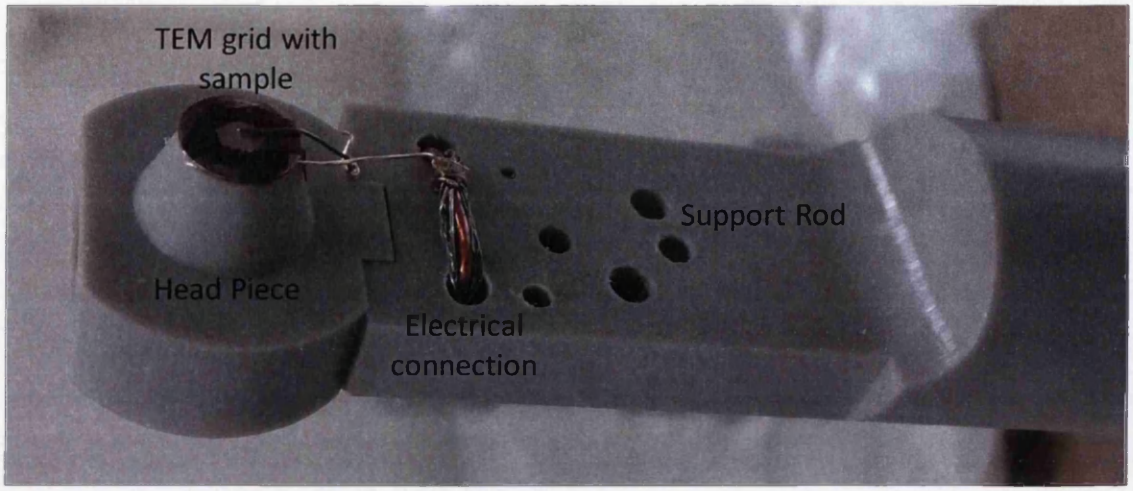

Figure 8.5: Photograph of the TEM sample holding system for use in the point-projection electron microscope, designed in conjunction with Helen Lewis. The other end of the support rod screws directly into a DN40CF flange attached to a bellows, with the rod passing the full length of the bellows. In this case the holder is configured to use a nanotip as the sample.

A groove in the top of the support rod neatly locates the head piece. The support rod has a threaded hole in the centre of the groove, allowing a screw to be used to affix the head piece. The screw enters through a hole in the top of the head piece, recessed bay in the bottom far from electron beam keeps the screw head from interfering with electron flight. Several holes in the front of the support rod serve the dual purpose of ensuring the screw hole is vented and providing a cable management system.

The head piece is designed to support a 3 mm diameter TEM grid as the sample. An OFHC copper disk with a central aperture of 2 mm is affixed to the front of the cone by a friction fit. The conical piece itself features an expanding aperture from 2 mm to allow any electrons passing through the copper to complete their paths without impacting the PEEK and causing it to charge. The TEM grid is placed concentrically over this aperture and colloidal graphite is applied around the edges to secure it to the copper. The graphite is mechanically strong enough to support the grid but can be easily removed with ethanol should the grid need to be replaced, and has the advantage of being electrically conductive so as not to interfere with grounding.

There are two configurations used to date in the point-projection microscope. The first applies when the sample is the TEM grid itself or is attached directly to the grid. In this case only the graphite coating around the edge is necessary to support the sample and grounding is achieved by a thin 100 μm gold wire which

as again attached to the copper via colloidal graphite and is threaded through the cable management holes to a grounding point. The alternative configuration is used when the target is a substantial object which cannot be supported by the grid such as a nanotip. In this case the TEM grid is kept grounded to provide a reference voltage and flatten the electric fields. When using a nanotip sample, as described below and shown in figure 8.5, the gap between the head piece and support rod is used as a clamp and the sample tip is bent upwards to sit in front of the grid without touching. The sample then may be independently electrically controlled.

8.3.2 The redesigned detector

A key problem highlighted by the experiments presented in chapters 5 and 6 is that with the detector design detailed in chapter 5 there is a large gap of approximately 13mm between the exit if the MCP and the phosphor screen. This is naturally a region of high charge density due to the gain in the MCP, and therefore Coulomb repulsion can smear the image before it arrives at the screen, reducing the resolution and rendering fine features such as interference fringes indistinguishable from the background.

This effect may be minimized by ensuring that the electrons arrive at the phosphor screen as quickly as possible, as the longer it takes them to travel the larger the deflection to their arrival point on the screen from the surrounding electrons. This may be done by two methods: reducing the distance between the plates and the screen, and by increasing the strength of the accelerating field that guides them into the phosphor. To this end the detector is redesigned so that both of these points are achieved.

The new detector utilizes the same basic components as the original design detailed in chapter 5, and is specifically designed for the purpose of point-projection microscopy. The detector is mounted using the same collar connected to the same feedthough flange, however it is typically mounted to the other side of the collar such that instead of resting in the aperture of the mounting flange it now sits protruding into the chamber itself, which improves pumping of the region behind the detector. Ceramic bushings are used to raise the PTFE support pieces from the flange, which are reversed such that electrons enter through what was the rear PTFE piece as described in chapter 5.

The structure of the new detector is shown in figure 8.6. The central electrode between the MCPs has been removed such that they now sit in direct face-to-face contact with the channels arranged as a chevron to maximise gain. Whilst this no longer allows the front and rear plates to be independently controlled, it enhances

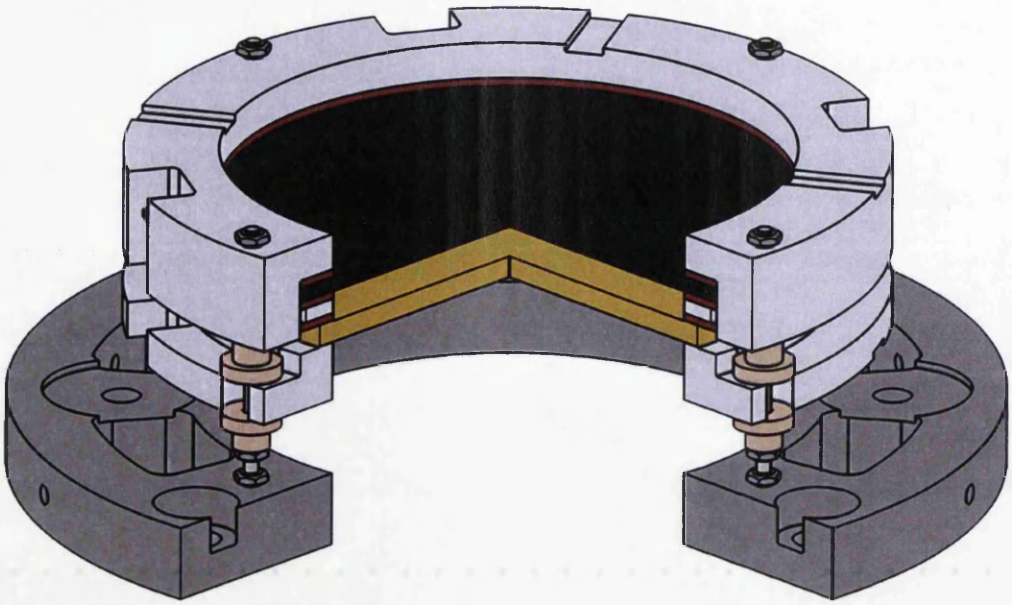

Figure 8.6: Illustration of the layout of the refined electron detector, showing the new compact design. Electrons enter from the top and pass through the MCPs (black) in a chevron before being pulled across the 3 mm gap to the phosphor screen (yellow). The detector is viewed from outside the chamber as before.

the resolution of the detector by removing a 1 mm region where both Coulomb expansion and natural divergence at the exit of the front plate could result in signal confined to one channel in the first plate occupying several channels in the second, enlarging and smearing features in the image. The electrodes at the front and back of the plates are retained to provide the bias voltage and may be powered through the same voltage divider as the old design or may be biased independently.

The phosphor screen has been removed from the original mounting supplied by Kimball and now sits within the same PTFE pieces used to hold the MCP's. The electrode removed from between the MCPs is placed on the front of the screen in order to apply a bias through the ITO coating to the phosphor. This electrode is separated from contact with the electrode at the exit of the MCP's by a 1 mm thick PTFE ring spacer. The end result is that the screen now sits just 3 mm from the exit of the second channel plate, a dramatic reduction from the 13 mm distance of the original design. This creates a much stronger electric field (by a factor of approximately 2.5) between the plates and the screen which, when combined with the reduced distance, results in electron travel times and thus spatial expansion effects due to space charge being significantly reduced.

The divergence of the beam through the plates is also reduced by bringing them

into contact, the spatial resolution of the detector is strongly enhanced (a single electron may now produce a spot on the screen as small as 50 μm) despite requiring an applied voltage upon the phosphor screen of only 3 kV as opposed to 4 kV in the previous design. The lower voltage requirement arises from the reduced expansion of the electron bunch; as the flux on a given area of signal is now increased for the same total electron number requiring a lower electron energy to ensure that florescence from the phosphor is triggered. The screen will trigger florescence as long as a minimum input power density of 5×10^{-5} Wcm^{-2} is achieved.

8.3.3 The vacuum chamber and frame

The entire frame has been redesigned from that used in chapters 4-6 with the primary purpose of achieving vibration isolation of the tip and sample. The bars defining the length of the frame have been extended to double their original length so that the frame is now longer than the optical table is wide. This allows the chamber to be located directly above the table rather than beside it as in previous experiments, and so allows the tip and the sample to be readily secured to the table to provide stability. The translation stages can then be mounted on the table rather than the chamber itself, allowing both tip and sample to be connected to the chamber only by a flexible bellows, significantly reducing the effect of vibrations arising from the pumps attached to the chamber. Neither the chamber nor frame is in contact with the optical table at any point except via these bellows, preventing vibrations originating in the pumps from travelling into the table and subsequently affecting both tip and sample vibrations and laser stability. As before the frame is manufactured from extruded aluminium with strengthening corner brackets.

The chamber retains the same 6-way DN40CF cross used in chapters 4, 5 and 6 to house the detector, in a new position suspended above the table. This positioning unfortunately renders the bottom arm of the cross unusable and as such it has been covered with a blank flange. The top arm is also sealed with a blank, to allow room for the backing line to a turbo pump near the interaction region. The outside arm aligned with the long axis of the frame houses the revised detector assembly and magnetic shield using the same feedthrough flange as previous experiments. The opposing arm houses an adapter leading to a DN40CF cube housing the interaction region discussed above. The remaining two arms aligned parallel to the optical bench house a DN160CF Turbo-pump (Pfieffer TMU 521 P) opposite an adapter flange hosting a dual Pirani/Bayard-Alpert pressure gauge (Pfieffer HPT100).

The cube housing the interaction region is equipped with a pair of DN40CF viewports on the horizontal axis to allow ingress and egress of laser light to the

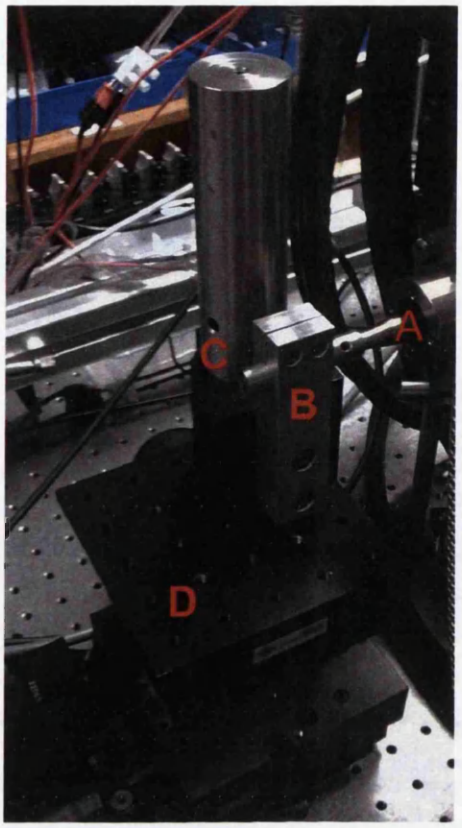

Figure 8.7: Photograph of vibration isolated tip motion system for use in the point-projection electron microscope. A) Rod supporting bellows from figure 8.4. B) Aluminium clamp piece supporting rod. C) Upright post supporting aluminium clamp to provide structural rigidity. D) Translation stages with stepper motors attached to the optical table, providing the tip with horizontal and longitudinal motion.

interaction region with sufficient room to illuminate both the source tip and the sample. The top of the cube is occupied by a conical DN40CF to DN63CF adapter which connects to a turbo pump (Pfieffer HiPace 80) to provide differential pumping between the interaction region and main chamber. Connected to the bottom of the cube is a steel bellows, allowing freedom of movement to the sample. The support rod of the sample holder screws into a flange attached to the far end of this bellows, which is in turn attached to translation stages mounted on the optical table. The final port, directly opposite the adapter leading to the DN160CF cross is occupied by the source tip mounting arrangement, as shown in figure 8.4. This bellows has an unusual arrangement in that the inside of the bellows is the air-side, with the face visible in the photo being exposed to vacuum. A rod extends inside the bellows from the piece where the mounting screw attaches to beyond the DN40CF flange, where it is gripped by an aluminium holder piece, in turn attached to translation stages bolted to the optical table as shown in figure 8.7.

8.3.4 Magnetic field negation

Due to the small distances used in points projection microscopy the accelerating between the nanotip and the sample must be kept relatively small to avoid the risk of electrical discharge. As a result at high magnifications the beam energy is typically low and the electrons are therefore vulnerable to deflection by the Earth's magnetic field. It is therefore necessary to ensure that the field is negated at all points on the electron flight path.

In the region of the detector this is easily accomplished by employing the same magnetic shield used for the VMI discussed in chapter 5. The mu-metal can encases all but approximately 2 cm of the electron flight path within the 6-way DN40CF cross, and provides sufficient to reduce Earth's field such that no effect is noticeable. Due to constriction of the adapter to the DN40CF cube and the requirements for access to the cube itself, however, physical shielding in this region is highly impractical and so the field must be negated by generating a magnetic field of equal magnitude and opposite vector to the Earth's field to ensure appropriate cancellation.

This is achieved by six electromagnetic coils arranged in pairs along three orthogonal axes aligned with the chamber, as shown in figure 8.8. The coils are would around aluminium rings with different diameters on each access to ensure that they fit through each other. The largest rings (labelled 1) are parallel to the table to control the vertical field, with an inner diameter of 22 inches. The second largest (labelled 2) have an inner diameter of 19 inches and are aligned parallel to the electron flight path to control the lateral field, and the final set (labelled 3) have an inner diameter of 16 inches and are aligned perpendicular to the electron flight path and control the longitudinal field.

Power to the coils is provided by three Thurlby-Thandar QL355T power supplies, capable of delivering up to 2 Amps at 30 Volts. The coils are wired in parallel such that one supply is used for both coils the same pair. The field produced by these coils with supplies at full capacity is over an order of magnitude greater than the field needed to directly cancel that of the Earth. This allows the coils to not only be used for negation but also steering of the electron bunch between the emitting nanotip and the sample at relatively low magnification (and therefore large distance between the tip and sample). This is an extremely useful property as aligning the tip and sample to be perfectly concentric is non-trivial and the extra three degrees of freedom provided by this process allow the equipment to be used without perfect alignment and give additional indicators by which perfect alignment can be achieved.

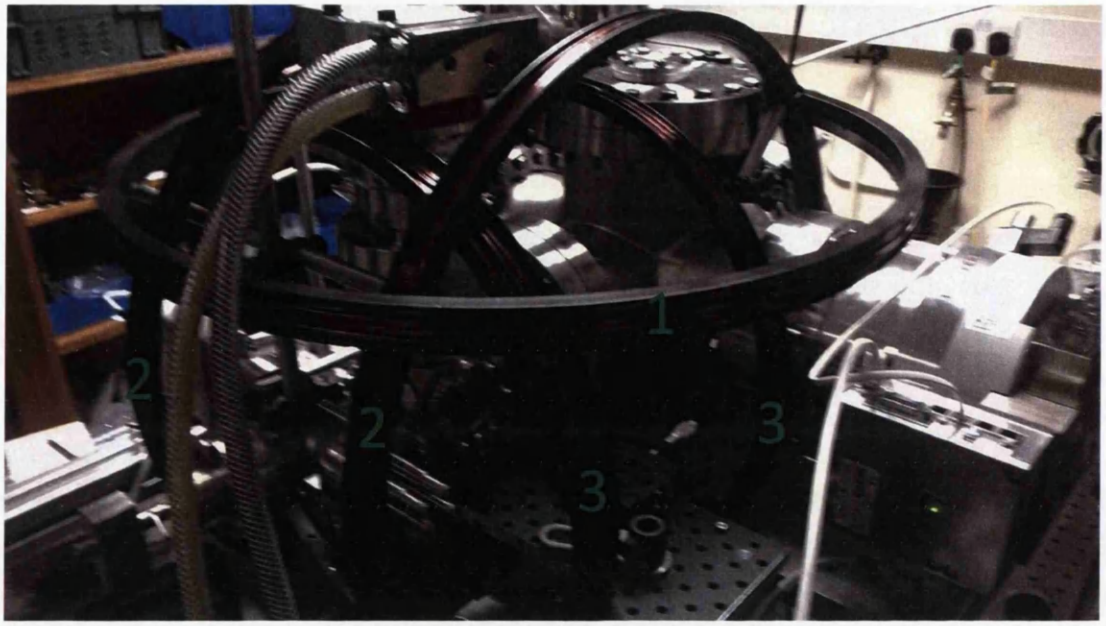

Figure 8.8: Image of the interaction section of the chamber showing the numbered coils to negate background magnetic fields and act as steering devices.

8.4 Microscopy of a TEM grid coated with a lacy carbon film

In order to verify the correct function of the ePPM apparatus the TEM grids used to support the samples were imaged at high magnification using both field emitted and laser driven electrons. These grids are regular with well defined dimensions allowing a measurement of magnification. Fine carbon features deposited onto the grids allow comparison of image clarity resulting from the two emission types.

8.4.1 Microscopy using field emitted electrons

Interaction region was configured such that the only items present were the source tip held in the clamp detailed above and connected to an external power supply (Stanford PS350), and a TEM grid on the sample support detailed above. The TEM grid selected (TAAB C269/C) has square apertures with a side length of 50 μm and a bar thickness of 34μm. The grid is coated with a lacey carbon film to provide additional features upon which to focus, with the carbon laces typically having a sub-micron diameter, although the thickness may vary drastically across different locations.

The tip was placed a few mm from the grid and made to field emit by applying several several hundred volts. The potential was monitored and adjusted whilst the

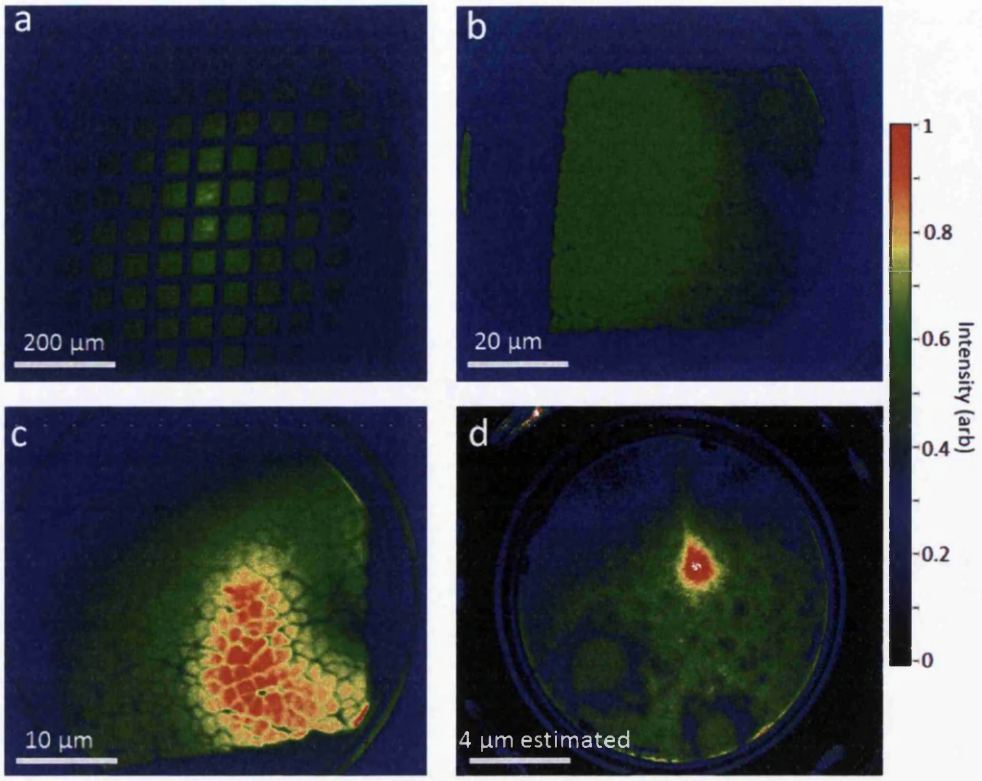

Figure 8.9: Point-projection electron microscope images of a lacey-carbon coated TEM grid at increasing magnification. a) Low magnification image showing the majority of the TEM grid, estimated magnification 100x. b) Zoomed image of a single 50 μm grid square, estimated magnification 1200x. At this magnification features in the carbon grid become visible, a hole in the film is clearly visible in the top right of the image. c) Further zoomed image of a single grid square (not the same square as panel (b)), estimated magnification is 2400x. At this magnification the carbon laces become clearly visible. d) Highest achievable zoom, focusing on individual holes in the carbon film. Magnification is estimated to be 4000x by translating the sample a known amount and measuring the translation of the image.

tip underwent self-cleaning to ensure a constant level of emission and to keep the detector from being saturated. Once emission stabilised and a clear image of the grid was visible without being obscured by secondary electrons the tip as slowly advanced towards the grid. During the process the voltage was reduced to keep the electric field strength (and thus the amount of emission) roughly constant. Several pauses in the advance were made when the tip was reshaped by the emission, to adjust the potential and ensure that a clear image could be retrieved and that the tip was undamaged.

Images of the grid were recorded at several distances (and thus several values of magnification) up to the point there vibration in the tip created significant blurring of the image and so rendered clear images at higher magnifications impossible. A

series of images at increasing magnification achieved by this method is shown in figure 8.9.

The four images displayed demonstrate the ability of the point-projection microscope to operate at a variety of magnifications by changing the distance between the source and sample. Figure 8.9(a) is comparable to a standard optical microscope, showing 100x magnification. As the magnification is increased a single grid square can be imaged, as shown in figure 8.9(c) and (d) at 1200x and 2400x magnification respectively, as well as structures in the coating. Finally figure 8.9(d) shows how individual features on the few micron scale in the lacey-carbon film can be imaged by increasing the magnification to approximately 4000x, much higher than is achievable by an optical microscope. At this point the tip is located just 107 μm from the sample, and attempting any higher magnification than this leads to a blurred image caused by vibration.

8.4.2 Microscopy using femtosecond laser driven photoelectrons

Following the success of imaging the TEM grid with field emitted electrons the experiment was repeated using femtosecond laser driven photoemission. This was performed using EPSRC Laser Loan Pool system UFL1, consisting of the Orpheus-N NOPA at 800 nm pumped by the Pharos laser system as discussed in chapter 3. This was achieved by setting the distance between the tip and grid such that a number of squares were visible in a microscope image obtained by DC field emission. The potential applied to the tip was then reduced until the electron signal dropped to zero, and the laser was applied to the tip to restore the image.

The beam path from the laser is illustrated in figure 8.10. The light from the Orpheus-N is steered onto the breadboard table T1 containing the compressor and FROG via periscope P1. The light is reflected from the splitter S1, passed through the neutral density filters at N1 and directed via retro-reflecting periscope P2 onto the second breadboard table T2 to ensure the beam is the correct height to enter the chamber. This table contains the final two steering mirrors and a 75 mm focusing lens. The beam is horizontally polarised by the periscope arrangement to match the axis of the nanotip, and so no waveplates are required. In addition to the final alignment mirrors before the chamber fine control is provided by the lens which is mounted on a 3-axis translation stage with micrometers and differential drives with 1 μm accuracy.

The beam was aligned centrally through the window using plumb-lines to ensure perpendicular travel to the axis of the tip. The focus was then gently steered onto

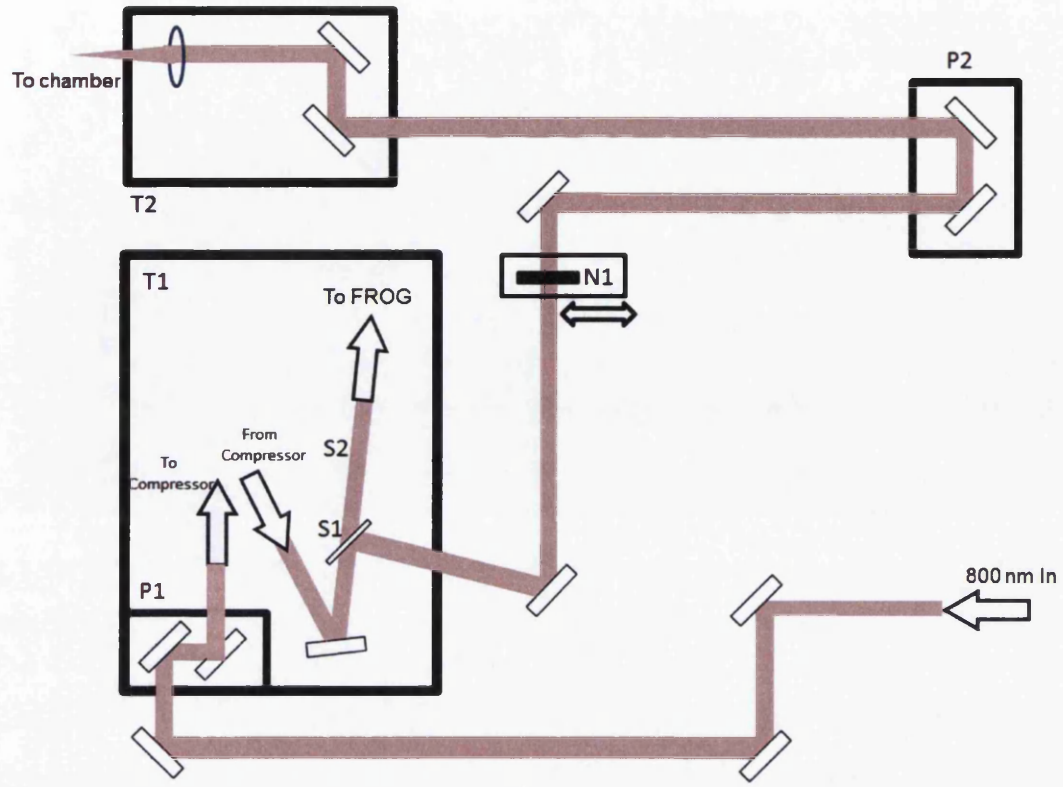

Figure 8.10: Map of the laser beam path used to induce femtosecond photoelectron emission from a tungsten nanotip. The Orpheus-N provides 800 nm light which is directed as shown. T1: Table containing compressor and FROG, T2: Table at entrance window to vacuum chamber containing final steering and focusing optics. P1 and P2: Periscopes to ensure correct beam height for each stage. S1: beam-splitter. N1: Neutral density filters giving control over pulse energy.

the end of the tip by slowly moving the lens until the first hints of a diffraction pattern were visible in the laser exit beam. The detector was then monitored as the beam was advanced further until sufficient electrons were measured to produce a clear image of the sample. Once a clear signal was verified magnification was increased by translating the lens to move the beam towards the sample, and then carefully advancing the tip after the laser beam until electron production was once again observed, producing a magnified image. This was repeated with increasing magnification until a significant loss of clarity in the magnified image due to the increasing effects of vibration of the tip at high magnification was observed.

The tip was positioned several hundred microns from the grid and the laser was slowly steered onto the tip such that an image was only just obtainable, in order to be emitting as few electrons per pulse as usably possible. Figure 8.11 shows a comparison of images of the lacey-carbon coated TEM grid obtained by femtosecond laser emitted photoelectrons and DC field emitted electrons at the

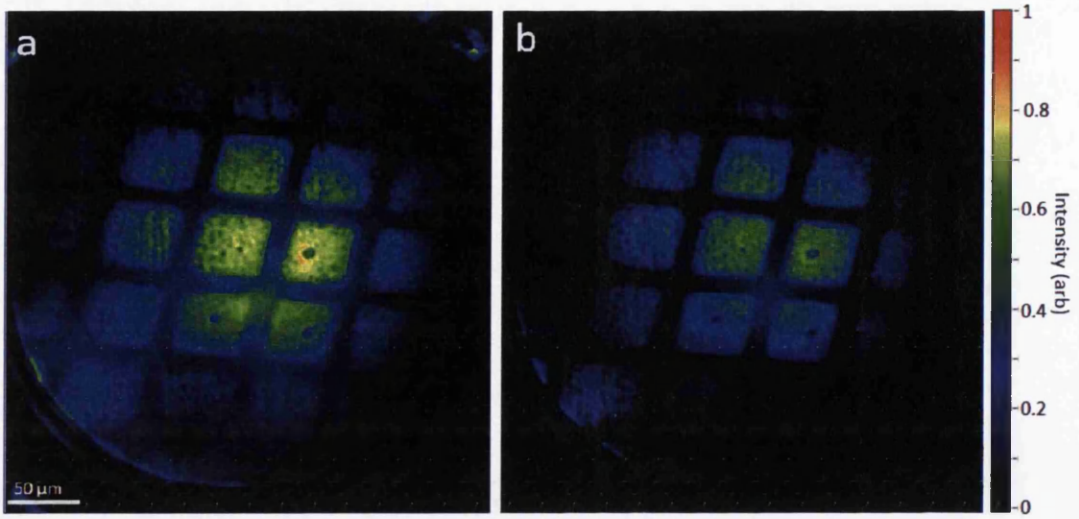

Figure 8.11: Comparison of point-projection electron microscope images of a lacey-carbon coated TEM grid obtained by DC field emission and laser emission. a) Image obtained by femtosecond laser emitted electrons, b) Image at the same position obtained by DC field emitted electrons after blocking the laser and increasing the voltage to induce emission. The magnification is approximately 215x.

same magnification (which is rather low at an estimated 215x). It is clear that the image obtained by the laser emitted electrons, figure 8.11(a), is comparable in clarity to that in figure 8.11(b) obtained by DC field emission. Some of the finer features in the carbon are not quite as clear when imaged with laser driven electrons, and there is a significant amount of background noise especially in the lower portion of the image. Nevertheless the clarity of figure 8.11(a) with respect to figure 8.11(b) shows that sufficiently few electrons are being emitted that space-charge is not a disadvantage, suggesting that on the order of a single electron per pulse is being emitted.

To examine the effect of space-charge on image clarity the tip was advanced further such that the image was zoomed onto a single grid square. The laser position on the tip was then adjusted along the tip axis and two images of the grid were recorded. The first, displayed in figure 8.12(a), is recorded with the laser focus squarely on the end of the tip leading to many electrons being emitted per shot (the exact number is undetermined but is likely on the order of 50-100). The laser focus was then moved off the tip and returned, stopping short such that a lower intensity was applied to the tip apex, reducing the number of electrons per shot emitted to less than 10. A second image was then recorded and is shown in figure 8.12(b).

The dependence of image clarity on electron count is immediately obvious. Figure 8.12(a) shows a much brighter image than figure 8.12(b) as expected, but also omit large amounts of detail. This detail is not simply swamped by the intensity,

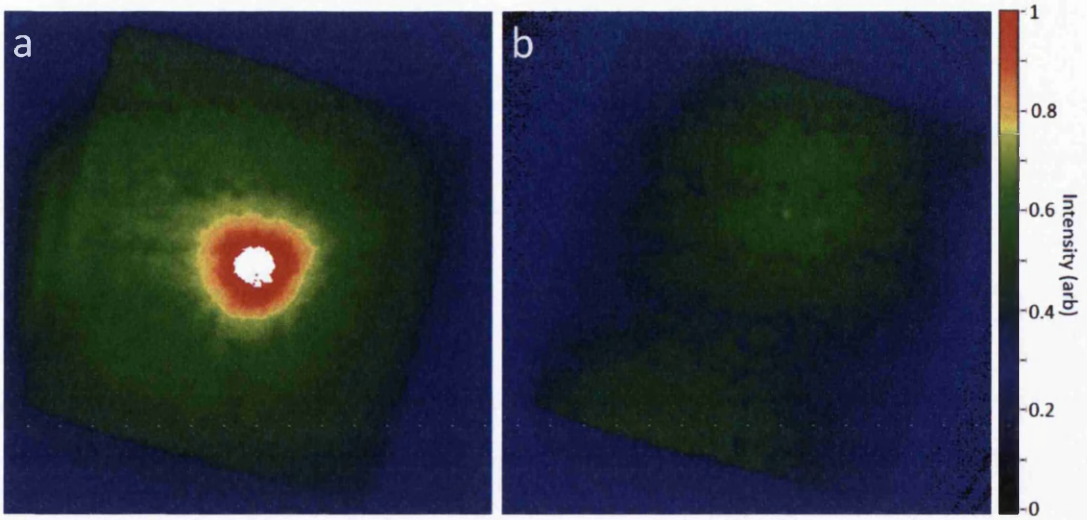

Figure 8.12: Comparison of point-projection electron microscope images of a lacey-carbon coated TEM grid obtained with high and low numbers of electrons per shot to investigate space-charge effects. a) Image obtained whilst emitting many electrons per shot (estimated at 50-100), b) Image at the same position obtained by moving the laser focus to reduce the intensity on the tip apex and produce few electrons per shot (estimated at 10 or below). The grid square side length is 50μm. The white region in (a) is the result of camera saturation.

contrast of the lacey-carbon signal is clearly reduced even in areas of similar brightness near the edge of the square. It appears therefore that space-charge is detrimental to this technique such that features on the order of 1μm become completely unresolvable when tens of electrons per pulse are present.

8.5 Time resolved pump-probe microscopy of a tungsten nanotip

Following verification that point-projection microscopy was possible using femtosecond laser driven photoelectrons without significant blurring due to space-charge, it was decided that the apparatus was ready to be utilised for pump-probe experiments. The target chosen was a second tungsten nanotip, the objective being to record the same process by which the photoelectrons are generated, using a femtosecond laser pump and an electron probe. This experiment was designed to push the boundaries of spatial resolution and to record the best possible temporal resolution, with the results providing an indicator of electron pulse length.

8.5.1 Experimental procedures

The interaction region was configured such that a second tungsten tip acting as the sample was was positioned in front of the lacy-carbon coated TEM grid. The end of this tip was aligned approximately to be radially central to the grid with a gap of approximately 0.2 mm between the end of the tip and the face of the grid, as shown in figure 8.13.This results in the sample tip sitting at a slight angle such that it points towards approximately 10 o'clock as seen by the source tip. The sample tip is electrically isolated from the grid by a small square of Kapton film, wedged between the shank of the sample tip and the grid face.

The sample tip is bent into shape before being secured in a friction fit between the head of the sample holder and the body, and retains its shape and end position through the natural stiffness of the tungsten. The opposite end of the tip is connected to a copper wire which feeds into the DN160CF cross through the adapter flange and outside the magnetic shield before being connected to a feedthrough, so that the sample tip can be independently controlled via an external supply (Thurlby-Thandar QL355T). This cable is surrounded by a coaxial shield, grounded to the chamber, to avoid the voltage causing disruption to the electron flight paths, and is held pinned against the chamber wall by a brass spring-clip in the neck of the adapter flange to keep the wire as far from the electron paths as possible. The TEM grid is grounded via the gold wire shown in figure 8.13 which is linked to the coaxial shield, ensuring that it provides a grounded reference point for the electrons.

The voltage on the sample tip is set to ensure that the electric field gradient between the emitting tip and the TEM grid remains as close to constant as possible, to ensure that the projected image is not disrupted. The correct voltage is obtained by observing the image on the detector and sweeping through a range of voltages until the image appears optimal, as shown in figure 8.14. When the potential is too low electrons are bent around the sample tip causing illumination in the areas which should be in shadow, leading to the image folding inward and the end of the tip becoming invisible, as shown in the red highlighted feature in figure 8.14(a). Conversely, setting the bias too high results in the imaging electrons being pushed away from the tip such that the shadow appears enlarged with blurred edges and a disproportionately rounded end, as shown in figure 8.14(f). This test is performed with the position and voltage of the source tip held constant throughout, such that the applied potential is below that required to induce field emission. Low intensity laser-driven emission is then used to achieve characterisation to avoid having to adjust potentials in order to keep the image brightness constant.

The full beam path from the laser into the chamber was configured as shown in

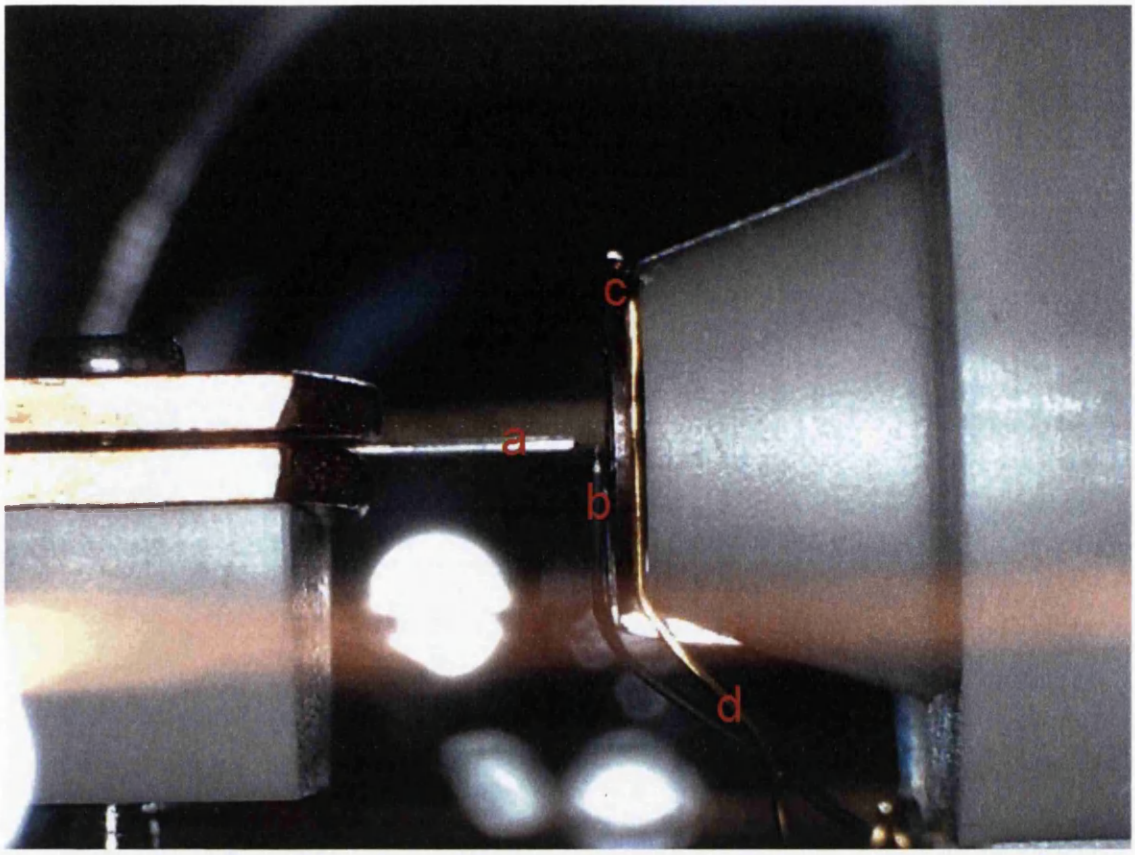

Figure 8.13: Photograph of the interaction region where the ePPM is configured to perform extremely high resolution microscopy of a second nanotip, as seen from the direction of the incident laser pulse. Due to parallax the scale bar is relevant only at the image depth where the tips meet. (a) Source tip, (b) Sample tip, (c) Grounded TEM grid and (d) Gold grounding wire. The source tip is approximately 150 μm from the sample tip, which in turn is approximately 200 μm from the TEM grid. The distance between the TEM grid and the detector is 43 cm.

figure 8.15. The light from the Orpheus-N at 800 nm is directed through a series of steering mirrors and onto the breadboard table T1 containing the compressor and FROG via periscope P1 in the same manner as before, however an additional beam splitter S2 is included at the exit of the compressor. The beam reflected from the splitter S1 is directed via retro-reflecting periscope P2 onto the second breadboard table T2 as before to ensure the beam is the correct height to enter the chamber. As before this table contains the final two steering mirrors and the focusing lens. This beam acts as the source beam as per figure 8.16 and is horizontally polarised by the periscope arrangement. The beam reflected from splitter S2 is passed onto a delay stage with 150 mm manual travel (Thorlabs LTS150/M) which can be controlled manually or by a computer and has a best resolution repeatable movement of 4 μm. The exit beam from the stage is directed by a steering mirror onto the 90 degree

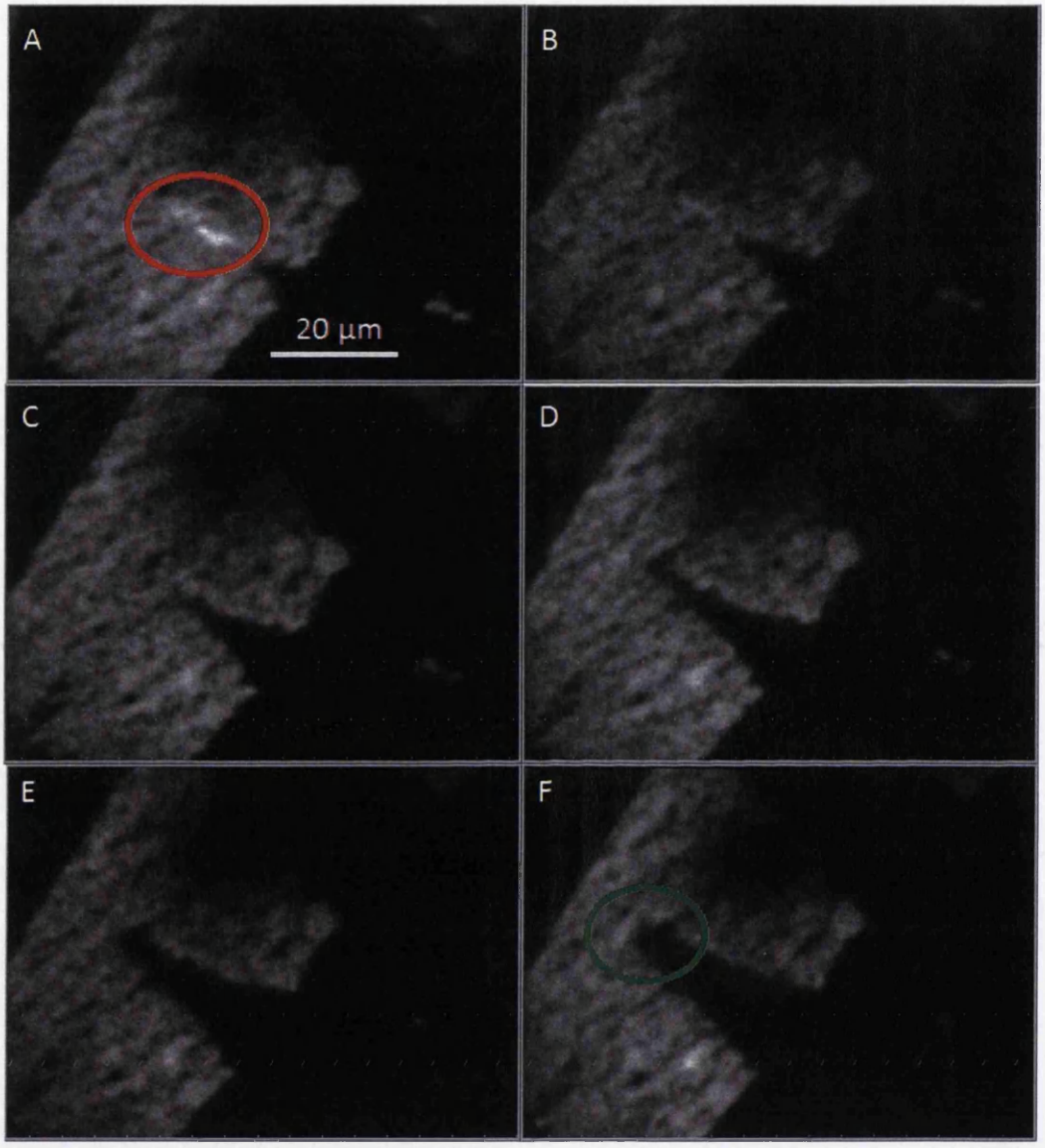

Figure 8.14: Determination of the correct voltage to apply to the sample nanotip to ensure minimal field disruption. In this case the source nanotip is held at 300 V and the voltages applied to the imaged nanotip are (a) 27 V, (b) 28 V, (c) 29 V, (d) 30 V, (e) 31 V and (f) 32 V. In this case the optimal sample tip voltage is estimated to be 29.5 V. The feature highlighted in red is an indicator that electrons passing each side of the tip are crossing, and the applied voltage is too low such that the tip is forming an electrostatic lens. Exaggerated rounding at the end of the sample tip image as highlighted in green is indicative of repulsion from the tip, revealing that the applied voltage is too high. The solid black lines arise from the shadow of the TEM grid, with finer features amongst the lit areas resulting from the lacey carbon film. The scale bar applies to the grid, which is at a different magnification to the tip, as determining the exact magnification of the tip is difficult.

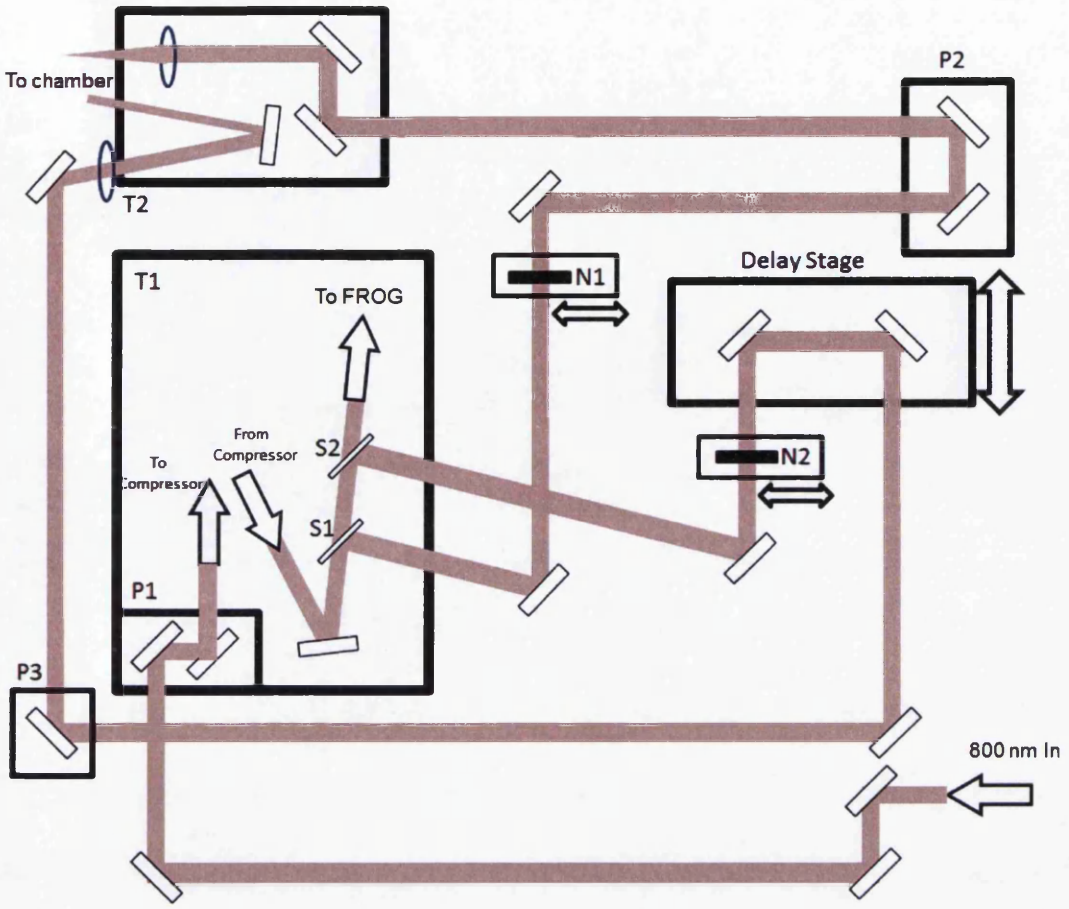

Figure 8.15: Map of the laser beam paths used to conduct pump-probe ePPM experiments showing charge effects on a tungsten nanotip. The Orpheus-N provides 800 nm light which is directed as shown. T1: Table containing compressor and FROG, T2: Table at entrance window to vacuum chamber containing final steering and focusing optics. P1, P2 and P3: Periscopes to ensure correct beam height for each stage. S1 and S2: beam-splitters. N1 and N2: Neutral density filters giving control over pulse energy.

periscope P3 which raises it to the correct height to enter the chamber, and directs it onto a penultimate alignment mirror, through a lens, and onto the final alignment mirror positioned on table T2 which directs the beam onto the sample nanotip so that it may act as a pump. The periscopes combine to ensure that this beam is vertically polarised. In the case of both beams the correct polarisation is defined only by the periscopes and no birefringent optics such as waveplates are required.

Both beams can be intersected by a flip mount (N1 and N2 in figure 8.15) which contain an adjustable stack of neutral density filters to provide control over pulse energy. In addition to the final alignment mirrors before the chamber fine control is provided by the lenses which are each mounted on a 3-axis translation stage with micrometers accurate to 5 μm for the pump beam lens and differential

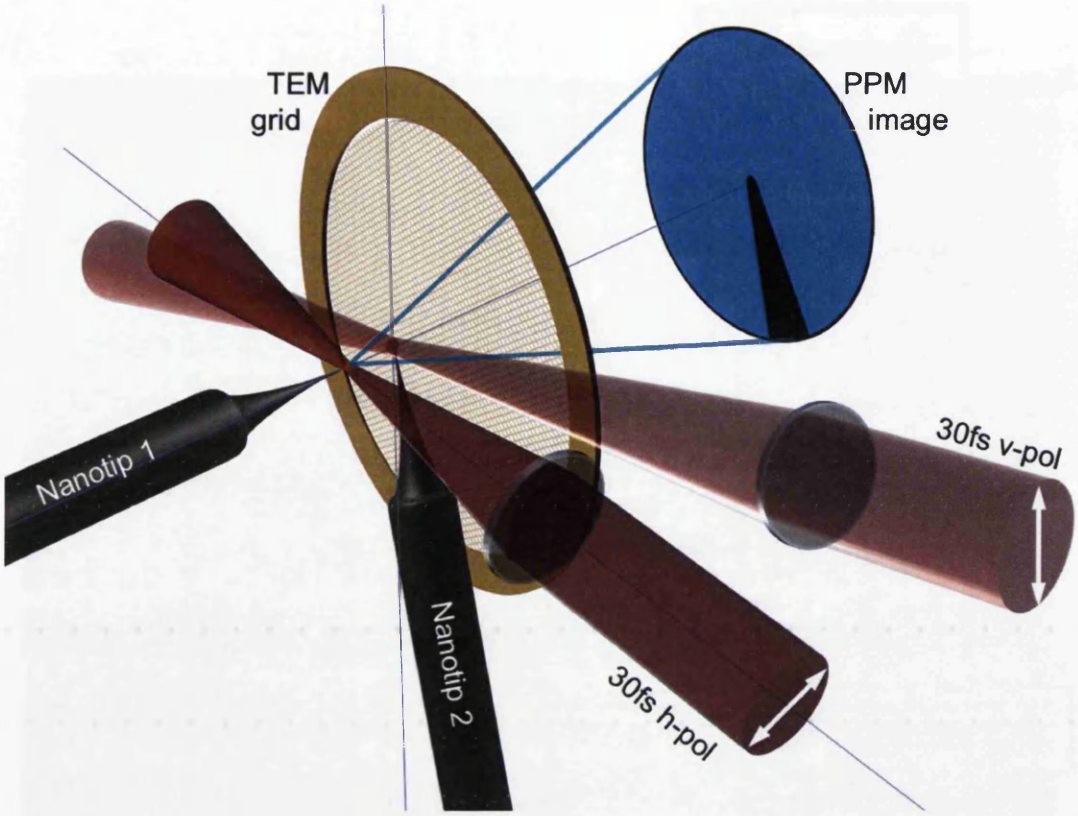

Figure 8.16: Illustration of the ePPM interaction region showing laser paths and polarisations.

drives with 1 μm accuracy (but substantial backlash) for the source beam. This additional capability is extremely useful when operating at high magnifications to ensure that a beam intended for one tip does not hit the other, potentially inducing significant damage to the tips or to the detector. This risk is further minimised by the perpendicular directions of the tips, which necessitate the use of different polarisations. As tips interact most strongly with light polarised along the tip axis [283], this minimises the effects felt by each tip arising from the light being applied to the other.

The beam alignment into the interaction region itself is portrayed in figure 8.16. The beam onto the source nanotip (labelled nanotip 1) is focussed with a 75 mm focal length lens situated after both alignment mirrors and close to the entrance window to the chamber. The pump beam onto sample nanotip (labelled nanotip 2) is focussed via a 25 cm focal length lens situated before the final alignment mirrors and is angled so that it passes above the lens in the source beam on a downward path as shown. This entry is convenient as it allows the light to enter at such an angle that it remains perpendicular to the axis of the sample tip, despite the tip being tilted. It also allows the two beams to be significantly spatially separated at

output such that they can be monitored by independent cameras. On exiting the tank, both beams are stopped by a florescent card beam block allowing she shadow of the tips and Fresnel diffraction patterns in the exit beams to be observed and used as alignment tools, as well as the shadows of additional alignment tools such as plumblines used to assist in ensuring that the beams pass straight through the window, especially along the axis of nanotip 1.

8.5.2 Results and analysis

Following pumping to 7×10^{-9} mbar and careful alignment of the two laser beams onto the source and sample tip, several attempts were made to observe time-dependent features in the microscope image of the sample nanotip. Initially this was a difficult process, as it was initially unknown how such features were expected to appear, or how intense they should be. This is further complicated by the time taken for electrons to travel from the source tip to the sample tip. Whilst using light as both a pump and a probe is simplified by the fact that the arrival times of the two pulses are well defined, using electrons as a probe does not allow for such convenience as many factors affect the flight time. Altering the magnification changes the flight time, as does changing the voltage, often necessary to remove field emission which can begin to occur as the source tip is reshaped by the laser. This results in the point of temporal overlap changing, requiring long detailed scans of the delay to identify t_0. Observing the first time-dependent signals was therefore a complex process which initially involved scanning the delay stage over the entire 150 mm range whilst watching the image for changes. Several attempts were unsuccessful due to the need for coarse stage movement which resulted in missing features and a lack of magnification.

After several attempted scans a small change in the shadow of the sample tip was seen. A systematic scan of delay was then performed about this point with a long exposure integration time over approximately 10^6 laser shots, although exposures as low as 7×10^5 shots and as high as 3.5×10^6 shots were used. Repeated scans were performed with the position of the laser onto the sample tip adjusted to produce a large effect allowing a series of repeatable images to be obtained. The clearest of these is presented in figure 8.17.

The first three panels of figures 8.17(a), (b) and (c) are all located prior to temporal overlap and show the long term stability of the image, with almost every detail being reproducible across the timescale of three exposures. Temporal overlap between the pump laser pulse and probe electron bunch begins to occur in figure 8.17(d), where it can be seen that the shadow of the very end of the tip begins to

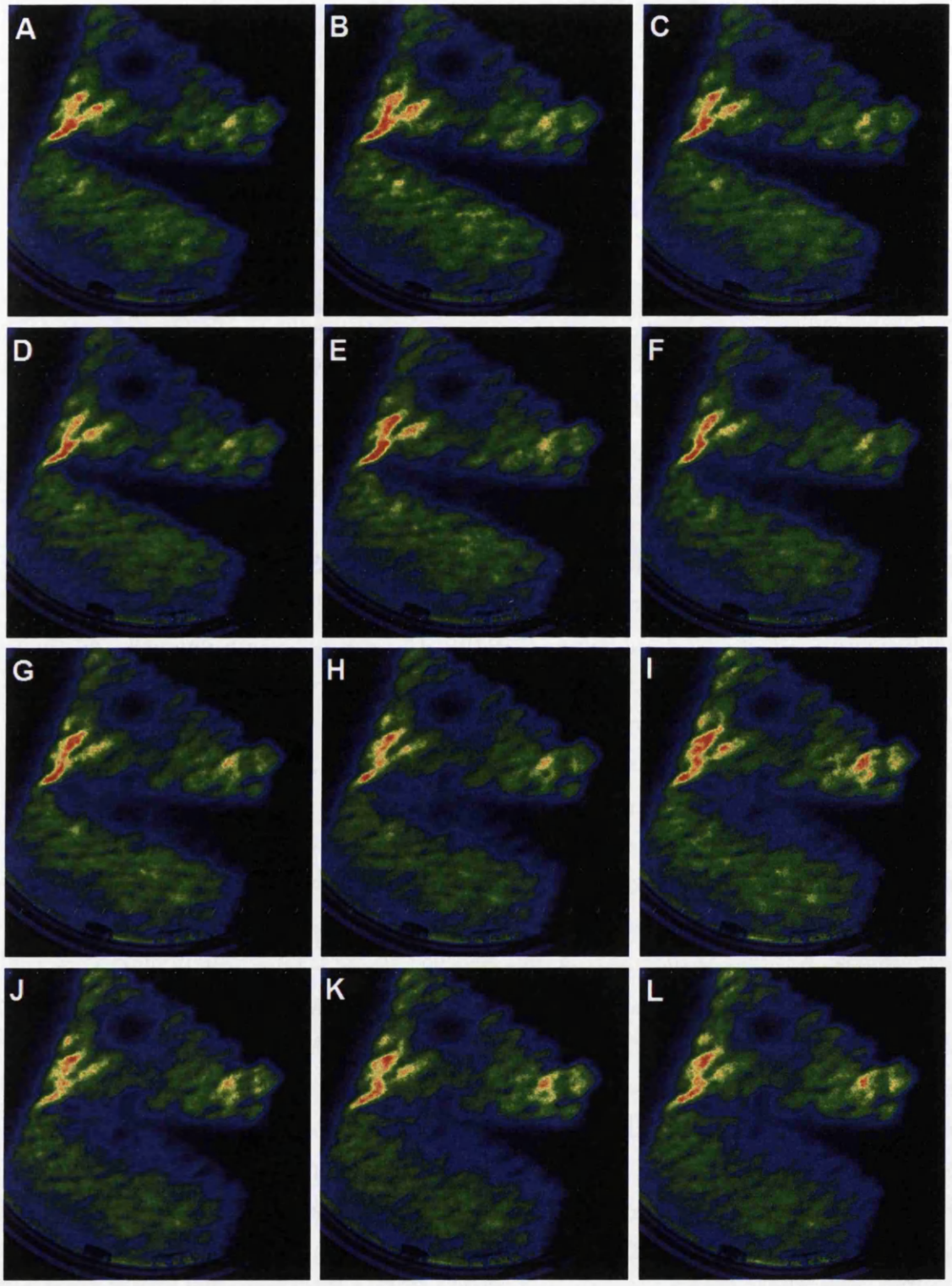

Figure 8.17: First images of time-dependent features resulting from laser pumping of a tungsten nanotip observed using short electron bunches. The delay between each panel is 330 fs.

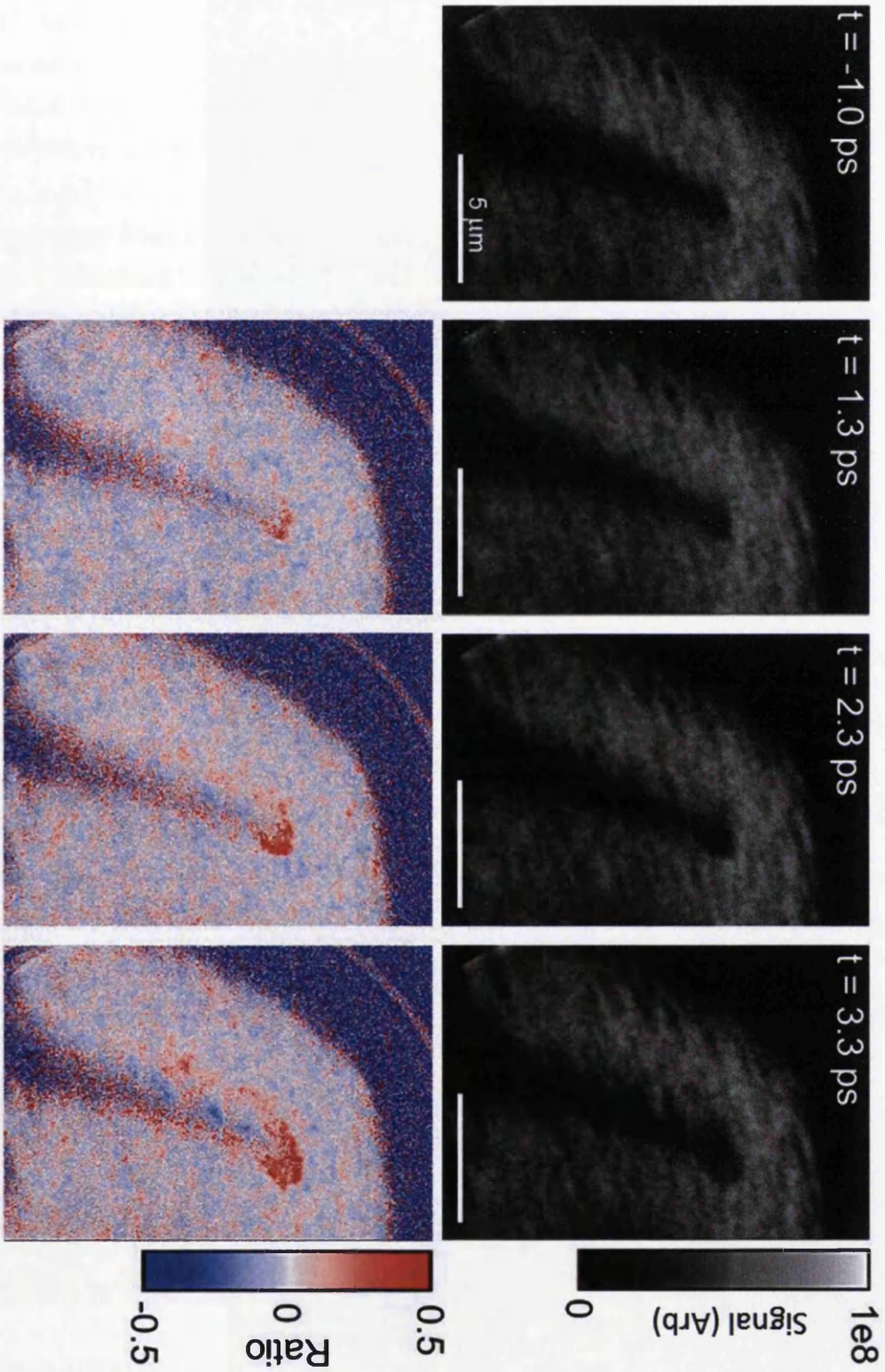

Figure 8.18: Difference images from the results of a detailed delay scan in point-projection microscopy of a tungsten nanotip, showing charge propagation along a tungsten nanotip as a function of time.

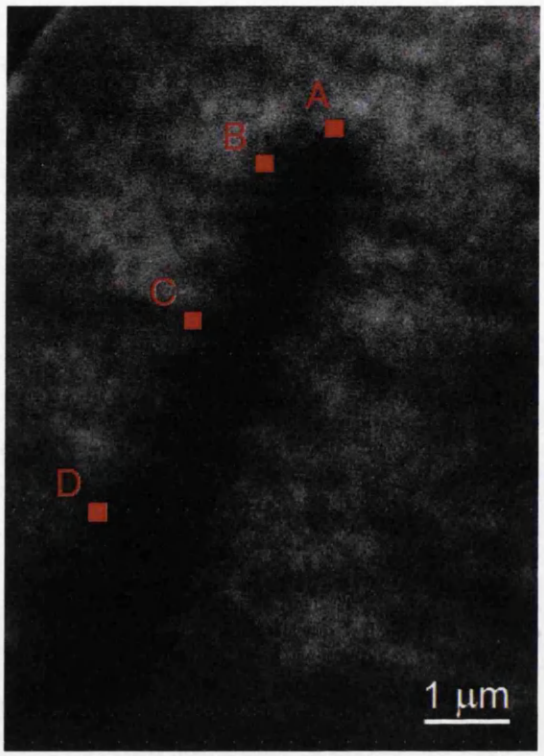

Figure 8.19: The four points along the edge of the tip at which charge is tracked as a function of time.

expand towards the direction of the incident light. The remaining panels of figure 8.17 show the evolution of the system as the delay is scanned further, with the increasing signal at the apex of the tip becoming visible first followed by an increase that appears to propagate down the tip away from the apex. Each image is separated from the preceding image by a delay of 330 fs.

It is believed that the expansion and propagation of the dark region with time shows regions of high charge density on the surface of the nanotip triggered by the laser pulse. These regions deflect passing electrons in the probe pulse expanding the shadow of the tip around the highest charge density regions. In order to quantify this effect another scan of delay was performed in finer steps of 5 μm, equating to a 33 fs delay. Image subtractions are then performed at several time delays to track the propagation of the change in signal down the length of the tip. A sample of these images at selected points is shown in figure 8.18.

The comparison reveals that the charge propagation appears to occur in stages. between temporal overlap and approximately 1.3 ps there is a strong but localised increase in charge density concentrated at the very end of the tip. Betwen 1.3 and 2.3 ps this charge cloud begins to expand away from the apex, before finally, between 2.3 and 3.3 ps, the charge cloud begins to propagate down the taper of the tip. This

occurs preferentially on the side of the tip from which the laser is incident. To quantify this further the propagation of the charge is along the entire delay scan by monitoring the signal at four key points on the image, shown in figure 8.19. The ratio value from figure 8.18 is plotted for each point on the delay scan and at each of the four key points in figure 8.20.

The combination of these figures shows that the the fastest rise times for the feature arising from a change in charge density occurs at the apex of the tip, with the feature reaching its maximum intensity in less than a picosecond, while the 20-80 time of the slope is approximately 300 fs. when moving to points further from the apex the rise time increases and the maximum value of the change decreases. Even a short distance from the apex at point (B) the peak of the change is not reached until 2 ps have elapsed. Point (C) features significant noise making quantification difficult, although the rise time appears to be on the order of 2.5 ps. Point (D), approximately 4 μm from the apex, takes nearly 3 ps to reach its peak value. The propagation changes in charge density away from the apex can therefore be said to travel at roughly 1.3×10^6 ms^{-1}.

The observed features may be explained by the laser pulse generating a plasmonic effect at the apex of the tip, leading to a highly localised region of charge which is disruptive to electrons in the probe pulse. This region of high charge density will then naturally spread due to Coulomb forces and attempt to reacquire an equilibrium state. As the charge moves down the taper the volume of tip available over which to redistribute is larger, hence it is natural that the movement will begin to slow and that the charge density at any given point along the taper will be lower than at the apex, hence the lowering of the peak value and lengthening of the rise time in figure 8.20.

These results demonstrate that time-resolved electron microscopy using femtosecond laser driven electrons from a tungsten nanotip is possible with sub-picosecond temporal resolution, even with a source to target distance on the order of 100 μm. The results shown in figure 8.20(a) indicate the ability to resolve features on the order of 300 fs, suggesting that the electron pulse is at least that short and implying on the order of 10 or fewer electrons per pulse. This is a major success and proves the viability of time-resolved point projection microscopy.

8.5.3 Estimation of the number of electrons per shot

To have full confidence in the above results it is necessary to determine the length and population of the electron bunches used to obtain time-resolved measurements of charge propagation along a tungsten nanotip, as this defines the maximum resolution

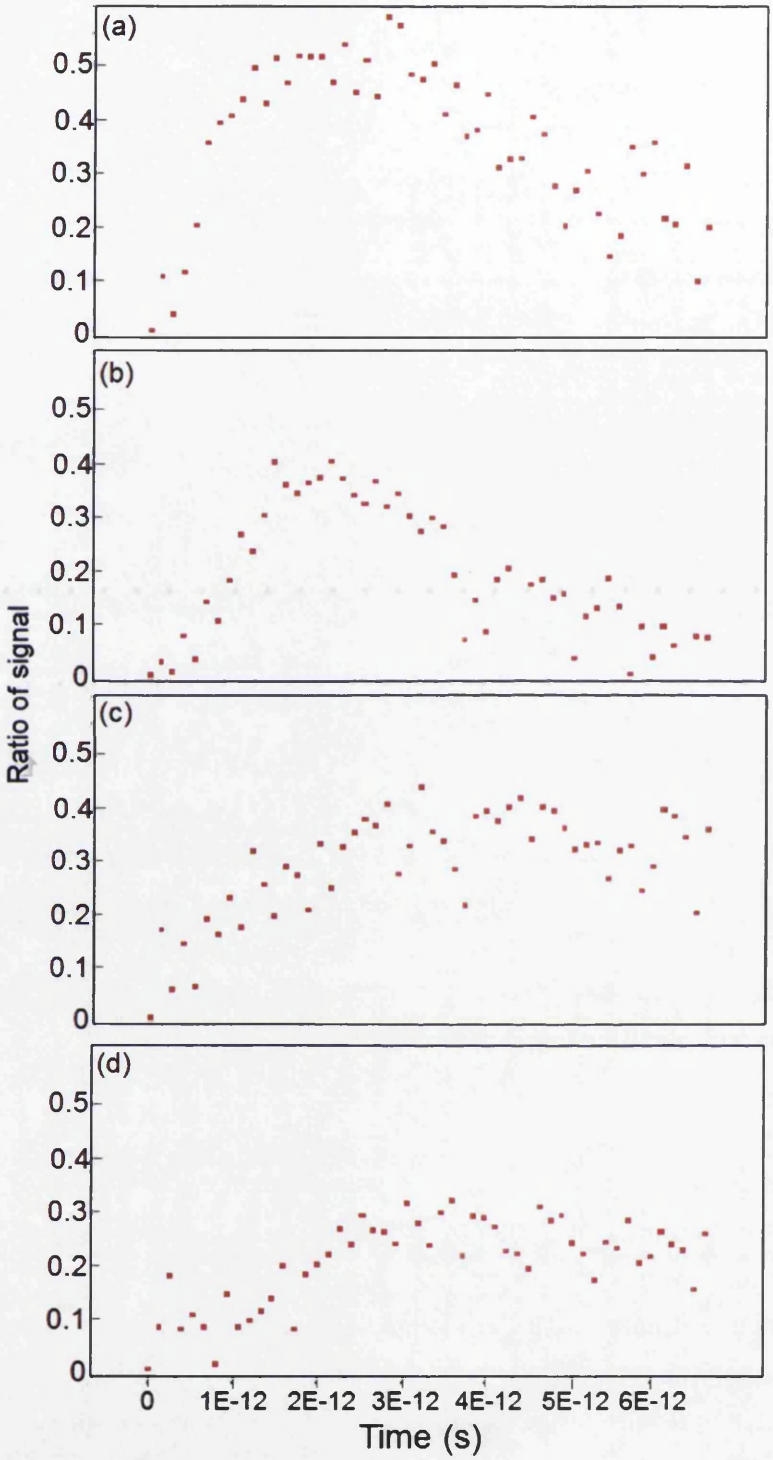

Figure 8.20: Graphs showing the change in signal arising from charge density variations at four points along a tungsten nanotip. The graph labels correspond to the points in figure 8.19. The fastest rise time is observed for the feature at the very apex of the tip, with the entire feature reaching full strength in less than a picosecond, with the 20-80 time of approximately 300 fs. The features become progressively slower to develop further from the apex.

possible. The high spatial and temporal resolution of the images in figures 8.17 and 8.18 suggest that the issue of space-charge has been overcome with a degree of success, and that emitting fewer electrons per shot at a high repetition rate is the optimal way of using femtosecond laser driven photoelectrons from a tungsten nanotip for microscopy. To confirm that this is actually the case, the detector was calibrated to provide an estimate of the number of electrons per bunch, allowing a check as to whether the assumption that sub-10 electron bunches are being produced is correct.

To achieve this the detector was set to a high enough gain to render single-electron detection possible, with the Pfieffer HPT100 pressure gauge operating in ion-gauge mode where the heated filament causes it to emit low energy thermionic electrons. A small bias of -3 V was then applied to the entrance of the channel plates to reject most of the electrons emitted by the gauge, allowing a sufficiently small number through that the impacts could be counted by eye. A sum image of 15 exposures was then recorded on the AVT F505 Pike camera, and a 5×5 pixel median filter applied via LabVIEW to isolate individual electron impacts. These were then counted by eye. Over several repeats it was determined that between 20 and 40 electrons per exposure was a reasonable estimate range.

This allowed a determination of the readout of the intensity value recorded by the data collection camera for a known number of incoming electrons. The electrons originating from the ion gauge only strike a small area of the detector (corresponding to approximately 200×120 pixels) due to restricted access through the holes in the mu-metal shield. By taking the ratio of the illuminated area and the area of the entire phosphor screen, and comparing the readout value of the camera with that of the recorded images presented in figure 8.18, it was estimated that an average of 7 electrons per laser shot were arriving at the detector. Although this measurement is somewhat rough, the fact that it provides an order of magnitude agreement with the ideal of sub-10 electrons per shot is highly encouraging.

8.6 Estimation of the electron bunch length

In order to analyse the results of this experiment fully simulations were performed to develop a theoretical expectation of pulse length with which to match the experimental results. With the calibration of the detector indicating fewer than 10 electrons per shot, it becomes feasible to perform simulations of electron bunch flight between the source tip and target tip to measure bunch length as a function of bunch population, with space-charge fully accounted for.

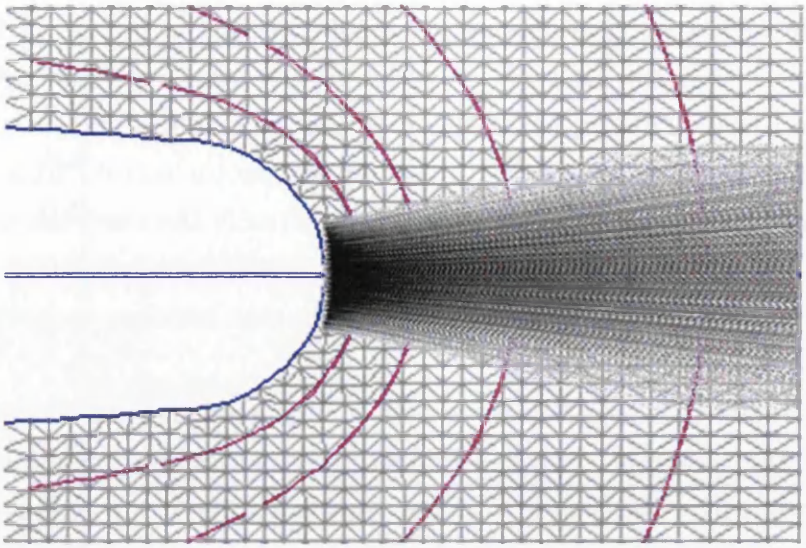

Figure 8.21: Illustration of the updated model of the nanotip for use in simulations to determine the effect of space-charge on electron bunch length. The particle trajectories in GPT are overlaid on the Superfish model showing a realistic curvature, adaptive mesh and field contours.

To achieve this it is necessary to expand on the field and grid construction presented in chapter 7 to accurately plot the electric field between the source tip and the TEM grid using distances and voltages matching the experiment. At this stage the sample tip is ignored, a reasonable approximation as the experimental results demonstrate that it can be held at a voltage which realistically approximates electrically floating. In order to do this correctly significant refinements were made to the mesh construction detailed in chapter 7. As well as altering the positions of the components, the source tip itself was reconstructed to more accurately reflect a realistic structure of the nanotip. Unlike in chapter 7, where the ideal single-atom tip is assumed and the mesh defining the boundary of the tip is drawn to a single point, the end of the tip must be accurately modelled to account for the real curvature. A tip of radius 50 nm is modelled, with an adaptive mesh size which ensures sufficient points around the end of the tip to remain accurate whilst increasing mesh spacing in empty regions and around larger components to keep the mesh usable within the limitations of computing resources. General Particle Tracer simulations of electron flight through this refined mesh are performed, tracking particle positions and velocities at regular time-steps to build up a full picture of particle trajectories in both space and momentum. The new tip shape, grid and initial particle distribution is shown in figure 8.21.

The key difference to the simulations in chapter 7 is that the strict conditions of an ideal scenario are relaxed. In addition to the refined tip geometry which more

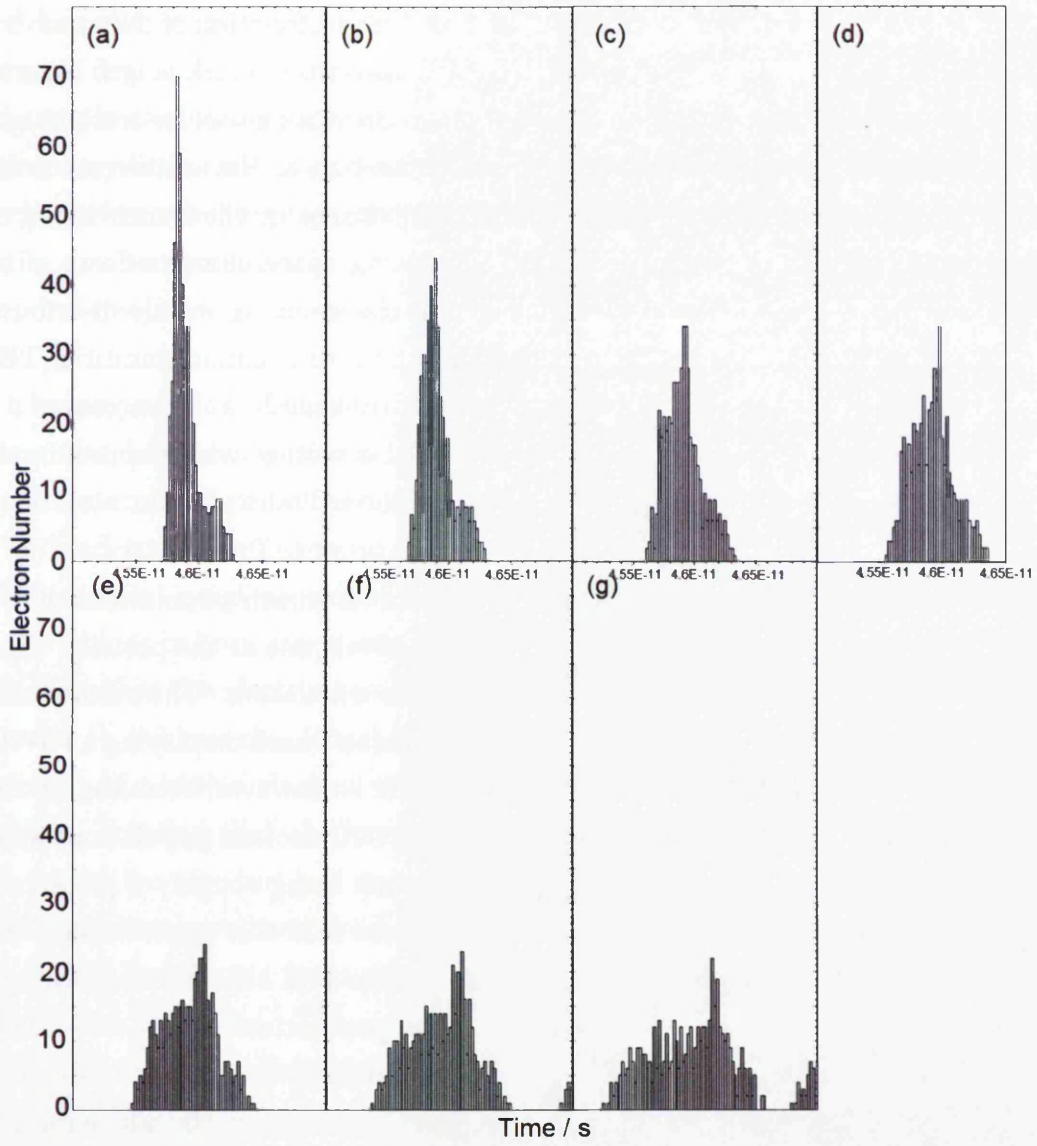

Figure 8.22: Histograms of simulated electron bunch length arrival times at the second nanotip as a function of electron bunch population, with space-charge accounted for. In each case 100 electrons are flown with a total bunch charge of Nq_e, where N is the population being simulated. This method ensures statistical significance. (a) space charge turned off in GPT, (b) N=1, (c) N=2, (d) N=3, (e) N=5, (f) N=7, (g) N=10.

accurately models the electric field and hence the initial acceleration of the electrons near the very end of the tip, the regime of one electron per shot is no longer assumed. Instead a large number of electrons are flown, with the GPT code modified to include accurate point-to-point space charge calculations . This allows a measurement of the bunch length as it passes the location of the sample tip as a function of the number of electrons in the bunch. Having an indication of the maximum bunch length from the temporal resolution of the experimental results, this provides a tool for retrieving an approximate value for the number of electrons in the bunch. To achieve statistical significance 100 particles are flown, with the total charge of the bunch being set to the desired simulated charge (i.e. when simulating space charge effects of a 7 electron bunch, 100 particles are flown with a total charge of $7q_e$ evenly distributed across all particles). The simulation includes only the source nanotip and the TEM grid. The omission of the sample nanotip is both reasonable and necessary, it is known from figure 8.14 that the sample tip is held at a voltage which approximates electrically floating, and its inclusion would break the cylindrical symmetry of the system upon which both Superfish and GPT rely in order to function correctly.

Figure 8.22 shows the results of these simulations for bunch populations of 1, 2, 3, 5, 7 and 10 electrons as a histogram of electron arrival time at the position where the sample tip would be had it been included in the simulation. The results show that the effect of space-charge is drastic, with a 3 electron bunch displaying a FWHM approximately twice that of a single electron bunch. It is, however, encouraging that these simulations predict that bunches of the ordre of 1-10 electron population should remain relatively short, with even a 10 electron bunch being roughly 1 picosecond long. Given the temporal resolution displayed in figure 8.20 this again implies that fewer than 10 electrons were present per pulse. The fact that this agrees with the rough calibration of the detector reinforces the population estimate. The fact that a feature on the scale of 300 fs was observed indicates that it is possible that an average of one electron per pulse was produced, achieving the ultimate goal of eliminating broadening due to space-charge and achieving the highest possible temporal resolution.

8.7 Concluding remarks

A point-projection electron microscope has been constructed that allows high resolution imaging of up to 4000x magnification to be performed at present using either DC field emitted electrons or femtosecond laser emitted photoelectrons, with vibration of the source nanotip being the primary limiting factor. This resolution could

potentially be enhanced further by increased vibrational isolation of the interaction region from the main vacuum chamber, or by removing vibration completely through the use of ion pumps in place of turbo-molecular pumps backed by a scroll pump which exhibits significant levels of vibration.

A key advantage of point-projection electron microscopy is that high spatial and temporal resolution are both achieved via the same mechanism of bringing the source and sample as close as possible. This results in femtosecond photoelectron bunches having very little time to expand, both from initial energy spread and space-charge effects, before reaching the sample, allowing an electron probe of remarkably high spatial and temporal resolution. Utilising this feature has allowed high spatial and temporal resolution pump-probe microscopy of charging effects in a tungsten nanotip to be performed.

The propagation of charge along a tungsten nanotip induced by a femtosecond laser pulse has been successfully tracked using ePPM with micron scale spatial resolution and sub-picosecond temporal resolution. This is the first measurement of its kind to be performed on a tungsten nanotip and highlights the potential of femtosecond point-projection electron microscopy for extremely high resolution measurements in both space and time. Features on the order of 300 fs were observed, indicating that the electrons pulse is at times on the order of 100-300 fs in duration. In order to achieve this length space-charge must be eliminated by producing on the order of a single electron with each laser shot. It appears that this has been achieved, showing that the key to achieving good temporal resolution of to use a high repetition rate but low power laser system and integrate over many shots.

Simulations have been conducted to calculate the effects of space-charge on electron bunch length as a function of bunch population for the specific field structure of the apparatus used. These simulations agree that the bunch lengths indicated by the results are realistic for the electron numbers believed to be present. This agreement provides strong reinforcement that the system is behaving as expected and is capable of femtosecond scale imaging when the conditions are correct. This good agreement leads to a reasonable conclusion that the experiment detailed in this chapter was highly successful, and that the project is ready to move to the next stages as detailed in chapter 9.

Chapter 9

Conclusions and outlook

9.1 Conclusions

Femtosecond laser induced photoemission from tungsten nanotips has been studied in order to determine their suitability as photocathodes for time-resolved electron microscopy and diffractive imaging of samples with femtosecond temporal resolution. These studies are relevant to tips electrochemically etched to an apex radius of 50-100 nm, as verified using the Fowler-Nordheim field emission technique.

A magnetic bottle spectrometer was constructed to examine the energy spectrum of strong-field photoelectrons from tungsten tips as a function of laser polarisation and bias voltage. Whilst this experiment was not entirely successful due to equipment shortcomings discussed in chapter 4, some interesting dependencies were revealed, notably that the emission is stronger when the polarisation is parallel to the tip and that there is a quantifiable increase in yield correlating with the applied bias voltage.

To circumvent the limitations relating to the equipment in chapter 4 a velocity map imaging spectrometer was constructed, allowing the energy and direction spectrum from a metal nanotip to be recorded simultaneously. It was confirmed that strong-field emission occurs within a well defined bandwidth over a hemisphere centred about the tip axis. Thermionic emission increases with intensity and is emitted toward the laser incidence direction with less well defined energy spectrum. This represents the first time that this spectrometry technique has been used successfully to examine photoemission from a solid, as proven by simultaneous focused emission from krypton gas.

Simulations have been performed of an electrostatic microlens to achieve collimation of electron bunches produced from a nanotip in order to flatten the wavefront for coherent diffraction measurements. The lens must be small to ensure that the elec-

tron bunch is short as it reaches the sample, as this ensures rapid delivery denying the electrons the chance to spread due to their energy bandwidth. This lens represents the smallest assembly simulated to date, but is still realistically constructible. It was found that when operating in the single shot regime (realistic with an oscillator as the laser) that it is possible to to controllably deliver sub-100 fs electron bunches to the sample. Optimum pulse lengths and energy bandwidths to achieve this have been identified.

Attempts were made at measuring the coherence of the strong-field emitted electron bunches by both off-axis and in-line holography. Neither of these attempts was successful, in both cases due to a lack of magnification such that interference fringes could not be resolved. In order to achieve the desired magnification in off-axis holography a new form of magnetic lens is required. In-line holography requires a the target wire to be a approximately two orders of magnitude thinner to avoid blocking the electron beam entirely at high magnifications.

Finally, nanotips have been employed as a source of electrons for imaging purposes. Using a dedicated point projection microscopy apparatus static images were taken of both a lacey-carbon covered TEM grid and a second nanotip. Static images at magnifications of up to 4000x were recorded. Time-resolved measurements were performed of a second nanotip under illumination from a 30 fs laser pulse, where the imaging probe electrons scattered from regions of high charge on the target nanotip induced by the pump pulse. Charge propagation was imaged as originating in a region of high density at the apex of the tip before rapidly progressing down the taper, preferentially occurring on the side facing the incoming pump pulse. Effects were imaged with a temporal resolution better than 300 fs, indicating that the imaging electron bunches were successfully restricted to a few hundred femtoseconds at the sample tip. To refine the length of the electron bunch simulations of the bunch with space-charge accounted for were performed. These simulations have confirmed that imaging was performed with an average of less than 10 electrons per shot, and in at least one case it appears that an average of one electron per laser shot was achieved, successfully eliminating the problem of space-charge.

9.2 Comment on nanotips as photocathodes

It can be concluded both from the results presented here and those being concurrently presented in the literature that metallic nanotips, in particular those manufactured from tungsten, are suitable sources of electron bunches for time-resolved imaging and microscopy. The spectrometry results from the VMI in particular and,

to a lesser extent the magnetic bottle, show that stable strong-field emission from a nanotip is fully achievable with careful selection and alignment of a femtosecond laser pulse. The magnetic bottle did not yield a substantial amount of quantitative data, but has allowed some qualitative assessment of how the voltage applied to the tip affects the energy of the emitted electrons and how to avoid damage to the tips, whereas the VMI produced substantial usable information regarding the emission characteristics of tungsten tips.

Tungsten tips have been measured to have extremely favourable emission properties, when they have undergone suitable cleaning. The disadvantage of tungsten relative to other materials such as gold is that oxides on the surface of the metal interfere negatively with the emission process, requiring the tip to be exposed to higher voltages or higher intensities to achieve emission. This emission is highly unstable until the oxides are removed and the tip stops reshaping. Once stability is achieved, however, tungsten nanotips can emit in well controlled fashion by field emission, be it driven by an applied voltage or by a femtosecond laser pulse. The results presented in chapter 5 reveal that this emission occurs in a well defined energy band, allowing temporal dispersion due to the initial energy bandwidth of the electrons to be calculated and compensated, as well as enabling precise calculation of electron arrival time at the sample for pump-probe experiments. Furthermore it is possible with tight focusing and careful positioning to ensure that thermionic emission of electrons is insignificant in comparison to the shorter and more coherent bunches produced by strong-field emission. Although attempts at measuring the coherence of the electrons were unsuccessful, combining the information obtained in this project with that already present in the literature leads to the conclusion that tungsten nanotips are highly suitable sources of electrons for both static and time-resolved diffraction and microscopy experiments. This is evidenced by the data presented in chapter 8, where it is proven that it is possible to induce laser emission in bunches with controllable population to overcome space-charge effects and keep electron bunches short.

9.3 Anticipated future directions of the project

As the suitability of nanoscale metal tips as photocathodes for time-resolved microscopy and imaging is confirmed, the next phase of research is to attempt to use femtosecond bunched from a nanotip source to perform systematic pump-probe studies of a variety of samples. Two possible avenues are envisioned for the future of this project, the first is to apply femtosecond electron diffraction in pump-probe

experiments to image biological samples in the liquid phase, the second is to use both time-resolved diffraction and microscopy experiments to image nanoplasmonics in samples ranging from nanostructures to the imaging of charge waves in exotic materials such as graphene.

9.3.1 Imaging of biological samples in graphene liquid cells

As stated in chapter 1, use of electrons for imaging biological molecules such as proteins will allow samples to be imaged without first being frozen onto a surface. The possibility of examining samples such as proteins in their natural environment (i.e. surrounded by water) will allow a greater understanding to be achieved as to how these molecules function in active biological systems. As ePPM will not be capable of achieving sufficient temporal and spatial resolution to achieve this, so eCDI must be used instead. This will require that the microlens simulated in chapter 7 be constructed and integrated into the existing apparatus detailed in chapter 8 in such a way that it can be inserted or removed at will to facilitate easy switching between ePPM and eCDI.

In order for this to be performed successfully the samples must be held in micron-scale droplets. Larger droplets will fail for two reasons: The first is that as the droplet size increases the ratio of surface area to volume decreases, weakening the droplet such that surface tension is too weak to maintain the droplet integrity in the vacuum. The second is that water is relatively dense and therefore cannot be approximated as transparent to low energy electrons. The probability that a given electron will scatter from water during transition through the droplet is obviously dependent on the depth of the droplet, with the relation following the form of the Beer-Lambert law, with a substantially higher attenuation constant than is typical for light. The exponential nature of this law reveals that as the thickness of the droplet increases the probability of an electron passing through without scattering from at least one water molecule rapidly drops to near zero. Having a droplet of shallow depth (sufficiently achieved with a diameter of sub-10 microns) is the only solution to ensuring that enough electrons reach the detector without scattering from the water for this configuration to be usable.

Furthermore, under UHV conditions even the smallest droplets of sub-1 micron diameter will not be held intact by surface tension long enough to become usable, and will succumb to evaporation into the vacuum before becoming usable[284, 285]. The droplets therefore require external support through confinement in a structure which is transparent to electrons. Breakthroughs towards achieving this have been made within the past three years, with droplets being suspended in micron-scale

liquid cells confined between two sheets of graphene[130, 228, 286]. The sheets are held together by the van der Waals force in the flat regions, forming pockets around the droplets shielding them from the vacuum. These can survive for hours in UHV conditions, days in high vacuum and up to seven months in desiccator storage[228].

These Graphene Liquid Cells (GLCs) are sufficiently transparent to electrons to allow direct scattering from the sample, with each layer having a transparency of approximately 74% at 100 eV[287]. Graphene also allows access to visible wavelengths of light[288] to provide optical pumping for time-resolved pump-probe experiments. Containing a sample within a GLC removes the need for an extensive preparation process, hopefully allowing the sample to retain its natural structure.

Research to date is inconclusive as to whether GLCs provide sufficient protection against the vacuum to allow the molecular structure to be preserved long enough for the chamber to reach stable UHV pressured and imaging to be performed. Determining whether this is the case is the next step to performing eCDI on samples in their native environments and obtaining time-resolved imaging of real biophysical processes.

This must be achieved through a multistage process. GLCs must first be manufactured containing only water. This would be done by applying a layer of graphene to a holey carbon coated TEM grid, before applying deionized water and covering with a second layer. As the layers are pressed together most of the water will be expelled with the remainder forming a series of pockets of few-micron diameter. The position of these may then be clearly identified using ePPM to image them in real space. These positions can then be targeted with eCDI to observe electron diffraction from the water droplets. All future experiments of this nature will detect a variety of overlaid diffraction patterns, arising not only from the sample but also from both the graphene and the water itself. This experiment will allow the patterns from graphene and water to be identified, ensuring that background subtraction revealing the signal from the sample is possible in he future.

The next stage is to determine how effective GLC's are at surviving UHV conditions. Water at the edge of the cell will naturally diffuse into the vacuum[228], inducing a temperature change freezing and crystallization of the remaining water. This process may be observed using both ePPM and eCDI, where a change in droplet size and diffraction pattern structure is anticipated. An opportunity arises here to observe freezing on the femtosecond timescale. Actively rupturing a GLC using a laser pulse will cause a rapid freezing to occur, originating local to the rupture and spreading throughout the cell.

The third stage in determining whether samples in solution can be imaged reli-

ably would be to embed a sample in the GLCs. An obvious choice would be a large protein that has a high electron scattering cross-section and a strong interaction with light in the visible wavelength. Photosynthetic proteins such as Photosystem-II (PS2) are excellent candidates based on these criteria. Applying eCDI to the GLC's and using the data obtained in the first and second stages the signal from PS2 can be isolated from the water and graphene signals. As the water in the GLC evaporates the protein will remain in the cell and deposit directly onto the surface of the graphene. If this transition from the solution phase to surface crystallization changes the structure of the protein then this should be observable as a change in diffraction pattern. This will indicate whether techniques such as cryo-TEM and x-ray imaging which require surface crystallization are meaningful in the diagnosis of complex bio-molecular systems.

The final stage would be to perform pump-probe experiments on the sample protein with temporal resolution on the order of 100 fs, possible with the lens discussed in chapter 7. Most photosynthetic proteins, including PS2, are highly responsive to optical pumping in the region of 450nm, where water is also highly transmissive. This pumping will induce charge and energy transport through the sample but also the transfer of charge between the protein and either the surrounding water or the graphene support. This process can be compared between molecules in the solution phase and those deposited onto a surface, revealing whether phase affects the outcome of pump-probe experiments. Achieving the necessary temporal resolution to achieve this would require of the order of a single electron per shot to avoid space-charge issues, at a high repetition rate to provide a usable amount of data quickly to account for the slowly changing condition of the GLC's. An oscillator would need to be employed to induce emission of the electron bunches to achieve this.

9.3.2 Direct imaging of nanoplasmonic effects

The study of plasmon propagation in nanosystems is a rapidly advancing field with the potential to define the next generation of a number of fields, from photovoltaic energy generation to optical logic gates. This cannot proceed until the time dependent behavior of nanoplasmons is directly revealed and quantified. One of the central points of this thesis is that the sharp curvature at the apex of a nanotip generates an enhancement of any applied electric field, which under intense laser light causes plasmons to form. This effect is not limited to nanotips, and plasmonic nanostructures can take many forms; the only condition is that they are shaped such that regions exist with a sub-100 nm radius of curvature, which generates a strong local enhancement of an incident laser field[289] regardless of the surrounding ge-

ometry. Even simple nanoscale spheres can exhibit a significant enhancement effect that could be imaged. As surface plasmons will preferentially occur and focus at these enhanced regions, plasmons can be confined to volumes an order of magnitude smaller than the diffraction limit of light. This allows manipulation of light to deliver energy to localised systems in a highly controlled fashion. Such systems include electronic devices, optical switches and even individual molecules, and is key to the current development of new technologies and techniques such as nano-manipulation and nanoscale sensors.

With the arrival of femtosecond laser pulses at the nanostructure following optical pumping it may be possible to directly observe the rapid switch on and off of plasmonic response. The plasmonic effects will interact strongly with the imaging electrons, allowing the formation and propagation of the plasmons to be imaged by point projection microscopy in a pump-probe experiment. This requires that the electron pulses by even shorter than those produced in the experiment detailed in chapter 8, necessitating that the source tip be brought even closer, requiring near perfect vibration isolation of the interaction region.

A potentially interesting first step would be to image plasmon propagation along a surface to a defined destination, the key process used in Scanning Near-field Optical Microscopy (SNOM). It has recently been demonstrated that it is possible to define the optimum wavelength of light with which nanostructures interact to form plasmons by etching a grating into the taper of an object such as a nanotip. A resonance at a particular wavelength of light can be established by the spacing of the grating[290]. Applying laser light directly to the grating induces a plasmon which propagates towards the apex of the tip, causing a small percentage of the incident light to be re-emitted as the plasmon reaches the apex[291]. The resonance allows etched nanotips to act as an optical switch and/or bandpass filter, activating a plasmon and photon emission in response to a particular wavelength of light, with the response becoming weaker as the wavelength shifts off-resonance with the grating. Pump-probe experiments could image plasmon propagation towards the apex and characterise it as a function of the wavelength of the incident light.

This technique could further be applied to systems of increasing complexity, such as a microscopic interconnected network of plasmonic structures. The wavelength response of individual structures depends on size, shape and material, however by forming bonded networks of nanoparticles the propagation of plasmonic response over a much larger entity becomes possible, with applications in communications, renewable energies, electronics and molecular sensing. The transport of plasmonic effects through such systems is not presently well mapped, and direct imaging could

allow the design of such systems to be altered to remove any obstacles to plasmon propagation and ensure the highest possible efficiency.

This can be achieved with the existing apparatus (provided vibration isolation is enhanced) by deploying threaded chains[292, 293]of nanoparticles to a thin substrate before being imaging with fs-ePPM. A plasmon in the NP chain will then be induced with a tunable femtosecond laser. As with a nanotip the resulting plasmon will deflect the passing electron pulse; changing laser-pump to electron-probe delay will allow the threaded chain plasmon response to be tracked in space and time. High intensity illumination of the NP chains at resonance will cause the links between NPs to melt, an easily visible effect which will provide a marker to help enable imaging of more subtle effects.

List of Figures

Bibliography

[1] Srinivasan, R., Lobastov, V., Ruan, C.-Y., and Zewail, A. *Helv. Chim. Acta*, 86(6):1761–1799, 2003. ISSN 1522-2675. doi: 10.1002/hlca.200390147.

[2] Sciaini, G. and Miller, R. J. D. *Reports on Progress in Physics*, 74(9):096101, 2011.

[3] Ishchenko, A. A., Aseyev, S. A., Bagratashvili, V. N., Panchenko, V. Y., and Ryabov, E. A. *Physics-Uspekhi*, 57(7):633, 2014.

[4] Hasselbach, F. *Reports on Progress in Physics*, 73(1):016101, 2010.

[5] Zewail, A. H. and Thomas, J. M. *4D Electron microscopy: Imaging in space and time.* Imperial College Press, London, 2010.

[6] Dwyer, J. R., Hebeisen, C. T., Ernstorfer, R., Harb, M., Deyirmenjian, V. B., Jordan, R. E., and Dwayne Miller, R. *Philosophical Transactions of the Royal Society of London A: Mathematical, Physical and Engineering Sciences*, 364 (1840):741–778, 2006. ISSN 1364-503X. doi: 10.1098/rsta.2005.1735.

[7] Watson, J. D. and Crick, F. H. C. *Nature*, 171(4356):737–738, April 1953. doi: 10.1038/171737a0.

[8] Franklin, R. E. and Gosling, R. G. *Nature*, 171(4356):740–741, April 1953. doi: 10.1038/171740a0.

[9] Norrish, R. G. W. and Porter, G. *Nature*, 164:658, 1949.

[10] Zewail, A. H. *The chemical bond: Structure and dynamics.* Academic Press, Boston, 1992.

[11] Zewail, A. H. *Femtochemistry: Ultrafast dynamics of the chemical bond.* World Scientific, Singapore, 1994.

[12] Zewail, A. H. *Pure Appl. Chem.*, 12:2219–2231, 2000.

[13] Miller, R. J. D., Ernstorfer, R., Harb, M., Gao, M., Hebeisen, C. T., Jean-Ruel, H., Lu, C., Moriena, G., and Sciaini, G. *Acta Crystallographica Section A*, 66(2):137–156, Mar 2010. doi: 10.1107/S0108767309053926.

[14] Ihee, H., Lobastov, V. A., Gomez, U. M., Goodson, B. M., Srinivasan, R., Ruan, C.-Y., and Zewail, A. H. *Science*, 291(5503):458–462, 2001. doi: 10.1126/science.291.5503.458.

[15] Kling, M. F., von den Hoff, P., Znakovskaya, I., and de Vivie-Riedle, R. *Phys. Chem. Chem. Phys.*, 15:9448–9467, 2013. doi: 10.1039/C3CP50591J.

[16] Assion, A., Baumert, T., Bergt, M., Brixner, T., Kiefer, B., Seyfried, V., Strehle, M., and Gerber, G. *Science*, 282(5390):919–922, 1998. doi: 10.1126/science.282.5390.919.

[17] Küpper, J., Stern, S., Holmegaard, L., Filsinger, F., Rouzée, A., Rudenko, A., Johnsson, P., Martin, A. V., Adolph, M., Aquila, A., Bajt, S. c. v., Barty, A., Bostedt, C., Bozek, J., Caleman, C., Coffee, R., Coppola, N., Delmas, T., Epp, S., Erk, B., Foucar, L., Gorkhover, T., Gumprecht, L., Hartmann, A., Hartmann, R., Hauser, G., Holl, P., Hömke, A., Kimmel, N., Krasniqi, F., Kühnel, K.-U., Maurer, J., Messerschmidt, M., Moshammer, R., Reich, C., Rudek, B., Santra, R., Schlichting, I., Schmidt, C., Schorb, S., Schulz, J., Soltau, H., Spence, H., John C. Starodub, D., Strüder, L., Thøgersen, J., Vrakking, J., Marc J. Weidenspointner, G., White, T. A., Wunderer, C., Meijer, G., Ullrich, J., Stapelfeldt, H., Rolles, D., and Chapman, H. N. *Phys. Rev. Lett.*, 112:083002, Feb 2014. doi: 10.1103/PhysRevLett.112.083002.

[18] Armstrong, B. *Thermochimica Acta*, 218(0):1 – 16, 1993. ISSN 0040-6031. doi: 10.1016/0040-6031(93)80408-3.

[19] Hildner, R., Brinks, D., and van Hulst, N. F. *Nat Phys*, 7(2):172–177, February 2011. ISSN 1745-2473. doi: 10.1038/nphys1858.

[20] Chao-Chao, Q., Xing-Dong, Z., Xian-Zhou, Z., and Yu-Fang, L. *Chinese Physics Letters*, 30(2):023302, 2013.

[21] Nuernberger, P., Vogt, G., Brixner, T., and Gerber, G. *Phys. Chem. Chem. Phys.*, 9:2470–2497, 2007. doi: 10.1039/B618760A.

[22] Shapiro, M. and Brumer, P. *Principles of the quantum control of molecular processes.* Wiley, 2003.

[23] Assion, A., Geisler, M., Helbing, J., Seyfried, V., and Baumert, T. *Phys. Rev. A*, 54:R4605–R4608, Dec 1996. doi: 10.1103/PhysRevA.54.R4605.

[24] Ford, B. J. *Single Lens: The Story of the Simple Miscroscope.* Harper Collins, 1985.

[25] Clegg, B. *The man who stopped time.* Joseph Henry Press, 2007.

[26] Tzallas, P., Skantzakis, E., Nikolopoulos, L. A. A., Tsakiris, G. D., and Charalambidis, D. *Nat Phys*, 7(10):781–784, October 2011. ISSN 1745-2473. doi: 10.1038/nphys2033.

[27] Nechay, B. A., Siegner, U., Achermann, M., Bielefeldt, H., and Keller, U. *Review of Scientific Instruments*, 70(6):2758–2764, 1999. doi: 10.1063/1.1149841.

[28] Papadogiannis, N. A., Witzel, B., Kalpouzos, C., and Charalambidis, D. *Phys. Rev. Lett.*, 83:4289–4292, Nov 1999. doi: 10.1103/PhysRevLett.83.4289.

[29] Corkum, P. *Nature*, 403(6772):845–846, February 2000. ISSN 0028-0836. doi: 10.1038/35002711.

[30] Chini, M., Mashiko, H., Wang, H., Chen, S., Yun, C., Scott, S., Gilbertson, S., and Chang, Z. *Opt. Express*, 17(24):21459–21464, Nov 2009. doi: 10.1364/OE.17.021459.

[31] Sansone, G., Poletto, L., and Nisoli, M. *Nat Photon*, 5(11):655–663, November 2011. ISSN 1749-4885. doi: 10.1038/nphoton.2011.167.

[32] Lefebvre, C., Nguyen-Dang, T. T., Dion, F., Vrakking, M. J. J., Serov, V. N., and Atabek, O. *Phys. Rev. A*, 88:053416, Nov 2013. doi: 10.1103/PhysRevA.88.053416.

[33] Kling, M. F. and Vrakking, M. J. *Annual Review of Physical Chemistry*, 59 (1):463–492, 2008. doi: 10.1146/annurev.physchem.59.032607.093532. PMID: 18031218.

[34] Corkum, P. B. and Chang, Z. *Opt. Photon. News*, 19(10):24–29, Oct 2008. doi: 10.1364/OPN.19.10.000024.

[35] Krausz, F. and Ivanov, M. *Rev. Mod. Phys.*, 81:163–234, Feb 2009. doi: 10.1103/RevModPhys.81.163.

[36] Grs, K. and Mller, R. *Physics Letters*, 5(3):179 – 181, 1963. ISSN 0031-9163. doi: 10.1016/S0375-9601(63)96191-7.

[37] Bayer, E., Hellwege, K., and Schaack, G. *Physics Letters*, 5(1):33 – 35, 1963. ISSN 0031-9163. doi: 10.1016/S0375-9601(63)80017-1.

[38] Yariv, A. *Journal of Applied Physics*, 36(2):388–391, 1965. doi: 10.1063/1.1713999.

[39] Strickland, D. and Mourou, G. *Optics Communications*, 56(3):219 – 221, 1985. ISSN 0030-4018. doi: 10.1016/0030-4018(85)90120-8.

[40] Elsaesser, T. *Accounts of Chemical Research*, 42(9):1220–1228, 2009. doi: 10.1021/ar900006u. PMID: 19425543.

[41] Rubtsov, I. V., Kumar, K., and Hochstrasser, R. M. *Chemical Physics Letters*, 402(46):439 – 443, 2005. ISSN 0009-2614. doi: 10.1016/j.cplett.2004.12.083.

[42] Cowan, M., Ogilvie, J., and Miller, R. *Chemical Physics Letters*, 386(13):184 – 189, 2004. ISSN 0009-2614. doi: 10.1016/j.cplett.2004.01.027.

[43] Kukura, P., McCamant, D. W., and Mathies, R. A. *Annual Review of Physical Chemistry*, 58(1):461–488, 2007. doi: 10.1146/annurev.physchem.58.032806.104456. PMID: 17105414.

[44] McCamant, D. W., Kukura, P., and Mathies, R. A. *Applied Spectroscopy*, 57 (11):1317–1323, 2003-11-01T00:00:00. doi: 10.1366/000370203322554455.

[45] Kukura, P., Frontiera, R., and Mathies, R. A. *Phys. Rev. Lett.*, 96:238303, Jun 2006. doi: 10.1103/PhysRevLett.96.238303.

[46] Shim, S. and Mathies, R. A. *The Journal of Physical Chemistry B*, 112(15): 4826–4832, 2008. doi: 10.1021/jp710518y. PMID: 18363396.

[47] Rontgen, W. C. In *Sitzungsberichte der Wurzburger Physik-medic. Gesellshaft*, volume 137, page 41, 1895.

[48] Bragg, W. L. Nobel Foundation, 1915.

[49] Yang, W., Huang, X., Harder, R., Clark, J. N., Robinson, I. K., and Mao, H.-k. *Nat Commun*, 4:1680–, April 2013. doi: 10.1038/ncomms2661.

[50] Wilkins, S. W. *Acta Crystallographica Section A*, 69(1):1–4, Jan 2013. doi: 10.1107/S0108767312048490.

[51] Hendrickson, W. A. *Acta Crystallographica Section A*, 69(1):51–59, Jan 2013. doi: 10.1107/S0108767312050453.

[52] Larochelle, S. *Nat Struct Mol Biol*, 20(9):1025–1025, September 2013. ISSN 1545-9993. doi: 10.1038/nsmb.2670.

[53] Malsch, F. *Naturwissenschaften*, 27:854–855, 1939.

[54] Cosslett, V. E. and Nixon, W. C. *X-ray Microscopy*. London: Cambridge University Press, 1960.

[55] Kirkpatrick, P. and Jr., H. H. P. volume 3 of *Advances in Biological and Medical Physics*, pages 247 – 283. Elsevier, 1953. doi: 10.1016/B978-1-4831-9926-9.50010-0.

[56] Schmahl, G. and Rudolph, D. *Optik*, 29:577–585, 1969.

[57] Niemann, B., Rudolph, D., and Schmahl, G. *Optics Communications*, 12(2): 160 – 163, 1974. ISSN 0030-4018. doi: 10.1016/0030-4018(74)90381-2.

[58] Niemann, B., Rudolph, D., and Schmahl, G. *Appl. Opt.*, 15(8):1883–1884, Aug 1976. doi: 10.1364/AO.15.001883.

[59] Niemann, B., Rudolph, D., and Schmahl, G. *Nuclear Instruments and Methods in Physics Research*, 208(13):367 – 371, 1983. ISSN 0167-5087. doi: 10.1016/0167-5087(83)91152-3.

[60] Plech, A., Kotaidis, V., Istomin, K., and Wulff, M. *Journal of Synchrotron Radiation*, 14(3):288–294, May 2007. doi: 10.1107/S0909049507011144.

[61] Ash, E. A., editor. *Scanned Image Microscopy*. London: Academic Press, 1980.

[62] Morrison, G. R., Bridgwater, S., Browne, M. T., Burge, R. E., Cave, R. C., Charalambous, P. S., Foster, G. F., Hare, A. R., Michette, A. G., Morris, D., Taguchi, T., and Duke, P. J. *Review of Scientific Instruments*, 60(7): 2464–2467, 1989. doi: 10.1063/1.1140700.

[63] Schmahl, G. and Rudolph, D., editors. *X-ray Microscopy*. Springer Series in Optical Sciences vol 43. Berlin: Springer-Verlag, 1984.

[64] Howells, M., Jacobsen, C., Kirz, J., Feder, R., McQuaid, K., and Rothman, S. *Science*, 238(4826):514–517, 1987. doi: 10.1126/science.3659925.

[65] McNulty, I., Kirz, J., Jacobsen, C., Anderson, E. H., Howells, M. R., and Kern, D. P. *Science*, 256(5059):1009–1012, 1992. doi: 10.1126/science.256.5059.1009.

[66] Trebes, J. E., Brown, S. B., Campbell, E. M., Matthews, D. L., Nilson, D. G., Stone, G. F., and Whelan, D. A. *Science*, 238(4826):517–519, 1987. doi: 10.1126/science.238.4826.517.

[67] Schoenlein, R. W., Chattopadhyay, S., Chong, H. H. W., Glover, T. E., Heimann, P. A., Shank, C. V., Zholents, A. A., and Zolotorev, M. S. *Science*, 287(5461):2237–2240, 2000. doi: 10.1126/science.287.5461.2237.

[68] Schoenlein, R. W., Leemans, W. P., Chin, A. H., Volfbeyn, P., Glover, T. E., Balling, P., Zolotorev, M., Kim, K.-J., Chattopadhyay, S., and Shank, C. V. *Science*, 274(5285):236–238, 1996. doi: 10.1126/science.274.5285.236.

[69] Ehrke, H., Tobey, R. I., Wall, S., Cavill, S. A., Först, M., Khanna, V., Garl, T., Stojanovic, N., Prabhakaran, D., Boothroyd, A. T., Gensch, M., Mirone, A., Reutler, P., Revcolevschi, A., Dhesi, S. S., and Cavalleri, A. *Phys. Rev. Lett.*, 106:217401, May 2011. doi: 10.1103/PhysRevLett.106.217401.

[70] Haddad, W. S., McNulty, I., Trebes, J. E., Anderson, E. H., Levesque, R. A., and Yang, L. *Science*, 266(5188):1213–1215, 1994. doi: 10.1126/science.266.5188.1213.

[71] Thieme J, U. E., Schmahl G and D, R., editors. *X-ray Microscopy and Spectromicroscopy*. Berlin: Springer-Verlag, 1998.

[72] Wei, D., Schneider, G., Niemann, B., Guttmann, P., Rudolph, D., and Schmahl, G. *Ultramicroscopy*, 84(34):185 – 197, 2000. ISSN 0304-3991. doi: 10.1016/S0304-3991(00)00034-6.

[73] Wang, Jacobsen, Maser, and Osanna. *Journal of Microscopy*, 197(1):80–93, 2000. ISSN 1365-2818. doi: 10.1046/j.1365-2818.2000.00629.x.

[74] Larabell, C. A. and Le Gros, M. A. *Molecular Biology of the Cell*, 15(3): 957–962, October 2003. ISSN 1059-1524.

[75] Miao, J., Charalambous, P., Kirz, J., and Sayre, D. *Nature*, 400(6742):342–344, July 1999. ISSN 0028-0836. doi: 10.1038/22498.

[76] Neutze, R., Wouts, R., van der Spoel D, Weckert, E., and Hajdu, J. *Nature*, 406, 2000. doi: 10.1038/35021099.

[77] Emma, P., Akre, R., Arthur, J., Bionta, R., Bostedt, C., Bozek, J., Brachmann, A., Bucksbaum, P., Coffee, R., Decker, F.-J., Ding, Y., Dowell, D., Edstrom, S., Fisher, A., Frisch, J., Gilevich, S., Hastings, J., Hays, G., Hering, P., Huang, Z., Iverson, R., Loos, H., Messerschmidt, M., Miahnahri, A., Moeller, S., Nuhn, H.-D., Pile, G., Ratner, D., Rzepiela, J., Schultz, D., Smith, T., Stefan, P., Tompkins, H., Turner, J., Welch, J., White, W., Wu, J., and Galayda, G. Y. . J. *Nat Photon*, 4(9):641–647, September 2010. ISSN 1749-4885.

[78] Yabashi, M., Tanaka, H., and Ishikawa, T. *Journal of Synchrotron Radiation*, 22(3):477–484, May 2015. doi: 10.1107/S1600577515004658.

[79] Chapman, H. N., Hau-Riege, S. P., Bogan, M. J., Bajt, S., Barty, A., Boutet, S., Marchesini, S., Frank, M., Woods, B. W., Benner, W. H., London, R. A., Rohner, U., Szoke, A., Spiller, E., Moller, T., Bostedt, C., Shapiro, D. A., Kuhlmann, M., Treusch, R., Plonjes, E., Burmeister, F., Bergh, M., Caleman, C., Huldt, G., Seibert, M. M., and Hajdu, J. *Nature*, 448(7154):676–679, August 2007. ISSN 0028-0836. doi: 10.1038/nature06049.

[80] Arnlund, D., Johansson, L. C., Wickstrand, C., Barty, A., Williams, G. J., Malmerberg, E., Davidsson, J., Milathianaki, D., DePonte, D. P., Shoeman, R. L., Wang, D., James, D., Katona, G., Westenhoff, S., White, T. A., Aquila, A., Bari, S., Berntsen, P., Bogan, M., van Driel, T. B., Doak, R. B., Kjaer, K. S., Frank, M., Fromme, R., Grotjohann, I., Henning, R., Hunter, M. S., Kirian, R. A., Kosheleva, I., Kupitz, C., Liang, M., Martin, A. V., Nielsen, M. M., Messerschmidt, M., Seibert, M. M., Sjohamn, J., Stellato, F., Weierstall, U., Zatsepin, N. A., Spence, J. C. H., Fromme, P., Schlichting, I., Boutet, S., Groenhof, G., Chapman, H. N., and Neutze, R. *Nat Meth*, 11(9):923–926, September 2014. ISSN 1548-7091. doi: 10.1038/nmeth.3067.

[81] Boll, R., Rouzee, A., Adolph, M., Anielski, D., Aquila, A., Bari, S., Bomme, C., Bostedt, C., Bozek, J. D., Chapman, H. N., Christensen, L., Coffee, R., Coppola, N., De, S., Decleva, P., Epp, S. W., Erk, B., Filsinger, F., Foucar, L., Gorkhover, T., Gumprecht, L., Homke, A., Holmegaard, L., Johnsson, P., Kienitz, J. S., Kierspel, T., Krasniqi, F., Kuhnel, K.-U., Maurer, J., Messerschmidt, M., Moshammer, R., Muller, N. L. M., Rudek, B., Savelyev, E., Schlichting, I., Schmidt, C., Scholz, F., Schorb, S., Schulz, J., Seltmann, J., Stener, M., Stern, S., Techert, S., Thogersen, J., Trippel, S., Viefhaus, J., Vrakking, M., Stapelfeldt, H., Kupper, J., Ullrich, J., Rudenko, A., and Rolles, D. *Faraday Discuss.*, 171:57–80, 2014. doi: 10.1039/C4FD00037D.

[82] Schmidt, M., Pande, K., Basu, S., and Tenboer, J. *Structural Dynamics*, 2(4): 041708, 2015. doi: 10.1063/1.4919903.

[83] McEvoy, J. P. and Zarante, O. *Introducing quantum theory.* Totem Books, 2004.

[84] de Broglie, L. *Foundations of Physics*, 1(1):5–15, 1970. ISSN 0015-9018. doi: 10.1007/BF00708650.

[85] Davisson, C. and Germer, L. H. *Phys. Rev.*, 30:705–740, Dec 1927. doi: 10.1103/PhysRev.30.705.

[86] Thomson, G. P. and Reid, A. *Nature*, 18:890, 1927.

[87] Ruska, E. In *Nobel Lecture*, 1986.

[88] Egerton, R. *Physical principles of electron microscopy.* Springer, 2005.

[89] Fink, M. and Bonham, R. A. *Review of Scientific Instruments*, 41(3):389–396, 1970. doi: 10.1063/1.1684523.

[90] Bonham, R. A. and Fink, M. *High energy electron scattering.* Van Nostrand Reinhold, New York, 1974.

[91] Fink, M., Moore, P. G., and Gregory, D. *The Journal of Chemical Physics*, 71(12):5227–5237, 1979. doi: 10.1063/1.438330.

[92] Ewbank, J. D., Schafer, L., Paul, D. W., Benston, O. J., and Lennox, J. C. *Rev. Sci. Instrum.*, 55(10):1598–1603, 1984. doi: 10.1063/1.1137624.

[93] Stearns, D. G. and Wiedwald, J. D. *Review of Scientific Instruments*, 60(6): 1095–1103, 1989. doi: 10.1063/1.1140323.

[94] Hetherington, C. *Materials Today*, 7(12):50 – 55, 2004. ISSN 1369-7021. doi: 10.1016/S1369-7021(04)00571-1.

[95] Haider, M., Hartel, P., Müller, H., Uhlemann, S., and Zach, J. *Philosophical Transactions of the Royal Society of London A: Mathematical, Physical and Engineering Sciences*, 367(1903):3665–3682, 2009. ISSN 1364-503X. doi: 10.1098/rsta.2009.0121.

[96] Hansen, T. W., Wagner, J. B., and Dunin-Borkowski, R. E. *Materials Science and Technology*, 26(11):1338–1344, 2010. doi: 10.1179/026708310X12756557336355.

[97] Mark, H. and Wierl, R. *Naturwissenschaften*, 18(9):205–205, 1930. ISSN 0028-1042. doi: 10.1007/BF01494849.

[98] Brockway, L. O. *Rev. Mod. Phys.*, 8:231–266, Jul 1936. doi: 10.1103/RevModPhys.8.231.

[99] Pauling, L. and Brockway, L. O. *Journal of the American Chemical Society*, 57(12):2684–2692, 1935. doi: 10.1021/ja01315a103.

[100] Trendelenburg, F. *Naturwissenschaften*, 21(8):173–177, 1933. ISSN 0028-1042. doi: 10.1007/BF01504056.

[101] Finbak, C. *Avh. Norsk Vidensk.-Akad. Oslo*, 13, 1937.

[102] Debye, P. *Phys. Z.*, 404:40–66, 1939.

[103] I. Hargittai, M. H. *Stereochemical Applications of Gas-Phase Electron Diffraction.* VCH New York, 1988.

[104] Goodman, P. *Fifty Years of Electron Diffraction.* D. Reidel Publishing, Dordrecht, 1981.

[105] Longchamp, J.-N., Latychevskaia, T., Escher, C., and Fink, H.-W. *Applied Physics Letters*, 101(11):113117, 2012. doi: 10.1063/1.4752717.

[106] Longchamp, J.-N., Latychevskaia, T., Escher, C., and Fink, H.-W. *Phys. Rev. Lett.*, 110:255501, Jun 2013. doi: 10.1103/PhysRevLett.110.255501.

[107] Ischenko, A., Golubkov, V., Spiridonov, V., Zgurskii, A., Akhmanov, A., Vabischevich, M., and Bagratashvili, V. *Applied Physics B*, 32(3):161–163, 1983. ISSN 0946-2171. doi: 10.1007/BF00688823.

[108] Rood, A. P. and Milledge, J. *J. Chem. Soc., Faraday Trans. 2*, 80:1145–1153, 1984. doi: 10.1039/F29848001145.

[109] Bartell, L. S. and Dibble, T. S. *J. Am. Chem. Soc.*, 112(2):890–891, 1990. doi: 10.1021/ja00158a071.

[110] Ewbank, J. D., Faust, W. L., Luo, J. Y., English, J. T., Monts, D. L., Paul, D. W., Dou, Q., and Schfer, L. *Review of Scientific Instruments*, 63(6):3352–3358, 1992. doi: 10.1063/1.1142552.

[111] A. A. Ischenko, J. D. E., L. Schafer. *Time resolved diffraction.* Oxford University Press, New York, 1997.

[112] Mourou, G. and Williamson, S. *Applied Physics Letters*, 41(1):44–45, 1982. doi: 10.1063/1.93316.

[113] Williamson, S., Mourou, G., and Li, J. C. M. *Phys. Rev. Lett.*, 52:2364–2367, Jun 1984. doi: 10.1103/PhysRevLett.52.2364.

[114] Williamson, S., Mourou, G., and Li, J. In Auston, D. and Eisenthal, K., editors, *Ultrafast Phenomena IV*, volume 38 of *Springer Series in Chemical Physics*, pages 114–117. Springer Berlin Heidelberg, 1984. ISBN 978-3-642-82380-0. doi: 10.1007/978-3-642-82378-7_33.

[115] Dudek, R. C. and Weber, P. M. *The Journal of Physical Chemistry A*, 105 (17):4167–4171, 2001. doi: 10.1021/jp010122t.

[116] Ruan, C.-Y., Lobastov, V. A., Srinivasan, R., Goodson, B. M., Ihee, H., and Zewail, A. H. *Proceedings of the National Academy of Sciences*, 98(13):7117–7122, 2001. doi: 10.1073/pnas.131192898.

[117] Ryu, S., Weber, P. M., and Stratt, R. M. *The Journal of Chemical Physics*, 112(3):1260–1270, 2000. doi: 10.1063/1.480678.

[118] Geiser, J. D. and Weber, P. M. *The Journal of Chemical Physics*, 108(19): 8004–8011, 1998. doi: 10.1063/1.476239.

[119] Ihee, H., Cao, J., and Zewail, A. H. *Chemical Physics Letters*, 281(13):10 – 19, 1997. ISSN 0009-2614. doi: 10.1016/S0009-2614(97)01167-6.

[120] Ligges, M., Streubhr, C., Brazda, T., Posth, O., Hassel, C., Dumpich, G., Zhou, P., and von der Linde, D. In *Symposium MM Ultrafast Processes in Materials Science*, volume 1230 of *MRS Proceedings*, 2009. doi: 10.1557/PROC-1230-MM03-08.

[121] Siwick, B. J., Dwyer, J. R., Jordan, R. E., and Miller, R. J. D. *Science*, 302 (5649):1382–1385, 2003. doi: 10.1126/science.1090052.

[122] van Oudheusden, T., Pasmans, P. L. E. M., van der Geer, S. B., de Loos, M. J., van der Wiel, M. J., and Luiten, O. J. *Phys. Rev. Lett.*, 105:264801, Dec 2010. doi: 10.1103/PhysRevLett.105.264801.

[123] Luiten, J., Oudheusden, T. V., Siwick, B., Jong, E. D., Root, W. O. t., and Geer, B. V. d. *Microscopy and Microanalysis*, 14:494–495, 8 2008. ISSN 1435-8115. doi: 10.1017/S1431927608082391.

[124] Quinonez, E., Handali, J., and Barwick, B. *Review of Scientific Instruments*, 84(10):103710, 2013. doi: 10.1063/1.4827035.

[125] Sciaini, G., Harb, M., Kruglik, S. G., Payer, T., Hebeisen, C. T., Heringdorf, F.-J. M. z., Yamaguchi, M., Hoegen, M. H.-v., Ernstorfer, R., and Miller, R. J. D. *Nature*, 458(7234):56–59, March 2009. ISSN 0028-0836. doi: 10.1038/nature07788.

[126] Eichberger, M., Schafer, H., Krumova, M., Beyer, M., Demsar, J., Berger, H., Moriena, G., Sciaini, G., and Miller, R. J. D. *Nature*, 468(7325):799–802, December 2010. ISSN 0028-0836. doi: 10.1038/nature09539.

[127] Vainshtein, K. *Structure analysis by electron diffraction.* Macmillan, New York, 1964.

[128] Meyer, J. C., Eder, F., Kurasch, S., Skakalova, V., Kotakoski, J., Park, H. J., Roth, S., Chuvilin, A., Eyhusen, S., Benner, G., Krasheninnikov, A. V., and Kaiser, U. *Phys. Rev. Lett.*, 108:196102, May 2012. doi: 10.1103/PhysRevLett.108.196102.

[129] Li, C., Cole, M. T., Lei, W., Qu, K., Ying, K., Zhang, Y., Robertson, A. R., Warner, J. H., Ding, S., Zhang, X., Wang, B., and Milne, W. I. *Advanced Functional Materials*, 24(9):1218–1227, 2014. ISSN 1616-3028. doi: 10.1002/adfm.201300322.

[130] Stoll, J. D. and Kolmakov, A. *Nanotechnology*, 23(50):505704, 2012.

[131] Mutus, J. Y., Livadaru, L., Robinson, J. T., Urban, R., Salomons, M. H., Cloutier, M., and Wolkow, R. A. *New Journal of Physics*, 13(6):063011, 2011.

[132] Muller, M., Paarmann, A., and Ernstorfer, R. *Nat Commun*, 5:–, October 2014. doi: 10.1038/ncomms6292.

[133] Ferray, M., L'Huillier, A., Li, X. F., Lompre, L. A., Mainfray, G., and Manus, C. *Journal of Physics B: Atomic, Molecular and Optical Physics*, 21(3):L31, 1988.

[134] Li, X. F., L'Huillier, A., Ferray, M., Lompré, L. A., and Mainfray, G. *Phys. Rev. A*, 39:5751–5761, Jun 1989. doi: 10.1103/PhysRevA.39.5751.

[135] Popmintchev, T., Chen, M.-C., Popmintchev, D., Arpin, P., Brown, S., Ališauskas, S., Andriukaitis, G., Bal?iunas, T., Mcke, O. D., Pugzlys, A., Baltuka, A., Shim, B., Schrauth, S. E., Gaeta, A., Hernndez-Garca, C., Plaja, L., Becker, A., Jaron-Becker, A., Murnane, M. M., and Kapteyn, H. C. *Science*, 336(6086):1287–1291, 2012. doi: 10.1126/science.1218497.

[136] Le, H. V., Dinh, K. B., Hannaford, P., and Dao, L. V. *Results in Physics*, 4 (0):113 – 116, 2014. ISSN 2211-3797. doi: 10.1016/j.rinp.2014.07.008.

[137] Sandberg, R. L., Paul, A., Raymondson, D. A., Hädrich, S., Gaudiosi, D. M., Holtsnider, J., Tobey, R. I., Cohen, O., Murnane, M. M., Kapteyn, H. C., Song, C., Miao, J., Liu, Y., and Salmassi, F. *Phys. Rev. Lett.*, 99:098103, Aug 2007. doi: 10.1103/PhysRevLett.99.098103.

[138] Waldecker, L., Bertoni, R., and Ernstorfer, R. *Journal of Applied Physics*, 117 (4):044903, 2015. doi: 10.1063/1.4906786.

[139] Gulde, M., Schweda, S., Storeck, G., Maiti, M., Yu, H. K., Wodtke, A. M., Schfer, S., and Ropers, C. *Science*, 345(6193):200–204, 2014. doi: 10.1126/science.1250658.

[140] Lahme, S., Kealhofer, C., Krausz, F., and Baum, P. *Structural Dynamics*, 1 (3):034303, 2014. doi: 10.1063/1.4884937.

[141] Baum, P. *Journal of Physics B: Atomic, Molecular and Optical Physics*, 47 (12):124005, 2014.

[142] Gao, M., Lu, C., Jean-Ruel, H., Liu, L. C., Marx, A., Onda, K., Koshihara, S.-y., Nakano, Y., Shao, X., Hiramatsu, T., Saito, G., Yamochi, H., Cooney, R. R., Moriena, G., Sciaini, G., and Miller, R. J. D. *Nature*, 496(7445):343–346, April 2013. ISSN 0028-0836. doi: 10.1038/nature12044.

[143] Jean-Ruel, H., Gao, M., Kochman, M. A., Lu, C., Liu, L. C., Cooney, R. R., Morrison, C. A., and Miller, R. J. D. *The Journal of Physical Chemistry B*, 117(49):15894–15902, 2013. doi: 10.1021/jp409245h. PMID: 24117385.

[144] Gerbig, C., Morgenstern, S., Sarpe, C., Wollenhaupt, M., and Baumert, T. In *Research in Optical Sciences*, page IT3D.3. Optical Society of America, 2012. doi: 10.1364/ICUSD.2012.IT3D.3.

[145] Morrison, V. R., Chatelain, R. P., Tiwari, K. L., Hendaoui, A., Bruhcs, A., Chaker, M., and Siwick, B. J. *Science*, 346(6208):445–448, 2014. doi: 10.1126/science.1253779.

[146] Chatelain, R. P., Morrison, V. R., Klarenaar, B. L. M., and Siwick, B. J. *Phys. Rev. Lett.*, 113:235502, Dec 2014. doi: 10.1103/PhysRevLett.113.235502.

[147] Hommelhoff, P., Kealhofer, C., and Kasevich, M. A. *Phys. Rev. Lett.*, 97: 247402, Dec 2006. doi: 10.1103/PhysRevLett.97.247402.

[148] Kruger, M., Schenk, M., Hommelhoff, P., Wachter, G., Lemell, C., and Burgdorfer, J. *New. J. Phys.*, 14(8):085019, 2012.

[149] Yalunin, S. V., Gulde, M., and Ropers, C. *Phys. Rev. B*, 84:195426, Nov 2011. doi: 10.1103/PhysRevB.84.195426.

[150] Reiss, H. R. *Phys. Rev. Lett.*, 101:043002, Jul 2008. doi: 10.1103/PhysRevLett.101.043002.

[151] Kruger, M., Schenk, M., Forster, M., and Hommelhoff, P. *J. Phys. B: At., Mol. Opt. Phys.*, 45(7):074006, 2012.

[152] Park, D. J., Piglosiewicz, B., Schmidt, S., Kollmann, H., Mascheck, M., and Lienau, C. *Phys. Rev. Lett.*, 109:244803, Dec 2012. doi: 10.1103/PhysRevLett.109.244803.

[153] Ropers, C., Solli, D. R., Schulz, C. P., Lienau, C., and Elsaesser, T. *Phys. Rev. Lett.*, 98:043907, Jan 2007. doi: 10.1103/PhysRevLett.98.043907.

[154] Schenk, M., Krüger, M., and Hommelhoff, P. *Phys. Rev. Lett.*, 105:257601, Dec 2010. doi: 10.1103/PhysRevLett.105.257601.

[155] Cade, N., Culfaz, F., Eligal, L., Ritman-Meer, T., Huang, F.-M., Festy, F., and Richards, D. *NanoBiotechnology*, 3(3-4):203–211, 2007. ISSN 1551-1286. doi: 10.1007/s12030-009-9020-x.

[156] Stckle, R. M., Suh, Y. D., Deckert, V., and Zenobi, R. *Chemical Physics Letters*, 318(13):131 – 136, 2000. ISSN 0009-2614. doi: 10.1016/S0009-2614(99)01451-7.

[157] Deckert, V. *Journal of Raman Spectroscopy*, 40(10):1336–1337, 2009. ISSN 1097-4555. doi: 10.1002/jrs.2452.

[158] Pettinger, B., Picardi, G., Schuster, R., and Ertl, G. *Single Molecules*, 3(5-6): 285–294, 2002. ISSN 1438-5171. doi: 10.1002/1438-5171(200211)3:5/6⟨285::AID-SIMO285⟩3.0.CO;2-X.

[159] Hansma, P. K. and Tersoff, J. *Journal of Applied Physics*, 61(2):R1–R24, 1987. doi: 10.1063/1.338189.

[160] Binnig, G. and Rohrer, H. *IBM J. Res. Dev.*, 44(1-2):279–293, January 2000. ISSN 0018-8646. doi: 10.1147/rd.441.0279.

[161] Binnig, G., Quate, C. F., and Gerber, C. *Phys. Rev. Lett.*, 56:930–933, Mar 1986. doi: 10.1103/PhysRevLett.56.930.

[162] Bryant, P. J., Miller, R. G., and Yang, R. *Applied Physics Letters*, 52(26): 2233–2235, 1988. doi: 10.1063/1.99541.

[163] Einstein, A. Nobel Foundation, 1921.

[164] Millikan, R. Nobel Foundation, 1923.

[165] Einstein, A. *Ann. Phys.*, 322:132–148, 1905.

[166] Aeschlimann, M., Schmuttenmaer, C. A., Elsayed-Ali, H. E., Miller, R. J. D., Cao, J., Gao, Y., and Mantell, D. A. *The Journal of Chemical Physics*, 102 (21):8606–8613, 1995. doi: 10.1063/1.468962.

[167] Petite, G., Agostini, P., Trainham, R., Mevel, E., and Martin, P. *Phys. Rev. B*, 45:12210–12217, Jun 1992. doi: 10.1103/PhysRevB.45.12210.

[168] Yalunin, S. V., Herink, G., Solli, D. R., Krger, M., Hommelhoff, P., Diehn, M., Munk, A., and Ropers, C. *Annalen der Physik*, 525(1-2):L12–L18, 2013. ISSN 1521-3889. doi: 10.1002/andp.201200224.

[169] Gilton, T. L., Cowin, J. P., Kubiak, G. D., and Hamza, A. V. *Journal of Applied Physics*, 68(9):4802–4810, 1990. doi: 10.1063/1.346137.

[170] Passlack, S., Mathias, S., Andreyev, O., Mittnacht, D., Aeschlimann, M., and Bauer, M. *Journal of Applied Physics*, 100(2):024912, 2006. doi: 10.1063/1. 2217985.

[171] Keldysh, L. V. *Soviet Physics JETP*, 20:1307–1314, 1965.

[172] Bunkin, E. V. and Fedorov, M. V. *Soviet Physics JETP*, 22:884–847, 1966.

[173] Reiss, H. R. *Phys. Rev. A*, 82:023418, Aug 2010. doi: 10.1103/PhysRevA.82. 023418.

[174] Aidelsburger, M., Kirchner, F. O., Krausz, F., and Baum, P. *Proceedings of the National Academy of Sciences*, 107(46):19714–19719, 2010. doi: 10.1073/ pnas.1010165107.

[175] Jensen, K. L., Feldman, D. W., Moody, N. A., and OShea, P. G. *Journal of Applied Physics*, 99(12):124905, 2006. doi: 10.1063/1.2203720.

[176] Borzenets, I. V., Yoon, I., Prior, M. W., Donald, B. R., Mooney, R. D., and Finkelstein, G. *Journal of Applied Physics*, 111(7):074703, 2012. doi: 10.1063/1.3702802.

[177] Melmed, A. J. *Journal of Vacuum Science & Technology B*, 9(2):601–608, 1991. doi: 10.1116/1.585467.

[178] Eisele, M., Kruger, M., Schenk, M., Ziegler, A., and Hommelhoff, P. *Review of Scientific Instruments*, 82(2):026101, 2011. doi: 10.1063/1.3534078.

[179] Mamin, H. J., Guethner, P. H., and Rugar, D. *Phys. Rev. Lett.*, 65:2418–2421, Nov 1990. doi: 10.1103/PhysRevLett.65.2418.

[180] Ren, B., Picardi, G., and Pettinger, B. *Review of Scientific Instruments*, 75 (4):837–841, 2004. doi: 10.1063/1.1688442.

[181] Kulawik, M., Nowicki, M., Thielsch, G., Cramer, L., Rust, H.-P., Freund, H.-J., Pearl, T. P., and Weiss, P. S. *Review of Scientific Instruments*, 74(2): 1027–1030, 2003. doi: 10.1063/1.1532833.

[182] Oliva, A. I., Romero G., A., Pea, J. L., Anguiano, E., and Aguilar, M. *Review of Scientific Instruments*, 67(5):1917–1921, 1996. doi: 10.1063/1.1146996.

[183] Song, J. P., Pryds, N. H., Glejbol, K., Morch, K. A., Tholen, A. R., and Christensen, L. N. *Review of Scientific Instruments*, 64(4):900–903, 1993. doi: 10.1063/1.1144140.

[184] Zhang, R. and Ivey, D. G. *Journal of Vacuum Science & Technology B*, 14(1): 1–10, 1996. doi: 10.1116/1.589029.

[185] Libioulle, L., Houbion, Y., and Gilles, J. *Review of Scientific Instruments*, 66 (1):97–100, 1995. doi: 10.1063/1.1146153.

[186] Lindahl, J., Takanen, T., and Montelius, L. *Journal of Vacuum Science & Technology B*, 16(6):3077–3081, 1998. doi: 10.1116/1.590445.

[187] Musselman, I. H. and Russell, P. E. *Journal of Vacuum Science & Technology A*, 8(4):3558–3562, 1990. doi: 10.1116/1.576507.

[188] Sorensen, A. H., Hvid, U., Mortensen, M. W., and Morch, K. A. *Review of Scientific Instruments*, 70(7):3059–3067, 1999. doi: 10.1063/1.1149891.

[189] Yao, I.-C., Lin, P., and Tseng, T.-Y. *Nanotechnology*, 20(12):125202, 2009.

[190] Xu, C. X. and Sun, X. W. *Applied Physics Letters*, 83(18):3806–3808, 2003. doi: 10.1063/1.1625774.

[191] Yao, L., Zheng, M., Ma, L., Li, W., Li, M., and Shen, W. *Nanoscale Research Letters*, 6(1):74, 2011. ISSN 1556-276X. doi: 10.1186/1556-276X-6-74.

[192] Wu, C.-C., Ou, K.-L., and Tseng, C.-L. *Nanoscale Research Letters*, 7(1):120, 2012. ISSN 1556-276X. doi: 10.1186/1556-276X-7-120.

[193] Sola, F., Biaggi-Labiosa, A., Fonseca, L., Resto, O., Lebron-Colon, M., and Meador, M. *Nanoscale Research Letters*, 4(5):431–436, 2009. ISSN 1556-276X. doi: 10.1007/s11671-009-9270-5.

[194] Bouhelier, A., Beversluis, M., Hartschuh, A., and Novotny, L. *Phys. Rev. Lett.*, 90:013903, Jan 2003. doi: 10.1103/PhysRevLett.90.013903.

[195] Stockman, M. I., Kling, M. F., Kleineberg, U., and Krausz, F. *Nat Photon*, 1(9):539–544, September 2007. ISSN 1749-4885. doi: 10.1038/nphoton.2007.169.

[196] Sussmann, F. and Kling, M. F. *Phys. Rev. B*, 84:121406, Sep 2011. doi: 10.1103/PhysRevB.84.121406.

[197] Herink, G., Wimmer, L., and Ropers, C. *New Journal of Physics*, 16(12):123005, 2014.

[198] Thomas, S., Wachter, G., Lemell, C., Burgdrfer, J., and Hommelhoff, P. *New Journal of Physics*, 17(6):063010, 2015.

[199] Muller, M., Paarmann, A., and Ernstorfer, R. *Nat Commun*, 5:–, October 2014. doi: 10.1038/ncomms6292.

[200] Mutus, J. Y., Livadaru, L., Urban, R., Pitters, J., Legg, A. P., Salomons, M. H., Cloutier, M., and Wolkow, R. A. *New Journal of Physics*, 15(7):073038, 2013.

[201] Kirchner, F. O., Lahme, S., Krausz, F., and Baum, P. *New Journal of Physics*, 15(6):063021, 2013.

[202] Lucier, A.-S. *Preparation and Characterization of Tungsten Tips Suitable for Molecular Electronics Studies.* PhD thesis, McGill University, Canada, February 2004.

[203] Hagedorn, T., Ouali, M. E., Paul, W., Oliver, D., Miyahara, Y., and Grtter, P. *Review of Scientific Instruments*, 82(11):113903, 2011. doi: 10.1063/1.3660279.

[204] Nakamura, Y., Mera, Y., and Maeda, K. *Review of Scientific Instruments*, 70 (8):3373–3376, 1999. doi: 10.1063/1.1149921.

[205] Ekvall, I., Wahlstrom, E., Claesson, D., Olin, H., and Olsson, E. *Measurement Science and Technology*, 10(1):11, 1999.

[206] Schottky, W. *Physik. Zeitschr*, 15:872–878, 1914.

[207] Forbes, R. G. In *Vacuum Nanoelectronics Conference (IVNC), 2011 24th International*, pages 113–114, July 2011.

[208] Stern, T. E., Gossling, B. S., and Fowler, R. H. *Proceedings of the Royal Society of London A: Mathematical, Physical and Engineering Sciences*, 124 (795):699–723, 1929. ISSN 0950-1207. doi: 10.1098/rspa.1929.0147.

[209] Gomer, R. *Field Emission and Field Ionization*, volume 9 of *Harvard Monographs in Applied Science.* 1961.

[210] M. K. Miller, M. G. H., A. Cerezo and FRS, G. D. W. S. *Atom Probe Field Ion Microscopy*, volume 52 of *Monographs on the Physics and Chemistry of Materials.* Clarendon Press, 1996.

[211] Michalik, A. M. and Sipe, J. E. *Journal of Applied Physics*, 99(5):054908, 2006. doi: 10.1063/1.2178855.

[212] Siwick, B. J., Dwyer, J. R., Jordan, R. E., and Miller, R. J. D. *Journal of Applied Physics*, 92(3):1643–1648, 2002. doi: 10.1063/1.1487437.

[213] Baum, P. and Zewail, A. H. *Proceedings of the National Academy of Sciences*, 104(47):18409–18414, 2007. doi: 10.1073/pnas.0709019104.

[214] Silfvast, W. T. *Laser Fundamentals.* Cambridge, 2008.

[215] Kuleshov, N. V., Lagatsky, A. A., Podlipensky, A. V., Mikhailov, V. P., and Huber, G. *Opt. Lett.*, 22(17):1317–1319, Sep 1997. doi: 10.1364/OL.22.001317.

[216] Trophème, B., Boulanger, B., and Mennerat, G. *Opt. Express*, 20(24):26176–26183, Nov 2012. doi: 10.1364/OE.20.026176.

[217] Frassetto, F., Cacho, C., Froud, C. A., Turcu, I. E., Villoresi, P., Bryan, W. A., Springate, E., and Poletto, L. *Opt. Express*, 19(20):19169–19181, Sep 2011. doi: 10.1364/OE.19.019169.

[218] Bryan, W. A., Frassetto, F., Froud, C. A., Turcu, I. C. E., King, R. B., Calvert, C. R., Nemeth, G. R. A. J., Villoresi, P., Poletto, L., and Springate, E. *New Journal of Physics*, 14(1):013057, 2012.

[219] Fork, R. L., Martinez, O. E., and Gordon, J. P. *Opt. Lett.*, 9(5):150–152, May 1984. doi: 10.1364/OL.9.000150.

[220] Trebino, R., DeLong, K. W., Fittinghoff, D. N., Sweetser, J. N., Krumbgel, M. A., Richman, B. A., and Kane, D. J. *Rev. Sci. Instrum.*, 68(9):3277–3295, 1997. doi: 10.1063/1.1148286.

[221] *Available at http://frog.gatech.edu/code.html.*

[222] Kruit, P. and Read, F. H. *Journal of Physics E: Scientific Instruments*, 16(4): 313, 1983.

[223] Tsuboi, T., Xu, E. Y., Bae, Y. K., and Gillen, K. T. *Review of Scientific Instruments*, 59(8):1357–1362, 1988. doi: http://dx.doi.org/10.1063/1.1139722.

[224] Eland, J. H. D., Vieuxmaire, O., Kinugawa, T., Lablanquie, P., Hall, R. I., and Penent, F. *Phys. Rev. Lett.*, 90:053003, Feb 2003. doi: 10.1103/PhysRevLett.90.053003.

[225] Radcliffe, P., Dsterer, S., Azima, A., Li, W., Plnjes, E., Redlin, H., Feldhaus, J., Nicolosi, P., Poletto, L., Dardis, J., Gutierrez, J., Hough, P., Kavanagh, K., Kennedy, E., Luna, H., Yeates, P., Costello, J., Delyseries, A., Lewis, C., Glijer, D., Cubaynes, D., and Meyer, M. *Nuclear Instruments and Methods in Physics Research Section A: Accelerators, Spectrometers, Detectors and Associated Equipment*, 583(23):516 – 525, 2007. ISSN 0168-9002. doi: 10.1016/j.nima.2007.09.014.

[226] Rijs, A., Backus, E., de Lange, C., Westwood, N., and Janssen, M. *Journal of Electron Spectroscopy and Related Phenomena*, 112(13):151 – 162, 2000. ISSN 0368-2048. doi: 10.1016/S0368-2048(00)00209-7. Molecular electron spectroscopy.

[227] Handschuh, H., Gantefr, G., and Eberhardt, W. *Review of Scientific Instruments*, 66(7):3838–3843, 1995. doi: 10.1063/1.1145446.

[228] Wang, C., Qiao, Q., Shokuhfar, T., and Klie, R. F. *Advanced Materials*, 26 (21):3410–3414, 2014. ISSN 1521-4095. doi: 10.1002/adma.201306069.

[229] Yanagisawa, H., Hafner, C., Doná, P., Klöckner, M., Leuenberger, D., Greber, T., Hengsberger, M., and Osterwalder, J. *Phys. Rev. Lett.*, 103:257603, Dec 2009. doi: 10.1103/PhysRevLett.103.257603.

[230] Yanagisawa, H., Hafner, C., Doná, P., Klöckner, M., Leuenberger, D., Greber, T., Osterwalder, J., and Hengsberger, M. *Phys. Rev. B*, 81:115429, Mar 2010. doi: 10.1103/PhysRevB.81.115429.

[231] Whitaker, B. J. *Imaging in Molecular Dynamics.* Cambridge University Press, 2003.

[232] Tsubouchi, M., Whitaker, B. J., Wang, L., Kohguchi, H., and Suzuki, T. *Phys. Rev. Lett.*, 86:4500–4503, May 2001. doi: 10.1103/PhysRevLett.86.4500.

[233] Catton, E. L. *Photoelectron Spectroscopy of Highly Oriented Pyrolytic Graphite Using Intense Ultrashort Laser Pulses.* PhD thesis, University of Birmingham, 2010.

[234] Parker, D. H. and Eppink, A. T. J. B. *The Journal of Chemical Physics*, 107 (7):2357–2362, 1997. doi: http://dx.doi.org/10.1063/1.474624.

[235] Liu, S.-Y., Alnama, K., Matsumoto, J., Nishizawa, K., Kohguchi, H., Lee, Y.-P., and Suzuki, T. *The Journal of Physical Chemistry A*, 115(14):2953–2965, 2011. doi: 10.1021/jp1098574. PMID: 21413769.

[236] Ghafur, O., Siu, W., Johnsson, P., Kling, M. F., Drescher, M., and Vrakking, M. J. J. *Rev. Sci. Instrum.*, 80(3):033110, 2009. doi: http://dx.doi.org/10.1063/1.3085799.

[237] OKeeffe, P., Feyer, V., Bolognesi, P., Coreno, M., Callegari, C., Cautero, G., Moise, A., Prince, K., Richter, R., Sergo, R., Alagia, M., de Simone, M., Kivimki, A., Devetta, M., Mazza, T., Piseri, P., Lyamayev, V., Katzy, R., Stienkemeier, F., Ovcharenko, Y., Mller, T., and Avaldi, L. *Nuclear Instruments and Methods in Physics Research Section B: Beam Interactions with Materials and Atoms*, 284(0):69 – 73, 2012. ISSN 0168-583X. doi: http://dx.doi.org/10.1016/j.nimb.2011.07.020. E-MRS 2011 Spring Meeting, Symposium M: X-ray techniques for materials research-from laboratory sources to free electron lasers.

[238] Bolognesi, P., Castrovilli, M., OKeeffe, P., Casavola, A., Catone, D., Turchini, S., and Avaldi, L. *Nuclear Instruments and Methods in Physics Research Section B: Beam Interactions with Materials and Atoms*, 279(0):118 – 123, 2012. ISSN 0168-583X. doi: http://dx.doi.org/10.1016/j.nimb.2011.10.063. Proceedings of the Fifth International Conference on Elementary Processes in Atomic Systems Belgrade, Serbia, 21-25 June 2011.

[239] OKeeffe, P., Bolognesi, P., Coreno, M., Moise, A., Richter, R., Cautero, G., Stebel, L., Sergo, R., Pravica, L., Ovcharenko, Y., and Avaldi, L. *Rev. Sci. Instrum.*, 82(3):033109, 2011. doi: http://dx.doi.org/10.1063/1.3563723.

[240] Remetter, T., Johnsson, P., Mauritsson, J., Varju, K., Ni, Y., Lepine, F., Gustafsson, E., Kling, M., Khan, J., Lopez-Martens, R., Schafer, K. J., Vrakking, M. J. J., and L/'Huillier, A. *Nat Phys*, 2(5):323–326, May 2006. ISSN 1745-2473.

[241] Johnsson, P., Siu, W., Gijsbertsen, A., Verhoeven, J., Meijer, A., van der Zande, W., and Vrakking, M. *J. Mod. Opt.*, 55(16):2693–2709, 2008. doi: 10.1080/09500340802393062.

[242] Smann, F., Zherebtsov, S., Plenge, J., Johnson, N. G., Kbel, M., Sayler, A. M., Mondes, V., Graf, C., Rhl, E., Paulus, G. G., Schmischke, D., Swrschek, P., and Kling, M. F. *Rev. Sci. Instrum.*, 82(9):093109, 2011. doi: http://dx.doi.org/10.1063/1.3639333.

[243] Vrakking, M. J. J. *Rev. Sci. Instrum.*, 72(11):4084–4089, 2001. doi: http://dx.doi.org/10.1063/1.1406923.

[244] Carley, R. E., Heesel, E., and Fielding, H. H. *Chem. Soc. Rev.*, 34:949–969, 2005. doi: 10.1039/B509463A.

[245] Minns, R. S., Patel, R., Verlet, J. R. R., and Fielding, H. H. *Phys. Rev. Lett.*, 91:243601, Dec 2003. doi: 10.1103/PhysRevLett.91.243601.

[246] Yoder, B. L., West, A. H. C., Schlppi, B., Chasovskikh, E., and Signorell, R. *The Journal of Chemical Physics*, 138(4):044202, 2013. doi: http://dx.doi.org/10.1063/1.4788620.

[247] Xiong, W., Hickstein, D. D., Schnitzenbaumer, K. J., Ellis, J. L., Palm, B. B., Keister, K. E., Ding, C., Miaja-Avila, L., Dukovic, G., Jimenez, J. L., Murnane, M. M., and Kapteyn, H. C. *Nano Letters*, 13(6):2924–2930, 2013. doi: 10.1021/nl401309z. PMID: 23688290.

[248] Delone, N. and Fedorov, M. *Progress in Quantum Electronics*, 13(4):267 – 298, 1989. ISSN 0079-6727. doi: 10.1016/0079-6727(89)90007-4.

[249] Eberly, J., Javanainen, J., and Rzaewski, K. *Physics Reports*, 204(5):331 – 383, 1991. ISSN 0370-1573. doi: 10.1016/0370-1573(91)90131-5.

[250] Kruger, M., Schenk, M., and Hommelhoff, P. *Nature*, 475(7354):78–81, July 2011. ISSN 0028-0836.

[251] Krger, M., Schenk, M., Frster, M., and Hommelhoff, P. *J. Phys. B: At., Mol. Opt. Phys.*, 45(7):074006, 2012.

[252] Barwick, B., Corder, C., Strohaber, J., Chandler-Smith, N., Uiterwaal, C., and Batelaan, H. *New Journal of Physics*, 9(5):142, 2007.

[253] Miao, J., Ohsuna, T., Terasaki, O., Hodgson, K. O., and O'Keefe, M. A. *Phys. Rev. Lett.*, 89:155502, Sep 2002. doi: 10.1103/PhysRevLett.89.155502.

[254] Zuo, J. M., Vartanyants, I., Gao, M., Zhang, R., and Nagahara, L. A. *Science*, 300(5624):1419–1421, 2003. doi: 10.1126/science.1083887.

[255] Zuo, J., Gao, M., Tao, J., Li, B., Twesten, R., and Petrov, I. *Microscopy Research and Technique*, 64(5-6):347–355, 2004. ISSN 1097-0029. doi: 10.1002/jemt.20096.

[256] Chang, C.-C., Kuo, H.-S., Hwang, I.-S., and Tsong, T. T. *Nanotechnology*, 20 (11):115401, 2009.

[257] Garcia, N. and Rohrer, H. *Journal of Physics: Condensed Matter*, 1(23):3737, 1989.

[258] Scheinfein, M. R., Qian, W., and Spence, J. C. H. *Journal of Applied Physics*, 73(5):2057–2068, 1993. doi: 10.1063/1.353151.

[259] Fink, H.-W., Stocker, W., and Schmid, H. *Phys. Rev. Lett.*, 65:1204–1206, Sep 1990. doi: 10.1103/PhysRevLett.65.1204.

[260] Hasselbach, F. *Reports on Progress in Physics*, 73(1):016101, 2010.

[261] Missiroli, G. F., Pozzi, G., and Valdre, U. *Journal of Physics E: Scientific Instruments*, 14(6):649, 1981.

[262] Tonomura, A. *Rev. Mod. Phys.*, 59:639–669, Jul 1987. doi: 10.1103/RevModPhys.59.639.

[263] Lichte, H. and Lehmann, M. *Reports on Progress in Physics*, 71(1):016102, 2008.

[264] Gabor, D. *Nature*, 161:777–778, 1948. doi: 10.1038/161777a0.

[265] Caprez, A., Bach, R., McGregor, S., and Batelaan, H. *Journal of Physics B: Atomic, Molecular and Optical Physics*, 42(16):165503, 2009.

[266] Mollenstedt, G. and Duker, H. *Zeitschrift fur Physik*, 145(3):377–397, 1956. ISSN 0044-3328. doi: 10.1007/BF01326780.

[267] Hwang, I.-S., Chang, C.-C., Lu, C.-H., Liu, S.-C., Chang, Y.-C., Lee, T.-K., Jeng, H.-T., Kuo, H.-S., Lin, C.-Y., Chang, C.-S., and Tsong, T. T. *New Journal of Physics*, 15(4):043015, 2013.

[268] Schutz, G., Rembold, A., Pooch, A., Meier, S., Schneeweiss, P., Rauschenbeutel, A., Gunther, A., Chang, W., Hwang, I., and Stibor, A. *Ultramicroscopy*, 141(0):9 – 15, 2014. ISSN 0304-3991. doi: 10.1016/j.ultramic.2014.02.003.

[269] Kibble, T. W. B. *Phys. Rev. Lett.*, 16:1054–1056, Jun 1966. doi: 10.1103/PhysRevLett.16.1054.

[270] Batelaan, H. *Rev. Mod. Phys.*, 79:929–941, Jul 2007. doi: 10.1103/RevModPhys.79.929.

[271] Hebeisen, C. T., Ernstorfer, R., Harb, M., Dartigalongue, T., Jordan, R. E., and Miller, R. J. D. *Opt. Lett.*, 31(23):3517–3519, Dec 2006. doi: 10.1364/OL.31.003517.

[272] Hebeisen, C. T., Sciaini, G., Harb, M., Ernstorfer, R., Dartigalongue, T., Kruglik, S. G., and Miller, R. J. D. *Opt. Express*, 16(5):3334–3341, Mar 2008. doi: 10.1364/OE.16.003334.

[273] Kapitza, P. L. and Dirac, P. A. M. *Mathematical Proceedings of the Cambridge Philosophical Society*, 29:297–300, 5 1933. ISSN 1469-8064. doi: 10.1017/S0305004100011105.

[274] Bucksbaum, P. H., Schumacher, D. W., and Bashkansky, M. *Phys. Rev. Lett.*, 61:1182–1185, Sep 1988. doi: 10.1103/PhysRevLett.61.1182.

[275] Freimund, D. L., Aflatooni, K., and Batelaan, H. *Nature*, 413(6852):142–143, September 2001. ISSN 0028-0836. doi: 10.1038/35093065.

[276] Stocker, W., Fink, H.-W., and Morin, R. *Ultramicroscopy*, 31(4):379 – 384, 1989. ISSN 0304-3991. doi: http://dx.doi.org/10.1016/0304-3991(89)90336-7.

[277] Fink, H.-W., Stocker, W., and Schmid, H. *Phys. Rev. Lett.*, 65:1204–1206, Sep 1990. doi: 10.1103/PhysRevLett.65.1204.

[278] Weber, D. H., Beyer, A., Völkel, B., and Gölzhäuser, A. *Small*, 6(12):1264–1267, 2010. ISSN 1613-6810. doi: 10.1002/smll.201000404.

[279] Mutus, J. Y., Livadaru, L., Robinson, J. T., Urban, R., Salomons, M. H., Cloutier, M., and Wolkow, R. A. *New Journal of Physics*, 13(6):063011, 2011.

[280] Mutus, J. Y., Livadaru, L., Urban, R., Pitters, J., Legg, A. P., Salomons, M. H., Cloutier, M., and Wolkow, R. A. *New Journal of Physics*, 15(7):073038, 2013.

[281] Beyer, A. and Glzhuser, A. *Journal of Physics: Condensed Matter*, 22(34):343001, 2010.

[282] Quinonez, E., Handali, J., and Barwick, B. *Review of Scientific Instruments*, 84(10):103710, 2013. doi: http://dx.doi.org/10.1063/1.4827035.

[283] Yanagisawa, H., Hafner, C., Doná, P., Klöckner, M., Leuenberger, D., Greber, T., Hengsberger, M., and Osterwalder, J. *Phys. Rev. Lett.*, 103:257603, Dec 2009. doi: 10.1103/PhysRevLett.103.257603.

[284] Smith, J. D., Cappa, C. D., Drisdell, W. S., Cohen, R. C., and Saykally, R. J. *J. Am. Chem. Soc.*, 128(39):12892–12898, 2006. doi: 10.1021/ja063579v. PMID: 17002384.

[285] Hoyst, R., Litniewski, M., Jakubczyk, D., Kolwas, K., Kolwas, M., Kowalski, K., Migacz, S., Palesa, S., and Zientara, M. *Reports on Progress in Physics*, 76(3):034601, 2013.

[286] Yuk, J. M., Park, J., Ercius, P., Kim, K., Hellebusch, D. J., Crommie, M. F., Lee, J. Y., Zettl, A., and Alivisatos, A. P. *Science*, 336(6077):61–64, 2012. doi: 10.1126/science.1217654.

[287] Mutus, J. Y., Livadaru, L., Robinson, J. T., Urban, R., Salomons, M. H., Cloutier, M., and Wolkow, R. A. *New Journal of Physics*, 13(6):063011, 2011.

[288] Mak, K. F., Sfeir, M. Y., Wu, Y., Lui, C. H., Misewich, J. A., and Heinz, T. F. *Phys. Rev. Lett.*, 101:196405, Nov 2008. doi: 10.1103/PhysRevLett.101.196405.

[289] Gramotnev, D. K. and Bozhevolnyi, S. I. *Nat Photon*, 8(1):13–22, January 2014. ISSN 1749-4885.

[290] Berweger, S., Atkin, J. M., Olmon, R. L., and Raschke, M. B. *The Journal of Physical Chemistry Letters*, 3(7):945–952, 2012. doi: 10.1021/jz2016268.

[291] Neacsu, C. C., Berweger, S., Olmon, R. L., Saraf, L. V., Ropers, C., and Raschke, M. B. *Nano Letters*, 10(2):592–596, 2010. doi: 10.1021/nl903574a. PMID: 20067296.

[292] Herrmann, L. O., Valev, V. K., Tserkezis, C., Barnard, J. S., Kasera, S., Scherman, O. A., Aizpurua, J., and Baumberg, J. J. *Nat Commun*, 5:–, July 2014. doi: 10.1038/ncomms5568.

[293] Esteban, R., Taylor, R. W., Baumberg, J. J., and Aizpurua, J. *Langmuir*, 28 (24):8881–8890, 2012. doi: 10.1021/la300198r. PMID: 22364608.